Directional Sensing and Actin Dynamics in *Dictyostelium Discoideum* Amoebae

A DISSERTATION

SUBMITTED TO THE FACULTY OF THE GRADUATE SCHOOL

OF THE UNIVERSITY OF MINNESOTA

BY

Varunyu Khamviwath

IN PARTIAL FULFILLMENT OF THE REQUIREMENTS

FOR THE DEGREE OF

Doctor of Philosophy

Hans G. Othmer, Adviser

August, 2012

Acknowledgements

I am grateful to Hans Othmer for his guidance, support, and care. Hans accepted me as his student, introduced me to mathematical biology, and always gave me insightful perspectives. His dedication to scientific advancement is exemplary and inspires me to carefully examine the implication of my work. I would like to thank Bernado Cockburn. Bernado instilled in me an interest in numerical analysis and gave me helpful advices. I would also like to thank my committee including Duane Nykamp, Yoichiro Mori, Douglas Arnold, Richard McGehee, and David Odde, for valuable comments and discussions.

In addition, I would like to thank Jifeng Hu, who worked closely with me on actin waves, for fruitful discussions and encouragement. I would like to thank everyone in Hans' group for their friendship and support.

For mom and dad

Contents

List of Tables

List of Figures

Chapter 1

Background

1.1 Eukaryotic chemotaxis

Chemotaxis, which is directed cell movement in response to external chemical gradients, is one of the most basic cell physiological responses and plays an essential role in many biological processes, such as embryogenesis, wound healing, metastasis, immune response, and inflammation.

The study of cell motility consists of many different aspects, and the study of chemotaxis in individual cells, in particular, poses two major questions. The first question is related to signal transduction: how cells detect an extracellular pattern of chemical stimuli, extract the information, and convert it into executable signals seen by autonomous force-generating intracellular components. The second question, which is closely related and equally important, addresses the mechanisms of formation and modification of internal structures to generate force and movement in response to the processed intracellular signals.

The current understanding of chemotaxis in flagellated bacteria such as *E. Coli* is fairly advanced. The movement of *E. Coli* can be described by a biased random walk,

whereby temporal gradients of attractants are translated into a bias in the frequency of changing directions. On the other hand, the chemotaxis of eukaryotic cells is poorly understood although it could potentially lead to a broad spectrum of biomedical applications. Despite decades of continuing research effort and much progress in recent years, our understanding of the overall process is still incomplete. Due to the complexity of the process, the study of eukaryotic chemotaxis has proceeded in two different directions, exploring the signal transduction network, and determining mechanisms of force and movement generation.

Upon exposure to an extracellular stimulus, eukaryotic cells extend their leading edges, enriched by force-generating networks of filamentous actin (F-actin), and attach them to the substratum while their trailing edges are being retracted. In contrast to bacterial chemotaxis where cells rely on a temporal gradient of chemoattractant to determine direction, eukaryotic cells also utilize a spatial gradient to sense direction. Due to the larger cell size and more developed machinery for chemotaxis, they are able to detect and translate a gradient of chemoattractant across the cells. The spatiotemporal chemotaxis was demonstrated in *Dictyostelium discoideum* by using Latrunculin A (LatA), an inhibitor of F-actin. Upon treatment with the drug, monomeric G-actin is sequestered and cannot form into F-actin. Due to depletion of G-actin, F-actin in pseudopods, the cell cortex, and other actin-rich structures completely depolymerizes. The cells become round and nonmotile. Despite their inability to produce F-actin and generate movement, the nonmotile *Dictyostelium* cells are able to polarize towards a gradient of 3'-5'-cyclic adenosine monophosphate (cAMP), a chemoattractant for *Dictyostelium*. Their leading edges are characterized by highly localized patches of phosphatidylinositol (3,4,5)-triphosphate (PIP_3), a phospholipid which colocallizes with F-actin at leading edges in motile cells, along the pheriphery.

Interestingly, the cellular slime mold *Dictyostelium discoideum* shares the same

amoeboid movement with other eukaryotic cells, especially neutrophils. Moreover, the key signaling pathways are conserved from the amoeba to higher eukaryotes. Because of its relatively small genome and ease of genetic manipulation, *Dictyostelium* has become an excellent model for studying eukaryotic chemotaxis and has advanced the study enormously.

1.2 *Dictyostelium discoideum*

The social amoeba *Dictyostelium discoideum* exemplifies the exploitation of oscillatory signaling for self-organization and survival. These cells normally live in forest soil, where they feed on bacteria. Upon starvation, amoebae become chemotactically sensitive to 3'-5'-cyclic adenosine monophosphate (cAMP) and acquire competence to relay cAMP signals within a period of six hours. After about eight hours, randomly located cells, called pacemakers, start to emit cAMP periodically. Surrounding cells relay the cAMP signal to more distant cells and move towards the cAMP source. Eventually the entire population collects into mound-shaped aggregates containing up to 10^5 cells. A mound elongates to form a slug, which topples over and migrates over the substratum. Meanwhile the cells start to differentiate into prestalk and prespore cells. Differentiation initially starts at random in the mound stage, but by a combination of cell sorting and positional signaling, the prestalk cells eventually end up in the anterior quarter of the slug, while the prespore cells occupy the remaining posterior part. When conditions for fruiting body formation are favorable, the slug tip is extended upwards, the anterior prestalk cells become immobilized in a central stalk tube, and the remaining cells use them as a support for upward movement. When the stalk has reached a certain length the prespore cells mature into spores, which remain dormant until they are dispersed and meet with conditions favorable for growth. Figure 1.1 depicts the multicellular developmental cycle of *Dictyostelium*.

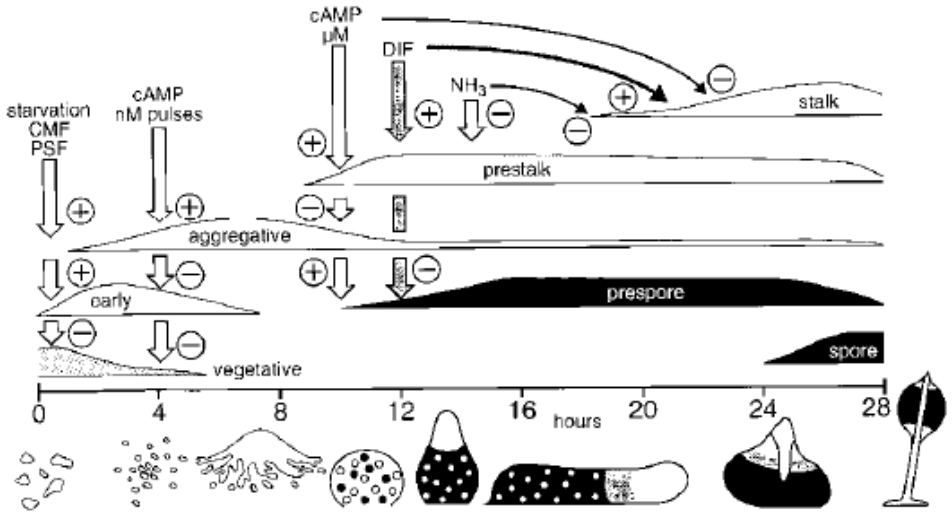

Figure 1.1: The temporal pattern of gene activation in the development of *Dictyostelium discoideum* [146].

The autonomous production and relay of cAMP pulses by starving cells results in a very efficient process of chemotactic aggregation, and cAMP oscillations subsequently organize the transformation of mounds into slugs, the migration of slugs over the substratum, and the culmination into fruiting bodies. These morphological changes are accompanied by a program of stage- and cell-type-specific gene expression, which ultimately causes amoebae to differentiate into accurately-regulated proportions of spore and stalk cells.

Extracellular cAMP also plays a crucial role in gene regulation during development. During aggregation, cAMP pulses strongly accelerate expression of components of the cAMP signaling system. During post-aggregative development cAMP directly induces

entry into the spore differentiation pathway, and, by inducing the synthesis of a stalk-cell-inducing factor, DIF, cAMP is also indirectly responsible for the differentiation of stalk cells.

1.3 Chemotaxis in *Dictyostelium discoideum* amoebe

Chemotaxis in *Dictyostelium* is observed during both growth and development phases. During the growth phase, they migrate towards folate secreted by bacteria to feed on them. Upon starvation, *Dictyostelium* cells develop into aggregates by secreting and moving upwards cAMP gradients. Our work focuses on the chemotaxis towards cAMP, which has been used extensively to study eukaryotic chemotaxis.

1.3.1 Gradient-dependent behaviors

A crawling *Dictyostelium* cell is elongated and has a distinct front and back. At the leading edge, the cell extends pseudopods, formed by local nucleation and polymerization of actin. Newly formed pseudopods are stabilized and thus form traction sites by adhering to a surface via transmembrane receptors. Actomyosin contraction at the rear and the sides of the cell leads to retraction of its uropod and pulls the cell forward.

Dictyostelium cells migrate differently under the range of cAMP gradients. Under a strong cAMP gradient, a *Dictyostelium* cell consistently extends pseudopods and moves directly towards the source. In contrast, simultaneous generation of multiple pseudopods on an existing protrusion is common under a shallow gradient [5]. They may become stabilized but only one pseudopod usually survives while others eventually retract. Occasionally, *de novo* pseudopods extend from the sides or the trailing edge. Andrew and Insall [5] argued that pseudopod generation is a spontaneous process while a chemoattractant gradient modulates survival of pseudopods. In fact, it is observed that *Dictyostelium* cells consistently extend pseudopods even in the absence of external cues

[127, 17]. In this case, they move in a zig-zag fashion with persistence time of around 10 minutes before the direction is lost. They tend to turn left and right alternately with random angles following an exponential distribution and 1-2 minutes on average between turns.

To explain *Dictyostelium* movement under the broad spectrum of signaling regimes, it is crucial to understand the signal-detection process induced by cAMP, the internal process which drives motility, and how they interact. The directional sensing machinery for *Dictyostelium* chemotaxis has been extensively studied and we will study possible mechanisms leading to spatial orientation of intracellular molecules related to motility. On the other hand, the internal process leading to random protrusions is not well understood. We will study related, yet more amendable, spontaneous organization of actin structures, called actin waves, predominantly observed during cell recovery after treatment with latrunculin A (LatA), an actin depolymerization drug [66]. Because actin waves are also observed in normal cells and share basic molecular elements with pseudopod extensions, we believe insights from the actin waves will lead to a better understanding of the random pseudopod formation.

1.3.2 Responses to chemical stimulation

Dictyostelium cellular responses pertinent to chemotaxis are formation of a branched network of filamentous actin (F-actin) at the anterior [152] and actomyosin complex, composed of crosslinked F-actin bundles and myosin II motors, at the posterior [19]. The formation of the branched F-actin network drives protrusion of pseudopods as F-actin pushes the cell membrane forward. Meanwhile, the contraction of actin bundles by myosin II is responsible for retraction of the trailing edge. In addition to the responses leading to cell movement, cAMP stimulation induces production and secretion of intracellular cAMP, which is used to relay the cAMP signal to distant cells during

aggregation. The signaling pathway for cAMP relay is tightly integrated with signaling pathways which regulate responses at the leading edge [64]. Figure 1.2 illustrates localization of some molecular components in a chemotaxing *Dictyostelium* cell.

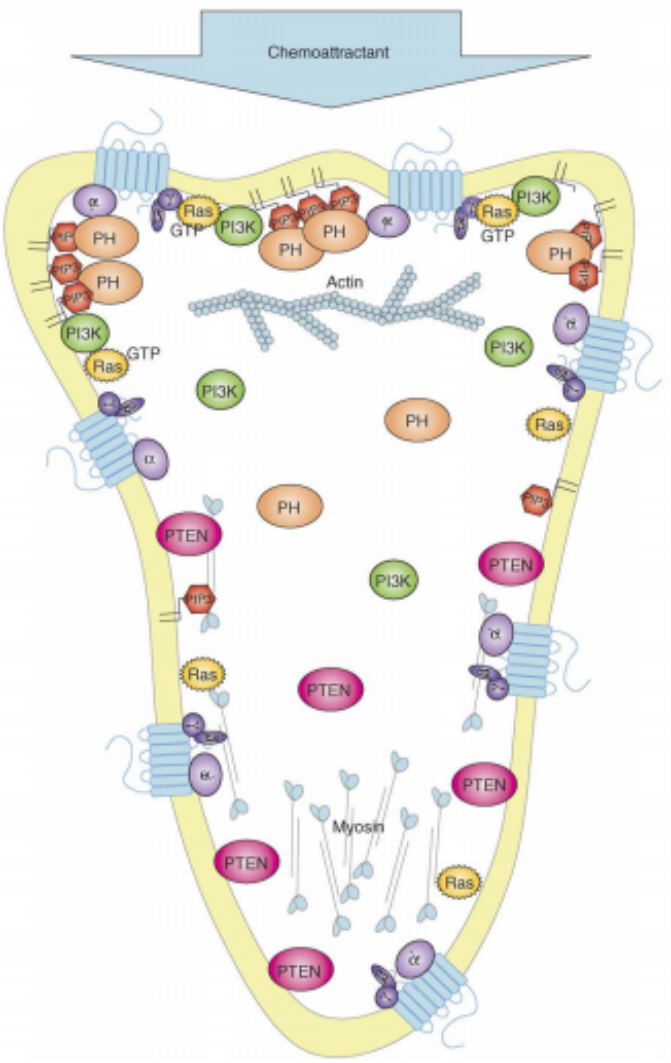

Figure 1.2: Illustration of a chemotactic *Dictyostelium* cell displaying localization of F-actin, myosin II, and other molecular components related to chemotaxis [35].

Uniform cAMP stimulation leads to a sharp increase in concentrations of F-actin

and various molecules such as PIP_3, cyclic guanosine monophosphate (cGMP), and intracellular cAMP. *In vivo* visualization reveals that the newly-produced F-actin and PIP_3 are localized at the cell pheriphery. At the same time, cells become immobile and pseudopod formation is inhibited. Then the cells retract existing pseudopodia and become round within 20 seconds after the introduction of cAMP, referred to as the cringe response. Correlated with the cringe response is a rapid drop in F-actin and PIP_3 to the prestimulated level, called adaptation. Subsequently, a second rise of F-actin and PIP_3 occurs at random locations of the plasma membrane along with pseudopod extensions. The localized response eventually ceases at the old sites as F-actin accumulates at new sites along the periphery, resulting in cells less polarized than unstimulated cells. Cell motility resumes 50-60 seconds after stimulation as the cells start extending pseudopodia.The level of total F-actin polymerization in the cells after the second rise remains above the basal level [79, 155].Figure 1.3 displays F-actin activity under uniform stimulation with $1\mu M$ cAMP.

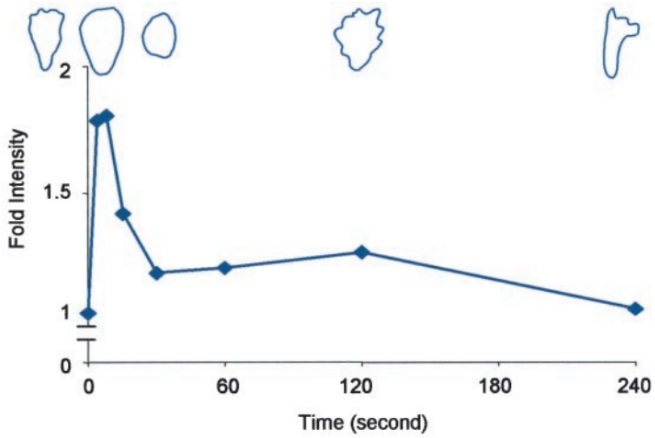

Figure 1.3: F-actin dynamics in *Dictyostelium* cells after 1 μM cAMP stimulation [39]. Associated cell shapes during the time course are depicted above the graph.

Unlike F-actin and PIP_3 activities, other cAMP-induced activities such as production and secretion of intracellular cAMP, association of myosin II with the cytoskeleton, activation of phospholipase C (PLC), and production of cGMP display full adaptation [143, 49, 108]. The adaptation of the intracellular cAMP and myosin II activities occur more slowly than other responses, within several minutes.

Adaptation allows *Dictyostelium* cells to respond to stimulation under a wide range of background cAMP levels. They respond to uniform cAMP stimulation with concentrations as low as 0.1 nM while the F-actin localization response becomes consistent at 1 nM [156, 22]. Incremental increases up to the saturating stimulus level of 1 μM in total cAMP concentration induce further responses in adapted cells [49, 76]. Although generation of random F-actin patches are observed in the adapted cells, they are capable of responding to further stimulation [156]. The sensitivity to the same level of stimulus is restored after a recovery period once the stimulus is removed [52, 197]. Figure 1.4 shows adapting cAMP-secretion responses by successive cAMP stimulation and recovery after removal of the stimulus.

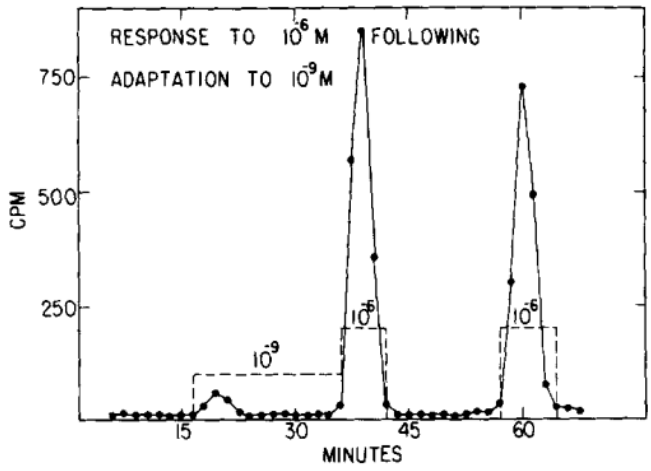

Figure 1.4: Adaptation of the cAMP-secretion response to successive stimulation [49].

Removal of cAMP induces retraction of pseudopodia, and rounding of cells. Eventually, random pseudopod extension and motility are resumed. Interestingly, simultaneous removal of a chemoattractant and introduction of a different chemoattractant with lower concentration evokes further extension of pseudopodia [50]. This implies that the adaptation mechanism lies early in the common signal transduction pathway.

Dictyostelium discoideum possesses an ability to move toward the source under a cAMP gradient as low as 2% across the cell [57, 132, 110]. Upon stimulation with a chemoattractant gradient, *Dictyostelium* cells display the same biphasic response as under a uniform stimulation. However, the second rise in F-actin and PIP_3 localization occurs around the location with the highest cAMP concentration [44]. During the second increase, cells in an early aggregation stage directly extend pseudopodia and develop polarization in the direction of the gradient. On the other hand, cells with more developed polarization tend to steer or to extend their pseudopodia at the leading edge toward the attractant source [39]. The cells maintain polarized morphology, polarization of signaling molecules, and movement towards the source while the gradient is applied. Figure 1.5 displays chemotaxis of *Dictyostelium* cells as they crawl towards micropipettes releasing cAMP. See [12] for chemotactic migration of swimming *Dictyostelium* cells.

Studies of cells immobilized by LatA suggested that the cAMP-induced localization of signaling molecules requires neither an actin cytoskeleton nor a morphology change. The induced gradient persists until the chemoattractant gradient is removed in the immobilized cells [149]. The ability to detect the static gradient is strong evidence that *Dictyostelium* responds to spatial gradients as well as temporal gradients of chemoattractants. The induced spatial response is sharply localized towards the cAMP source, which thereby greatly amplifies the spatial gradient of cAMP itself. Moreover, when a cAMP source is rotated around a LatA-treated cell, localization of signaling molecules

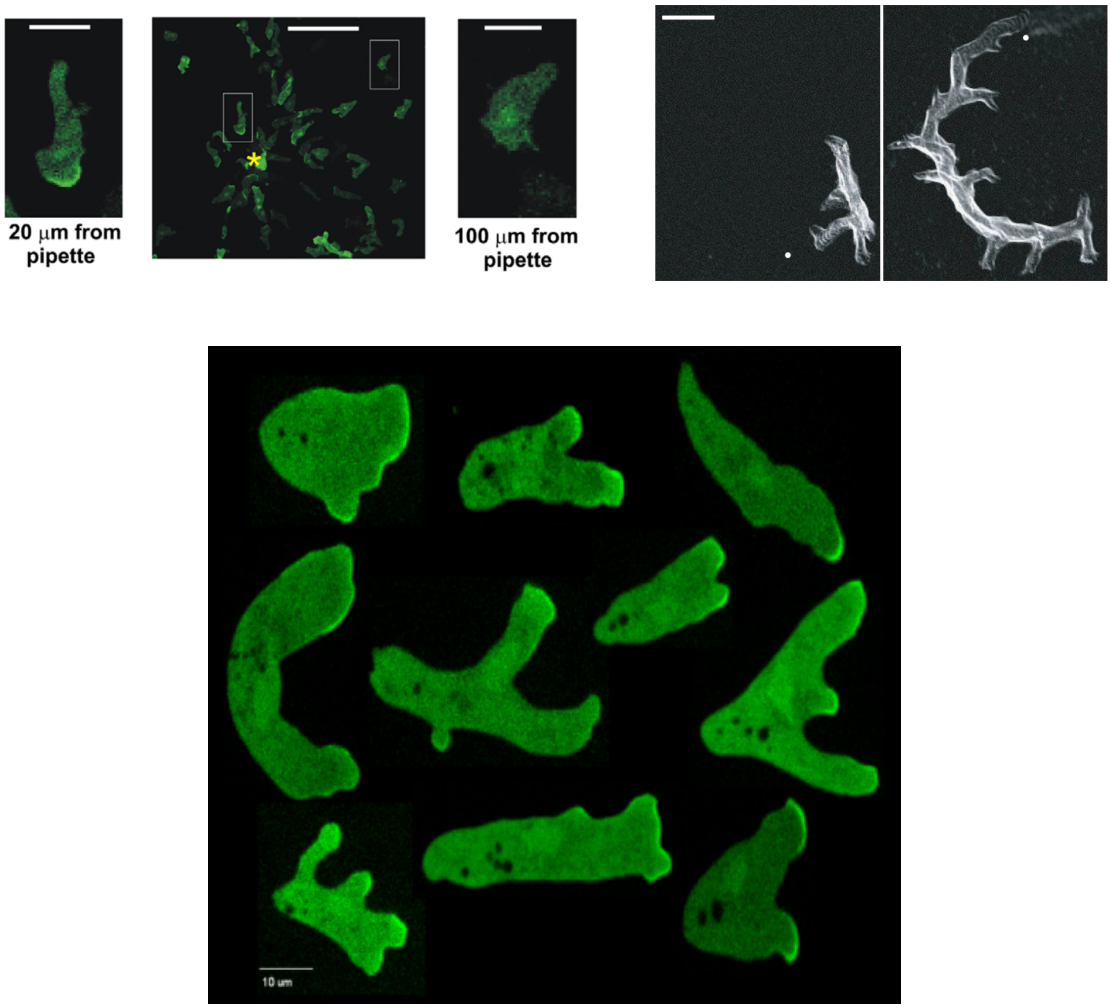

Figure 1.5: *Dictyostelium* chemotaxis towards micropipettes. *(Upper left)* Cells expressing PH_{CRAC}-GFP, a reporter for PIP_3, migrate towards a micropipette filled with $100\mu M$ cAMP [22]. *(Upper right)* Overlays of a polarized *Dictyostelium* cell chemotaxing towards a micropipette releasing $1\mu M$ cAMP which is moved from the bottom to the top-right area of the screen [5]. *(Lower)* Localization of Ras activity in *Dictyostelium* cells with various shapes under a static cAMP gradient [167].

follows the rotation of the gradient source. Multiple sources of chemoattractant simultaneously induce localization of signaling molecules at multiple sites of *Dictyostelium* cells immobilized by LatA [90, 196].

1.3.3 Spontaneous behaviors of actin network

Dictyostelium cells are able to move in the absence of external chemoattractants by periodically extending pseudopods at random locations around the membrane. This random migration allows the *Dictyostelium* cells to explore their environment. Three-dimensional visualization reveals that the extensions undergo specific sequences of events, indicating that internal machinery is involved. Because F-actin polymerization is required for the pseudopod extensions and the spontaneous localization of signaling molecules normally associated with pseudopods such as PIP_3, it is suggested that F-actin is the driving force for the spontaneous activity [191, 162]. The dendritic network, a highly-branched F-actin network which drives pseudopod extensions, is a common structure among eukaryotic cells. Figure 1.6 depicts the dendritic network in fish epidermal keratocytes.

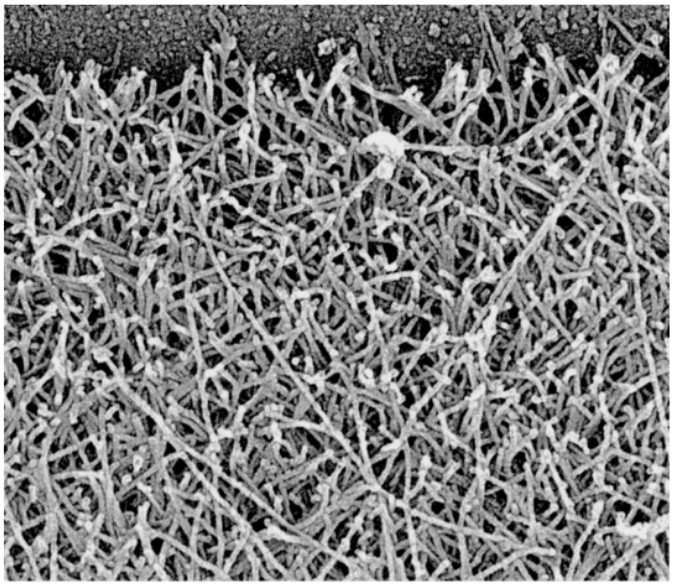

Figure 1.6: An electron micrograph of a migrating keratocyte shows the dendritic network at the leading edge [151].

In addition to its presence in pseudopod extensions, F-actin is also highly enriched in other cellular structures on the membrane such as filopodia, phagosomes, and macropinosomes. Filopodia are long thin cell extensions which are related in multiple cellular processes including long-range cell-to-cell communication and detection of extracellular gradients. Phagosomes and macropinosomes are related to internalization, or uptake, of large particles such as pathogens and extracellular fluids respectively [190].

Actin waves

Interestingly, different structures of F-actin consisting of foci and motile bands are observed on the substrate-attached cell surface [187, 23, 51]. In contrast to well-defined actin-rich structures, they typically do not face the cell border. The foci are stationary and have a lifetime of between 7-10 seconds. The motile bands, also called actin waves, have been implicated in formation of other actin structures. They propagate on the cell-substrate surface and cause membrane extensions when they are in contact with the cell membrane. Moreover, it is observed that actin waves convert into phagocytic cups upon contact with external particles [67].

The actin waves can be efficiently observed in *Dictyostelium* cells during recovery from LatA treatment. Application of 5 μM LatA causes disintegration of the actin network in the cell cortex and leading edges into mobile patches and clusters after 20 seconds. Within 10 minutes, the cells become round and immobile as the fluorescent probes for F-actin are uniformly distributed within the cytosol. Removal of LatA allows the cells to regain the normal actin organization within an hour. The actin waves are the prominent feature of F-actin structures during the last phase before the cells are fully recovered. The phase with dominent actin waves can be prolonged if the concentration LatA is diluted to 1 μM instead of being removed.

After removal of LatA, F-actin dynamics undergoes three distinct phases. First,

dynamic foci of F-actin are formed throughout the substrate-cell surface. The motile patches are able to divide and fuse with each other. They also grow and fade away independently of other foci. Then, the actin patches are transformed into actin waves as they fuse into clusters and accumulate around the cell border forming a contiguous area. The bottom cell-surface area is extended as the contiguous area enclosed by the actin waves expands. The third phase is characterized by the evolution of the actin waves. Eventually, the activity of the actin waves declines as the normal actin network is recovered [66].

The actin waves are generally formed into a closed band which continuously alters its shape by propagating, expanding, and retracting on the cell-substrate surface. The propagation speed of the wave fronts is around 6 $\mu m/min$. Wave fronts are capable of abruptly changing their propagating directions, causing an expanding enclosed area to retract and an retracting area to expand. A closed band can break into spiral waves where the broken ends of the band connect with the band at the other side of the area, forming two separate enclosed areas. As the newly-formed enclosed areas continue to evolve, they may collide and fuse into one area while the colliding wave fronts are annihilated. In some cases, one of the newly-formed closed bands shrinks and diminishes and the surviving area eventually expands to cover the substrate-cell surface. There are also instances when a broken band collapses and the entire actin wave is annihilated [187, 66, 165, 24]. Figure 1.7 displays evolution of actin waves in *Dictyostelium* cells.

The three-dimensional structure of the actin waves has been studied using z-scan confocal microscopy. The scans reveal a regular profile of actin wave fronts. The actin structure extends steeply into the cytosol at the front, reaching the height of 1-2 μm into the cytoplasm. Behind the peak, it gradually slopes down towards the back. The length of an entire actin wave front is approximately 1.8 μm. In addition to the prominent wave fronts, the z-scan images also show an actin structure of less density in the area enclosed

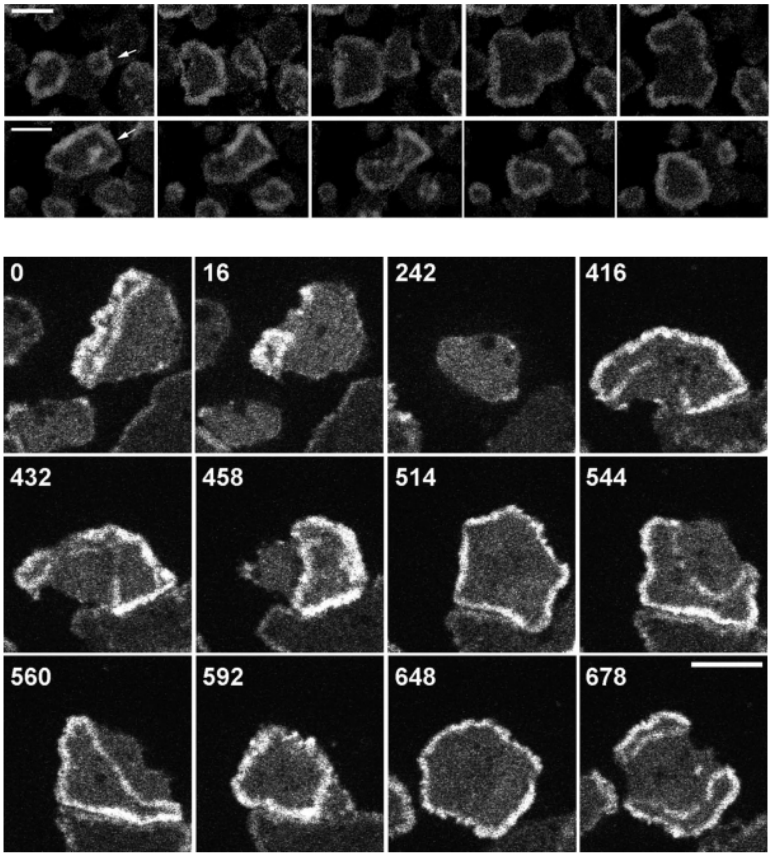

Figure 1.7: Actin waves in normal and LatA-treated cells. *(Top panel)* Wild-type *Dictyostelium* cells exhibit actin waves which fuse and later form spiral waves *(top row)* and an actin wave which breaks into two waves *(bottom row)* [187]. Images are 15 s and 25 s apart in the top and bottom rows respectively. *(Bottom panel)* Evolution of actin waves in a LatA-treated cell displays expansion, retraction, separation, and collapse of the waves. The cell becomes in contact with another cell between 416 s and 592 s [165].

by the waves that connects wave fronts [66, 24]. In untreated cells, a three-dimensional hemispherical structure of actin waves that extends through the entire height of the cell, approximately 6 μm, has been observed [187].

In fluorescence recovery after photobleaching (FRAP) experiments, bleached spots of the F-actin marker and other molecular constituents are stationary with respect to wave propagation [24]. The authors used this data to preclude the possibility that

existing filaments are transported as the actin waves propagate and supports a model where new filaments are continuously generated at the wave fronts while aging filaments towards the back are recycled.

1.4 Signal-transduction network

Dictyostelium chemotactic responses involve multiple signaling pathways which collectively contribute to pseudopod extensions at the front, retraction of uropods at the back, and secretion of cAMP. Blocking one signaling pathway results in mild chemotaxis defects such as reduced migration speed or the inability to chemotax under shallow gradients. However, the mutants *Dictyostelium* cells are able to maintain a high chemotaxis index and migrate efficiently towards the cAMP source under large cAMP gradients [121, 40, 183, 186]. In contrast, disrupting multiple pathways leads to more impaired directionality and ultimately to a complete loss in chemotactic ability. A recent study by Kortholt et al. [110] reports chemotactic efficiency when various combinations of known pathways are disrupted. In this section, we will discuss *Dictyostelium* chemotaxis pathways, their activities, and their importance for chemotactic responses.

1.4.1 G-protein coupled receptors

The first step in *Dictyostelium* chemotaxis involves binding of a chemoattractant by G-protein coupled receptors (GPCRs). GPCRs, which constitute a large family of seven transmembrane receptor proteins, mediate signals by activating heterotrimeric G proteins. The *Dictyostelium* GPCRs that bind cAMP are called cARs. cAR1 has high affinity for cAMP and is essential for signal transduction during early development and chemotaxis [106].

A cAMP-bound GPCR acts as a guanine nucleotide exchange factor (GEF), which exchanges guanosine-5'-triphosphate (GTP) for guanosine diphosphate (GDP), for the

Gα subunit of the heterotrimeric G protein, causing dissociation between the active Gα subunit and the G$\beta\gamma$ subunits. Free Gα and G$\beta\gamma$ subunits serve different functions and have different downstream effectors. Hydrolysis of GTP in the Gα subunit induces reassociation, which diminishes active G-protein subunits when external cAMP is removed. It is not clear how GPCR is coupled with the heterotrimeric G protein although a recent study suggests that they are only coupled as they interact [198].

There are only one Gβ subunit and one Gγ subunit present in *Dictyostelium*. They form the G$\beta\gamma$ complex, which is responsible for most cAMP-mediated responses. Removal of the β subunit of the heterotrimeric G protein, which directly interacts with membrane-bound receptors introduces severe defects in chemotaxis and cAMP secretion, and cGMP production [193]. The mechanism by which G$\beta\gamma$ mediates chemotaxis signals is poorly understood. Among the closest effectors of G$\beta\gamma$ are presumably the guanine nucleotide exchange factors (GEFs) of the Ras subfamily of small G-proteins. RasC and RasG, which are regulated by RasGEFA (also known as AleA) and RasGEFR respectively, are crucial for cAMP-mediated responses. Disruption of RasC and RasG activities leads to severe defects in chemotaxis and signal relay [97, 36, 14, 110]. In a recent study, G$\beta\gamma$ has been found to interact directly with *Dictyostelium* ElmoE, a part of the evolutionarily conserved Elmo/Dock complex, upon cAMP stimulation. ElmoE associates with a Dock-like protein and is necessary for activation of the small GTPase RacB, implicating a role in branching nucleation of F-actin. The first peak of F-actin activity under a uniform dose of cAMP is reduced in *elmoE−* cells. Nevertheless, lack of ElmoE activity does not effect Ras activity and vice versa [199].

Three Gα subunits have been identified in cAMP signal-transduction pathways. Gα_1 and Gα_2 are linked with cAR1 and act as activator and inhibitor of PLC respectively [16]. Gα_9 has also been shown to negatively regulate overall responses [15, 29]. However, the connection between Gα_9 and cellular responses is poorly understood.

Studies have shown that distribution of cAR1 remains uniform under a cAMP stimulation. The G-protein subunits remain free when cAMP is present and reassociate when cAMP is removed, suggesting that adaptation does not occur at this level [89, 196, 197]. Under a gradient, the intracellular Gβ subunit is slightly polarized toward the cAMP source [93]. However, the polarization of the Gβ subunit is absent under treatment with LatA [93, 196].

1.4.2 Ras subfamily proteins

The Ras subfamily of small G-proteins are GTPases that function like molecular switches, cycling between the active GTP-bound stage and the inactive-GDP bound stage. They are active in the GTP-bound stage. Activation of Ras proteins is regulated by GEFs which exchange GTP for GDP. GTPase-activating proteins (GAPs) deactivate Ras proteins by stimulating their GTP hydrolysis activity.

Two Ras-subfamily proteins, RasC and RasG, are necessary for chemotactic responses at the leading edge and the trailing edge. They are also necessary for the activation of adenylyl cyclase expressed during aggregation (ACA), which converts ATP into cAMP used in the signal relay [14, 110]. RasC is necessary for the activity of the target of rapamycin complex 2 (TORC2) pathway, while RasG is a dominant regulator for the phosphatidylinositol 3-kinases (PI3K) pathway. Moreover, $rasC-/rasG-$ cells fail to produce cGMP, which promotes myosin II activity, and cannot suppress pseudopod extensions at the back.

RasC and RasG appear to be upstream effectors in the *Dictyostelium* chemotaxis pathways. They display biphasic responses, similarly to F-actin and PIP_3, upon cAMP stimulation. Their cAMP-induced activities are abolished in $g\alpha 2$ null, $g\beta$ null, or cAR null mutants. However, their activation does not require any known pathways for *Dictyostelium* chemotaxis, including the presence of F-actin [96, 161, 110].

RasG is found to uniformly localize along the plasma membrane regardless of cAMP stimulation, although GFP-tagged RasG is also found in the cytosol [161]. The activation of RasC and RasG are regulated by RasGEFA and RasGEFR respectively [97]. In addition to the cAMP-induced activity, RasG is also active in random pseudopod extensions. This spontaneous activity is independent of cAMP stimulation, as they are observed in $g\beta$ null mutants. Inhibition of either PI3K or F-actin activity disrupts the RasG activity and the pseudopod extension, indicating a positive feedback loop involving RasG, PI3K, and F-actin [162].

GAPs are negative regulators of Ras. The only known RasGAP related to *Dictyostelium* chemotaxis is DdNF1 [203]. DdNF1 is partly responsible for deactivation of RasG. Mutants lacking DdNF1 display chemotaxis and cytokinesis defects. cAMP-mediated activity of RasB and RasG are elevated while RasC activity is unaffected in these mutants. A recent study by Lee et al. [122] found that the presence of myosin II has a negative effect on Ras activity although it remains unclear how Ras is regulated by myosin II.

1.4.3 Parallel signaling pathways

Many signaling pathways are responsible for chemotactic activities in *Dictyostelium*. Four key pathways that have been identified consist of the PI3K pathway, the TORC2 pathway, the phospholipase A2 (PLA2) pathway, and the soluble guanylyl cyclase (sGC) pathway [186, 175]. Inhibition of these pathways leads to a decreased ability of *Dictyostelium* cells to migrate towards a cAMP source [110, 183, 186]. Figure 1.8 displays an overview of established signaling pathways in *Dictyostelium* chemotaxis.

The PI3K pathway involves regulation of PIP_3 by PI3K and phosphatase and tensin homolog (PTEN). PIP_3 is a specific binding target for proteins containing the pleckstrin homology domain (PH domain). Production of PIP_3 triggers localization and activation

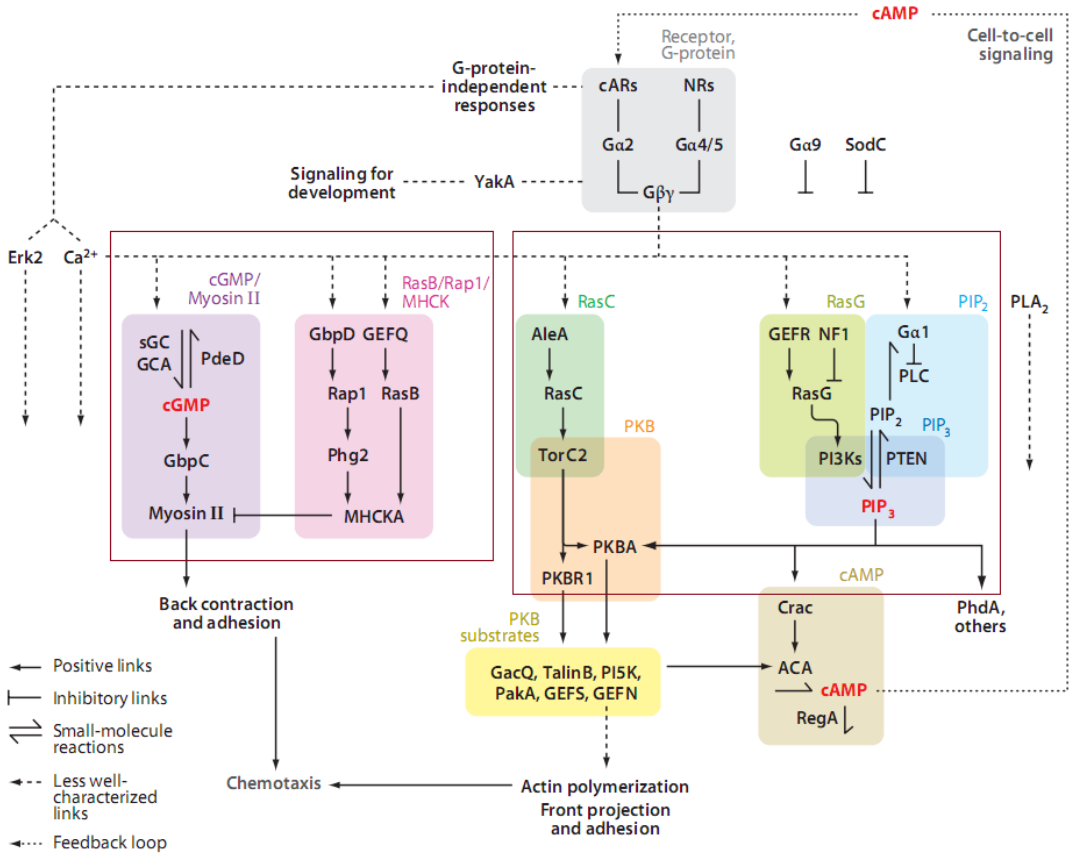

Figure 1.8: Summary of the signalling network controlling chemotaxis and intracellular cAMP production in *Dictyostelium discoideum* [175]. The diagram shows the GC pathway *(far left)*, the Rap1 and RasB pathways *(left)*, the TORC2 pathway *(middle)*, the PI3K pathway *(right)*, and the PLA2 pathway *(far right)*. The recently-found pathway involving the activation of RacB, which is also downstream of PIP_3, through ElmoE is missing from the diagram.

of its binding partners and eventually leads to F-actin polymerization and production of intracellular cAMP. This phospholipid signaling is the first recognized pathway and was believed to be solely responsible for cell reorientation under cAMP stimulation until Hoeller and Kay [85] showed that *Dictyostelium* cells with totally-disrupted PI3K pathway migrate towards a cAMP source with the chemotaxis index indistinguishable from

wild-type cells. Nevertheless, it remains the best understood pathway in *Dictyostelium* chemotaxis and the next section is devoted for discussion of this particular pathway.

TORC2 is activated at the front of migrating cells by RasC. It is necessary for the activation of ACA which produces intracellular cAMP, and the disruption of TORC2 leads to mild chemotaxis defects [121, 30, 36]. Furthermore, TORC2 is required for activation of protein kinase Bs (PKBs) including PKBR1 and PKBA. PKBR1 is constitutively localized on the membrane while PKBA is found in the cytosol and localizes to the membrane by binding to PIP_3 via its PH domain. TORC2 phosphorylates the hydrophobic motif (HM) of PKBR1 and PKBA while their full activation requires phosphorylation of both HM and the activation loop (AL). AL is phosphorylated by phosphoinositide-dependent kinase 1 (PDK1). The membrane localization, but not activation, of PDK1 is regulated by binding to PIP_3 via its PH domain [128, 100, 99]. Known immediate effectors of the TORC2 pathways include PAKa, TalinB, RasGEFN, RasGEFS, a PI(4)P 5-kinase domain containing protein and a RhoGAP-domain containing protein GACQ. These effectors are phospharylated transiently upon a uniform stimulation of cAMP via PKBR1 and PKBA. It has been observed that PAKa is crucial for myosin II filament assembly [42]. However, direct roles of this pathway on F-actin polymerization and ACA activation are unclear.

PLA2 was identified in *Dictyostelium* chemotaxis independently by genetic screens [40] and use of phamacological drugs [183]. They observed that inhibition of PLA2 activity, in addition to inhibition of PI3K, leads to a lower first peak of cAMP-induced F-actin activity and a lower chemotaxis index in *Dictyostelium* cells migrating towards a cAMP source. PLA2 is an enzyme that catalytically hydrolyzes phospholipids and releases arachidonic acid (AA) and lysophospholipids. *Dictyostelium* PLA2 converts phosphatidylcholine (PC) into lysophosphatidlycholine *in vitro*. PLA2 activity leads to Ca^{2+} influxes, both from the intracellular store and externally [164, 170]. Upon cAMP

stimulation, the level of AA transiently increases although the localization of PLA2 is not affected [40]. Direct connections of PLA2 activity to chemotaxis are unknown although it is observed that PLA2 is required for directional persistence of migrating cells as it enhances pseudopod splitting from existing pseudopods [17].

Dictyostelium possesses two guanylyl cyclases (GCs), guanylyl cyclase A (GCA) and sGC. Both produce cGMP although only sGC is predominant for cAMP-induced cGMP activation [185, 159]. sGC is localized to the leading edge in migrating cells and plays a cGMP-independent role in enhancing directionality of chemotaxing cells [185, 17]. Although there are four cGMP-binding proteins (Gbps) in *Dictyostelium*, only GbpC is activated by binding to cGMP. Although the membrane localization of GbpC is independent of cGMP, its activation by cGMP leads to association of myosin II filaments with actin bundles at the cell posterior. Moreover, GbpC activity leads to activation of myosin light chain kinase A (MLCKA) which induces contraction activity of the actomyosin complexes [20, 21, 70].

In addition to the four main pathways, there are less identified pathways such as the direct-Gβ activation of RacB through ElmoE, which possibly forms into an evolutionarily-conserved Elmo/Dock complex with either DdDockC or DdzizA [199]. Since RacB activity is associated with F-actin polymerization, this more direct activation could bypass and serve as an alternative to RacB activation mediated by PIP_3. Furthermore, the activation of Rap1, a Ras subfamily protein, by the GEF domain of GbpD has been linked to PI3K activation and the activity of Phg2, a serine/threonine-specific kinase which colocalize with Rap1 at the leading edge. Phg2 activity, in turn, leads to phospharylation of myosin heavy chains (MHCs) and prevent assembly of myosin II filaments at the leading edge. This Rap1 activity has been shown to be downstream of RasC and RasG [107, 91, 14, 109]. Another pathway which suppresses myosin II localization at the leading edge involves the activity of RasB. RasGEFQ, which is localized

to the cortex in an F-actin dependent manner, activates RasB upon cAMP stimulation. Activated RasB regulates myosin heavy chain kinase A (MHCKA), which is autophospharylated when localized to the cortex, supposedly by enhancing its localization to the leading edge. MHCKA, in turn, phospharylates MHC thereby preventing myosin II filament assembly [136].

In summary, there are many signaling pathways which regulate F-actin, myosin II, and ACA activities. Although each pathway may lead to multiple responses at the anterior and the posterior, they act in concert and are able to compensate for a missing pathway inhibited by gene deletion or pharmacological drugs. Recent experiments reveal roles of PLA and cGMP in directional persistence while PI3K activity and localization of sGC mediate directional bias [17, 18]. PI3K activity has also been implicated in random membrane protrusions, dose-dependent cAMP-induced patches, pseudopod extension rate, and polarity [162, 156, 5, 40]. Despite considerable understanding how each pathway ultimately affects chemotactic responses, the mechanisms of most pathways still need to be worked out.

1.4.4 Phospholipid signaling pathway

The phospholipid pathway, or PI3K pathway, mediates chemotactic signals by providing membrane binding sites for PIP_3-specific PH-domain containing proteins. PI3K converts phosphatidylinositol (4,5)-biphosphate ($PI(4,5)P_2$, abbreviated as PIP_2) into PIP_3, allowing membrane localization of the PH-domain containing proteins. The production of PIP_3 is complemented by the activity of PTEN which converts PIP_3 into PIP_2. In addition to PIP_3, phosphatidylinositol (3,4)-biphosphate ($PI(3,4)P_2$) can provide binding sites for the PH-domain containing proteins. It is regulated similarly to PIP_3 by PI3K and PTEN with phosphatidylinositol 4-phosphate (PI4P) as the substrate. Because the PI3K activity is usually measured as localization of a PH-domain

containing protein, the observed activity represents the combined activity of PIP_3 and $PI(3,4)P_2$.

The activity of the PI3K pathway is triggered by PI3K activation. PI3K is localized to the cortex in an F-actin, but not PI3K-activity, dependent manner. Although PI3K activity is not observed in *racC−* mutants, it has been observed in LatA-treated cells, where F-actin is dissolved and cells become round and flattened [161, 80, 119]. Membrane-bound PI3K requires independent activation before it becomes active. Known activators of PI3K are RasG and Rap1 [61, 14, 109]. Active PI3K converts PIP_2 into PIP_3 and this activity is complemented by PTEN. The membrane-localization and activity of PTEN is dependent on binding of its PIP_2 binding (PBD) domain to PIP_2, which is abundant in vegetative cells. In migrating cells, PTEN is found at the trailing edge and sides of the cells. Once localized on the plasma membrane, PTEN dephosphorylates the D3 position of PIP_3 and converts it into PIP_2. The activity of PTEN may be regulated indirectly by PLC as it can hydrolyze PIP_2 into inositol(1,4,5)-triphosphate ($InsP_3$) and diacylglycerol (DAG). In *plc* null mutants, transient PTEN detachment from the membrane under uniform stimulation is not observed [108]. Unlike other molecules in the *Dictyostelium* chemotaxis pathway, the activity of PLC is mediated by $G\alpha_2$ and inhibited by $G\alpha_1$. PLC is transiently activated upon cAMP stimulation and displays full adaptation. The PLC activity is also tightly coupled with the intracellular calcium level. This interaction has been studied by Kang and Othmer [101]. In an experiment by Keizer-Gunnink et al. [102], *Dictyostelium* cells migrate away from 8CPT-cAMP, a chomorepellant which inhibits PLC activity, in a PLC- and PI3K-dependent manner. It was suggested that cell polarization and PI3K responses under 8CPT-cAMP stimulation is mediated by PLC.

The PI3K activity leads to localization of PH-domain containing proteins, which serve various functions. Although F-actin is still polarized by a cAMP gradient when

the PI3K activity is inhibited by LY294002, a PI3K-inhibition drug, this PI3K activity is necessary for random pseudopod extensions and the second peak of the F-actin activity under uniform cAMP stimulation. Production of cGMP, in contrast, is normal when PI3K is inhibited [60, 39, 129, 162].

Immediate PIP_3 effectors includes PKBA, PDK1, cytosolic regulator of adenylyl cyclase (CRAC), and three *Dictyostelium* class-I myosins (myoD, myoE, myoF). Localization of CRAC to the membrane is necessary for cAMP production by ACA [88]. The localization of PKBA and PDK1 contributes to the activity of PKBA and PKBR1, which are also effectors of the TORC2 pathway. PAKa, which is an effector of PKBA and PKBR1, localizes to the trailing edge in migrating cells and enhances myosin II filament assembly. Disruption of PAKa leads to severely decreased cAMP-mediated myosin II assembly and a rapid loss of cell polarity [42]. The triple knockout of the PIP3-binding class I myosins severely reduce cAMP-mediated F-actin activity [37]. However, the roles of myoD, myoE, and myoF in *Dictyostelium* chemotaxis are still unknown.

In addition to the known immediate effectors of PIP_3, Rac-subfamily GTPases including RacB and RacC have been linked to PI3K and F-actin activities. Both RacB and RacC bind to WASP, a major regulator of F-actin branch nucleation, although RacC better stimulates WASP activation. The WASP activity mediated by Rac is crucial for F-actin polymerization. *racC* null mutants lack polarized F-actin organization and a prominant leading edge. Moreover, cells expressed with dominant-negative RacC, which cannot be activated and cannot bind to WASP, display more severe defects. They have a minimal level of F-actin and cannot migrate towards a chemoattractant source [80].

RacB displays a biphasic activity upon cAMP simulation similar to F-actin. *racB* null mutants display reduced F-actin polymerization and myosin II assembly. RacB regulation of myosin II is likely mediated by PAKc, its direct effector. Although the

activation of RacB via ElmoE is independent of PI3K, its activation via RacGEF1 is downstream of PI3K. Disruption of the PI3K activity lead to a small decrease in the first peak and a significant loss of the second peak of its biphasic response. In contrast, PTEN-deficient cells display elevated second peak of RacB activation. RacGEF1 was identified as a direct regulator of RacB and its localization to F-actin sites enhances activation of RacB. A portion of RacGEF1 is found to localized at the cell cortex in vegetative cells. cAMP stimulation induces localization of RacGEF1 to the cortex in a PI3K-dependent manner. In migrating cells, RacGEF1 localizes to the leading edge and, to a lesser extent, to the trailing edge both of which are regions of F-actin localization [120, 150].

In contrast to RacB, the activity of RacC is slightly decreased by 20-30 % within 5-10 seconds after cAMP stimulation. Then it is increased to 150-160 % of the unstimulated level after 30-45 seconds. RacC colocalizes with F-actin at the leading edge, newly-formed pseudopods, the trailing edge, and vesicles within cells while its activity is concentrated at the leading edge. RacC is necessary for the second peak of the F-actin biphasic response. Overexpression of RacC leads to an elevated level of F-actin which is markedly decreased after applying LY294002. In $racC-$ cells, basal membrane localization of PI3K is not observed. Moreover, only small amount of PI3K and PKBA localizes to the membrane upon cAMP stimulation. Because the PI3K localization is also reduced in WASP^{TK} mutants, which have low amount of WASP, PI3K does not bind to RacC directly [80]. RacC associates with DockD, a protein which also associates with Elmo1 and localizes to the leading edge by PI3K activity. Hence, it is hypothesized that RacC may be activated downstream of PIP_3 via DockD [148].

Positive feedback has been observed in the PI3K pathway as unstimulated cells, as well as $g\beta$ null mutants, possess spontaneous localization of PIP_3 to parts of the cell membrane. The activity is independent of external stimulation and coincides with local

F-actin activity and pseudopod extensions. This local PIP_3 activity also leads to activation and localization of upstream regulators including Ras and PI3K. This spontaneous activity is necessary for random cell movement. Inhibition of either PI3K activity or F-actin leads to disruption of this spontaneous activity although small pseudopodial projections are observed in absence of the PI3K activity. Interestingly, the local activity does not depend on the TORC2 pathway and substrate attachment. Moreover, disruption of RasG only leads to mild defects in the spontaneous activity. [161, 162].

The phospholipid signaling pathway is ideal for the study of chemotactic responses because many pathway components and their relationships have been identified. There also exist substantial quantitative measurements of responses in this pathway. In particular, works by Janetopoulos et al. [90], Xu et al. [196, 197] offer quantitative benchmarks of the chemotactic responses of round LatA-treated cells to various types of cAMP stimulation. Although the PI3K pathway is coupled to other pathways and is, by itself, not necessary for directional sensing due to the alternate pathways, it is a good model system to study various properties of the chemotactic responses. In particular, adaptation to uniform stimulation and amplification of spatial gradients are key properties which allow cells to develop polarization robustly under small gradients of the chemoattractant. Moreover, this pathway is directly responsible for the spontaneous activity of F-actin localization, pseudopod protrusions, and random motility.

1.5 Organization of actin structures

1.5.1 Dendritic actin network

The actin network found in pseudopodia protrusions and actin waves is rich in Arp2/3, a protein that binds to a actin filament and forms an actin branch where a new actin filament can grow on. This type of actin network, called the dendritic actin network,

is highly-branched and is characteristically different from the actin network found in the cell cortex, which are crosslinked filament bundles. This crosslinked actin network is characterized by myosin II and bundling and crosslinking proteins such as fascin, α-actinin, cortexillin, and the ERM (ezrin, radixin, and moesin) family of proteins.

The branching of actin filaments via Arp2/3 occurs near the plasma membrane [118]. This process is facilitated by class I nucleation promoting factors (NPFs) such as SCAR/WAVE, WASP, and N-WASP. These three members of the Wiskott-Aldrich syndrome protein (WASP) family are the most studied activators of Arp2/3. SCAR/WAVE, WASP, and N-WASP are cytosolic molecules whose localization and activity are downstream of phospholipids. They are recruited to the plasma membrane by PIP_2 while PIP_3 is also found to recruit WASP in *Dictyostelium*. Their activation mechanisms are unclear although Rac and Cdc42 are thought to be among the activators. Because of the affinity to both Arp2/3 and a G-actin subunit at the C-terminus, it is believed that they act as a scaffold for nucleation of daughter filaments and deliver them to existing filaments [139, 153, 32]. Because N-WASP and Cdc42 are not present in *Dictyostelium* the creation of the dendritic actin network in *Dictyostelium* presumably occurs downstream of Rac, where activated WASP or SCAR/WAVE binds to Arp2/3 and G-actin to create a new branch.

1.5.2 Spontaneous actin waves

Molecular constituents typically observed in actin structures have been studied in actin waves. Arp2/3 is generally enriched at actin wave fronts and, to a lesser extent, within the area enclosed by wave fronts. Its localization overlaps with markers for F-actin, indicating that the actin waves are composed of highly branched actin networks. myosin II, on the other hand, is not integrated into the actin waves. It is, in fact, enriched in the external area which is not enclosed by the wave fronts. Lack of myosin II activity does

not impair wave formation, forward propagation, and retraction. Despite association of Arp2/3 with the actin waves, deletion of SCAR/WAVE does not preclude the presence of the actin waves and Arp2/3 localization within the waves. Moreover, the actin waves are present in $g\beta$ null mutants, implying that the process is independent of chemoattractants [23, 51, 24, 165].

In addition to Arp2/3, certain molecules including MyoB, CARMIL, and coronin are closely associated with the fronts of the actin waves. MyoB is a single-headed motor protein with a low duty ratio motor. It binds to the plasma membrane via PIP_2 and PIP_3 although its collocalization with F-actin requires the actin-binding site in its head [179, 28]. CARMIL is an adaptor protein that binds to MyoB, Arp2/3, and capping protein *in vitro*. Its binding to capping protein is found to inhibit barbed-end capping of actin filaments while its affinity to MyoB and Arp2/3 has suggested a link between MyoB and actin nucleation activity [95, 200]. Coronin is a class II NPF which has specificity for Arp2/3 and F-actin. A wide array of distinct roles of coronin homologs across cell lines have been observed *in vitro* including inhibition of actin-filament nucleation by Arp2/3 sequestration, stabilization of ATP- and ADP·P_i-bound actin within filaments, severing ADP-bound actin within flaments, and bundling of actin filaments [63]. Coronin also antagonizes cortactin, a class II NPF which stabilizes actin branches, and destabilizes actin filament branches by localizing at the branches and inducing dissociation of Arp2/3. It is found to associate with actin filament branches *in vivo*, causing increased branch angles and increased variation of the angles. The destabilized branches eventually detach as coronin dissociate from them [31]. Furthermore, an abrupt disassembly of actin filaments by the concerted activity of coronin, cofilin, and actin-interacting protein 1 (aip1) has been observed *in vitro* [25, 117].

As previously observed to decorate within lamellipodia, MyoB, CARMIL, and coronin are found at the fronts of actin waves. Figure 1.9 depicts their localization within

the actin waves. Consistent with their presence in pseudopod protrusions, the localiza-

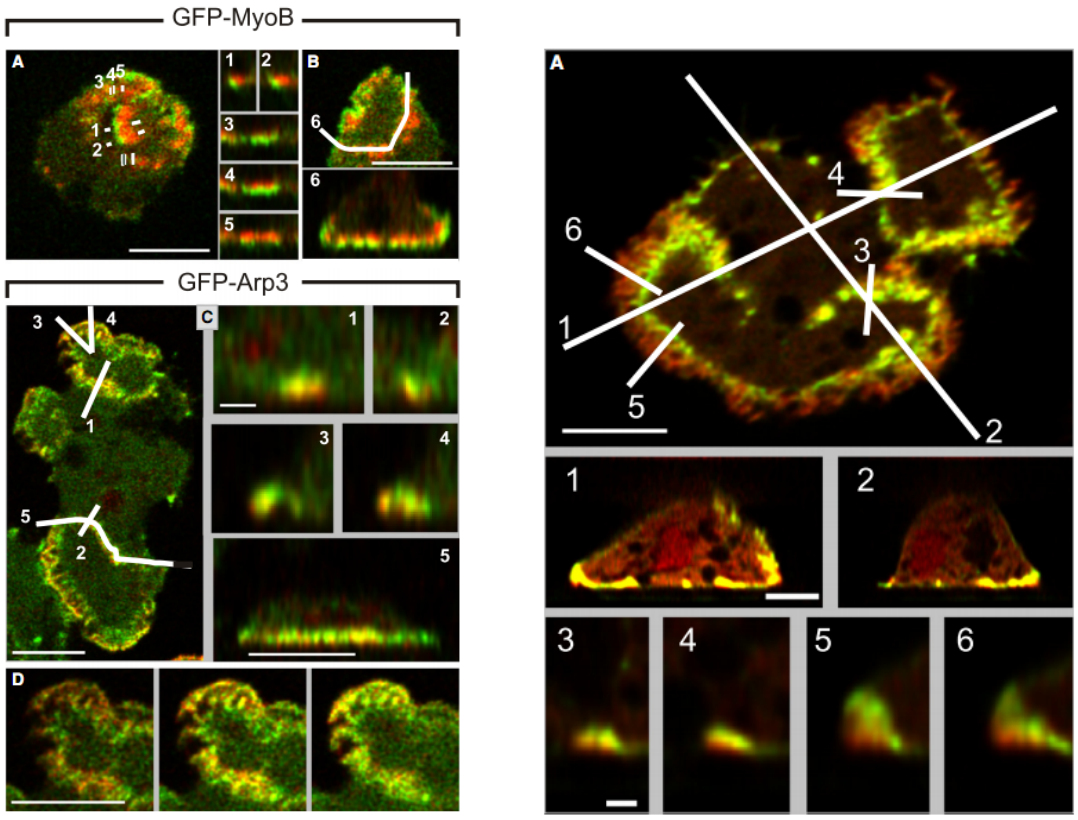

Figure 1.9: Localization of MyoB, Arp2/3, and coronin within actin waves in *Dictyostelium* cells during recovery from LatA treatment [24]. *(Upper left)* MyoB *(green)* is localized in front of actin-wave *(red)* fronts in horizontal planes *(A, B)* close to the substrate-attached bottom cell surface. Relative localization in vertical cross sections through the wave fronts *(1, 2)* and parallel to the wave fronts *(3-6)* is shown along the line scans. *(Lower left)* Arp2/3 *(green)* localization is shown relative to F-actin *(red)* on planes *(C, D)* close to the substrate surface and vertical sections along line scans through *(1-4)* and parallel to *(5)* the wave fronts. *(Right)* Coronin *(green)* is localized behind the actin waves *(red)* close to the bottom cell surface *(A)*. Its localization in veritcal planes through the wave fronts *(1-6)* is displayed along the line scans.

tion of MyoB and CARMIL appear to be leading the actin wave fronts while coronin is behind the fronts. Cross sections obtained by z-scans reveal that MyoB is localized at the bottom of the waves. Its localization extends further into the cytosol towards

the wave front, covering the entire height at the front, while it becomes concentrated only close to the plasma membrane right behind the front, and hardly observable at any height in the middle of of the waves. When an actin wave meets a cell border, the MyoB layer is bent around the border and the actin structure is extended horizontally towards the cytosol. In contrast to MyoB, coronin is found to decorate the top of the actin waves throughtout the entire length. In the front, where the F-actin layer is thick, the coronin layer is seperated from the membrane. The coronin layer joins the membrane towards the back of the waves. This is the reason why coronin is found behind the wave fronts by the total internal reflection fluorescence (TIRF) microscopy, which only captures two-dimensional images at the bottom surface, extending 100-200 nm from the membrane. The localization of MyoB, CARMIL, and coronin, along with the declining thickness of the F-actin layer towards the back is consistent with a high polymerization rate at the front of the waves and continuous depolymerization along the entire wave length. It also suggests the roles of MyoB in initialization of actin polymerization at the front and coronin in termination of polymerization at the top and the back of the waves [84, 24].

A closed front of the actin waves partitions the cell-substrate surface into an enclosed area and an external area with distinct biochemical properties. Furthermore, the localization and activity of the molecules within the enclosed and external areas are dynamic and coincide with the propagation of the actin waves. Figure 1.10 displays localization of signaling molecules associated with the enclosed area and the external area. The enclosed area is enriched in PIP_3 and activated Ras, indicating high PI3K activity. The peaks of PIP_3 and Ras activity are found in the middle of the enclosed area while the wave fronts coincide with a transition zone where low PIP_3 density and low Ras activation are observed outside. In fact, the activity of PI3K is essential for formation of the actin waves. Its inhibition by LY294002 completely abolishes active actin waves on

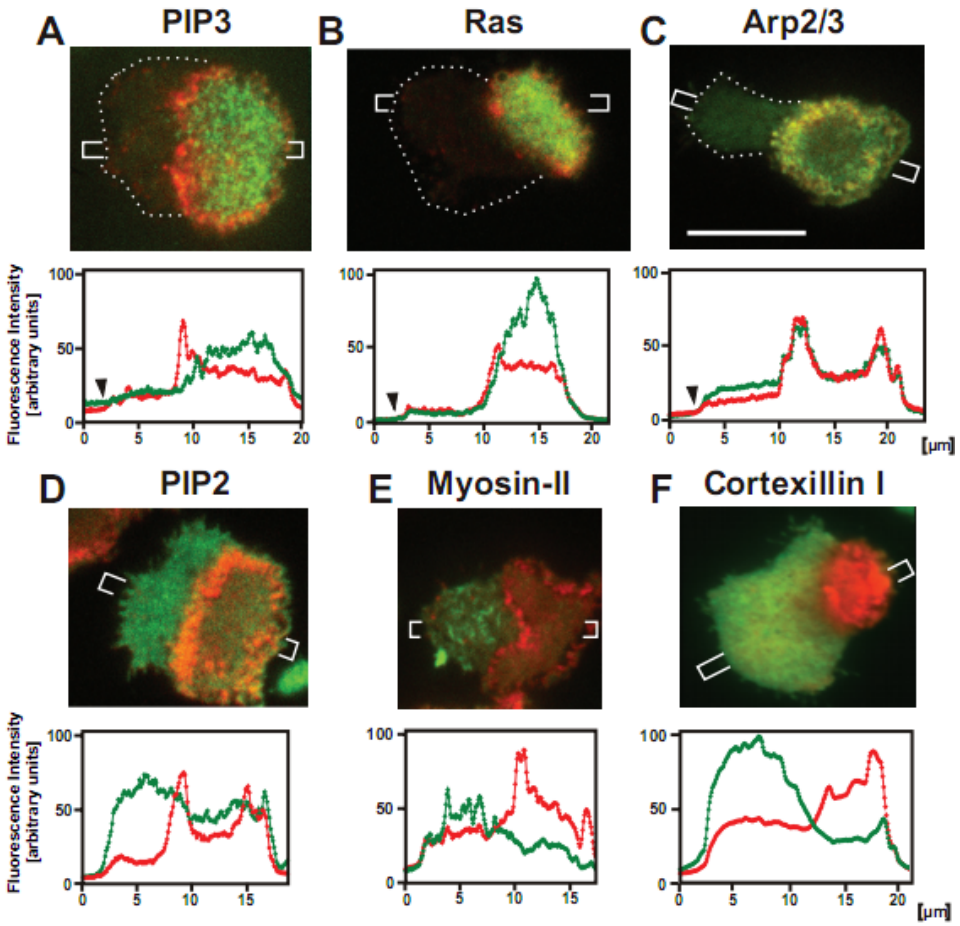

Figure 1.10: Localization of proteins and phospholipids *(green)* within the area enclosed by actin waves *(red)* and the external area. TIRF images display localization of the molecules close to the cell-substrate surface. Fluorescence intensities along line scans are given below the images [68].

the cell-substrate surface within 2 minutes. Moreover, the actin waves recover within 3 minutes after romoval of the drug [67, 65, 68]. In contrast, the outer area is enriched by myosin II, cortexillin I, and PTEN. Cortexillin I is an actin-filament bundling protein and the dominence of myosin II and cortexillin I is consistent with a loose network of bundled actin filaments observed within the external area. Three-dimensional images show that PTEN is not only enriched in the external area of the cell-substrate surface,

but also throughout the nonattached area of the cell membrane. The actin waves are observed in *pten* null mutants. However, the abrupt change between expansion and retraction of enclosed areas is not present. Instead, when an actin wave is initiated, the enclosed area, which may split, continues expansion until it collapses into spiral waves [165, 68].

Similar wave organizations have been observed in both *Dictyostelium* and neutrophils. In neutrophils, the so-called Hem-1 waves has been observed on the cell-substrate membrane. Hem-1 is a component of the WAVE2 complex in neutrophils. It is homologous to Nap-1 in the *Dictyostelium* SCAR/WAVE complex. In this type of waves, Hem-1 initially accumulates into foci on the membrane, which burst into many discrete wave fronts. The Hem-1 waves are generally observed near the leading edge and their activities are highly correlated with leading-edge advancement. F-actin is found behind Hem-1 waves and inhibition of F-actin by LatA increases both wave lifetime and intensity while the propagation speed is decreased. Therefore, it was suggested that F-actin acts as an inhibitor for Hem-1 localization to the membrane and the Hem-1 waves [189]. In *Dictyostelium* cells, it is found that PIP_3 waves which rotate on the edge on the cell-substrate surface can be organized spontaneously without chemoattratant stimulation and F-actin activity. The *Dictyostelium* cells were treated with $5\mu M$ LatA and $4mM$ caffeine to inhibit F-actin and cAMP production by adenylyl cyclase. Reciprocal localization of PIP_3 and PTEN is observed on the cell edge. In addition to the continuous propagation on the cell edge, generation, seperation, fusion, and reversal of the propagation direction of the domains are observed. These PIP_3 waves are sensitive to inhibition of PI3K and PTEN [8]. A similar behavior between PTEN and PIP_3 is also observed in actin waves. Therefore, this organization may, in fact, be a three-dimensional dynamics and categorized as a form of the actin waves [68].

The initiation and the structure of the actin waves has been related to several cellular

processes. First, actin patches during the initiation phase are correlated with clathrin-coated structures (CSSs) which are involved in endocytosis. Most of the actin patches during the initialization stage are formed at cites of CSS internalization while CSSs are arrested at the plasma membrane before removeal of LatA [165, 65]. Furthermore, relative localization of F-actin and PIP_3 within the actin waves, including the toroid-like structure, resembles the localization in phagocytic cups. Coronin is also observed to cap F-actin structures during frustrated phagocytosis. In fact, wave-forming cells exhibit high propensity for phagocytosis [67, 160]. Finally, a recent experiment by Case and Waterman [34] connected actin waves observed in U2OS cells, a human osteosarcoma cell line, to cellular adhesion. The actin waves observed in these cells are followed by integrin waves. The integrin waves are distinct from other integrin-containing structures including podosomes, invadopodia, and focal adhesions. Both actin and integrin waves are dependent on the activity of integrin as their frequency is reduced when integrin functions are blocked by antibodies. The frequency of the waves is also ECM-dependent and reduced in cells placed on poly-L-lysine-coated coverslips. Nevertheless, it is unclear how the actin waves observed in these cells are compared to previously-observed actin waves.

The biochemical basis leading to the initiation and the behaviors of the actin waves is not well understood. In particular, the roles of proteins which are integrated to the wave fronts including MyoB, CARMIL, and coronin are not well established. Moreover, although endocytosis and adhesion have been linked to the inititation of the actin waves, it is unclear which biological processes are the key drivers. Fortunately, the activity of PI3K, a crucial element of the actin waves, is relatively well understood. Its positive feedback with F-actin, observed in unstimulated cells by Sasaki et al. [162], may be able to help explain parts of the actin wave behaviors. This feedback mechanism will be an important part of our model for actin waves.

1.6 Current state of research

This section summarizes existing work on the chemotactic signaling pathway and the spontaneous actin waves. We start with open issues and then explain how models have been proposed to address these problems. Finally, we describe how our work contributes to understanding of the physical problems.

1.6.1 Chemotactic signaling models

Features of the signaling pathway

Key properties of the chemotactic signal-transduction pathway which are important for survival and functions of *Dictyostelium* and related eukaryotic cells may be categorized as follows:

Adaptation

> Cells must be responsive to stimulation with mean concentration spanning several orders of magnitude. *Dictyostelium* cells, in particular, respond to stimulation at levels ranging from 0.1 nM to 1 μM. In addition, cells are able to adapt to extended exposure to stimulus and respond to further increases in the stimulus level. In particular, *Dictyostelium* cells display a biphasic response to uniform cAMP stimulation where the second phase corresponds to extensions of random pseudopodia and membrane ruffles. Finally, after removal of stimulus, cells must be able to respond to the previous level of stimulation. The recovery period for *Dictyostelium* cells is several minutes.

Gradient amplification

> Internal orientation is developed towards a stimulus source under a small

stimulus gradient, as low as few percent, across the cell length. In this process, internal gradients of signaling molecules amplify the chemoattractant gradient by multiple folds. Furthermore, the localization of internal activities is removed after the stimulation ceases. The orientation also follows changes of the stimulus gradient. Multiple sources of chemoattractant can induce simultaneous localized activities at their closest sites.

Polarization

In unstimulated cells, internal molecules, including F-actin, localize at random sites along the membrane causing pseudopod protrusions and motility. Differentiated *Dictyostelium* cells, like neutrophils, may develop polarity and move in a persistant, but random, direction. These cells display chemokinesis. In particular, under uniform concentration of chemoattractant, their polarity is enhanced and the speed of their random movement is increased. The polarity may also be strengthened during prolonged chemotaxis. Highly polarized cells are more resistant to direction changes. Imposing or changing chemoattractant gradients causes pseudopod formation near the current front and cells gradually make a U-turn towards the chemoattractant source. Only strong gradients can lead to direct reorientation towards the new source.

In addition to the essential features, there are other observed behaviors which are less crucial to overall functions such as responses in mutants and transient reversal of internal orientation when cells are subjected to a uniform stimulation shortly after removal of chemoattractant gradient.

A related problem is how different pathways contribute to the overall cellular responses including F-actin, myosin II, and cAMP-secretion activities and how this mechanism allows them to reliably function when some pathways are inhibited. To solve this

problem, more details of the remaining pathways are needed. The problem is beyond the scope of this work.

Existing models

Mathematical models have been proposed to explain particular aspects of the chemotactic behavoirs of *Dictyostelium discoideum* and other eukaryotic cells. We categorize the models into three groups:

Models with spontaneous polarization and protrusion

The main feature of the models with spontaneous polarization is that they develop clear orientation of chemical activities under initial conditions or stimulation with random fluctuations. Alternatively, they may develop transient and random protrusions. Some models also respond to stimulus gradients by orienting themselves in the direction of gradient. These types of models are based on local systems which are bistable. Meinhardt [135] first proposed a mechanism based on Turing-instability which continuously exhibits random protrusions. Subsequently, other Turing-type models are developed along with stimulus-induced orientation [174, 140, 147]. Among these models, Subramanian and Narang [174] includes an adaptation step to produce adaptation to perfectly uniform stimulation. Another type of models based on bistability is wave-based. Edelstein-Keshet and colleagues proposed wave-based models based on interactions between Rho, Rac, and Cdc42 which are found in many cell types, but not in *Dictyostelium* [131, 92, 47]. Analysis of wave-based models can be found in [138]. In addition to the two main types, bistability has been used to produce transient localization [82] and stimulus-biased orientation [195]. Gamba et al. [62] proposed a polarization and stimulus-biased orientation model of PIP_3 based on phase separation. In summary,

the models in this class are able to capture spontaneous protrusion and polarization. Most of them are able to orient towards a stimulus gradient in a highly amplified manner although their responses are generally not biphasic and lack adaptation to uniform stimuli. The major drawback of most models of this type is that the bistability is obtained by artificially adding nonlinear cooperativity to simple interaction terms. Only the models by Otsuji et al. [147], Gamba et al. [62] are biophysically faithful. Nevertheless, Otsuji's model is based on mechanisms not present in *Dictyostelium* and the responses in Gamba's model follow a much slower time scale for chemotactic activities.

Models with adaptation

Levchenko and Iglesias [125] first proposed a model with adaptation based on a simple feedforward system similar to one proposed by Othmer and Schaap [146]. In this model, a positive feedback based on substrate delivery for PIP_3 is used to amplify spatial gradients. However, the phosphoinositide-substrate delivery is hypothesized and the model does not display a biphasic response. This adaptation scheme used in this model became widely known as Local-Excitation-Global-Inhibition (LEGI) system. Later, Iglesias and coworkers published a series of work based on the LEGI scheme [114, 115, 130, 116, 195]. Artificial cooperativity [130] and a bistable system [195] has been used to amplify stimulus gradients and to obtain biphasic responses and spontaneous activities. However, no realistic mechanism for gradient amplification has been proposed. Alternatively, Levine et al. [126] proposed a balanced inactivation model based on recombination of molecules. Although this model possesses adaptation and spatial sensitivity, the inactivation mechanism is more suited for the heterotrimeric G proteins which do not display these responses.

Biologically-based models which exhibit both adaptation and gradient amplification have been proposed by Skupsky et al. [168] and Meier-Schellersheim et al. [134]. In Skupsky's model, adaptation depends on saturation in a similar fashion to an adaptation model for bacterial chemotaxis analyzed by Yi et al. [202]. On the other hand, Meier-Schellersheim's model employs feedforward adaptation. Both models rely on positive feedback for gradient amplification. In particular, Meier-Schellersheim et al. [134] quantitatively reproduced experimentally observed biphasic PIP_3 and PTEN responses. However, both models include many hypothesized steps and fail to offer physical explainations how the simulated responses are achieved.

Gradient-amplifying models without spontaneous polarization and adpatation

Postma and Van Haastert [154] proposed a scheme for gradient amplification based on depletion of an effector which amplify the receptor-mediated signal. High spatial sensitivity is achieved by limited availability of the effector which is recruited by the output activity, forming a feedback loop. Chemorepulsion was modeled by Alam-Nazki and Krishnan [2], using PI3K-PTEN-PLC interactions on phosphoinositides. However, the model assumes artificial cooperativity and its response lacks adaptation. Finally, Onsum and Rao [145] modeled oreintation by assuming mutual inhibition between frontness and backness incorporated by PI3K and Rho respectively.

In addition to the gradient-sensing and polarization models, statistical properties of pseudopod extensions have been studied [182, 127] and used to reproduce observed migration paths and chemotaxis index [10, 77]. Simple Turing-type models have also been integrated with artificial mechanisms for membrane extension to generate shape changes and migration paths [83, 141].

Currently, there is no biophysically-sound model which possesses both adaptation and gradient amplification and offers a simple explanation how these properties are obtained. We seek to fill this gap by analyzing the adaptation and gradient-amplification properties and pose a model which is a cascade of adaptation and gradient-amplification subsystems. The model will be based on known regulation steps of the signal-transduction pathway. Chapter 2 is devoted to analysis of the properties as separate modules. Our model for the chemotactic pathway is proposed in Chapter 3. Its responses will be quantitatively compared to experimentally-observed biphasic responses. Finally, the effect of cell morphology on chemotactic responses will be studied. In particular, it will be shown that polarization under uniform stimulation may be explained by our model with nonsymmetric cell shapes.

1.6.2 Actin wave models

Emergence and sustained dynamics of actin waves are highly complicated processes. There are many interesting aspects of the actin waves that may be elucidated by mathematical modeling. First, the actin waves are formed spontaneously on the cell-substrate interface. The initiation is arguably caused by either endocytosis or substrate adhesion. Once the actin waves are formed, their propagation dynamics is sustained without external stimulation. They are a three-dimensional structure with characteristic shape, size, and propagation speed. They display complicated dynamics such as toroid-like waves, which are developed from broken wave fronts, and sudden changes in the propagation direction. Furthermore, there are many related proteins with specific localization within the wave structure whose interactions with the actin waves are unclear. Finally, it is unclear if the actin waves observed in *Dictyostelium* share the same underlying processes with the actin waves observed in higher organisms and other wave structures such as the PIP_3 waves.

A comprehensive model of actin waves would likely involve numerous constituents, many of which are still poorly understood. Therefore, current modeling efforts focus on specific aspects of the waves. Several models have been proposed to capture spontaneous initiation and qualitative behaviors of the early-stage actin waves [192, 195, 33] and Hem-1 waves [189, 54]. There are also models of spontaneous actin patches which exhibits similar structures as in the early-stage actin waves [53, 55, 82].

Interestingly, despite being used to reproduce different phenomina, these models are fundamentally similar. They are based on an autocatalytic activity of an activator, the observed species, and a slow inhibition by an inhibitor induced by the activator. Based on this concept, Weiner, Marganski, Wu, Altschuler, and Kirschner [189] use a heuristic model to capture traveling Hem-1 waves. The Fitzhugh-Nagumo model for wave propagation on exitable media has been used to explain local bistability [13] and capture emergence of actin patches [82] and traveling waves [195]. Xiong et al. [195] combines an excitable system with an adaptive upstream signaling pathway to simulate stimulus-biased random actin waves.

Actin-filament dynamics has been incorporated into more detailed models. This class of models are able to exhibit motile actin spots and traveling waves. Whitelam et al. [192] proposed a model which incorporated orientation to the FitzHugh-Nagumo model. This model is capable of displaying spot formation, spot dynamics, and traveling waves. On the other hand, Doubrovinski and Kruse [53] proposed models with individual-filament dynamics coupled with different regulation schemes for NPFs, including FitzHugh-Nagumo type activation and active transport via F-actin. These models selectively exhibit either motile spots or traveling waves, depending on parameter values [54, 53, 55]. Currently, the most detailed model based on molecular processes is proposed by Carlsson [33]. A stochastic description is employed to handle filament dynamics which includes a full network structure. The model is able to capture both

spot and traveling wave dynamics.

The existing models of the actin waves provide a conceptual framework to qualitatively explain distinct behaviors of the early-stage actin waves. However, most models do not include the actin dynamics, which is crucial, and neglect integral molecular players of the actin waves such as Arp2/3, MyoB, coronin, and PIP_3. Moreover, the understanding of sustained propagation of the actin waves, complicated wave dynamics, roles of the constituents, and quantitative features of the actin waves such as their speed and shape, and even the mechanism for wave initiation is still an open question. Most importantly, the FitzHugh-Nagumo model for excitable media, which is the universal feature of these models, cannot explain the abrupt changes in the propagation direction of the actin waves. These issues are also not addressed by the existing stochastic model, which incorporates detailed actin dynamics. A realistic continuous description of the actin waves which is amenable for analysis is needed to understand these aspects of the actin waves.

In Chapter 4, we will develop a model for the actin waves which incorporates the dynamics of the filamentous actin network and molecular signaling of the upstream pathway which is missing in the existing models. Activities of coronin and PIP_3 will be incorporated in this model to reproduce the propagation and shape characteristics of the actin waves. Furthermore, observed localization, dynamics, and roles of coronin and PIP_3 will be studied. Our results suggest an alternate mechanism for the propagation of the actin waves and provide an insight into the transition from localized F-actin spots into the propagating waves.The model also provides a connection between PTEN activity and the actin-wave dynamics and partly explains why the abrupt changes in the propagation direction are not observed when PTEN is inhibited.

Chapter 2

Modular analysis of chemotactic signal-transduction networks

A modular approach is adopted to analyze the chemotactic pathways in *Dictyostelium*, which adapt to uniform stimulation while spatial gradients of the external signal are greatly amplified. We suggest that such behaviors can be produced by a cascade of an adaptation subnetwork and a gradient-amplification subnetwork. We first explore conditions which allow us to independently analyze the subnetworks as separate modules. Then we study and analyze possible candidates for the adaptation and gradient-amplification modules. In the next chapter, the most physiologically plausible adaptation and gradient-amplification modules are combined to obtain a simple modular model of the chemotactic pathways.

2.1 Modularization

Cells are composed of a large number of different types of molecules that act in concert to give rise to specific cellular functions. An influential work by Hartwell et al. [81]

suggested that the functional relation between these molecules is modular such that a cellular behavior can be broken down into subtasks where each subtask involves only a discrete group of a small number of molecule types with close relationship among them. This idea also applies to other biological systems such as the gene transcription network and the neural networks in the brain. The modular structure introduces robustness of discrete module functions within a system while allows the system to evolve and adapt to its environment by altering interactions between the modules.

Experimental observations support the modular signaling structure. Data-mining techniques have been used to identify network clusters of interacting proteins in Yeast proteome [158, 171], Drosophila melanogaster proteome [69], metabolic networks [157, 75], and mammalian cell-cycle regulatory network [105]. Moreover, evolutionary-conserved protein domains such as Pleckstrin homology (PH) domain serve as molecular adaptors to specific partners. Interaction between proteins carrying such domains and common effectors/regulators may serve as interconnections between functional modules.

Design and analysis of large biological systems as interconnecting modules is advantagous as it greatly reduces the system complexity. A system can be broken down into modules which serve specific functions and can be analyzed individually. Many regulatory systems have been analyzed in this fashion [125, 204, 166, 9, 38]. To aid design and analysis of modular systems, functional modules have been studied as logical units [3, 4] and other signaling components [181]. Moreover, sensitivity analysis of modular systems has been developed in the context of Metabolic Control Theory [98, 27].

In the studies of modular biological systems, it is usually assumed that relationship between modules is unidirectional. This means the activity of an upstream module is isolated from activities of its downstream modules. This assumption makes the analysis of the modules independent regardless of their interconnections, but it is not necessarily satisfied when molecular binding is involved at the interconnections. The activity of

the output of the upstream module is affected by sequestration into complexes with its effectors in the downstream module. Vecchio et al. [184] showed that neglecting this interdependence could lead to wrong predictions of system behaviors. They termed this effect as 'retroactivity' and proposed a design principle to reduce retroactivity in transcription regulation systems. In this section, we consider a condition which ensures low retroactivity in molecular regulatory systems governed by enzymetic reactions.

Consider the interconnections between an upstream module and N downstream modules in Figure 2.1. A common output U of an upstream module serves as an input of downstream modules which activates components $X_i,\ i = 1, \ldots, N$. Suppose U is regulated by an activator E and an inhibitor I within the upstream module. Assume further that the total amount of U is conserved.

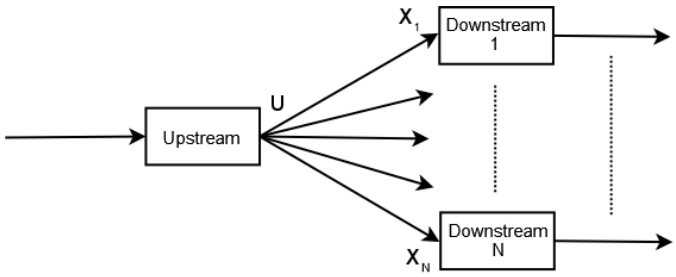

Figure 2.1: Illustration of connecting modules: the upstream module has output U which acts as the input for the downstream modules.

Activities of the downstream modules depend on the concentration of U. To quantify the effect of the interconnections, we consider how U is sequestered in complexes with X_i's. Reactions involving U are

$$E^* + U \underset{k_U^r}{\overset{k_U^f}{\rightleftharpoons}} [E^* \cdot U] \xrightarrow{k_U^c} E^* + U^*$$

$$I^* + U^* \underset{k_{U^*}^r}{\overset{k_{U^*}^f}{\rightleftharpoons}} [I^* \cdot U^*] \xrightarrow{k_{U^*}^c} I^* + U$$

$$U^* + X_1 \underset{k^r_{X_1}}{\overset{k^f_{X_1}}{\rightleftharpoons}} [U^* \cdot X_1] \xrightarrow{k^c_{X_1}} U^* + X_1^*$$

$$\vdots$$

$$U^* + X_N \underset{k^r_{X_N}}{\overset{k^f_{X_N}}{\rightleftharpoons}} [U^* \cdot X_N] \xrightarrow{k^c_{X_N}} U^* + X_N^*$$

The dynamics of different forms of the intermodular effector U are described by

$$\begin{aligned}
\frac{dU}{dt} &= -k^f_U E^* \cdot U + k^r_U [E^* \cdot U] + k^c_{U^*} [I^* \cdot U^*] \\
\frac{dU^*}{dt} &= -k^f_{U^*} I^* \cdot U^* + k^r_{U^*} [I^* \cdot U^*] + k^c_U [E^* \cdot U] \\
&\quad - \sum_{i=1}^{N} \left(k^f_{X_i} U^* \cdot X_i + (k^r_{X_i} + k^c_{X_i}) [U^* \cdot X_i] \right) \\
\frac{d[E^* \cdot U]}{dt} &= k^f_U E^* \cdot U - (k^r_U + k^c_U)[E^* \cdot U] \\
\frac{d[I^* \cdot U^*]}{dt} &= k^f_{U^*} I^* \cdot U^* - (k^r_{U^*} + k^c_{U^*})[I^* \cdot U^*] \\
\frac{d[U^* \cdot X_i]}{dt} &= k^f_{X_i} U^* \cdot X_i - (k^r_{X_i} + k^c_{X_i})[U^* \cdot X_i]
\end{aligned}$$

for $i = 1, \ldots, N$. We also have a conservation condition

$$U_T = U + U^* + [E^* \cdot U] + [I^* \cdot U^*] + \sum_{i=1}^{N} [U^* \cdot X_i].$$

The dynamics of the upstream module is affected by terms involving X_i and $[U^* \cdot X_i]$. These terms are retroactivity imposed by the downstream modules. If the effect of retroactivity is negligible, we say that the modules are *weakly-coupled*. To determine when the modules are weakly-coupled at steady state, we first consider steady-state

relationships

$$k_U^f E^* \cdot U = K_{m_U}[E^* \cdot U]$$

$$k_{U^*}^f I^* \cdot U^* = K_{m_{U^*}}[I^* \cdot U^*]$$

$$k_{X_i}^f U^* \cdot X_i = K_{m_{X_i}}[U^* \cdot X_i]$$

$$k_{U^*}^c[I^* \cdot U^*] = k_U^c[E^* \cdot U]$$

$$U_T = U + U^* + [E^* \cdot U] + [I^* \cdot U^*] + \sum_{i=1}^{N}[U^* \cdot X_i]$$

where $K_{m_Z} = (k_Z^c + k_Z^r)/k_Z^f$ denotes the Michealis constant for the species Z. At steady state, the upstream and downstream modules are coupled only by the conservation condition for U. Therefore, they are steady-state weakly-coupled when $\sum_{i=1}^{N}[U^* \cdot X_i] << U_T$. This condition is satisfied when $X_i/K_{m_{X_i}} << 1,\ i = 1, \ldots, N$ since

$$\frac{[U^* \cdot X_i]}{U_T} \leq \frac{[U^* \cdot X_i]}{U^*} = \frac{X_i}{K_{m_{X_i}}}.$$

Physically, it means that the steady-state responses of modules can be analyzed independently if the first activation step of each module operates deep in the linear region of the Michaelis-Menten kinetics.

The following result shows that the upstream and the downstream modules are weakly-coupled and they can be analyzed independently when they are steady-state weakly-coupled and the intermodular complexes $[U^* \cdot X_i]$ equilibrate rapidly.

Theorem 1. *Suppose that $X_i/K_{m_{X_i}} << 1$ and the pseudo-steady-state hypothesis (PSSH) can be applied to $[U^* \cdot X_i]$ for each $i = 1, \ldots, N$. Then the upstream and downstream modules are weakly-coupled. Furthermore, the downstream modules can be analyzed independently where the effective activation rates of X_i due to U^* follows the*

mass action kinetics $(k^c_{X_i}/K_{m_{X_i}})U^* \cdot X_i$.

Proof. Define $\tilde{U} = U + [E^* \cdot U] + [I^* \cdot U^*]$ so that the conservation condition for U reads

$$U_T = \tilde{U} + U^* + \sum_{i=1}^{N} [U^* \cdot X_i].$$

For each i, apply the PSSH to the intermodular complex $[U^* \cdot X_i]$ and use the conservation condition so

$$K_{m_{X_i}}[U^* \cdot X_i] = X_i \left(U_T - \tilde{U} - \sum_{i=1}^{N} [U^* \cdot X_i] \right)$$

for $i = 1, \ldots, N$. We claim

$$[U^* \cdot X_i] = \frac{(U_T - \tilde{U}) X_i / K_{m_{X_i}}}{1 + \sum_{k=1}^{N} X_k / K_{m_{X_k}}}$$

To check the claim, we compute

$$\begin{aligned}
X_i \left(U_T - \tilde{U} - \sum_{i=1}^{N} [U^* \cdot X_i] \right) &= X_i \left(U_T - \tilde{U} - \sum_{i=1}^{N} \frac{(U_T - \tilde{U}) X_i / K_{m_{X_i}}}{1 + \sum_{k=1}^{N} X_k / K_{m_{X_k}}} \right) \\
&= X_i (U_T - \tilde{U}) \left(1 - \sum_{i=1}^{N} \frac{X_i / K_{m_{X_i}}}{1 + \sum_{k=1}^{N} X_k / K_{m_{X_k}}} \right) \\
&= \frac{X_i (U_T - \tilde{U})}{1 + \sum_{k=1}^{N} X_k / K_{m_{X_k}}} \\
&= K_{m_{X_i}} [U^* \cdot X_i]
\end{aligned}$$

Therefore, the conservation condition for U reads

$$U_T = \tilde{U} + U^* + \sum_{i=1}^{N} [U^* \cdot X_i]$$

$$= \tilde{U} + U^* + (U_T - \tilde{U}) \left(1 - \frac{1}{1 + \sum_{k=1}^{N} X_k / K_{m_{X_k}}} \right)$$

Using the assumption $X_i / K_{m_{X_i}} << 1$ for each i, we get

$$U_T = \tilde{U} + U^* = U + U^* + [E^* \cdot U] + [I^* \cdot U^*].$$

Since terms involving X_i are not present in the differential equations for $U, [E^* \cdot U], [I^* \cdot U^*]$, the conservation condition implies that the upstream and downstream modules are weakly-coupled.

The second asserttion follows immediately since the activation rate is

$$k^c_{X_i} [U^* \cdot X_i] = \frac{k^c_{X_i}}{K_{m_{X_i}}} U^* \cdot X_i.$$

□

Note that this result also applies when there are many activators of X_i, both when the activators are within the same upstream modules or are part of different upstream modules. When an activator of X_i is part of the downstream module, a slight modification on the analysis of the downstream module is needed, although the upstream module can still be analyzed independently.

2.2 Adaptation

In this section, a general adaptation property in biological systems is first analyzed. Then detailed analyses of steady-state and dynamic behaviors of the most plausible model for adaptation in *Dictyostelium* chemotaxis are given. Both theoretical and numerical results wil be presented.

2.2.1 Types of adaptation

Adaptation in biological systems, loosely speaking, is a property of a system whose temporal response subjected to a defined set of inputs experiences an extreme change transiently before returning its basal (or normal) state. As commonly used in the literature, perfect adaptation refers to an ability of the response to recover precisely to the normal state and partial adaptation refers to recovery to a level that is between the normal state and the response peak (or trough). Usually, stimulations are in the form of a sudden change in the input level and adaptation is associated with an ability to undergo similar responses after further stimulations. Although, partial adaptation may be a result of a simple negative feedback, perfect adaptation is much harder to achieve. Nevertheless, a fascinating nature of many organisms is that they can adapt perfectly to several orders of magnitude of spatially-uniform, or averaged, stimuli.

Adaptation of a system with parameters k to external signals requires its internal states $u(S(t), k, t)$ to compensate for the stimulations. We denote the internal variables at steady state, if it exists, by

$$u_{ss}(S(t), k) := \lim_{t\to\infty} u(S(t), k, t)$$

However, for adaptation to a constant stimulation $S(t) \equiv S$ for $t \geq 0$, the response $R(u(S, k, t), S)$ of the system should return to its resting level at steady state, i.e.

$$R_{ss}(u_{ss}, S, k) := \lim_{t\to\infty} R(u(S, k, t), S) \equiv R_{ss}(k)$$

where $R_{ss}(k)$ is the resting level of the response which depends only on the system parameters. The following definition for perfect adaptation provides robustness to slight variations in the system parameters.

Definition 1 A system is said to *adapt perfectly* to a constant stimulus if its steady-state response is independent of the level of the stimulus over an appropriate range of parameters.

Example 1

Consider a cartoon system for adaptation proposed by Othmer and Schaap [146]

$$\frac{du_1}{dt} = \frac{f(S(t)) - (u_1 + u_2)}{\tau_e}$$
$$\frac{du_2}{dt} = \frac{f(S(t)) - u_2}{\tau_a}$$
$$u_1(0) = u_2(0) = 0$$

with a constant input $S(t) \equiv S_0$, parameters $k = (\tau_e, \tau_a)$, and the output $R(u, S, t) = u_1(t)$. The system can be viewed as an excitation-inhibition system where u_1, u_2 are stimulated by S and u_2, in turn, inhibits u_1. The system can be solved analytically

$$u_1 = \frac{f(S_0)\tau_a}{\tau_a + \tau_e}\left(e^{-t/\tau_a} - e^{-t/\tau_e}\right)$$
$$u_2 = f(S_0)\left(1 - e^{-t/\tau_a}\right)$$

and $u_1 \to 0$ as $t \to \infty$ regardless of $S_0,\ \tau_a,\ \tau_e > 0$, *i.e.* the system perfectly adapts under all feasible parameter values and stimulus levels. Note that $\lim_{t\to\infty} u_2 = S_0$ to compenstate for the stimulus level.

There have been a few results on perfectly adapting systems. Othmer and Schaap [146] showed that a system described by ODEs adapts perfectly under uniform stimuli if and only if the level sets of its steady-state response are tangent to the gradient of

the steady states of its internal variables with respect to the stimulus. The *internal model principle* (IMP), introduced by Francis and Wonham [59], gives an interpretation for perfect adaptation to general external signals. The principle states that perfectly adapting systems must incorporate an internal model of the external signals. This paper and subsequent work are rooted in the control system literature and assume that the system is composed of a plant and a controller. Sontag [169] extended this principle to more general nonlinear systems, which are more suitable for system biology. It can be shown that this version of IMPs applies to the system in Example 1.

Assuming that a steady-state solution of all internal variables is known, the result by Othmer and Schaap readily provides a testable condition for perfect adaptation. However, the definition of perfect adaptation is idealized. Most biological systems, in fact most physical systems, do not adapt perfectly under arbitrarily large inputs. A recent work by Andrews et al. [6] introduced the notion of approximate adaptation and extended IMP to approximate models. Unfortunately, the definition is not easily testable and fails to address robustness, which is an important property for biological adapting systems. Therefore, it cannot be used as a criteria for physiological models.

Motivated by approximations used in adaptation models, we propose an alternative definition for approximate adaptation with a consideration for robustness, and provide a testable condition to identify systems which adapt approximately.

Definition 2 A system with parameters $k \in \mathcal{P}$ and a steady-state response $R_{ss}(u_{ss}, S, k) \in \mathbb{R}_+$ subjected to a constant level of stimulus S is said to *adapt in the parametric limit* to a constant stimulus if there exists a function $f : \mathcal{P} \to \mathbb{R}$ of parameters k so that for any $M > 0, \epsilon > 0$ there is a $\delta > 0$ such that either of the following is true for all k with $f(k) < \delta$.

(i) $|R_{ss}(u_{ss}, S_1, k) - R_{ss}(u_{ss}, S_2, k)| < \epsilon R_{ss}(u_{ss}, S_2, k) \quad \forall S_1, S_2 < M$

(small-signal adaptation)

(ii) $|R_{ss}(u_{ss}, S_1, k) - R_{ss}(u_{ss}, S_2, k)| < \epsilon R_{ss}(u_{ss}, S_2, k) \quad \forall S_1, S_2 > M$

(large-signal adaptation)

In the case (i), we say the system *adapts by linearity*. In the case (ii), we say the system *adapts by saturation*.

The domain $\mathcal{P}$ of parameters may be a hypercube $\mathbb{R}_+^m$, for example. Essentially, the condition requires that a steady-state response under any levels of stimulus bounded by M is close, in a relative sense, to all other steady-state responses subjected to the stimulus bounded by M. Given stimulus and error bounds, an adaptation region, an open subset of $\mathcal{P}$ represented by the vertical strip of the shaded area in Figure 2.2, can be determined. In contrast, for perfectly adapting systems, parameters which lead to perfect adaptation are determined by equalities and form a close subset of $\mathcal{P}$.

The two cases reflect different requirements for adapting systems. Adaptation by linearity is reflected by perturbations, approximated by a linear system, from the the state with no stimulus. On the other hand, adaptation by saturation reflects a state where increasing the stimulus further does not affect the steady-state response.

Definition 3 If a system adapts in the parametric limit to a constant stimulus S, we say that the *approximate response* of the system with parameter k is

$$R_{ss}(k) = \begin{cases} \lim_{S \to 0} R_{ss}(u_{ss}, S, k) & \text{if the systems adapts by linearity.} \\ \lim_{S \to \infty} R_{ss}(u_{ss}, S, k) & \text{if the systems adapts by saturation.} \end{cases}$$

The following sufficient conditions are useful for identifying a system which adapts in the parametric limit. It will be applied to cases where the steady-state response is determined by a balance between activation and inactivation, both regulated by an upstream regulator.

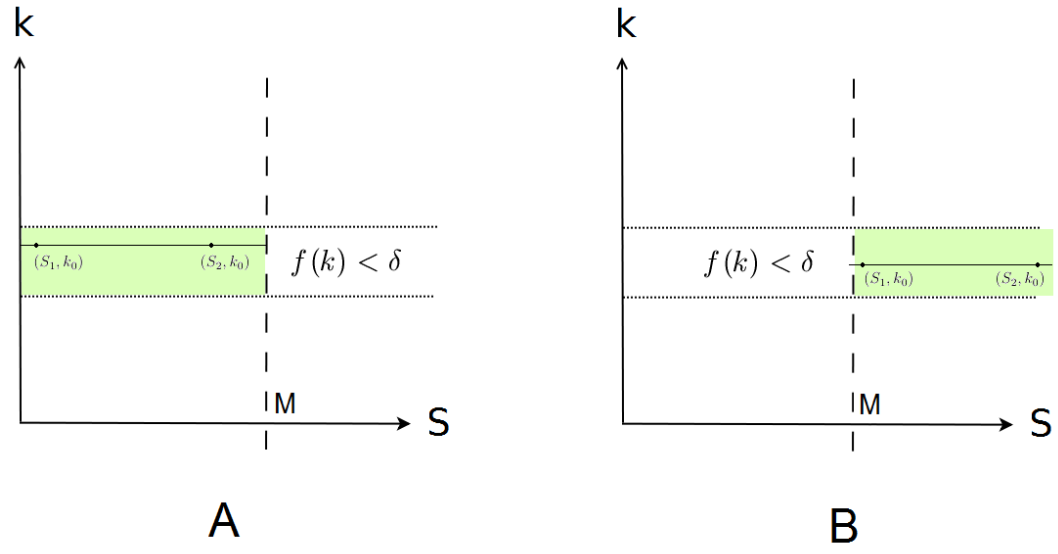

Figure 2.2: The parameter space of systems which adapt in the parametric limit. In each graph, a horizontal line represents a system with parameters k_0. In the shaded area, responses at any two points on the line are within ϵ times the norms of each other. (A) adaptation by linearity. (B) adaptation by saturation.

Lemma 1. *Assume $R_{ss}(u_{ss}, S, k) \geq 0$. Suppose there exists $f : \mathcal{P} \to \mathbb{R}$ so that for each $M > 0$ and $0 < \gamma < 1$, there are $\delta > 0$, $0 \leq \sigma_1, \sigma_2 \leq \gamma$ such that the following is true:*

$$f(k) < \delta \quad \Longrightarrow \quad \exists A > 0 \text{ such that } \begin{cases} \dfrac{R_{ss}(u_{ss}, S, k)}{1 - \sigma_1 - R_{ss}(u_{ss}, S, k)} - A > -\gamma A \\ \dfrac{R_{ss}(u_{ss}, S, k)}{1 - \sigma_2 - R_{ss}(u_{ss}, S, k)} - A < \gamma A \end{cases}$$

either (i) for all $S < M$, or (ii) for all $S > M$. Then the system adapts in the parametric limit. The system adapts by linearity in case (i) and adapts by saturation in case (ii). In each case, the approximate response due to parameter k is

$$R_{ss}(k) = \lim_{\gamma \to 0} \frac{A}{1 + A}.$$

Proof. Fix $M, \epsilon > 0$. Take $0 < \gamma < \min\left(\frac{1}{2}, \frac{\epsilon}{12}\right)$. There exist $\delta > 0$, $0 \leq \sigma_1, \sigma_2 \leq \gamma$, and $f : \mathcal{P} \to \mathbb{R}$ that satisfy the hypothesis. Take k with $f(k) < \delta$. Then for any $S < M$ $(S > M)$,

$$\begin{aligned} \frac{R_{ss}(u_{ss}, S, k)}{1 - \sigma_1 - R_{ss}(u_{ss}, S, k)} - A > -\gamma A \implies & \frac{R_{ss}(u_{ss}, S, k)}{1 - \sigma_1 - R_{ss}(u_{ss}, S, k)} > (1 - \gamma)A \\ \implies & R_{ss}(u_{ss}, S, k) > \frac{(1 - \sigma_1)(1 - \gamma)A}{1 + (1 - \gamma)A} \\ & > \frac{(1 - \gamma)^2 A}{1 + (1 - \gamma)A} \end{aligned} \tag{2.1}$$

and

$$\begin{aligned} \frac{R_{ss}(u_{ss}, S, k)}{1 - \sigma_2 - R_{ss}(u_{ss}, S, k)} - A < \gamma A \implies & \frac{R_{ss}(u_{ss}, S, k)}{1 - \sigma_2 - R_{ss}(u_{ss}, S, k)} < (1 + \gamma)A \\ \implies & R_{ss}(u_{ss}, S, k) < \frac{(1 - \sigma_2)(1 + \gamma)A}{1 + (1 + \gamma)A} \\ & < \frac{(1 + \gamma)A}{1 + (1 + \gamma)A} \end{aligned} \tag{2.2}$$

For any $S_1, S_2 < M$ $(S_1, S_2 > M)$,

$$|R_{ss}(u_{ss}, S_1, k) - R_{ss}(u_{ss}, S_2, k)| < \frac{(1 + \gamma)A}{1 + (1 + \gamma)A} - \frac{(1 - \gamma)^2 A}{1 + (1 - \gamma)A}$$

and

$$\epsilon R_{ss}(u_{ss}, S_2, k) > \epsilon \frac{(1 - \gamma)^2 A}{1 + (1 - \gamma)A}.$$

So, we have $|R_{ss}(u_{ss}, S_1, k) - R_{ss}(u_{ss}, S_2, k)| < \epsilon R_{ss}(u_{ss}, S_2, k)$ if

$$\begin{aligned} \frac{(1 + \gamma)A}{1 + (1 + \gamma)A} < (1 + \epsilon)\frac{(1 - \gamma)^2 A}{1 + (1 - \gamma)A} \iff & \frac{(1 + \gamma) + (1 - \gamma^2)A}{(1 - \gamma)^2(1 + (1 + \gamma)A)} < 1 + \epsilon \\ \iff & \frac{3\gamma - \gamma^2 + (\gamma - \gamma^3)A}{(1 - \gamma)^2(1 + (1 + \gamma)A)} < \epsilon \end{aligned}$$

Since

$$\frac{3\gamma-\gamma^2+(\gamma-\gamma^3)A}{(1-\gamma)^2(1+(1+\gamma)A)}<\frac{3\gamma+\gamma A}{(1-\gamma)^2(1+(1+\gamma)A)}<\frac{3\gamma}{(1-\gamma)^2}<\epsilon,$$

it follows that $|R_{ss}(u_{ss},S_1,k)-R_{ss}(u_{ss},S_2,k)|<\epsilon R_{ss}(u_{ss},S_2,k)$ for k with $f(k)<\delta$.

For the approximate response, let $\gamma\to 0$ in (2.1) and (2.2), while M may be decreased (or increased) if necessary to keep $f(k)<\delta$. Then,

$$\frac{A}{1+A}=\lim_{\gamma\to 0}\frac{(1-\gamma)^2A}{1+(1-\gamma)A}\le\lim_{\gamma\to 0}R_{ss}(u_{ss},S,k)\le\lim_{\gamma\to 0}\frac{(1+\gamma)A}{1+(1+\gamma)A}=\frac{A}{1+A}$$

□

Example 2

As an application of Lemma 1, we analyze adaptation properties of the local-excitation global-inhibition (LEGI) model proposed by Levchenko and Iglesias [125]. In the paper, an approximation of the model, when activities of both activating and inactivating enzymes are small, was shown to perfectly adapt. We will prove that the model itself adapts by linearity by under a particular condition, and adapts by saturation under a different condition.

The adaptation model of Levchenko and Iglesias is described by

$$\begin{aligned}
S+E_1 &\xrightarrow{k_{11}} S+E_1^* \\
E_1^* &\xrightarrow{k_{12}} E_1 \\
S+E_2 &\xrightarrow{k_{21}} S+E_2^* \\
E_2^* &\xrightarrow{k_{22}} E_2 \\
W+E_1^* &\xrightarrow{k_1} W^*+E_1^*
\end{aligned} \tag{2.3}$$

$$W^* + E_2^* \xrightarrow{k_2} W + E_2^*$$

where W denotes a substrate, E_i denote enzymes, S denotes the stimulus, k are rate constants, and the superscript identifies active species. The total amount of each chemical substance, denoted by the subscript T, is conserved unless explicitly expressed. The response of the system is the amount of the activated substrate W^*. By mass action kinetics

$$\frac{dW^*}{dt} = k_1 W \cdot E_1^* - k_2 W^* \cdot E_2^*,$$
$$\frac{dE_i^*}{dt} = k_{i1} S \cdot E_i - k_{i2} E_i^*$$

At a steady state, we have the relation

$$\frac{W^*}{W} = \frac{k_1 E_1^*}{k_2 E_2^*}, \tag{2.4}$$

$$E_i^* = \frac{k_{i1}}{k_{i2} + k_{i1} S} E_{iT} \cdot S \tag{2.5}$$

Adaptation occurs when the fraction of active substrate is independent of the stimulus level, which happens if and only if $\frac{E_1^*}{E_2^*}$ is constant in the steady state for the operating range of the stimulus. This condition rarely occurs physiologically and is impossible for this model. Instead, the system can be shown to adapt in the parametric limit.

Proposition 1. *The system (2.3) adapts in the parametric limit*

(i) *by linearity with* $f_1(k) := \frac{k_{11}}{k_{12}} + \frac{k_{21}}{k_{22}}$ *and an approximate response*

$$W^*{}_{ss}(k) = \frac{k_1 k_{11} k_{22} E_{1T}}{k_2 k_{21} k_{12} E_{2T} + k_1 k_{11} k_{22} E_{1T}} W_T,$$

(ii) *by saturation with* $f_2(k) := \frac{k_{12}}{k_{11}} + \frac{k_{22}}{k_{21}}$ *and an approximate response*

$$W^*{}_{ss}(k) = \frac{k_1 E_{1T}}{k_2 E_{2T} + k_1 E_{1T}} W_T$$

Proof. (i) Given $M > 0$ and $0 < \gamma < 1$, let $\delta = \dfrac{\gamma}{M}$. Fix k such that $f_1(k) < \delta$. So $\dfrac{k_{11}}{k_{12}}, \dfrac{k_{21}}{k_{22}} < \delta$. For $S < M$ we have, by (2.4) and (2.5),

$$\frac{W^*}{W} = \left(\frac{k_1 k_{11} E_{1T}}{k_2 k_{21} E_{2T}}\right) \frac{k_{22} + k_{21} S}{k_{12} + k_{11} S}$$

Now,

$$\frac{k_{22} + k_{21} S}{k_{12} + k_{11} S} < \frac{k_{22}(1 + \delta M)}{k_{12}} = \frac{k_{22}}{k_{12}}(1 + \gamma)$$

and

$$\frac{k_{22} + k_{21} S}{k_{12} + k_{11} S} > \frac{k_{22}}{k_{12}(1 + \delta M)} = \frac{k_{22}}{k_{12}} \frac{1}{(1 + \gamma)} > \frac{k_{22}}{k_{12}}(1 - \gamma)$$

So,

$$\frac{k_1 k_{11} k_{22} E_{1T}}{k_2 k_{21} k_{12} E_{2T}}(1 - \gamma) < \frac{W^*}{W} = \frac{W^*}{W_T - W^*} = \frac{W^*/W_T}{1 - W^*/W_T} < \frac{k_1 k_{11} k_{22} E_{1T}}{k_2 k_{21} k_{12} E_{2T}}(1 + \gamma)$$

We have that

$$\left| \frac{W^*/W_T}{1 - W^*/W_T} \right| < \gamma \frac{k_1 k_{11} k_{22} E_{1T}}{k_2 k_{21} k_{12} E_{2T}}$$

By lemma 1, the system adapts by linearity and

$$\frac{W^*}{W_T} = \frac{k_1 k_{11} k_{22} E_{1T}}{k_2 k_{21} k_{12} E_{2T} + k_1 k_{11} k_{22} E_{1T}}$$

(ii) The proof is similar to case (i). Take $\delta = \gamma M$.

□

The system adapts by linearity when the amount of activated enzymes of both types are almost proportional to the level of the stimulus or a common regulator, which

happens as the activation of both enzymes is far from saturation. On the other hand, the system adapts by saturation when activation of both enzymes is saturated, i.e. $E_1^* \approx E_{1T}$ and $E_2^* \approx E_{2T}$.

The original assumption of Levchenko and Iglesias leads to a system with low activity of both activating and inactivating enzymes, which may raise an issue whether signals can be efficiently transduced by this system. However, if the enzymes are highly catalytic or outnumber the substrate, signals could still be effectively transmitted through the pathway.

In the case of saturation, the system turns out to be nonresponsive to stimulations and is not capable of signaling itself. However, when such system is integrated into a larger network, the network can inherit its adaptive properties. Fully adapted models such as ones in [11, 168] exploit saturation of some chemical species to eliminate the effects of stimuli.

2.2.2 Adaptation models

Adaptation is a common feature in biological signaling systems. Various models with the adaptation property have been proposed in different organisms. Although these models are different, the underlying mechanisms for adaptation display common themes. In this section, we give a summary of the mechanisms for adaptation of molecular regulatory networks, both extracted from models and proposed, in the literature. The mechanisms are simplified where possible. In particular, complex formation in regulation steps is omitted so that a regulator is independent of the state of its immediate downstream species. We also propose several mechanisms for adaptation which have not appeared in the literature.

Because of the simplification, adaptation of these modules are perfect. Table 2.1

displays signaling diagrams, equations, and references for the adaptation modules. The following conventions are used in these diagrams and all signaling diagrams throughout the thesis, unless specified otherwise.

Nodes

- A node refers to a signaling molecule. There are two types of nodes. The first type, called *independent nodes*, consists of nodes which are not connected by any solid arrows. We call nodes that are connected by solid arrows as *conservation nodes*.

- An independent node represents a signaling molecule which consists of interconvertible active and inactive forms. The inactive form is not explicitly noted and assumed to be abundant. Spontaneous deactivation of the active form at a linear rate is also implicitly assumed. Alternatively, an independent node may represent a molecule that spontaneously decays, or is consumed at a constant rate.

- A group of conservation nodes connected by solid arrows, called *conservation group*, represents different forms of the same molecules where a conservation law applies. External production of a member of a conservation group is depicted either by solid arrow originating from an empty node or a dashed arrow originating from a regulator node which represent spontaneous and regulated production respectively. Similarly, a solid arrow pointing from a conservation node towards an empty node depicts external consumption of a conservation group. In the case where no other solid arrow originates from a conservation node, the solid arrow pointing to an empty node may be omitted and spontaneous consumption or decay of the molecule is implicitly assumed.

Arrows

- Dashed arrows denote positive regulation where the *regulator*, the molecule at the pointing node, is not affected. If a dashed arrow points to a node, it represents activation (or an activity that results in production) of the inactive molecule (or the molecule that spontaneously decays) by the regulator at a linear rate. If a dashed arrow points to a solid arrow, it represents an interconversion which depends linearly on the regulator and the substrate. Both types of regulation follows the Michealis-Menten kinetics for enzymetic activation where the enzyme operates in the linear region.

- A solid arrow denotes conversion of a substrate into a product at a linear rate. If a solid arrow is pointed to by a dashed arrow, the conversion rate also depends linearly on the regulator.

- A bar-headed dash line represents an inhibition. If it points to a node , the activation rate of the regulated molecule is inverse-proportional to the inhibitor. One may rationalize this kind of regulation as a short hand for a two-step regulation shown below

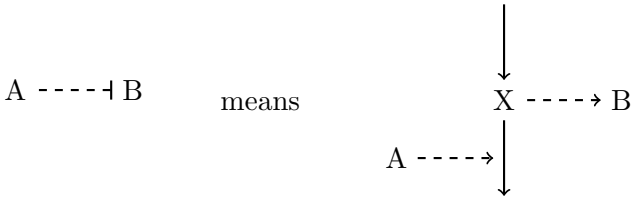

where X is a hidden intermediate effector which equilibrates rapidly. The PSSH on X implies $X = k/A$.

- A dashed arrow pointing to a dashed arrow implies cooperative regulation by multi-step activation. The cooperative regulation may also be explicitly, but not equivalently, specified using the Hill function (for example, see Section 2.3.2). A

bar-headed dashed line poniting to a dashed arrow may be used as a short hand for the following two-step regulation

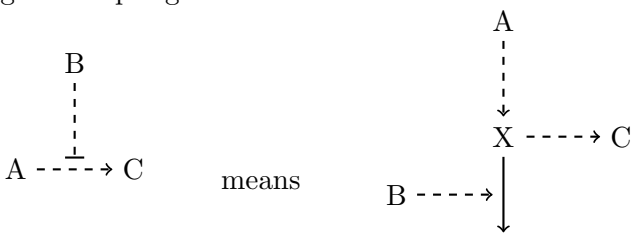

where the hidden intermediate X equilibrates repidly and the PSSH gives $X = kA/B$.

- Consumption of a molecule in the saturated region of the Michealis-Menten kinetics is zero-order. It is represented by a solid arrow with *"Const"*.

Table 2.1: Adaptation modules in biological signaling systems

Feedforward systems		
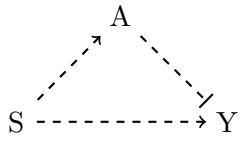	$\frac{dA}{dt} = k_1 S - k_2 A$ $\frac{dY}{dt} = k_3 S/A - k_4 Y$ *Effect of S and A on production of Y is multiplicative.*	EGF to ERK activation, glucose to insulin release, ATP to intracellular calcium release, nitric oxide to NF-κB activation, and microRNA regulation, as referenced in Kim et al. [104]. Other systems include regulation of active EIIA in E. Coli carbohydrate uptake [112], PKA regulation of transcription factor CREB [73], and cAMP adaptation in Dictyostelium [163].

Table 2.1: (continued)

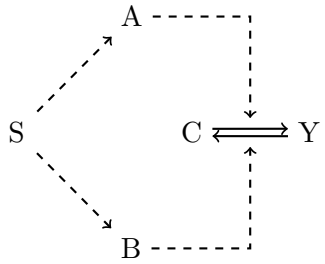	$\frac{dA}{dt} = k_1 S - k_2 A$ $\frac{dB}{dt} = k_3 S - k_4 B$ $\frac{dY}{dt} = k_5 A \cdot C - k_6 B \cdot Y$ $Y + C = const$	Models of PIP_3 adaptation [125, 134] and PLC adaptation [16] to cAMP in Dictyostelium
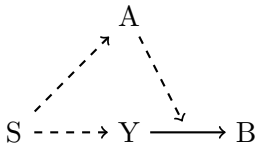	$\frac{dA}{dt} = k_1 S - k_2 A$ $\frac{dB}{dt} = k_3 A \cdot Y - k_4 B$ $\frac{dY}{dt} = k_5 S - k_3 A \cdot Y$	Model for adaptation of adenylyl-cyclase activity in *Dictyostelium* by Tang and Othmer [177, 178]
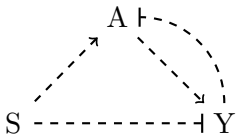	$\frac{dA}{dt} = k_1 S/Y - k_2 A$ $\frac{dY}{dt} = k_3 A/S - k_4 Y$	Simplified scheme for a model of adaptation in bacterial chemotaxis by Spiro et al. [172]
Integral control based on saturation		
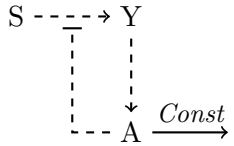	$\frac{dA}{dt} = k_1 Y - k_2$ $\frac{dY}{dt} = k_3 S/A - k_4 Y$ *Degradation of A is enzymetic at saturation, i.e.* $A >> K_M$.	Models of bacterial chemotaxis by Barkai and Liebler [202, 11] and eukaryotic chemotaxis by Skupsky et al. [168]. Other adaptation schemes relying on saturation can be found in [144]
Positive-feedback adaptation		
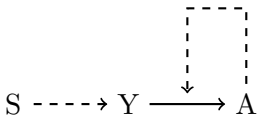	$\frac{dA}{dt} = k_1 Y \cdot A - k_2 A$ $\frac{dY}{dt} = k_3 S - k_1 Y \cdot A$	Newly proposed module for adaptation

Table 2.1: (continued)

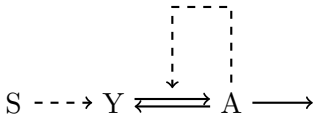	$\frac{dA}{dt} = k_1 Y \cdot A - (k_2 + k_3)A$ $\frac{dY}{dt} = k_4 S + k_3 A - k_1 Y \cdot A$	Newly proposed module for adaptation
BioNetUnit		
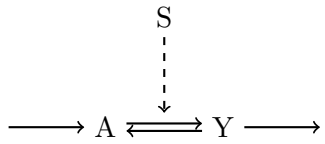	$\frac{dA}{dt} = k_1 + k_2 Y - k_3 S \cdot A$ $\frac{dY}{dt} = k_3 S \cdot A - (k_2 + k_4)Y$	Biochemical network unit, proposed by Csikasz-Nágy and Soyer [45]

2.2.3 Steady-state analysis of *Dictyostelium* adaptation module

Current biological knowledge for the *Dictyostelium* signal transduction pathway suggests that adaptation occurs at the activation of Ras and the LEGI feedforward model proposed by Levchenko and Iglesias [125], among the adaptation models summarized in the previous section, fits well with the current knowledge. We have shown in Example 2 that this model adapts by linearity. However, it is unclear that a more realistic model described by enzymatic reactions would have the same adaptation property. In this section, we introduce a more realistic model for the adaptation module which is described by enzymatic reactions. We assume that the adaptation module and the gradient-amplification module are weakly-coupled so that they can be analyzed separately. It turns out that our detailed system adapts by linearity under certain conditions.

Consider a feedforward activation-inactivation system

$$
\begin{aligned}
S + E_1 &\underset{k^r_{E_1}}{\overset{k^f_{E_1}}{\rightleftharpoons}} [SE_1] \xrightarrow{k^c_{E_1}} S + E_1^* \\
E_1^* &\xrightarrow{k^2_{E_1}} E_1 \\
S + E_2 &\underset{k^r_{E_2}}{\overset{k^f_{E_2}}{\rightleftharpoons}} [SE_2] \xrightarrow{k^c_{E_2}} S + E_2^* \\
E_2^* &\xrightarrow{k^2_{E_2}} E_2 \\
W + E_1^* &\underset{k^r_{W}}{\overset{k^f_{W}}{\rightleftharpoons}} [WE_1^*] \xrightarrow{k^c_{W}} W^* + E_1^* \\
W^* + E_2^* &\underset{k^r_{W^*}}{\overset{k^f_{W^*}}{\rightleftharpoons}} [W^*E_2^*] \xrightarrow{k^c_{W^*}} W + E_2^*
\end{aligned}
\tag{2.6}
$$

where E_1, E_2 are activated by S while activation and inactivation of W are regulated by E_1, E_2 respectively. We call it the stimulus-enzyme-substrate (SES) system. Table 2.2 illustrates how the SES system may describe Ras adaptation.

Table 2.2: Correspondence between the SES model and the Ras activation pathway.

Ras activation module	**SES system**
$G_{\beta\gamma}$	S
$RasGEF$	E_1
$RasGAP$	E_2
$RasGEF^*$	E_1^*
$RasGAP^*$	E_2^*
$[G\beta\gamma \cdot RasGEF]$	$[SE_1]$
$[G\beta\gamma \cdot RasGAP]$	$[SE_2]$
Ras	W
Ras^*	W^*
$[Ras \cdot RasGEF^*]$	$[WE_1^*]$
$[Ras^* \cdot RasGAP^*]$	$[WE_2^*]$

Although the signaling pathway involves molecules that freely diffuse in the cytosol, adaptation is a cell response subjected to spatially uniform stimulations. We assume that the cell is radially symmetric so that the adaptation response depends only on the cell radius. Because all activations occur at the cell membrane, we can simplify the analysis by considering a local system at membrane described fully by ODEs. We will later demonstate numerically that the adaptation result carries on to a two-dimensional system with diffusive species, which are enzymes E_1, E_2 in this case.

In a local SES system, rates of change of molecular species are described by

$$\frac{dE_1^*}{dt} = -k_{E_1}^2 E_1^* - k_W^f W \cdot E_1^* + k_{E_1}^c [SE_1] + (k_W^c + k_W^r)[WE_1^*] \tag{2.7a}$$

$$\frac{dE_2^*}{dt} = -k_{E_2}^2 E_2^* - k_{W^*}^f W^* \cdot E_2^* + k_{E_2}^c [SE_2] + (k_{W^*}^c + k_{W^*}^r)[W^* E_2^*] \tag{2.7b}$$

$$\frac{d[SE_i]}{dt} = -(k_{E_i}^r + k_{E_i}^c)[SE_i] + k_{E_i}^f S \cdot E_i \tag{2.7c}$$

$$\frac{dE_i}{dt} = -k_{E_i}^f S \cdot E_i + k_{E_i}^r [SE_i] + k_{E_i}^2 E_i^* \tag{2.7d}$$

$$\frac{dW}{dt} = -k_W^f W \cdot E_1^* + k_W^r [WE_1^*] + k_{W^*}^c [W^* E_2^*] \tag{2.7e}$$

$$\frac{dW^*}{dt} = -k_{W^*}^f W^* \cdot E_2^* + k_{W^*}^r [W^* E_2^*] + k_W^c [WE_1^*] \tag{2.7f}$$

$$\frac{d[WE_1^*]}{dt} = -(k_W^r + k_W^c)[WE_1^*] + k_W^f W \cdot E_1^* \tag{2.7g}$$

$$\frac{d[W^* E_2^*]}{dt} = -(k_{W^*}^r + k_{W^*}^c)[W^* E_2^*] + k_{W^*}^f W^* \cdot E_2^* \tag{2.7h}$$

with assumed conservation of chemical molecules

$$S_T = S + [SE_1] + [SE_2]$$

$$E_{1T} = E_1 + [SE_1] + E_1^* + [WE_1^*]$$

$$E_{2T} = E_2 + [SE_2] + E_2^* + [W^* E_2^*]$$

$$W_T = W + W^* + [WE_1^*] + [W^*E_2^*]$$

In steady state, (2.7c) with the conservation law for S implies

$$[SE_i] = \frac{S \cdot E_i}{K_{m_{E_i}}}$$

$$S = \frac{S_T}{1 + \frac{E_1}{K_{m_{E_1}}} + \frac{E_2}{K_{m_{E_2}}}}$$

Note that S is proportional to S_T when $E_1 \approx E_{1T}$, $E_2 \approx E_{2T}$ or $\frac{E_1}{K_{m_{E_1}}} + \frac{E_2}{K_{m_{E_2}}} << 1$. It can also be deduced from Equations (2.7e)–(2.7h) that

$$K_{m_W}[WE_1^*] = W \cdot E_1^*$$

$$K_{m_{W^*}}[W^*E_2^*] = W^* \cdot E_2^*$$

$$k_W^c[WE_1^*] = k_{W^*}^c[W^*E_2^*]$$

A relation between E_i and E_i^* follows from (2.7d)

$$E_i^* = \left(\frac{k_{E_i}^c}{k_{E_i}^2 K_{m_{E_i}}}\right) S \cdot E_i$$

Therefore,

$$\frac{W^*}{W} = \frac{\left(\frac{k_W^c}{K_{m_W}}\right)\left(\frac{k_{E_1}^c}{K_{m_{E_1}}}\right)\left(\frac{E_1}{k_{E_1}^2}\right)}{\left(\frac{k_{W^*}^c}{K_{m_{W^*}}}\right)\left(\frac{k_{E_2}^c}{K_{m_{E_2}}}\right)\left(\frac{E_2}{k_{E_2}^2}\right)} \tag{2.8}$$

It is now apparent that if enzyme-substrate complexes are negligible compared to the total substrate concentration, i.e. $W_T \approx W + W^*$, then adaptation depends solely

on the ratio between the free unactivated enzymes. If we have $E_{iT} \approx E_i$ for $i = 1, 2$, the system approximately adapts with

$$w^* = \frac{C}{1+C}$$

where $w^* := \frac{W^*}{W_T}$ is the fraction of activated substrate and

$$C := \frac{\left(\frac{k^c_W}{K_{m_W}}\right)\left(\frac{k^c_{E_1}}{K_{m_{E_1}}}\right)\left(\frac{E_{1T}}{k^2_{E_1}}\right)}{\left(\frac{k^c_{W^*}}{K_{m_{W^*}}}\right)\left(\frac{k^c_{E_2}}{K_{m_{E_2}}}\right)\left(\frac{E_{2T}}{k^2_{E_2}}\right)} \tag{2.9}$$

Now, we determine under which conditions the key assumptions for low enzyme activations and negligible enzyme-substrate complexes are satisfied. In steady state, the conservation of E_{1T}, E_{2T} implies

$$E_1 = \frac{E_{1T}}{1 + \frac{S}{K_{m_{E_1}}}\left(1 + c_{E_1}\left(1 + \frac{W}{K_{m_W}}\right)\right)}$$

$$E_2 = \frac{E_{2T}}{1 + \frac{S}{K_{m_{E_2}}}\left(1 + c_{E_2}\left(1 + \frac{W^*}{K_{m_{W^*}}}\right)\right)}$$

where $c_{E_i} = \frac{k^c_{E_i}}{k^2_{E_i}}$. The steady-state concentration of W^* can be found by solving the cubic equation

$$\begin{aligned} &\gamma d W^{*3} + (\gamma\sigma - cdeE_{1T} - adE_{2T})W^{*2} \\ &+(-c\gamma W_T - ce\sigma E_{1T})W^* + c^2 e W_T E_{1T} = 0 \end{aligned} \tag{2.10}$$

where

$$
\begin{aligned}
a &= 1 + \frac{S}{K_{m_{E_1}}}(1 + c_{E_1}) \\
b &= \frac{c_{E_1} S}{K_{m_{E_1}} K_{m_W}} \\
c &= 1 + \frac{S}{K_{m_{E_2}}}(1 + c_{E_2}) \\
d &= \frac{c_{E_2} S}{K_{m_{E_2}} K_{m_{W^*}}} \\
e &= \left(\frac{k_W^c / K_{m_W}}{k_{W^*}^c / K_{m_{W^*}}} \right) \left(\frac{c_{E_1} / K_{m_{E_1}}}{c_{E_2} / K_{m_{E_2}}} \right) \\
\gamma &= bE_{2T} - deE_{1T} = b \left(E_{2T} - \frac{k_W^c}{k_{W^*}^c} E_{1T} \right) \\
\sigma &= E_{2T} \left(\frac{b}{e} + d \right) + c - dW_T
\end{aligned}
$$

Other steady-state concentrations are given by

$$
\begin{aligned}
W &= W_T - W^* - \left(\frac{b}{e} + d \right) \frac{E_{2T} W^*}{c + dW^*} \\
E_1 &= \frac{E_{1T}}{a + bW} \\
E_2 &= \frac{E_{2T}}{c + dW^*}
\end{aligned}
$$

Note that while a, b, c, d, e are positive parameters, γ, σ may be negative.

It is inconvenient to solve (2.10) and determine the appropriate root. However, the analysis can be simplified since $W, W^* < W_T$. Low enzyme activations occur when

$$
\begin{aligned}
\frac{S}{K_{m_{E_1}}} \left(1 + c_{E_1} \left(1 + \frac{W_T}{K_{m_W}} \right) \right) &<< 1 \\
\frac{S}{K_{m_{E_2}}} \left(1 + c_{E_2} \left(1 + \frac{W_T}{K_{m_{W^*}}} \right) \right) &<< 1
\end{aligned}
$$

Assuming low enzyme activations, it follows that

$$\begin{aligned}\frac{[WE_1^*]}{W_T} &= \frac{[WE_1^*]}{E_{1T}}\frac{E_{1T}}{W_T} << \frac{E_{1T}}{W_T}\\ \frac{[W^*E_2^*]}{W_T} &= \frac{[W^*E_2^*]}{E_{2T}}\frac{E_{2T}}{W_T} << \frac{E_{2T}}{W_T}\end{aligned}$$

Therefore, enzyme-substrate complexes are negligible when enzyme activations are low and the total substrate concentration is not too small compared to the total enzyme concentrations. The following main result is built on this analysis.

Proposition 2. *The SES system (2.6) adapts by linearity in the parametric limit*

$$f(k) := \frac{1+2E_{1T}/W_T}{K_{m_{E_1}}}\left(1+c_{E_1}\left(1+\frac{W_T}{K_{m_W}}\right)\right)+\frac{1+2E_{2T}/W_T}{K_{m_{E_2}}}\left(1+c_{E_2}\left(1+\frac{W_T}{K_{m_{W^*}}}\right)\right)\to 0$$

with an approximate response $W^{*k}_{ss} = \dfrac{C}{1+C}W_T$ *where* C *is defined as in (2.9).*

Proof. Given $M > 0$ and $0 < \gamma < 1$, let $\delta = \gamma M$. Fix k such that $f_1(k) < \delta$. For $S_T < M$,

$$\begin{aligned}\frac{[WE_1^*]}{W_T} &= S\frac{c_{E_1}}{K_{m_{E_1}}}\frac{W}{K_{m_W}}\frac{E_1}{E_{1T}}\frac{E_{1T}}{W_T}\\ &< M\frac{c_{E_1}}{K_{m_{E_1}}}\frac{W_T}{K_{m_W}}\frac{E_{1T}}{W_T}\\ &< \frac{M\delta}{2}\\ &= \frac{\gamma}{2}\end{aligned}$$

Similarly, we have $\dfrac{[WE_1^*]}{W_T} < \dfrac{\gamma}{2}$. By (2.8),

$$\frac{W^*}{W_T - [WE_1^*] - [W^*E_2^*] - W^*} = C\left(\frac{E_1/E_{1T}}{E_2/E_{2T}}\right)$$

$$= C \left[\frac{1 + \frac{S}{K_{m_{E_2}}} \left(1 + c_{E_2} \left(1 + \frac{W^*}{K_{m_{W^*}}}\right)\right)}{1 + \frac{S}{K_{m_{E_1}}} \left(1 + c_{E_1} \left(1 + \frac{W}{K_{m_W}}\right)\right)} \right]$$

We have estimates

$$\begin{aligned}
\frac{w^*}{1-\gamma-w^*} &> \frac{W^*}{W_T - [WE_1^*] - [W^*E_2^*] - W^*} \\
&> \frac{C}{1 + \frac{S}{K_{m_{E_1}}} \left(1 + c_{E_1} \left(1 + \frac{W_T}{K_{m_W}}\right)\right)} \\
&> \frac{C}{1 + M\delta} \\
&= \frac{C}{1+\gamma} \\
&> C(1-\gamma)
\end{aligned}$$

and

$$\begin{aligned}
\frac{w^*}{1-w^*} &< \frac{W^*}{W_T - [WE_1^*] - [W^*E_2^*] - W^*} \\
&< C \left[1 + \frac{S}{K_{m_{E_1}}} \left(1 + c_{E_1} \left(1 + \frac{W_T}{K_{m_W}}\right)\right)\right] \\
&< C(1 + M\delta) \\
&= C(1+\gamma)
\end{aligned}$$

By Lemma 1, the system adapts by linearity and

$$w^* = \frac{C}{1+C}$$

□

When the enzyme activation is linear but the enzyme-substrate complexes are not negligible, we have

$$\frac{W^*}{W_T} = \frac{C}{1 + C + S\left(\frac{E_{1T}c_{E_1}k_W^c}{K_{m_{E_1}}K_{m_W}}\right)\left(\frac{1}{k_W^c} + \frac{1}{k_{W^*}^c}\right)}$$

which is a function of the total stimulus S_T. So, adaptation requires both low enzyme activations, specifically within linear regions, and low levels of the enzyme-substrate complexes. The adaptation fails when one of the conditions is missing.

We have shown that the SES system, which is a detailed activator-inhibitor model for Ras adaptation, adapts by linearity. Although, the requirement on low enzyme activities may raise an issue on how the signal is effectively transmitted, it has been observed that only 3 percent of Ras is activated at the peak after uniform cAMP stimulation [161]. In the next section, we will analyze the dynamics of this system to understand the dynamics of experimentally-observed adaptation responses.

2.2.4 Asymptotic analysis of *Dictyostelium* adaptation module

To analyze the dynamics of each process, we first nondimensionalize the SES system. The PSSH is applied to obtain approximate systems which can be better analyzed.

Nondimensionalization

In order to study dynamics of the model and compare it to *Dictyostelium* response dynamics, we normalize each chemical species by its approximated steady-state value. Recall the governing differential equations

$$\frac{dE_1^*}{dt} = -k_{E_1}^2 E_1^* - k_W^f W \cdot E_1^* + k_{E_1}^c [SE_1] + (k_W^c + k_W^r)[WE_1^*]$$
$$\frac{dE_2^*}{dt} = -k_{E_2}^2 E_2^* - k_{W^*}^f W^* \cdot E_2^* + k_{E_2}^c [SE_2] + (k_{W^*}^c + k_{W^*}^r)[W^* E_2^*]$$

$$\frac{d[SE_i]}{dt} = -(k^r_{E_i} + k^c_{E_i})[SE_i] + k^f_{E_i} S \cdot E_i$$
$$\frac{dE_i}{dt} = -k^f_{E_i} S \cdot E_i + k^r_{E_i}[SE_i] + k^2_{E_i} E^*_i$$
$$\frac{dW}{dt} = -k^f_W W \cdot E^*_1 + k^r_W [WE^*_1] + k^c_{W^*}[W^* E^*_2]$$
$$\frac{dW^*}{dt} = -k^f_{W^*} W^* \cdot E^*_2 + k^r_{W^*}[W^* E^*_2] + k^c_W [WE^*_1]$$
$$\frac{d[WE^*_1]}{dt} = -(k^r_W + k^c_W)[WE^*_1] + k^f_W W \cdot E^*_1$$
$$\frac{d[W^* E^*_2]}{dt} = -(k^r_{W^*} + k^c_{W^*})[W^* E^*_2] + k^f_{W^*} W^* \cdot E^*_2$$

The following are steady-state limits of the adapting system which adapts by linearity:

$$E_i = E_{iT}, \quad W = \frac{1}{1+C} W_T, \quad [WE^*_1] = \frac{W_T}{K_{m_W}} \frac{1}{1+C} \alpha_1, \quad [SE_i] = \frac{1}{c_{E_i}} \alpha_i$$
$$E^*_i = \alpha_i, \quad W^* = \frac{C}{1+C} W_T, \quad [W^* E^*_2] = \frac{W_T}{K_{m_{W^*}}} \frac{C}{1+C} \alpha_2,$$

where various constants are introduced

$$c_{E_i} = \frac{k^c_{E_i}}{k^2_{E_i}}, \qquad \alpha_i = \frac{\bar{S}}{K_{m_{E_i}}} c_{E_i} E_{iT},$$
$$\beta = \frac{k^c_W / K_{m_W}}{k^c_{W^*} / K_{m_{W^*}}}, \qquad C = \frac{\left(\frac{k^c_W}{K_{m_W}}\right)\left(\frac{k^c_{E_1}}{K_{m_{E_1}}}\right)\left(\frac{E_{1T}}{k^2_{E_1}}\right)}{\left(\frac{k^c_{W^*}}{K_{m_{W^*}}}\right)\left(\frac{k^c_{E_2}}{K_{m_{E_2}}}\right)\left(\frac{E_{2T}}{k^2_{E_2}}\right)} = \beta \frac{\alpha_1}{\alpha_2}$$

In addition, the *free* stimulus concentration is normalized by its resting, or basal, level $\bar{S}$. The nondimensionalized variables are as follows

$$s = \frac{S}{\bar{S}}, \qquad e_i = \frac{E_i}{E_{iT}}, \qquad e^*_i = \frac{E^*_i}{\alpha_i}, \qquad [se_i] = \frac{[SE_i]}{\frac{1}{c_{E_i}} \alpha_i}$$

$$w = \frac{W}{\frac{1}{1+C}W_T}, \quad w^* = \frac{W^*}{\frac{C}{1+C}W_T}, \quad [we_1^*] = \frac{[WE_1^*]}{\frac{W_T}{K_{m_W}}\frac{1}{1+C}\alpha_1}, \quad [w^*e_2^*] = \frac{[W^*E_2^*]}{\frac{W_T}{K_{m_{W^*}}}\frac{C}{1+C}\alpha_2}$$

The transient peak in the response before adaptation is caused by rapid activation and subsequently regulated by the slower inactivating enzyme. Therefore, the dynamics of the inactivating enzyme is crucial in studying dynamics of the adapting response. We choose to normalize time by the stimulus-binding time constant of the inactivating enzyme at the basal stimulus level, i.e.

$$\tau = k_{E_2}^f \bar{S}t := \lambda_1 t$$

The nondimensionalized equations are

$$\epsilon_2 \frac{de_1^*}{d\tau} = \frac{k_{E_1}^2}{k_{E_2}^r + k_{E_2}^c}(-e_1^* + [se_1]) + \frac{1}{1+C}\frac{k_W^f W_T}{k_{E_2}^r + k_{E_2}^c}(-w \cdot e_1^* + [we_1^*]) \tag{2.11a}$$

$$\epsilon_2 \frac{de_2^*}{d\tau} = \frac{k_{E_2}^2}{k_{E_2}^r + k_{E_2}^c}(-e_2^* + [se_2]) + \frac{C}{1+C}\frac{k_{W^*}^f W_T}{k_{E_2}^r + k_{E_2}^c}(-w^* \cdot e_2^* + [w^*e_2^*]) \tag{2.11b}$$

$$\frac{de_1}{d\tau} = -\frac{k_{E_1}^f}{k_{E_2}^f} s \cdot e_1 + \frac{k_{E_1}^r}{K_{m_{E_1}} k_{E_2}^f}[se_1] + \frac{k_{E_1}^c}{K_{m_{E_1}} k_{E_2}^f} e_1^* \tag{2.11c}$$

$$\frac{de_2}{d\tau} = -s \cdot e_2 + \frac{k_{E_2}^r}{k_{E_2}^r + k_{E_2}^c}[se_2] + \frac{k_{E_2}^c}{k_{E_2}^r + k_{E_2}^c} e_2^* \tag{2.11d}$$

$$\epsilon_2 \frac{d[se_1]}{d\tau} = \frac{k_{E_1}^r + k_{E_1}^c}{k_{E_2}^r + k_{E_2}^c}(-[se_1] + s \cdot e_1) \tag{2.11e}$$

$$\epsilon_2 \frac{d[se_2]}{d\tau} = -[se_2] + s \cdot e_2 \tag{2.11f}$$

$$\frac{dw}{d\tau} = c_{E_1}\frac{E_{1T}}{K_{m_{E_1}}}\left(-\frac{k_W^f}{k_{E_2}^f} w \cdot e_1^* + \frac{k_W^r}{K_{m_W} k_{E_2}^f}[we_1^*] + \frac{k_W^c}{K_{m_W} k_{E_2}^f}[w^*e_2^*]\right) \tag{2.11g}$$

$$\frac{dw^*}{d\tau} = c_{E_2}\frac{E_{2T}}{K_{m_{E_2}}}\left(-\frac{k_{W^*}^f}{k_{E_2}^f} w^* \cdot e_2^* + \frac{k_{W^*}^r}{K_{m_{W^*}} k_{E_2}^f}[w^*e_2^*] + \frac{k_{W^*}^c}{K_{m_{W^*}} k_{E_2}^f}[we_1^*]\right) \tag{2.11h}$$

$$\epsilon_2 \frac{d[we_1^*]}{d\tau} = \frac{k_W^r + k_W^c}{k_{E_2}^r + k_{E_2}^c}(-[we_1^*] + w \cdot e_1^*) \tag{2.11i}$$

$$\epsilon_2 \frac{d[w^* e_2^*]}{d\tau} = \frac{k_{W^*}^r + k_{W^*}^c}{k_{E_2}^r + k_{E_2}^c}(-[w^* e_2^*] + w^* \cdot e_2^*) \tag{2.11j}$$

where $\epsilon_2 = \dfrac{k_{E_2}^f \bar{S}}{k_{E_2}^r + k_{E_2}^c} = \dfrac{\bar{S}}{K_{m_{E_2}}}$ is the ratio between λ_1 and the turnover time constant $\lambda_2 = k_{E_2}^r + k_{E_2}^c$ of the stimulus-enzyme complex $[SE_2]$. The conservation law for the stimulus can be used to determine

$$s = s_T - \frac{E_{1T}}{K_{m_{E_1}}}[se_1] - \frac{E_{2T}}{K_{m_{E_2}}}[se_2]$$

where $s_T := \dfrac{S_T}{\bar{S}}$.

As a necessary condition for linear enzyme activation, ϵ_2 is a small parameter. We can characterize chemical processes as *fast processes* and *slow processes* according to these time scales.

Model Reduction

It is natural to assume that the turnover rate of $[se_1]$ is at least the same order as the $[se_2]$ turnover rate because the activity of the activator is faster than the activity of the inhibitor. Applying the PSSH to the system, we get

$$[se_i] = \frac{s_T e_i}{1 + \dfrac{E_{1T}}{K_{m_{E_1}}} e_1 + \dfrac{E_{2T}}{K_{m_{E_2}}} e_2} = s \cdot e_i$$

for $i = 1, 2$ which yields a reduction

$$\epsilon_2 \frac{de_1^*}{d\tau} = \frac{k_{E_1}^2}{k_{E_2}^r + k_{E_2}^c}(-e_1^* + s \cdot e_1) + \frac{1}{1 + C} \frac{k_W^f W_T}{k_{E_2}^r + k_{E_2}^c}(-w \cdot e_1^* + [we_1^*]) \tag{2.12a}$$

$$\epsilon_2 \frac{de_2^*}{d\tau} = \frac{k_{E_2}^2}{k_{E_2}^r + k_{E_2}^c}(-e_2^* + s \cdot e_2) + \frac{C}{1+C}\frac{k_{W^*}^f W_T}{k_{E_2}^r + k_{E_2}^c}(-w^* \cdot e_2^* + [w^* e_2^*]) \tag{2.12b}$$

$$\frac{de_1}{d\tau} = \frac{k_{E_1}^c}{K_{m_{E_1}} k_{E_2}^f}(-s \cdot e_1 + e_1^*) \tag{2.12c}$$

$$\frac{de_2}{d\tau} = \frac{k_{E_2}^c}{k_{E_2}^r + k_{E_2}^c}(-s \cdot e_2 + e_2^*) \tag{2.12d}$$

$$\frac{dw}{d\tau} = c_{E_1}\frac{E_{1T}}{K_{m_{E_1}}}\left(-\frac{k_W^f}{k_{E_2}^f} w \cdot e_1^* + \frac{k_W^r}{K_{m_W} k_{E_2}^f}[we_1^*] + \frac{k_W^c}{K_{m_W} k_{E_2}^f}[w^* e_2^*]\right) \tag{2.12e}$$

$$\frac{dw^*}{d\tau} = c_{E_2}\frac{E_{2T}}{K_{m_{E_2}}}\left(-\frac{k_{W^*}^f}{k_{E_2}^f} w^* \cdot e_2^* + \frac{k_{W^*}^r}{K_{m_{W^*}} k_{E_2}^f}[w^* e_2^*] + \frac{k_{W^*}^c}{K_{m_{W^*}} k_{E_2}^f}[we_1^*]\right) \tag{2.12f}$$

$$\epsilon_2 \frac{d[we_1^*]}{d\tau} = \frac{k_W^r + k_W^c}{k_{E_2}^r + k_{E_2}^c}(-[we_1^*] + w \cdot e_1^*) \tag{2.12g}$$

$$\epsilon_2 \frac{d[w^* e_2^*]}{d\tau} = \frac{k_{W^*}^r + k_{W^*}^c}{k_{E_2}^r + k_{E_2}^c}(-[w^* e_2^*] + w^* \cdot e_2^*) \tag{2.12h}$$

Next, the characteristic of Ras activation response in the *Dictyostelium* chemotaxis pathway is used to determine an additional fast process.

The activation of Ras reaches a peak within 10 seconds then drops near the basal level by 30 seconds, when the second rise begins. The concentration of the activated molecules is roughly twice the resting level. To achieve the large activation peak in the stimulus-enzyme-substrate system, the activating enzyme needs either considerable time or speed to act on the substrate before the activity of the inactivating enzyme rises. In order to avoid a third time scale, we identify the first term of (2.12a) as a fast process and apply the PSSH to obtain the reduced model

$$\epsilon_2 \frac{de_2^*}{d\tau} = \frac{k_{E_2}^2}{k_{E_2}^r + k_{E_2}^c}(-e_2^* + s \cdot e_2) + \frac{C}{1+C}\frac{k_{W^*}^f W_T}{k_{E_2}^r + k_{E_2}^c}(-w^* \cdot e_2^* + [w^* e_2^*])$$

$$\frac{de_2}{d\tau} = \frac{k_{E_2}^c}{k_{E_2}^r + k_{E_2}^c}(-s \cdot e_2 + e_2^*)$$

$$\frac{dw}{d\tau} = c_{E_1}\frac{E_{1T}}{K_{m_{E_1}}}\left(-\frac{k^f_W}{k^f_{E_2}}w\cdot e^*_1 + \frac{k^r_W}{K_{m_W}k^f_{E_2}}[we^*_1] + \frac{k^c_W}{K_{m_W}k^f_{E_2}}[w^*e^*_2]\right)$$

$$\frac{dw^*}{d\tau} = c_{E_2}\frac{E_{2T}}{K_{m_{E_2}}}\left(-\frac{k^f_{W^*}}{k^f_{E_2}}w^*\cdot e^*_2 + \frac{k^r_{W^*}}{K_{m_{W^*}}k^f_{E_2}}[w^*e^*_2] + \frac{k^c_{W^*}}{K_{m_{W^*}}k^f_{E_2}}[we^*_1]\right)$$

$$\epsilon_2\frac{d[we^*_1]}{d\tau} = \frac{k^r_W + k^c_W}{k^r_{E_2} + k^c_{E_2}}(-[we^*_1] + w\cdot e^*_1)$$

$$\epsilon_2\frac{d[w^*e^*_2]}{d\tau} = \frac{k^r_{W^*} + k^c_{W^*}}{k^r_{E_2} + k^c_{E_2}}(-[w^*e^*_2] + w^*\cdot e^*_2)$$

where quasi-steady states are $e^*_1 = [se_1] = s\cdot e_1$ and $[se_2] = s\cdot e_2$. Fast variables e_1 and s can be found as functions of $[we^*_1], e_2$ by solving algebraic equations

$$\left(\alpha_1\left(1+\frac{1}{c_{E_1}}\right)s + E_{1T}\right)e_1 + \frac{W_T}{K_{m_W}}\frac{1}{1+C}\alpha_1[we^*_1] = E_{1T}$$

$$s\left(1 + \frac{E_{1T}}{K_{m_{E_1}}}e_1 + \frac{E_{2T}}{K_{m_{E_2}}}e_2\right) = s_T$$

If we further assume that the turnovers of $[we^*_1]$ and $[w^*e^*_2]$ are fast processes, the model is further reduced to

$$\frac{de^*_2}{d\tau} = \delta(-e^*_2 + s\cdot e_2)$$

$$\frac{de_2}{d\tau} = \frac{k^c_{E_2}}{k^r_{E_2} + k^c_{E_2}}(-s\cdot e_2 + e^*_2)$$

$$\frac{dw}{d\tau} = c_{E_1}\frac{E_{1T}}{K_{m_{E_1}}}\frac{k^c_W}{K_{m_W}k^f_{E_2}}(-w\cdot e^*_1 + w^*\cdot e^*_2)$$

$$\frac{dw^*}{d\tau} = c_{E_2}\frac{E_{2T}}{K_{m_{E_2}}}\frac{k^c_{W^*}}{K_{m_{W^*}}k^f_{E_2}}(-w^*\cdot e^*_2 + w\cdot e^*_1)$$

where $\delta = \dfrac{k^2_{E_2}}{\epsilon_2(k^r_{E_2} + k^c_{E_2})} = \dfrac{k^2_{E_2}}{\bar{S}k^f_{E_2}} \approx O(1)$ and e^*_1, s are determined by the conservation

laws

$$e_1^*\left(\frac{1}{s}+\frac{\bar{S}}{K_{m_{E_1}}}\left(1+c_{E_1}\left(1+\frac{W_T}{K_{m_W}}\frac{w}{1+C}\right)\right)\right)=1$$

$$\left(\frac{E_{1T}}{K_{m_{E_1}}}e_1^*+s\left(1+\frac{E_{2T}}{K_{m_{E_2}}}e_2\right)\right)=s_T$$

Note the similarity of this system to nondimensionalization of the model described by (2.3), assuming the activation of e_1 is fast.

Further approximation can be done by invoking a necessary condition for linear enzyme activations. In this case, $\frac{\bar{S}}{K_{m_{E_1}}}\left(1+c_{E_1}\left(1+\frac{W_T}{K_{m_W}}\frac{w}{1+C}\right)\right) << 1$ gives an approximate of e_1^* by $s \approx O(1)$. The approximated system is,

$$\begin{aligned}
\frac{de_2^*}{d\tau} &= \delta(-e_2^*+s\cdot e_2)\\
\frac{de_2}{d\tau} &= \frac{k_{E_2}^c}{k_{E_2}^r+k_{E_2}^c}(-s\cdot e_2+e_2^*)\\
\frac{dw}{d\tau} &= c_{E_1}\frac{E_{1T}}{K_{m_{E_1}}}\frac{k_W^c}{K_{m_W}k_{E_2}^f}(-w\cdot s+w^*\cdot e_2^*)\\
\frac{dw^*}{d\tau} &= c_{E_2}\frac{E_{2T}}{K_{m_{E_2}}}\frac{k_{W^*}^c}{K_{m_{W^*}}k_{E_2}^f}(-w^*\cdot e_2^*+w\cdot s)
\end{aligned}$$

where $s=\dfrac{s_T}{1+\dfrac{E_{1T}}{K_{m_{E_1}}}+\dfrac{E_{2T}}{K_{m_{E_2}}}e_2}$.

The approximate system can be further simplified by symmetries

$$\frac{k_{E_2}^c}{k_{E_2}^r+k_{E_2}^c}\frac{de_2^*}{d\tau}=-\delta\frac{de_2}{d\tau}$$

$$c_{E_2}\frac{E_{2T}}{K_{m_{E_2}}}\frac{k_{W^*}^c}{K_{m_{W^*}}k_{E_2}^f}\frac{dw}{d\tau}=-c_{E_1}\frac{E_{1T}}{K_{m_{E_1}}}\frac{k_W^c}{K_{m_W}k_{E_2}^f}\frac{dw^*}{d\tau}$$

Exploiting the symmetries along with $w(0), w^*(0) \approx 1$ and a condition for adaptation

$\alpha_2/E_{2T} << 1$ (low activation of E_2), we reach a simple approximated form of the system

$$\frac{de_2^*}{d\tau} = \delta\left(s - e_2^*\right) = \frac{k_{E_2}^2}{\bar{S}k_{E_2}^f}\left(s - e_2^*\right) \tag{2.13a}$$

$$\begin{aligned}\frac{dw^*}{d\tau} =& -\left(c_{E_2}\frac{E_{2T}}{K_{m_{E_2}}}\frac{k_{W^*}^c}{K_{m_{W^*}}k_{E_2}^f}\right)e_2^* \cdot w^* - \left(c_{E_1}\frac{E_{1T}}{K_{m_{E_1}}}\frac{k_W^c}{K_{m_W}k_{E_2}^f}\right)s \cdot w^* \\ &+ \left(c_{E_1}\frac{E_{1T}}{K_{m_{E_1}}}\frac{k_W^c}{K_{m_W}k_{E_2}^f} + c_{E_2}\frac{E_{2T}}{K_{m_{E_2}}}\frac{k_{W^*}^c}{K_{m_{W^*}}k_{E_2}^f}\right)s\end{aligned} \tag{2.13b}$$

where

$$s = \frac{s_T}{1 + \frac{E_{1T}}{K_{m_{E_1}}} + \frac{E_{2T}}{K_{m_{E_2}}}}$$

A quick observation of (2.13a) suggests that activation of e_2^* is independent of substrate activity in the simplified model. The time constant for e_2^* activation is $\frac{\bar{S}k_{E_2}^f}{k_{E_2}^2}$, which scales to $\frac{1}{k_{E_2}^2}$ in actual time. Interestingly, the activation time of e_2^* is determined by its spontaneous decay rate. The dynamics of w^*, on the other hand, depends on e_2^*. A lower bound of its decay rate is $c_{E_1}\frac{E_{1T}}{K_{m_{E_1}}}\frac{k_W^c}{K_{m_W}k_{E_2}^f}s$, which translates to $\frac{E_{1T}}{K_{m_{E_1}}}\frac{k_W^c}{K_{m_W}}\frac{c_{E_1}}{1 + E_{1T}/K_{m_{E_1}} + E_{2T}/K_{m_{E_2}}}S_T$ in actual time. Therefore, the adaptation time depends on these parameters. In particular, it is inverse-proportional to the stimulation level.

It can be seen from Equation 2.13 that the reduced model adapts perfectly since $e_2^* \overset{t\to\infty}{\longrightarrow} s$, forcing $w^* = 1$ in steady-state. In fact, this equation can be solved explicitly. The solution is

$$e_2^* = s + (1 - s)e^{-\delta t}$$

$$w^* = \sum_{n=0}^{\infty} \gamma_n e^{-n\delta t} - \Gamma e^{-\kappa(1+C)st + \frac{\kappa(s-1)}{\delta}\left(1-e^{-\delta t}\right)}$$

where

$$\begin{aligned}
\kappa &= c_{E_2} \frac{E_{2T}}{K_{m_{E_2}}} \frac{k^c_{W^*}}{K_{m_{W^*}} k^f_{E_2}} \\
\gamma_0 &= 1 \\
\gamma_n &= \frac{[-\kappa(s-1)]^n}{\prod_{i=1}^{n}(i\delta - \kappa(1+C)s)}, \quad n = 1, 2, ... \\
\Gamma &= \sum_{n=0}^{\infty} \gamma_n
\end{aligned}$$

The dimensionalized form of the approximate system gives a simple perfectly-adapting model for the activator-inhibitor system. In simplified notations,

$$\left.\begin{aligned}
\begin{bmatrix} \frac{du_1}{dt} \\ \frac{du_2}{dt} \end{bmatrix} &= \begin{bmatrix} -k_1 u_1 + k_2 S \\ -k_3 u_1 u_2 - k_4 S u_2 + k_5 S \end{bmatrix} := F(u, S; k) \\
R(t) &= u_2 := G(u(t))
\end{aligned}\right\} \tag{2.14}$$

where

$$\begin{aligned}
&u_1 = E_2^*, \quad k_1 = k^2_{E_2}, \quad k_3 = k^c_{W^*}/K_{m_{W^*}}, \quad k_5 = c_{E_1} \frac{E_{1T}}{K_{m_{E_1}}} \frac{k^c_W}{K_{m_W}} W_T, \\
&u_2 = W^*, \quad k_2 = k^2_{E_2}\alpha_2/\bar{S}, \quad k_4 = c_{E_1} \frac{E_{1T}}{K_{m_{E_1}}} \frac{k^c_W}{K_{m_W}}
\end{aligned}$$

Note that k_1, k_2, k_3, k_4, k_5 are independent. The above system has only one equilibrium point at $(u_1, u_2) = \left(\frac{k_2 S}{k_1}, \frac{k_1 k_5}{k_2 k_3 + k_1 k_4}\right)$, implying perfect adaptation of u_2. The Othmer-Schaap criterion for perfect adaptation can also be used to check the adaptation property of this model. If the 2-state adaptation model is linearized around its steady

state, the linearization is equivalent to the cartoon model analyzed in Example 1.

In summary, the dynamics of the SES system has been analyzed based on the following assumptions: adaptation by linearity, fast turnover of enzyme-substrate complexes, and fast activation/slow inhibition. At different levels of simplification, we have shown that the LEGI adaptation model and the cartoon model can be obtained from the SES system. A 2-state nonlinear model which captures essential adaptation dynamics of the SES system has been obtained and shown to adapt perfectly. We have identified time constants for inactivating-enzyme activation, substrate activation, and substrate adaptation. In particular, the adaptation time of the system is inverse-proportional to the stimulus level.

Numerics

We use a Matlab stiff ODE solver to test our analysis of adaptation dynamics of the SES system and compare it to the reponses of the simplified 2-state system. Parameters with arbitrary units used in the simulations are given in Table 2.3.

RasGEF		RasGAP		Ras	
Parameter	Value	Parameter	Value	Parameter	Value
E_{1T}	1	E_{2T}	1	W_T	1
$k^f_{E_1}$	0.5	$k^f_{E_2}$	5	k^f_W	10000
$k^r_{E_1}$	500	$k^r_{E_2}$	100	k^r_W	50
$k^c_{E_1}$	1	$k^c_{E_2}$	0.01	k^c_W	500
$k^2_{E_1}$	1000	$k^2_{E_2}$	0.05	$k^f_{W^*}$	10000
				$k^r_{W^*}$	50
				$k^c_{W^*}$	500

Table 2.3: Parameter values for the SES system.

First, the system is subjected to different stimulation levels which are applied at $t = 10$ seconds. Figure 2.3 displays the levels of w^* after stimulation in the full model and the 2-state model described by Equation (2.14). The simulation results confirm

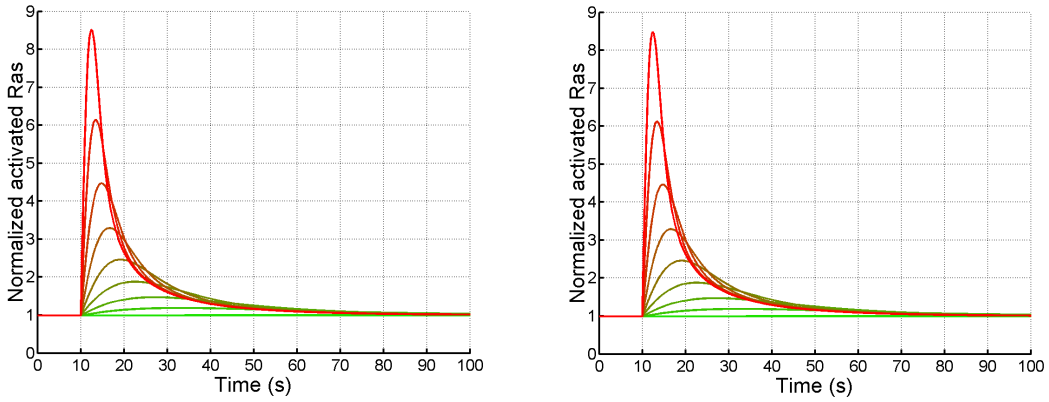

Figure 2.3: Normalized substrate-activation dynamics induced by a uniform stimulus with concentration ranging from 1x to 256x of the basal level. *(Left)* Full SES model *(Right)* 2-state approximation.

our analysis of the adaptation properties. The system adapts in the steady-state and the adaptation time is dependent on the level of the steady-state stimulus. The system adapts approximately in 30 seconds which agrees with experimental observations in *Dictyostelium*. In addition, one can see that the two-state model produces responses which are quantitatively similar to the responses of the full model while it is much simpler. Figure 2.4 displays the difference between the responses of these models, normalized by instantenous responses of the SES model. The model reduction by PSSH introduces large initial errors, especially for large responses. However, the errors decrease rapidly. The positive and negative errors are due to overestimation of the activation and inactivation speed respectively.

We then examine how the system reacts when the applied stimulus is removed. Figure 2.5 displays the levels of activated Ras after down-stimulation in the full model.

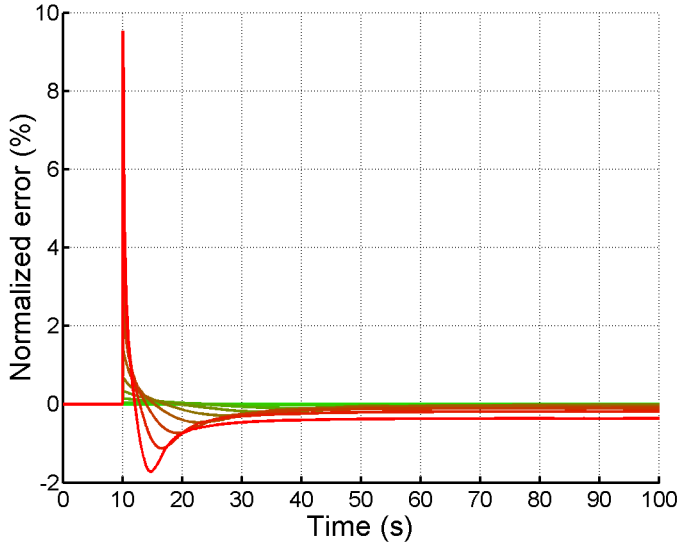

Figure 2.4: Relative difference between substrate activities of the 2-state model and the SES model. The stimulation levels are the same as in Figure 2.3.

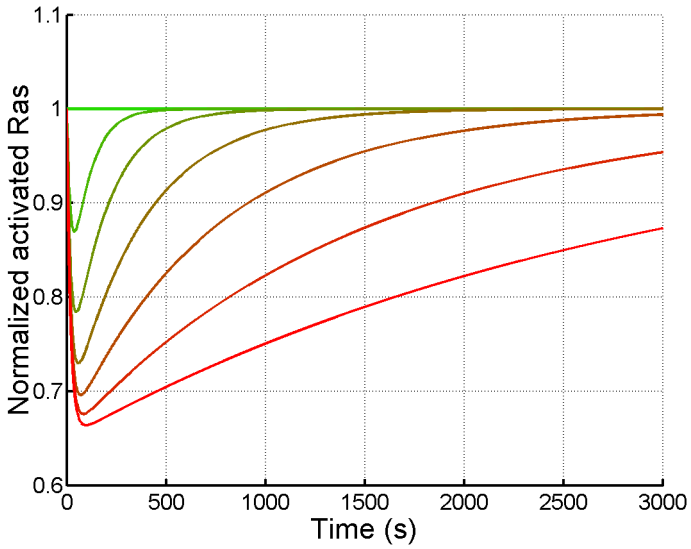

Figure 2.5: Normalized substrate activation induced by uniform removal of the ambient stimulus with resulting concentration ranging from 1/64x to 1x of the basal level.

The adaptation is very slow because it depends on the stimulus levels which are lower than the basal level. Similarly, removal of the stimulus after the responses have adapted induces a transient state with lower-than-normal Ras activity. In Figure 2.6, adaptation time after the stimulus is removed is in line with the *recovery time* of several minutes that *Dictyostelium* is unresponsive to further stimuli after the original stimulus is removed [197]. The simulation also reveals that RasGAP deactivation is slower than RasGEF

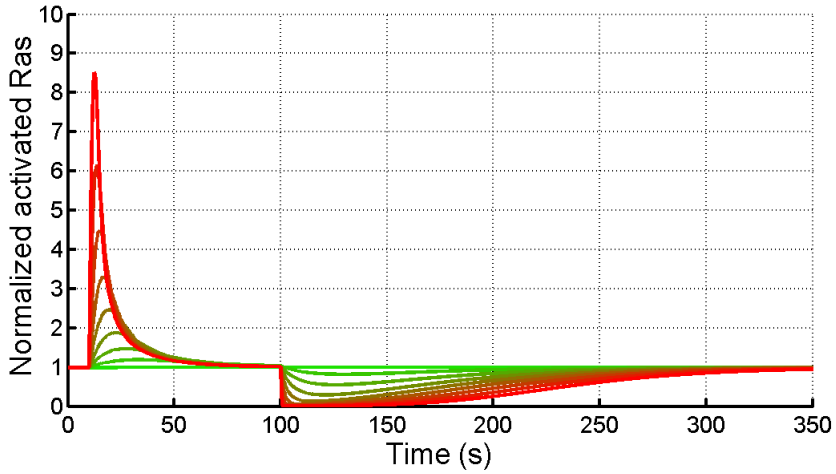

Figure 2.6: Normalized substrate activation induced by introduction and removal of a uniform stimulus. The stimulus is introduced at 10 seconds and removed at 100 seconds. The levels of the stimulus are the same as in Figure 2.3.

deactivation (result not shown). Moreover, the delay in Ras activation recently observed by Zhang et al. [203] in $nfaA-$ mutants, which exhibit low RasGAP level, can be explained by the dependency of the Ras activation speed on E_{2T} in (2.11h).

The numerical simulations show that the adaptation property of the SES system is robust and that the 2-state model is a good approximation to the SES system. Nevertheless, we found that the response dynamics of the adapting system is sensitive to the choice of parameters.

2.3 Gradient Amplification

Sensitivity to a small spatial gradient of stimulation is a vital property in cell motility. In the context of chemotaxis, cells can detect a small end-to-end difference, as low as 2 %, in stimulus levels and respond correctly by orienting themselves and moving in a favorable direction [132, 57, 110]. This mechanism could have been as simple as a constant gain if not for adaptation, another vital property in cellular chemotaxis. When adaptation comes into play, developing this sensitivity becomes much more complicated as cells have to be sensitive to relative levels, instead of absolute levels, of stimulations.

Despite a considerable amount of experimental and numerical studies on *Dictyostelium* chemotaxis, an effective measurement tool for spatial sensitivity has never been established or used. To properly quantify gradient amplification, we first develop a measure for spatial sensitivity. Later, we will use it to test gradient-amplifying models.

2.3.1 Spatial sensitivity

Measurement of spatial sensitivity is fundamentally different from measuring absolute sensitivity. To distinguish this subtle difference, we first discuss absolute sensitivity, also commonly known as *the amplification factor* or *gain*, which is a standard terminology in eletrical engineering and control theory. It is how much a system magnifies its response $R(u(k, S(t), t), S(t))$ with respect to its input $S(t)$, which will be abbreviated as $R(t)$ and $S(t)$ respectively while $R_{ref}(t) = R(u(k, S_{ref}(t), t), S_{ref}(t))$ denotes the response by a reference input $S_{ref}(t)$. There are many ways to quantify steady-state gain, subject to a constant input. The simplest way is

$$g_{absolute} = \frac{\Delta R_{ss}}{\Delta S} = \frac{R_{ss} - R_{ss,ref}}{S - S_{ref}} \tag{2.15}$$

where R_{ss} is the steady-state response, when the system is subjected to a constant input S. For linear stable systems, (2.15) becomes $g_{absolute} = R_{ss}/S$ since

$$0 = \dot{u} = Au + BS$$
$$R = Cu + DS$$

implies $R = (CA^{-1}B + D)S$ at steady state. In addition to gain, which is an absolute measure, one may also measure *incremental gain*, or *sensitivity*, by

$$g(S) = \lim_{S_1 \to S} \frac{R_{ss}(S) - R_{ss}(S_1)}{S - S_1} = \frac{dR_{ss}}{dS}(S)$$

For linear systems, gain and sensitivity are identical. *Normalized gain* and *normalized sensitivity* [111, 103] are probably the most common ways of measuring signal amplification

$$\bar{g}_{absolute} = \frac{\Delta R_{ss}/R_{ss,ref}}{\Delta S/S_{ref}},$$
$$\bar{g}(S) = \frac{dR_{ss}/R_{ss}}{dS/S} = \frac{d\log R_{ss}}{d\log S}(S)$$

in nonlinear systems. Note that $\bar{g}_{absolute} = \bar{g}(S) = 1$ for linear systems. If one is more interested in transient input or response, e.g. in bacterial chemotaxis [172], different measures may be used

$$g_{total} = \frac{\int_{t_0}^{\infty}(R(t) - R_{ss})dt}{\int_{t_0}^{\infty}(S(t) - S_{ss})dt},$$
$$g_{\infty} = \frac{\sup\limits_{t<\infty} R(t)}{\sup\limits_{t<\infty} S(t)}.$$

In contrast to the absolute sensitivity which measures the actual signal level, the

spatial sensitivity is used to measure orientation or polarity of the response caused by the polarity of the input. As we can see later in Chapter 3, the response polarity depends not only on the system dynamics but also on other factors such as shape and size of the domain and the spatial profile of the input. The direction of the response polarity may be different from the direction of the input polarity when the response is dominated by the other factors. Moreover, the spatial profile of the input may be irrugular and non-static, having no clear polarity, changing polarity, or polarity in multiple directions, which complicates quantification of the spatial sensitivity. For example, spatial profiles of cAMP generated by a nearby *Dictyostelium* cell, as seen by a responding cell, have been studied by Dallon and Othmer [46]. Despite these difficulties, one should only consider the response polarity contributed by the input rather than the total response polarity when the spatial sensitivity is measured.

In special cases, the polarity of the response aligns, possibly in the reverse direction, with the polarity of the input. For example, this occurs when a linear-gradient input, which is affine in space, is applied to a symmetric cell which does not exhibit an irregular response, such as ones caused by Turing bifurcation. In such cases, one may measure the spatial sensitivity by comparing the polarity of the response to the polarity of the input. The following is a direct extension of $g_{absolute}$ for linear systems, with $R_{ss,ref} = S_{ref} = 0$.

Definition 4 *Linear gradient amplification, or spatial gain,* of a chemotactic signaling process subjected to a steady input is defined as

$$G_{absolute} = \lim_{t\to\infty} \frac{\max\limits_{x\in\Omega} R(x,S,t) - \min\limits_{x\in\Omega} R(x,S,t)}{\max\limits_{x\in\Omega} S(x) - \min\limits_{x\in\Omega} S(x)} := \frac{R_{\max,ss} - R_{\min,ss}}{S_{\max} - S_{\min}} := \frac{\Delta_s R_{ss}}{\Delta_s S}$$

where $R(x,S,t) = R(u(x,k,S(\cdot),t),S(x))$ and Ω is the spatial domain where R is defined. In cases where the spatial profile of the input can be parameterized, we may analogously define *spatial sensitivity* by fixing S_{min} while changing S_{max} by varying a

parameter which defines the input gradient. For an input with $S_{max} = S_{min} + \delta$, the spatial sensitivity is

$$G_{\Delta_s S}(\delta; S_{\min}) = \lim_{\delta_1 \to \delta} \frac{\Delta_s R_{ss}(S) - \Delta_s R_{ss,1}(S_1)}{\Delta_s S - \Delta_s S_1} = \frac{d\left(\Delta_s R_{ss}\right)}{d\delta}$$

where $\Delta_s R_{ss}(S) = \max_{x \in \Omega} R_{ss}(x, S) - \min_{x \in \Omega} R_{ss}(x, S)$ and $\min_{x \in \Omega} S = \min_{x \in \Omega} S_1$.

Remark As an example, a static linear-gradient input in the domain $x \in [0, 2]$ can be parameterized as $S(x) = \alpha + \beta x$. For $\beta > 0$, we have $\delta = 2\beta$ and $G_{\Delta_s S}(\delta; S_{\min}) = \frac{1}{2} \frac{d\left(\Delta_s R_{ss}\right)}{d\beta}$.

Remark If the system depends only on local dynamics, i.e. there is no communication between state variables at different points in the domain, the terms involving the minimum cancel out and we have

$$G_{\Delta_s S}(\delta; S_{\min}) = \frac{dR_{ss}}{dS}(S_{\min} + \delta) = \frac{dR_{ss}}{dS}(S_{\max})$$

which can be conveniently defined as $G_{\Delta_s S}(S_{\max})$. This is also true if the system is linear.

The spatial gain and the spatial sensitivity are suitable for linear systems, where variables can take negative values. However, they are not unit-free and give incorrect measurements for amplification of the polarity, which should not exceed unity for linear systems. This is an undesirable feature for chemotaxis. The following example illustrates the concepts of spatial gain and spatial sensitivity in linear systems.

Example 3

Let $x \in [0, 1]$. Consider a generaliztion of the linear system in Example 1 with diffusing

constituents:

$$\frac{\partial u_1}{\partial t} = D_e \frac{\partial^2 u_1}{\partial x^2} + \frac{k(S(x) - u_2) - u_1}{\tau_e}$$
$$\frac{\partial u_2}{\partial t} = D_a \frac{\partial^2 u_2}{\partial x^2} + \frac{S(x) - u_2}{\tau_a}$$
$$\frac{\partial u_1}{\partial x} = \frac{\partial u_2}{\partial x} = 0, \quad x = 0, 1$$
$$u_1(x, 0) = u_2(x, 0) = 0$$

where the parameters are positive-valued and the system response is $R = u_1$. To determine the spatial sensitivity of the system, we are interested in the steady-state response due to a static linear gradient

$$S(x) = \alpha + \beta x.$$

At steady state, the PDEs reduce to ODEs

$$\frac{\partial^2 u_1}{\partial x^2} = \frac{u_1 + k(u_2 - S(x))}{\tau_e D_e}$$
$$\frac{\partial^2 u_2}{\partial x^2} = \frac{u_2 - S(x)}{\tau_a D_a}$$
$$\frac{\partial u_1}{\partial x} = \frac{\partial u_2}{\partial x} = 0, \quad x = 0, 1$$

whose solutions are

$$u_{1,ss}(x) = \frac{k\beta}{(\tau_e D_e/\tau_a D_a - 1)} \left[\frac{\sqrt{\tau_e D_e}}{\cosh\left(1/2\sqrt{\tau_e D_e}\right)} \sinh\left(\frac{x - 1/2}{\sqrt{\tau_e D_e}}\right) \right.$$
$$\left. - \frac{\sqrt{\tau_a D_a}}{\cosh\left(1/2\sqrt{\tau_a D_a}\right)} \sinh\left(\frac{x - 1/2}{\sqrt{\tau_a D_a}}\right) \right]$$

$$u_{2,ss}(x) = \alpha + \beta x - \frac{\beta\sqrt{\tau_a D_a}}{\cosh\left(1/2\sqrt{\tau_a D_a}\right)} \sinh\left(\frac{x - 1/2}{\sqrt{\tau_a D_a}}\right)$$

when $\tau_e D_e, \tau_a D_a > 0$, and $\tau_e D_e \neq \tau_a D_a$. In this case, the steady-state response $R_{ss}(x) = u_{1,ss}(x)$ depends only on the slope of the input. The absolute level of the input does not affect the response because of linearity of the system.

The spatial gain of the system

$$G_{absolute} = \frac{2k}{(\tau_e D_e/\tau_a D_a - 1)} \left[\sqrt{\tau_e D_e} \tanh\left(\frac{1}{2\sqrt{\tau_e D_e}}\right) - \sqrt{\tau_a D_a} \tanh\left(\frac{1}{2\sqrt{\tau_a D_a}}\right)\right]$$

is independent of the absolute level and the slope of the linear gradient, and coincides with the spatial sensitivity, *i.e.* $\mathrm{G}_{\Delta_s S} = G_{absolute}$. For fixed τ_e, τ_a, D_e, D_a, the spatial gain can become arbitrarily large as $k \to +\infty$ although the system is linear. Figure 2.7 displays $G_{absolute}$ at different parameter values.

The full evolution of the system, which is exponentially decaying in time, can be solved analytically using expansions. For instance,

$$u_2(x,t) = (\alpha + \beta/2)\left(1 - e^{-t/\tau_a}\right) - \sum_{n=1}^{\infty} \frac{4\beta\cos(c_n x)}{\tau_a D_a c_n^4 + c_n^2}\left(1 - e^{-(D_a c_n^2 + 1/\tau_a)t}\right)$$

where $c_n = (2n-1)\pi$.

The *Dictyostelium* chemotactic signaling system behaves nonlinearly with respect to input gradients. Experimental results by Fisher et al. [57], Janetopoulos et al. [90], and Ma et al. [130] suggest that *Dictyostelium* chemotactic signaling responds to the normalized level of the spatial gradient. The following measure of signal amplification which better captures nonlinearity has been used by Ma et al. [130] to quantify gradient amplification.

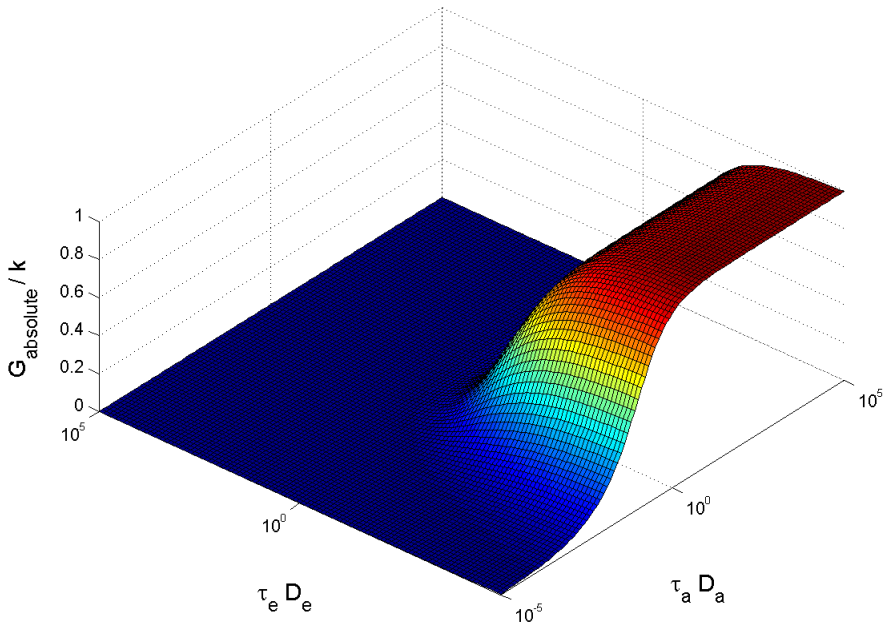

Figure 2.7: The spatial gain of the simple adaptation system in Example 3, computed at steady state as a function of system parameters

Definition 5 *The gradient magnification ratio* of a chemotactic signaling process subjected to a static input $S(x)$ is defined as

$$G_{ratio} = \frac{R_{\max,ss}/R_{\min,ss}}{S_{\max}/S_{\min}}$$

The gradient magnification ratio is an intuitive way to think about gradient amplification as it reflects magnification of gradient ratios. Note that it only applies to positive-value signals. Although the gradient magnification ratio is unit-free and correctly captures the condition when there is no magnification, it has a major drawback. Its value approaches unity when $S_{\max}/S_{\min}$ is small. Therefore, it is not suitable for measurement of small end-to-end gradients, which is common in chemotaxis.

It is desirable to extend normalized gain and normalized sensitivity to spatial amplification. One may naively use

$$\bar{G} = \frac{\Delta_s R_{ss}/\bar{R}}{\Delta_s S/\bar{S}}$$

where $\bar{S}, \bar{R}$ are some reference input and response levels. This is an absolute measure which allows comparison between gradient-amplifying models. However, it is unclear how the reference levels are choosen, especially when $\Delta_s S$ is large. Furthermore, the analysis of individual models necessitates a normalized incremental measure which cannot be easily extended from this definition. The following extension of the spatial gain circumvents these problems.

Definition 6 Suppose that both S and R do not change signs. Then *normalized gradient amplification*, or *normalized spatial gain*, of a chemotactic signaling process subjected to a steady input is defined as

$$\bar{G}_{absolute} = \frac{\log\left(R^+_{\max,ss}/R^+_{\min,ss}\right)}{\log\left(S^+_{\max}/S^+_{\min}\right)} = \frac{\Delta_s \log R^+_{ss}}{\Delta_s \log S^+}$$

where $S^+(x) = |S(x)|$, $S^+_{\max} = \max_{x\in\Omega} S^+$, and $\Delta_s \log R^+_{ss}(S) = \max_{x\in\Omega} \log R^+_{ss}(x,S) - \min_{x\in\Omega} \log R^+_{ss}(x,S)$. If the spatial profile of the input is parameterizable, we may define *normalized spatial sensitivity*

$$\bar{G}_{\Delta_s S}(\gamma; S^+_{\min}) = \lim_{\gamma_1\to\gamma} \frac{\Delta_s \log(R^+_{ss}) - \Delta_s \log(R^+_{ss,1})}{\Delta_s \log(S^+) - \Delta_s \log(S^+_1)} = \frac{d\left(\Delta_s \log(R^+_{ss})\right)}{d\gamma}$$

where $S^+_{\max} = e^\gamma S^+_{\min}$ and $S^+_{\min} = S^+_{1,\min}$.

Remark If either R or S switches its sign, its normalization cannot be meaningfully used.

Remark If the system depends only on local dynamics and both S, R are positive-valued, we have

$$\bar{G}_{\Delta_s S}(\gamma; S^+_{\min}) = \frac{d \log R_{ss}}{d \log S}(S_{\max}) = \frac{S_{\max}}{R_{\max,ss}} \frac{dR_{ss}}{dS}(S_{\max}) = \frac{S_{\max}}{R_{\max,ss}} G_{\Delta_s S}(S_{\max}) = \bar{g}(S_{\max})$$

and

$$\bar{G}_{absolute} = \frac{1}{\Delta_s \log S} \int_{S=S_{\min}}^{S=S_{\max}} \bar{g}(S) d \log S$$

Normalized spatial gain and normalized spatial sensitivity do not suffer from small spatial gradients like the gradient magnification ratio and is better suited for *Dictyostelium* chemotaxis than spatial gain and spatial sensitivity. The normalized spatial gain, which is an absolute measure, can be used to benchmark models for spatial gradient amplification while the normalized spatial sensitivity is suitable for analysis of individual models. In particular, its relationship to the normalized sensitivity will be used to analyze simplified models for gradient amplification. In Chapter 3, the gradient ratio will be used when we compare numerical results to available experimental data.

2.3.2 Models for sensitivity

In this section, we discuss simple modules which amplify gradients. To make analysis possible and preclude different permutations of diffusing species, we neglect diffusion and consider only local dynamics. Although an introduction of diffusion 'smooths' spatial profiles of responses and reduce gradient-amplification effectiveness, the results still hold qualitatively for most systems. With this simplification, the normalized spatial sensitivity is equivalent to the normalized sensitivity. Therefore, we consider highly-sensitive systems as candidates for gradient-amplifying systems.

A classical way to produce high sensitivity is to include cooperative binding in the

form of a Hill term [72]. This mechanism leads a large plateau of the amplifying region with normalized spatial sensitivity close to the order of the Hill term. This mechanism is physically suitable in systems with cooperative bindings. However, it has been routinely used in other systems, usually with a high cooperativity order, as a recipe to obtain high sensitivity.

Alternatively, Goldbeter and Koshland [71] discovered a condition, termed as zero-order ultrasensitivity, for the simple covalent-modification, or enzymetic-activation, system which leads to high sensitivity. This mechanism for high sensivity has been successfully applied to highly-sensitive systems [87] and used to create bistability and switches [38, 56]. Nevertheless, the condition is very sensitive to concentrations of the interacting species. We found that the application of the zero-order ultrasensitivity scheme to the SES system breaks down when diffusion is introduced.

It has been suggested and accepted that positive feedbacks lead to systems with high sensitivity [103]. We argue, with a simple example, that the positive feedback alone is not sufficient to obtain high sensitivity.

Recently, Moore et al. [137] observed that gradient amplification is acheived when Hill-type cooperativity is complemented by a positive feedback in a diffusive system. In fact, this combination has been used to obtain bistability and a switch-like behavior [56, 7] in nondiffusive systems. Although the work by Tyson and Othmer [180] has discussed bistability and given a thorough stability analysis of a similar mechanism in the context of metabolic pathways, a careful analysis on this particular model has never been given. In particular, it is unclear how this system can achieve high sensitivity or serve as a biological switch. We will show that this model, in different parameter regimes, may become a biological switch, act like an hysteresis, or lead to high sensitivity, exceeding one with the cooperativity alone.

Several complicated models on *Dictyostelium* chemotaxis have successfully produced

gradient amplification. Because of the complexity, the systems cannot be thoroughly analyzed and their gradient-amplifying property has been attributed to positive feedback [134, 168]. We argue that, in fact, the gradient-amplifying property in these systems is due to combinations of cooperativity and positive feedbacks. We propose simple and biologically-faithful models which underline the actual source of gradient amplification. Among these models, the model with implicit cooperativity and a positive feedback is strongly supported by the existing knowledge of the *Dictyostelium* chemosensing pathway and it will be used in our model of *Dictyostelium* chemotaxis.

Because the analysis is similar between the models, we only give detailed analysis for the positive-feedback models with Hill-type and implicit cooperativity. Nevertheless, we want to emphasize a general principle that high sensitivity may not be achieved in linear or sublinear systems, even with positive feedbacks. However, if superlinear sensitivity has been obtained either by cooperativity or zero-order ultrasensitivity, a positive feedback may greatly amplify this sensitivity. Other cooperativity models which obtain high sensitivity through a positive feedback will be summarized at the end of this section.

A model with Hill-type cooperativity and positive feedback

A Hill term is derived as a steady-state concentration of an active complex $[X \cdot S^n]$ in a simple model of cooperative binding

$$nS + X \underset{k_2}{\overset{k_1}{\rightleftharpoons}} X \cdot S^n$$

where X is the substrate bound by S. The steady-state concentration of the complex is given by $[X \cdot S^n] = X_T S^n/(K_d + S^n)$ where $K_d = k_2/k_1$ is the dissociation constant. Assuming the complex rapidly equilibrates, the activity of the complex follows the above

expression. Normally, Hill cooperativity introduces high normalized sensitivity with a maximum close to n at a low input level [72].

In this section, we show that large steady-state sensitivity can be achieved without exploiting an artificially large Hill coefficient. In particular, we analyze a simple model with Hill cooperativity and positive feedback whose response is very sensitive to inputs within some parameter regions. Consider a system

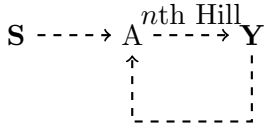

which is described by

$$\frac{dA}{dt} = k_1 S + k_2 Y - k_3 A$$
$$\frac{dY}{dt} = k_4 \frac{A^n}{K_d + A^n} - k_5 Y$$

In the steady state, one has

$$k_1 S = m_1 A - m_2 \left(\frac{A^n}{m_3 + A^n} \right) \tag{2.16}$$
$$k_2 Y = m_2 \left(\frac{A^n}{m_3 + A^n} \right) \tag{2.17}$$

where $m_1 = k_3,\ m_2 = k_2 k_4 / k_5$, and $m_3 = K_d$. Assuming there is one steady state for a given S, the normalized sensitivity is

$$\bar{g} = \frac{S}{Y}\frac{dY}{dS} = n \left(\frac{m_3}{m_3 + A^n} \right) \left(\frac{m_1 A - m_2 (A^n/(m_3 + A^n))}{m_1 A - n m_2 (A^n/(m_3 + A^n))(m_3/(m_3 + A^n))} \right)$$

First, consider the case with no cooperativity, i.e. $n = 1$. In this case, the Hill term

becomes a Michaelis-Menten term and there is only one positive steady state

$$A = \frac{1}{2m_1}\left(m_2 + k_1 S - m_1 m_3 + \sqrt{(m_2 + k_1 S - m_1 m_3)^2 + 4k_1 m_1 m_3 S}\right)$$
$$Y = \frac{1}{2k_2}\left(m_2 - k_1 S - m_1 m_3 + \sqrt{(m_2 + k_1 S - m_1 m_3)^2 + 4k_1 m_1 m_3 S}\right)$$

For the positive steady state, $(m_3 + A)m_1 - m_2 > 0$. Using this relation, one can easilly show that the positive steady state is stable. The system has normalized sensitivity

$$\bar{g} = \frac{(m_3 + A)m_1 - m_2}{(1 + A/m_3)(m_3 + A)m_1 - m_2} < 1$$

Therefore, the simple feedback system with no cooperativity has one stable positive steady state and is gradient-attenuating in all parameter ranges.

For the case with cooperativity, we analyze the system when $n = 2$. We first analyze the steady states. The RHS of (2.16) is a continuous function

$$f(A) = m_1 A - m_2\left(\frac{A^2}{m_3 + A^2}\right)$$

Since $f(0) = 0$ and $\lim_{A\to+\infty} f(A) = +\infty$, (2.16) has at least one positive real root for each $S \in [0, \infty)$. Putting (2.16) in a polynomial form, the steady states of the system correspond to the solutions of

$$p(A) = m_1 A^3 + (-m_2 - k_1 S)A^2 + m_1 m_3 A - k_1 m_3 S = 0$$

The Routh-Hurwitz theorem implies that the real part of all roots are positive. Since $p(A)$ has real coefficients, its complex roots are in complex conjugates and p(A) has either one or three positive real roots. Since $f(0) = 0$ and $f'(0) > 0$, (2.16) has three positive real roots at some S if and only if $f'(A) < 0$ for some A. Looking at derivatives

of f

$$f'(A) = m_1 - \frac{2m_2m_3A}{(m_3 + A^2)^2}$$
$$f''(A) = 2m_2m_3\left(\frac{3A^2 - m_3}{(m_3 + A^2)^3}\right)$$

one knows that f has one inflection point at $A = \sqrt{m_3/3}$ and f' is decreasing for $A < \sqrt{m_3/3}$. Hence, multiple positive roots occurs if and only if $f'(\sqrt{m_3/3}) < 0$, which is when

$$m_2^2 > \frac{64}{27}m_1^2m_3 \approx 2.37\ m_1^2m_3 \tag{2.18}$$

Therefore, the system has multiple steady states for some S if and only if (2.18) is satisfied.

Next, we analyze stability of the steady states. The Jacobian matrix of the linearized system is

$$J = \begin{bmatrix} -m_1 & k_2 \\ \frac{2m_3k_4A_{ss}}{(m_3+A^2)^2} & -k_5 \end{bmatrix}$$

which has characteristic equation

$$\lambda^2 + (m_1 + k_5)\lambda + m_1k_5 - \frac{2k_2m_3k_4A_{ss}}{(m_3 + A_{ss}^2)^2} = 0$$

Hence,

$$\begin{aligned} \text{The system is stable} &\iff m_1k_5 - \frac{2k_2m_3k_4A_{ss}}{(m_3 + A_{ss}^2)^2} > 0 \\ &\iff m_1 > \frac{2(k_2k_4/k_5)m_3A_{ss}}{(m_3 + A_{ss}^2)^2} = m_1 - f'(A_{ss}) \\ &\iff f'(A_{ss}) > 0 \end{aligned}$$

Therefore, when there is one steady state, it is stable. When there are three steady states, the middle-valued steady state is unstable and the other two are stable.

The multiple-steady-state case may give rise to two behaviors: hysteresis and a switch [181]. Hysteresis occurs when there is one steady state at $S = 0$. If there are three steady states at $S = 0$, the system is a switch. Since $f(A) = 0$ if and only if

$$(m_1 A^2 - m_2 A + m_1 m_3)A = 0,$$

we have a switch when $m_2^2 < 4m_1^2 m_3$ and hysteresis otherwise. Therefore, the system behaves differently according the the value of $m_2^2/m_1^2 m_3$, as depicted in Figure (2.8). Signal-response curves when the system is a hysteresis and a switch are shown in Figure (2.9).

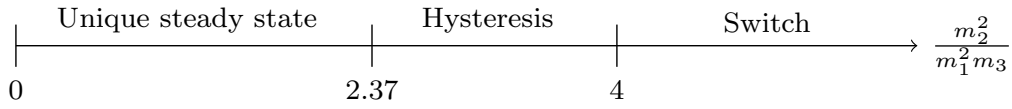

Figure 2.8: Steady-state regimes determined by system parameters.

Although a hysteresis may lead to very high local sensitivity, it can also lead to trigger waves when coupled with diffusion, as observed in [92], where activation in a small region eventually leads to high activity in the entire domain. In the "wave-pinning" polarization scheme, conditions on diffusion constants are needed to maintain polarization where low activity and high activity coexist in the steady state [92, 138]. In this case, a small input gradient could lead to strong polarization of the response, which does not agree well with the experimental observations [90, 130].

A more controllable scheme for gradient amplification is based on the one steady-state regime. The following analysis applies to the case with $n > 1$. Since $\bar{g} = \frac{S}{Y}\frac{dY}{dS} > 0$

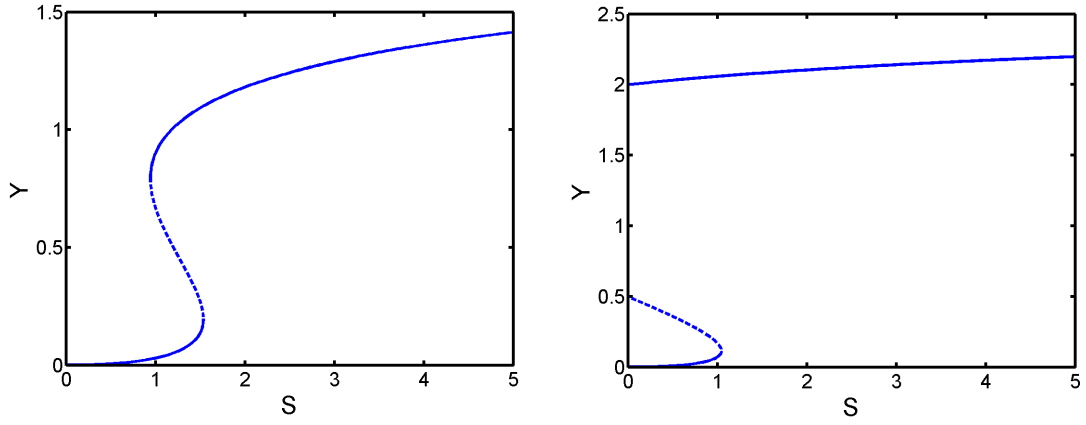

Figure 2.9: The model with Hill-type cooperativity ($n = 2$) and positive feedback leads to different steady-state behaviors: *(Left)* a hysteresis ($m_1 = m_3 = 1, m_2 = 1.8$), *(Right)* a switch ($m_1 = m_3 = 1, m_2 = 2.5$). Solid and dashed lines denote stable and unstable steady states respectively.

in this regime and $m_1 A - m_2(A^n/(m_3 + A^n)) = k_1 S$, one has $m_1 A - n m_2(A^n/(m_3 + A^n))(m_3/(m_3 + A^n)) > 0$. So

$$\begin{aligned}
\bar{g} - n &= n\left(\frac{m_3}{m_3 + A^n}\right)\left(\frac{m_1 A - m_2(A^n/(m_3 + A^n))}{m_1 A - n m_2(A^n/(m_3 + A^n))(m_3/(m_3 + A^n))}\right) - n \\
&= n\left[\left(\frac{m_1 A - m_2(A^n/(m_3 + A^n))}{m_1 A((m_3 + A^n)/m_3) - n m_2(A^n/(m_3 + A^n))}\right) - 1\right] \\
&= nA^n\left(\frac{(n-1)m_2/(m_3 + A^n) - m_1 A/m_3}{m_1 A((m_3 + A^n)/m_3) - n m_2(A^n/(m_3 + A^n))}\right) \\
&> 0
\end{aligned}$$

for small A. In fact, the normalized sensitivity can be much higher than n when the system approaches the multiple steady-state regime, i.e. when $m_2^2/m_1^2 m_3$ is slightly less than 2.37. Note that for $n = 1$, the first term of the numerator is zero. Figure 2.10 displays normalized sensitivity as a function of the input level when $n = 2$.

We have analyzed a model with Hill-type cooperativity coupled with a positive feedback and shown that the model may become an irreversible switch, a bistable system,

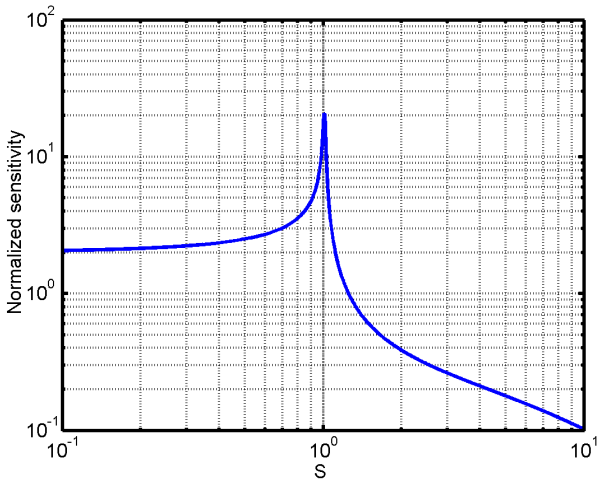

Figure 2.10: Normalized sensitivity under the unique steady-state regime of the system with Hill cooperativity and positive feedback ($n = 2, m_1 = m_3 = 1, m_2 = 1.5$)

or a spatial-gradient amplifier, depending on parameter choices. Ferrell and Xiong [56] proposed a similar model for biological switches where cooperativity is embedded in the positive feedback.

Implicit cooperativity and positive feedback

Consider another model for gradient amplification based on cooperativity and positive feedback. This model is interesting because the cooperativity does not stem from multiple regulation pathways originated by a common regulator. Rather, the cooperativity is introduced by regulation of distinct states of the substrate A by the input and the positive feedback. A similar scheme based on substrate delivery was proposed by Levchenko and Iglesias [125].

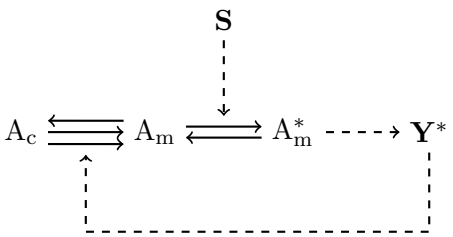

$$
\begin{aligned}
Y^* + A_c &\xrightarrow{k_{A_m}} Y^* + A_m \\
A_c &\underset{k_{A_c}}{\overset{k_{b,A_m}}{\rightleftharpoons}} A_m \\
S + A_m &\xrightarrow{k_{A_m^*}} S + A_m^* \\
A_m^* &\xrightarrow{k_{d,A_m}} A_m \\
A_m^* + Y &\xrightarrow{k_{Y^*}} A_m^* + Y^* \\
Y^* &\xrightarrow{k_Y} Y
\end{aligned}
$$

For simplicity, we assume that Y is abundant compared to Y^*. Notice that we explicitly include spontaneous activation (binding to membrane in this case) of A_c while it should be small and could be neglect in other models. In this model, this term is important as it prevents the system from being permanently trapped in the fully inactive state A_c. The spatial-invariance system is described by

$$
\begin{aligned}
\frac{dA_m}{dt} &= k_{b,A_m} A_c + k_{A_m} Y^* \cdot A_c + k_{d,A_m} A_m^* - k_{A_c} A_m - k_{A_m^*} S \cdot A_m \\
\frac{dA_m^*}{dt} &= k_{A_m^*} S \cdot A_m - k_{d,A_m} A_m^* \\
\frac{dY^*}{dt} &= k_{Y^*} A_m^* \cdot Y - k_Y Y^* \\
A_c + A_m + A_m^* &= A_0 = \text{const} \\
Y &\approx Y_0 = \text{const}
\end{aligned}
$$

At steady-state, we have

$$
m_1(1 + m_2 S){Y^*}^2 + (1 + m_4 + m_2 m_4 S - m_1 m_2 m_3 A_0 S)Y^* - m_2 m_3 m_4 A_0 S = 0
$$

where $m_1 = k_{A_m}/k_{A_c}$, $m_2 = k_{A_m^*}/k_{d,A_m}$, $m_3 = k_{Y^*} Y_0/k_Y$, and $m_4 = k_{b,A_m}/k_{A_c}$. Notice

that the quadratic equation has one positive real root and one negative real root. To determine stability of the positive steady state, we first transform the system with $A_m = A_0 - A_c - A_m^*$ so that the linearization of

$$\begin{aligned}
\frac{dA_c}{dt} &= k_{A_c}A_0 - (k_{b,A_m} + k_{A_c} + k_{A_m}Y^*)A_c - k_{A_c}A_m^* \\
\frac{dA_m^*}{dt} &= k_{A_m^*}A_0 S - k_{A_m^*}S \cdot A_c - \left(k_{d,A_m} + k_{A_m^*}S\right)A_m^* \\
\frac{dY^*}{dt} &= k_{Y^*}Y_0 A_m^* - k_Y Y^* \\
A_c + A_m + A_m^* &= A_0 = \text{const}
\end{aligned}$$

has a Jacobain matrix

$$J = \begin{bmatrix}
-(k_{b,A_m} + k_{A_c} + k_{A_m}Y_{ss}^*) & -k_{A_c} & 0 \\
-k_{A_m^*}S & -\left(k_{d,A_m} + k_{A_m^*}S\right) & 0 \\
0 & k_{Y_{ss}^*}Y_0 & -k_Y
\end{bmatrix}$$

The characteristic equation is

$$\begin{aligned}
(\lambda + k_Y)\big[\lambda^2 &+ (k_{b,A_m} + k_{A_c} + k_{A_m}Y_{ss}^* + k_{d,A_m} + k_{A_m^*}S)\lambda + k_{b,A_m}k_{d,A_m} \\
&+ k_{b,A_m}k_{A_m^*}S + k_{A_m}k_{d,A_m}Y_{ss}^* + k_{A_m}k_{A_m^*}S \cdot Y_{ss}^* + k_{A_c}k_{d,A_m}\big] = 0
\end{aligned}$$

The quadratic term in the bracket has positive coeffiecients for the positive steady state. Therefore, the positive steady state is stable.

The normalized sensitivity of the system is

$$\bar{g} = \frac{m_2m_3m_4A_0 + (m_1m_2m_3A_0 - m_2m_4)Y^* - m_1m_2Y^{*2}}{(1/S + m_4/S + m_2m_4 - m_1m_2m_3A_0)Y^* + 2m_1(1/S + m_2)Y^{*2}}$$

To demonstrate the gradient-amplifying property of this system, we look at the case

$k_{b,A_m} << 1$, which should be natural that the spontaneous activity of A is small and becomes higher when a signal is present. Consider the simplified system with $k_{b,A_m} = 0$. Then the steady-state concentration satisfies

$$m_1(1 + m_2S){Y^*_{ss}}^2 + (1 - m_1m_2m_3A_0S)Y^*_{ss} = 0$$

which has solutions $Y^*_{ss} = 0$ or $Y^*_{ss} = \dfrac{m_2m_3A_0S - 1/m_1}{1 + m_2S}$. Since all decay terms in the system are first-order, the positive-valued region of the phase space is invariant. The nonzero solution becomes negative for $m_1m_2m_3A_0S < 1$, which implies that $Y^*(t)$ converges to zero for small S. When $S > 1/m_1m_2m_3A_0$, $Y^*(t)$ converges to the positive stationary point except for a small starting region near the origin in (A_m, A^*_m, Y^*) coordinates. Therefore, large signal amplification can be expected near the critical stimulus concentration, even when $k_{b,A_m} > 0$ but is small enough. Normalized sensitivity of the response under different values of $k_{b,A_m} > 0$ is shown in Figure 2.11. We can see that in an appropriate range of S the system possesses sensitivity equivalent to a Hill term with $n > 10$.

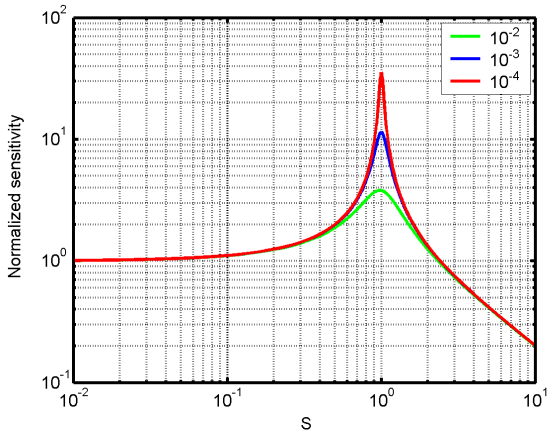

Figure 2.11: Normalized sensitivity of Y^* at different values of $k_{b,A_m} > 0$ where other parameters are fixed at one.

Summary of gradient-amplifying modules

Table 2.4 summarizes existing and newly proposed gradient amplification modules. For each module, signaling diagrams, closed forms for normalized sensitivity (if not possible, steady-state relations will be given), and plots of the normalized sensitivity are given. More details for existing modules can be found in the references.

Table 2.4: Gradient-amplifying modules in biological signaling systems

Cooperative systems		
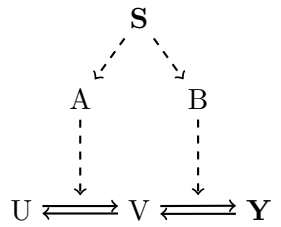 $\bar{g} = 2 - \frac{2m_1S^2 + m_2S}{m_1S^2 + m_2S + 1}$ < 2	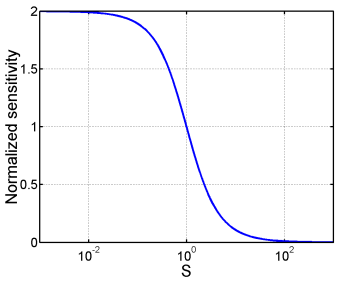 $m_1 = 1,\ m_2 = 1$	Multi-step activation, such as protein phosphorylation after membrane recruitment by a parallel pathway, and cooperative binding, e.g. oxygen binding to hemoglobin, display this type of cooperativity.
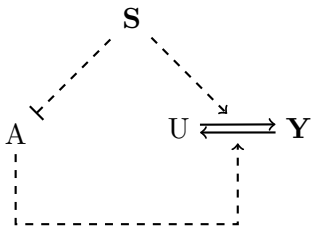 $\bar{g} = \frac{m_1S + 2m_2S^2}{(1 + m_1S + m_2S^2)(m_1S + m_2S^2)}$ < 2	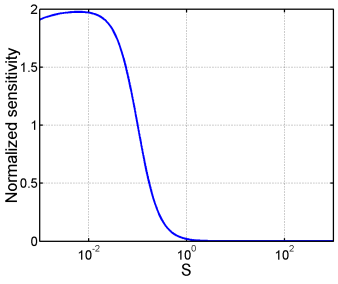 $m_1 = 0.01,\ m_2 = 100$	Used in an eukaryotic directional-sensing model by Ma et al. [130] as "complementary regulation".

Table 2.4: (continued)

Hill cooperativity with a positive feedback		
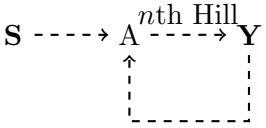 $\bar{g} = \frac{nm_3}{m_3 + A^n} \frac{m_1 A - \frac{m_2 A^n}{m_3 + A^n}}{m_1 A - \frac{nm_2 m_3 A^n}{(m_3 + A^n)^2}}$ $m_4 S = m_1 A - m_2 \left(\frac{A^n}{m_3 + A^n} \right)$	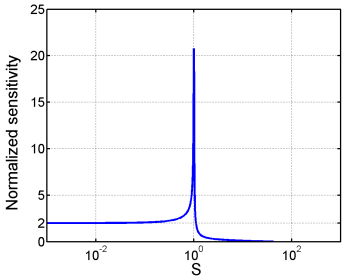 $n = 2,\ m_1 = 1,$ $m_2 = 1.5,\ m_3 = 1$	A combination of a Hill term and a positive feedback. With $n = 1$, or no cooperativity, $\bar{g} < 1$. For $n \geq 2$, the system can display either gradient amplification [123, 137] or a switch-like behavior [56], depending on parameter regimes.
Cooperative systems with a positive feedback		
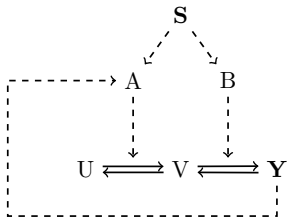 $0 = \alpha V^2 + \beta V + \gamma$ $Y = m_1 V \cdot S$ $\alpha = m_4 m_1 S^2 + (m_3 + 1) m_4 S$ $\beta = m_1 S^2 + (1 + m_3 - m_4) S + m_2$ $\gamma = -S$	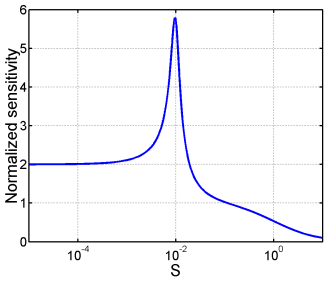 $m_1 = 1,\ m_2 = 1,$ $m_3 = 0.1,\ m_4 = 100$	Newly proposed module for gradient amplification. The sensitivity to directional gradient in the eukaryotic chemosensing model by Meier-Schellersheim et al. [134] is most likely caused by this mechnism.
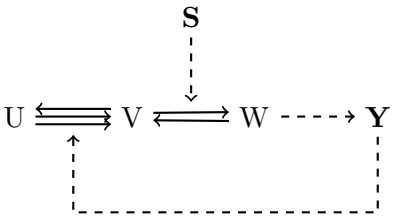 $0 = \alpha Y^2 + \beta Y + \gamma$ $\alpha = m_1 m_2 S + m_1$ $\beta = m_2 (m_4 - m_1 m_3) S + 1 + m_4$ $\gamma = -m_2 m_3 m_4 S$	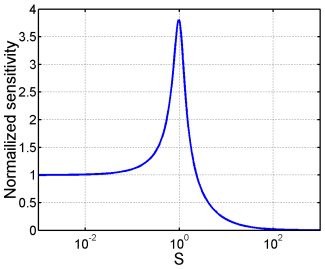 $m_1 = 1,\ m_2 = 1,$ $m_3 = 1,\ m_4 = 0.01$	Newly proposed module for gradient amplification. This system is special in that the cooperativity is a part of the positive feedback.

Table 2.4: (continued)

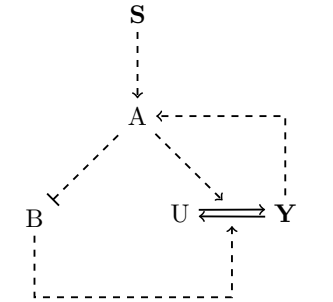 $S = \frac{1}{m_4}\left(\frac{m_3 A}{1-A} - \frac{m_2 A^2}{1+m_2 A^2}\right)$ $Y = \frac{m_1 A + m_2 A^2}{1 + m_1 A + m_2 A^2}$	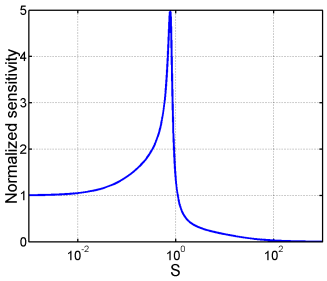 $m_1 = 0.1,\ m_2 = 5,$ $m_3 = 1,\ m_4 = 0.1$	Newly proposed module for gradient amplification. The spatial sensitivity displayed by the directional sensing model by Skupsky et al. [168] is potentially derived from this mechanism.
Zero-order ultrasensitivity (Goldbeter and Koshland [71])		
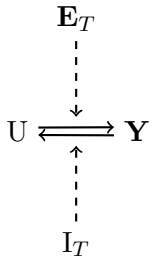 *Exception to the standard diagram.* *Operates on full enzyme kinetics.* *Requires* (i) $U + V >> [EU] + [IY]$ (ii) $E << [EU]$ *or* $I << [IY]$ $m_1 \frac{E_T}{I_T} = \frac{y(m_2 + 1 - y)}{(m_3 + y)(1 - y)}$ where $y = \frac{Y}{Y + U + [EU] + [IY]}$ *is the normalized response.*	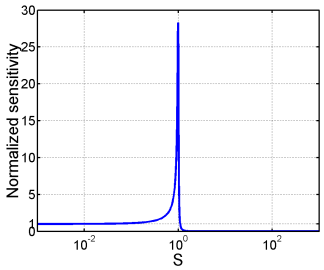 $m_1 = 1,\ m_2 = m_3 = 0.01$	Conservation of the activator E and the inhibitor I is required. Also, either of them needs to work in saturation region (small m_2, m_3). A necessary condition is sensitive to upstream systems. See [124, 194] for related schemes.

2.4 Discussion

We have proposed and summarized a collection of basic reaction-based modules for steady-state adaptation and high sensitivity. They are not only applicable to chemotactic pathways but also to other biochemical systems displaying these features.

The simple modules may be combined into more complicated models while their properties are preserved as long as the effect of intermodular complexes is negligible. In particular, steady-state analysis of any interconnecting modules may be decoupled if the amount of the effector in the upstream module arrested in the intermodular complexes is small compared to the total amount of the effector. In addition, their dynamics can also be decoupled if the complexes equilibrates rapidly.

A realistic activation-inhibition model called SES system has been analyzed and shown to possess steady-state adaptation similarly to the simple LEGI system [125] when certain conditions are satisfied. An analysis of the dynamics of the SES system reveals that the system may transiently have high or low activity depending on the activation time of the activator and the inhibitor. This activation time solely depends on the spontaneous rate constant of the enzymes. More importantly, we showed that the response adaptation time is proportional to the inverse of the stimulation level. A 2-state nonlinear description for the system which accurately captures the essential adaptation dynamics has been obtained.

We showed that a positive feedback in linear (or sublinear) systems does not introduce sensitivity. However, if the positive feedback is coupled with cooperativity, the system can develop high sensitivity and may even possess multiple steady states. We gave several examples of such systems and provide detailed analyses for two particular systems. First, a Hill-type cooperative system with a positive feedback has been used to describe an irreversible cell fate of *Xenopus* oocyte [56] and gradient detection in *S. cerevisiae* [137]. We show that this system can behave differently either as an irreversible

switch, a reversible switch (hysteresis), or a single steady-state highly-sensitive system, depending on one system parameter. The other system involves cooperativity which is implicit. Unlike other cooperative systems whose sensitivity directly reflects total cooperativity when their inputs are small, the sensitivity of this system becomes unity at a low input level. This model is fundamentally similar to the substate-delivery model [125] and diffusion-translocation model [154]. Our analysis leads to an understanding of the high sensitivity in this system.

Our proposed high-sensitivity models provide robust and biochemically-realistic alternatives to traditional highly-sensitive systems as building blocks for complicated spatially-distributed signal transduction models. In particular, one of these modules has been utilized in our chemotactic-signaling model in *Dictyostelium discoideum*.

Chapter 3

Directional sensing in dictyostelium amoebe

3.1 Cellular adaptation of Ras activity

In this section, the local SES system analyzed in sections 2.2.3 and 2.2.4 is coupled with enzyme diffusion to describe evolution of Ras-activation response on a circular disk. The model should adapt to spatially-uniform signals and reflects a spatial gradient amplification of a directional stimulation.

A local-excitation global-inhibition (LEGI) principle has been proposed to model adapting systems which exhibit biased responses under directional stimulation [125, 130]. This scheme is based on fast-activation of a slowly-diffusing activator and slow-activation of a fast-diffusing inhibitor [125, 154]. The response gradient is developed by an imbalance between activator and inhibitor gradients.

In fact, spatial gradients of the enzymes do not depend solely on diffusion. When a diffusing enzyme is activated on the cell membrane and spontaneously deactivates in the cytosol, the gradient of its activity depends on *characteristic degradation length*

$\alpha = \sqrt{D/k_d}$ where k_d and D are spontaneous deactivation rate and diffusion constant respectively. Therefore, two enzymes may have very different gradients while they diffuse equally rapidly.

For simplified activation of an enzyme, which may be either the activator or the inhibitor, on a circular disk described by

$$\begin{aligned} \frac{\partial E^*}{\partial t} &= D_E \nabla^2 E^* - k_E E^* && \text{in } \Omega \\ D_E \frac{\partial E^*}{\partial n} &= k_{E^*} S \cdot (E_0 - E^*) && \text{on } \partial\Omega \end{aligned}$$

with a conservation condition $E + E^* = E_0$ in Ω, one can use radial symmetry to analytically solve for the steady-state concentration of the activated enzyme [26]

$$E^*(r) = \frac{c}{r}\left(e^{r/\alpha} - e^{-r/\alpha}\right)$$

where $\alpha = \sqrt{D_E/k_E}$ and $c \propto S$, assuming $\left.\frac{\partial E^*}{\partial r}\right|_{r=0} = 0$. Figure 3.1 displays radial profiles of enzyme activity under different degradation rates.

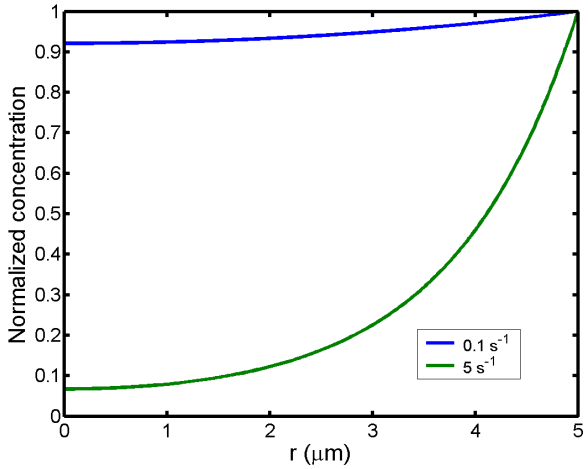

Figure 3.1: Steady-state intracellular concentration at different degradation rates of an enzyme activated at the boundary of a circular domain. $R = 5\ \mu m,\ D = 5\ \mu m^2/s$.

Because the concentrations of both enzymes at the membrane are proportional to the stimulus, the adaptation property still holds on the circular disk. On a more general 2-dimensional domain, we expect a nonuniform adaptation response. In particular, higher activity should be observed in regions with a high ratio of boundary length to surface area as the activator has less characteristic degradation length and cannot be distributed as well as the inhibitor. The regions with a high length-area ratio locally magnify this effect causing local above-average activity. A complementary effect should be observed in regions with a low length-area ratio. This particular effect of cell shapes on chemotactic responses has been observed in neurons [142]. We will study this effect numerically in section 3.2.2.

We next develop a finite element algorithm to numerically test the adaptation property of the SES system with restricted diffusion where only activated inhibitor may diffuse within the disk.

3.1.1 Numerical algorithm

A finite-element based algorithm is developed to solve a system of reaction-diffusion equations which includes interactions between boundary and domain variables.

Reaction-Diffusion Equations

Consider a system of reaction-diffusion equations

$$\left.\begin{aligned} \frac{\partial \boldsymbol{u}}{\partial t} &= D\nabla^2\boldsymbol{u} - a_1(\boldsymbol{u},\boldsymbol{u}) - b_1(\boldsymbol{u}) && \text{in } \Omega \times (0,T] \\ \frac{\partial \boldsymbol{v}}{\partial t} &= -\pi_v\left(a_2(\boldsymbol{w},\boldsymbol{w}) + b_2(\boldsymbol{w}) + b_3(\boldsymbol{w})f\right) && \text{on } \Gamma \times (0,T] \end{aligned}\right\} \tag{3.1}$$

with boundary and initial conditions

$$\left.\begin{aligned} D_N \frac{\partial \boldsymbol{u}}{\partial n} &= -\pi_u \left(a_2(\boldsymbol{w},\boldsymbol{w}) + b_2(\boldsymbol{w}) + b_3(\boldsymbol{w}) f\right) && \text{on } \Gamma \times (0,T] \\ \boldsymbol{u} &= \boldsymbol{u_0} && \text{on } \Omega \times \{t=0\} \\ \boldsymbol{v} &= \boldsymbol{v_0} && \text{on } \Gamma \times \{t=0\} \end{aligned}\right\} \tag{3.2}$$

where

$$\boldsymbol{u}(t) = (u_1(t), \ldots, u_{\kappa_1}(t)) \in H^{1,\kappa_1}(\Omega)$$

$$\boldsymbol{v}(t) = (v_1(t), \ldots, v_{\kappa_2}(t)) \in H^{1,\kappa_2}(\Gamma)$$

$$\boldsymbol{w} = (\boldsymbol{u}|_\Gamma, \boldsymbol{v}) \in H^{1,\kappa_1+\kappa_2}(\Gamma)$$

and $f(t) \in L^2(\Gamma)$ while

$$H^{1,\kappa_1}(\Omega) := \left\{ \boldsymbol{\phi} : \Omega \to \mathbb{R}^{\kappa_1} \,\middle|\, \int_\Omega |\boldsymbol{\phi}|^2 \, dx < \infty \text{ and } \int_\Omega |D\boldsymbol{\phi}|^2 \, dx < \infty \right\}$$

Matrices D, D_N are diagonal and positive definite with diagonal elements d_k, $k = 1, \ldots, \kappa_1$. Also, $a_1 : \mathbb{R}^{\kappa_1} \times \mathbb{R}^{\kappa_1} \to \mathbb{R}^{\kappa_1}$ and $a_2 : \mathbb{R}^{\kappa_1+\kappa_2} \times \mathbb{R}^{\kappa_1+\kappa_2} \to \mathbb{R}^{\kappa_1+\kappa_2}$ are bilinear mappings, $b_1 : \mathbb{R}^{\kappa_1} \to \mathbb{R}^{\kappa_1}$ and $b_2, b_3 : \mathbb{R}^{\kappa_1+\kappa_2} \to \mathbb{R}^{\kappa_1+\kappa_2}$ are linear mappings, and $\pi_u : \mathbb{R}^{\kappa_1+\kappa_2} \to \mathbb{R}^{\kappa_1}$ and $\pi_v : \mathbb{R}^{\kappa_1+\kappa_2} \to \mathbb{R}^{\kappa_2}$ are projections. In particular, a_i are symmetric, bounded, and coersive. We write

$$a_1(\boldsymbol{x},\boldsymbol{y}) := \sum_{k=1}^{\kappa_1} \left(\sum_{i,j=1}^{\kappa_1} a_1^{k,ij} x_i y_j \right) \boldsymbol{e_k} := \sum_{k=1}^{\kappa_1} \left(\boldsymbol{x} \cdot A_1^k \boldsymbol{y} \right) \boldsymbol{e_k}$$

$$a_2(\boldsymbol{\xi},\boldsymbol{\upsilon}) := \sum_{k=1}^{\kappa_1+\kappa_2} \left(\sum_{i,j=1}^{\kappa_1+\kappa_2} a_2^{k,ij} \xi_i \upsilon_j \right) \boldsymbol{e_k} := \sum_{k=1}^{\kappa_1+\kappa_2} \left(\boldsymbol{\xi} \cdot A_2^k \boldsymbol{\upsilon} \right) \boldsymbol{e_k}$$

$$b_1(\boldsymbol{x}) := \sum_{k=1}^{\kappa_1} \left(\sum_{i=1}^{\kappa_1} b_1^{k,i} x_i \right) \boldsymbol{e_k} := B_1 \boldsymbol{x}$$

$$b_2(\boldsymbol{\xi}) := \sum_{k=1}^{\kappa_1+\kappa_2} \left(\sum_{i=1}^{\kappa_1+\kappa_2} b_2^{k,i} \xi_i \right) \boldsymbol{e_k} := B_2 \boldsymbol{\xi}$$

$$b_3(\boldsymbol{\xi}) := \sum_{k=1}^{\kappa_1+\kappa_2} \left(\sum_{i=1}^{\kappa_1+\kappa_2} b_3^{k,i} \xi_i \right) \boldsymbol{e_k} := B_3 \boldsymbol{\xi}$$

for $\boldsymbol{x}, \boldsymbol{y} \in \mathbb{R}^{\kappa_1}$ and $\boldsymbol{\xi}, \boldsymbol{\upsilon} \in \mathbb{R}^{\kappa_1+\kappa_2}$.

Space discretization

For $k_1 = 1, \ldots, \kappa_1$ and $k_2 = 1, \ldots, \kappa_2$, we have $u_{k_1}(t) \in H^1(\Omega)$ and $v_{k_2}(t) \in H^1(\Gamma)$ respectively. Equation (3.1) and (3.2) has the weak form

$$\begin{aligned}
\left(\frac{\partial u_{k_1}}{\partial t}, \varphi \right)_\Omega &= -d_{k_1} \left\langle \nabla u_{k_1}, \nabla \varphi \right\rangle_\Omega && \forall \varphi \in H^1(\Omega),\ \forall t \in (0,T] \\
&\quad - \frac{d_{k_1}}{d_{N,k_1}} \left(\boldsymbol{w} \cdot A_2^{k_1} \boldsymbol{w} + \boldsymbol{e_{k_1}} \cdot B_2 \boldsymbol{w} + \boldsymbol{e_{k_1}} \cdot f B_3 \boldsymbol{w}, \varphi \right)_\Gamma \\
&\quad - \left(\boldsymbol{u} \cdot A_1^{k_1} \boldsymbol{u}, \varphi \right)_\Omega - \left(\boldsymbol{e_{k_1}} \cdot B_1 \boldsymbol{u}, \varphi \right)_\Omega \\
(u_{k_1}, \varphi)_\Omega &= (u_{k_1,0}, \varphi)_\Omega && \forall \varphi \in H^1(\Omega),\ t = 0 \\
\left(\frac{\partial v_{k_2}}{\partial t}, \chi \right)_\Gamma &= - \left(\boldsymbol{w} \cdot A_2^{\kappa_1+k_2} \boldsymbol{w} + \boldsymbol{e_{\kappa_1+k_2}} \cdot B_2 \boldsymbol{w} + \boldsymbol{e_{\kappa_1+k_2}} \cdot f B_3 \boldsymbol{w}, \chi \right)_\Gamma && \forall \chi \in H^1(\Gamma),\ \forall t \in (0,T] \\
(v_{k_2}, \chi)_\Gamma &= (v_{k_2,0}, \chi)_\Gamma && \forall \chi \in H^1(\Gamma),\ t = 0
\end{aligned}$$

Take $\mathcal{M} = \mathcal{N} \subset H^1(\Omega)$ with basis $\{\phi_1, \ldots, \phi_{N_1}\}$ as test functions for $u_{k_1}(t)$ and $\mathcal{M}_\Gamma = \mathcal{N}_\Gamma = \mathcal{M}|_\Gamma \subset H^1(\Gamma)$ with basis $\{\phi_{p_1}|_\Gamma, \ldots, \phi_{p_{N_2}}|_\Gamma\}$, where $||\phi_{p_n}||_{H^1(\Gamma)} > 0$ for $n = 1, \ldots, N_2$, $N_2 < N_1$, as test functions for $v_{k_2}(t)$. Trial functions have the forms $u_{h,k_1}(t) = \sum_{n=1}^{N_1} \alpha_n^{k_1}(t) \phi_n \in \mathcal{M}$, $v_{h,k_2}(t) = \sum_{n=1}^{N_2} \beta_n^{k_2}(t) \phi_{p_n}|_\Gamma \in \mathcal{M}_\Gamma$ and $\boldsymbol{w}_h(t) =$

$(\boldsymbol{u}_h(t), \boldsymbol{v}_h(t)) \in \mathcal{M}_\Gamma^{\kappa_1+\kappa_2}$. Write $w_{h,k}(t) = \sum_{n=1}^{N_2} \gamma_n^k(t)\phi_{p_n}|_\Gamma$ so that

$$\gamma_n^k(t) = \begin{cases} \alpha_{p_n}^k(t) & ,1 \le k \le \kappa_1 \\ \beta_n^{k-\kappa_1}(t) & ,\kappa_1 < k \le \kappa_1 + \kappa_2 \end{cases}$$

The discrete weak formulation is to find $\boldsymbol{u}_h(t), \boldsymbol{v}_h(t)$ such that

$$\begin{aligned} \sum_{n=1}^{N_1} \dot{\alpha}_n^{k_1} (\phi_n, \phi_q)_\Omega = &-d_{k_1} \sum_{n=1}^{N_1} \alpha_n^{k_1} \langle \nabla\phi_n, \nabla\phi_q \rangle_\Omega \qquad \forall t \in (0,T] \\ &- \frac{d_{k_1}}{d_{N,k_1}} \sum_{i,j=1}^{\kappa_1+\kappa_2} \sum_{m,n=1}^{N_2} a_2^{k_1,ij} \gamma_m^i \gamma_n^j (\phi_{p_m}\phi_{p_n}, \phi_q)_\Gamma \\ &- \frac{d_{k_1}}{d_{N,k_1}} \sum_{i=1}^{\kappa_1+\kappa_2} \sum_{m=1}^{N_2} b_2^{k_1,i} \gamma_m^i (\phi_{p_m}, \phi_q)_\Gamma \\ &- \frac{d_{k_1}}{d_{N,k_1}} \sum_{i=1}^{\kappa_1+\kappa_2} \sum_{m=1}^{N_2} b_3^{k_1,i} \gamma_m^i (f\phi_{p_m}, \phi_q)_\Gamma \\ &- \sum_{i,j=1}^{\kappa_1} \sum_{m,n=1}^{N_1} a_1^{k_1,ij} \alpha_m^i \alpha_n^j (\phi_m\phi_n, \phi_q)_\Omega \\ &- \sum_{i=1}^{\kappa_1} \sum_{m=1}^{N_1} b_1^{k_1,i} \alpha_m^i (\phi_m, \phi_q)_\Omega \end{aligned}$$

$$\alpha_q^{k_1}(0) = \alpha_{q,0}^{k_1}$$

for $q = 1, \ldots, N_1,\ k_1 = 1, \ldots, \kappa_1$ where $\sum_{n=1}^{N_1} \alpha_{n,0}^{k_1}\phi_n = \pi_{\mathcal{M}}(u_{k_1,0})$ and

$$\begin{aligned} \sum_{n=1}^{N_2} \dot{\beta}_n^{k_2} (\phi_{p_n}, \phi_{p_r})_\Gamma = &- \sum_{i,j=1}^{\kappa_1+\kappa_2} \sum_{m,n=1}^{N_2} a_2^{\kappa_1+k_2,ij} \gamma_m^i \gamma_n^j (\phi_{p_m}\phi_{p_n}, \phi_{p_r})_\Gamma \qquad \forall t \in (0,T] \\ &- \sum_{i=1}^{\kappa_1+\kappa_2} \sum_{m=1}^{N_2} b_2^{\kappa_1+k_2,i} \gamma_m^i (\phi_{p_m}, \phi_{p_r})_\Gamma \end{aligned}$$

$$- \sum_{i=1}^{\kappa_1+\kappa_2} \sum_{m=1}^{N_2} b_3^{\kappa_1+k_2,i} \gamma_m^i \left(f\phi_{p_m}, \phi_{p_r}\right)_\Gamma$$

$$\beta_r^{k_2}(0) = \beta_{r,0}^{k_2}$$

for $r = 1, \ldots, N_2,\ k_2 = 1, \ldots, \kappa_2$ where $\sum_{n=1}^{N_2} \beta_{n,0}^{k_2} \phi_{p_n} = \pi_{\mathcal{M}|_\Gamma}(v_{k_2,0})$. Clearly, the discrete weak formulation is a system of ODEs.

To represent the ODEs in the matrix form, write the degrees of freedom as

$$\boldsymbol{\zeta}(t)^T = \left(\boldsymbol{\alpha^1}(t)^T, \ldots, \boldsymbol{\alpha^{\kappa_1}}(t)^T, \boldsymbol{\beta^1}(t)^T, \ldots, \boldsymbol{\beta^{\kappa_2}}(t)^T\right)$$

where $\boldsymbol{\alpha^i}(t)^T = \left(\alpha_1^i(t), \ldots, \alpha_{N_1}^i(t)\right)$ and $\boldsymbol{\beta^i}(t)^T = \left(\beta_1^i(t), \ldots, \beta_{N_2}^i(t)\right)$. Let

$$\Phi_1^T = (\phi_1, \ldots, \phi_{N_1})$$
$$\Phi_2^T = (\phi_{p_1}, \ldots, \phi_{p_{N_2}})$$

and define

$$M_\Omega = \int_\Omega \Phi_1 \otimes \Phi_1^T \ dx$$
$$M_{g,\Omega} = \int_\Omega g\Phi_1 \otimes \Phi_1^T \ dx$$
$$M_\Gamma^{i,j} = \int_\Gamma \Phi_i \otimes \Phi_j^T \ dx$$
$$M_{g,\Gamma}^{i,j} = \int_\Gamma g\Phi_i \otimes \Phi_j^T \ dx$$

for $i = 1, 2,\ j = 1, 2$ and where $\otimes$ denotes the Kronecker product and g is a scalar

function. The Kronecker product between matrices $A_{m\times n}, B_{p\times q}$ is defined as

$$A \otimes B = \begin{bmatrix} a_{11}B & \cdots & a_{1n}B \\ \vdots & \ddots & \vdots \\ a_{m1}B & \cdots & a_{mn}B \end{bmatrix}_{mp\times nq}$$

For example,

$$M_\Gamma^{1,2} = \begin{bmatrix} (\phi_1, \phi_{p_1})_\Gamma & \cdots & (\phi_1, \phi_{p_{N_2}})_\Gamma \\ \vdots & \ddots & \vdots \\ (\phi_{N_1}, \phi_{p_1})_\Gamma & \cdots & (\phi_{N_1}, \phi_{p_{N_2}})_\Gamma \end{bmatrix}_{N_1\times N_2}$$

Also, define

$$C = \begin{bmatrix} \langle \nabla\phi_1, \nabla\phi_1 \rangle_\Omega & \cdots & \langle \nabla\phi_1, \nabla\phi_{N_1} \rangle_\Omega \\ \vdots & \ddots & \vdots \\ \langle \nabla\phi_{N_1}, \nabla\phi_1 \rangle_\Omega & \cdots & \langle \nabla\phi_{N_1}, \nabla\phi_{N_1} \rangle_\Omega \end{bmatrix}_{N_1\times N_1}$$

Finally, we may partition a matrix $A_{(\kappa_1+\kappa_2)\times(\kappa_1+\kappa_2)}$ into blocks

$$A = \begin{bmatrix} A^{1,1} & A^{1,2} \\ A^{2,1} & A^{2,2} \end{bmatrix}$$

with submatrices $A^{1,1}_{\kappa_1\times\kappa_1}, A^{1,2}_{\kappa_1\times\kappa_2}, A^{2,1}_{\kappa_2\times\kappa_1}$, and $A^{2,2}_{\kappa_2\times\kappa_2}$. Then we can put the discrete weak formulation into the matrix form

$$\begin{bmatrix} I_{\kappa_1} \otimes M_\Omega & 0 \\ 0 & I_{\kappa_2} \otimes M_\Gamma^{2,2} \end{bmatrix} \dot{\boldsymbol{\zeta}}(t) + \begin{bmatrix} D \otimes C & 0 \\ 0 & 0 \end{bmatrix} \boldsymbol{\zeta}(t) = \Lambda(f(t))\boldsymbol{\zeta}(t) + \mathcal{S}(\boldsymbol{\zeta}(t), \boldsymbol{\zeta}(t)) \qquad (3.3)$$

for $t \in (0, T]$ with an initial condition

$$\boldsymbol{\zeta}(0) = \boldsymbol{\zeta_0}$$

where RHS involves a linear reaction term

$$\Lambda(f(t)) = \begin{bmatrix} \Lambda_{1,1} & \Lambda_{1,2} \\ \Lambda_{2,1} & \Lambda_{2,2} \end{bmatrix}$$

with

$$\Lambda_{1,1} = -B_1 \otimes M_\Omega - DD_N^{-1} B_2^{1,1} \otimes M_\Gamma^{1,1} - DD_N^{-1} B_3^{1,1} \otimes M_{f(t),\Gamma}^{1,1}$$

$$\Lambda_{1,2} = -DD_N^{-1} B_2^{1,2} \otimes M_\Gamma^{1,2} - DD_N^{-1} B_3^{1,2} \otimes M_{f(t),\Gamma}^{1,2}$$

$$\Lambda_{2,1} = -B_2^{2,1} \otimes M_\Gamma^{2,1} - B_3^{2,1} \otimes M_{f(t),\Gamma}^{2,1}$$

$$\Lambda_{2,2} = -B_2^{2,2} \otimes M_\Gamma^{2,2} - B_3^{2,2} \otimes M_{f(t),\Gamma}^{2,2}$$

and a nonlinear reaction term

$$\mathcal{S}(\boldsymbol{x}, \boldsymbol{y}) = \sum_{l=1}^{\kappa_1 N_1 + \kappa_2 N_2} \left(\boldsymbol{x} \cdot S^l \boldsymbol{y} \right) \boldsymbol{e_l}$$

where

$$S^l = \begin{cases} \begin{bmatrix} -A_1^{k_1} \otimes M_{\phi_n,\Omega} - \frac{d_{k_1}}{d_{N,k_1}} A_2^{k_1,1,1} \otimes M_{\phi_n,\Gamma}^{1,1} & -\frac{d_{k_1}}{d_{N,k_1}} A_2^{k_1,1,2} \otimes M_{\phi_n,\Gamma}^{1,2} \\ -\frac{d_{k_1}}{d_{N,k_1}} A_2^{k_1,2,1} \otimes M_{\phi_n,\Gamma}^{2,1} & -\frac{d_{k_1}}{d_{N,k_1}} A_2^{k_1,2,2} \otimes M_{\phi_n,\Gamma}^{2,2} \end{bmatrix}, & 1 \le l \le \kappa_1 N_1 \\ \begin{bmatrix} -A_2^{\kappa_1+k_2,1,1} \otimes M_{\phi_{p_m},\Gamma}^{1,1} & -A_2^{\kappa_1+k_2,1,2} \otimes M_{\phi_{p_m},\Gamma}^{1,2} \\ -A_2^{\kappa_1+k_2,2,1} \otimes M_{\phi_{p_m},\Gamma}^{2,1} & -A_2^{\kappa_1+k_2,2,2} \otimes M_{\phi_{p_m},\Gamma}^{2,2} \end{bmatrix}, & \kappa_1 N_1 < l \le \kappa_1 N_1 + \kappa_2 N_2 \end{cases}$$

with $k_1 = \left\lceil \frac{l}{N_1} \right\rceil$, $n = l - N_1 \left\lfloor \frac{l}{N_1} \right\rfloor$, $k_2 = \left\lceil \frac{l-\kappa_1 N_1}{N_2} \right\rceil$, $m = l - \kappa_1 N_1 - N_2 \left\lfloor \frac{l-\kappa_1 N_1}{N_2} \right\rfloor$, i.e.

$$\zeta_l = \begin{cases} \alpha_n^{k_1}, & 1 \le l \le \kappa_1 N_1 \\ \beta_m^{k_2}, & \kappa_1 N_1 < l \le \kappa_1 N_1 + \kappa_2 N_2 \end{cases}$$

Numerical Solutions of the Nonlinear ODEs

Various time-discretization methods can be used to solve (3.3) numerically, assuming the problem is well-posed and a stable full discretization converges. Because of the stiffness introduced by discretization of the Lagrange operator, there is a severe limitation of the time step. To use a reasonable step size, an implicit method is needed. However, this leads to a large system of quadratic equations at each time step, which can be expensive to solve. A simple way linearize the numerical method is to use lagged reaction terms. For example, the Crank-Nicholson method with lagged reaction terms and a constant step size Δt is

$$\begin{bmatrix} I_{\kappa_1} \otimes M_\Omega & 0 \\ 0 & I_{\kappa_2} \otimes M_\Gamma^{2,2} \end{bmatrix} \left(\frac{\boldsymbol{\zeta^{k+1}} - \boldsymbol{\zeta^k}}{\Delta t} \right) + \begin{bmatrix} D \otimes C & 0 \\ 0 & 0 \end{bmatrix} \left(\frac{\boldsymbol{\zeta^{k+1}} + \boldsymbol{\zeta^k}}{2} \right) = \Lambda^k \boldsymbol{\zeta^k} + \mathcal{S}(\boldsymbol{\zeta^k}, \boldsymbol{\zeta^k})$$

$$\boldsymbol{\zeta^0} = \boldsymbol{\zeta_0}$$

for $k = 0, \ldots, N-1$ where $\boldsymbol{\zeta}^k = \boldsymbol{\zeta}(t_k)$, $t_k = k\Delta t$, and $t_N = T$. Because of the lagged terms, this method of time discretization is only first-order accurate. Fortunately, the special structure of the bilinear term $\mathcal{S}(\boldsymbol{\zeta}, \boldsymbol{\zeta})$ allows a linearization which is second-order accurate in time

$$\begin{bmatrix} I_{\kappa_1} \otimes M_\Omega & 0 \\ 0 & I_{\kappa_2} \otimes M_\Gamma^{2,2} \end{bmatrix} \left(\frac{\boldsymbol{\zeta^{k+1}} - \boldsymbol{\zeta^k}}{\Delta t} \right) + \begin{bmatrix} D \otimes C & 0 \\ 0 & 0 \end{bmatrix} \left(\frac{\boldsymbol{\zeta^{k+1}} + \boldsymbol{\zeta^k}}{2} \right) = \left(\frac{\Lambda^{k+1} \boldsymbol{\zeta^{k+1}} + \Lambda^k \boldsymbol{\zeta^k}}{2} \right) + \mathcal{S}(\boldsymbol{\zeta^{k+1}}, \boldsymbol{\zeta^k})$$

$$\boldsymbol{\zeta^0} = \boldsymbol{\zeta_0}$$

To show the second-order accuracy, note that (3.3) can be written as

$$\boldsymbol{u_t} = A(t)\boldsymbol{u} + \mathcal{B}(\boldsymbol{u}, \boldsymbol{u})$$

where $u \in \mathbb{R}^n$ and $\mathcal{B}(\boldsymbol{u}, \boldsymbol{v}) = \sum_{i=1}^{n} (\boldsymbol{u} \cdot B^i \boldsymbol{v}) \boldsymbol{e_i}$ with symmetric B^i. The scheme is then

$$\left(\frac{\boldsymbol{u^{k+1}} - \boldsymbol{u^k}}{\Delta t} \right) = \left(\frac{A^{k+1}\boldsymbol{u^{k+1}} + A^k \boldsymbol{u^k}}{2} \right) + \mathcal{B}(\boldsymbol{u^{k+1}}, \boldsymbol{u^k})$$

for $k = 1, \ldots, N-1$ and $\boldsymbol{u^0} = \boldsymbol{u_0}$. We have the following expansions

$$\left(\frac{\boldsymbol{u^{k+1}} - \boldsymbol{u^k}}{\Delta t} \right) = \boldsymbol{u_t^{k+1/2}} + \mathcal{O}(\Delta t)^2$$
$$\left(\frac{A^{k+1}\boldsymbol{u^{k+1}} + A^k \boldsymbol{u^k}}{2} \right) = A^{k+1/2}\boldsymbol{u^{k+1/2}} + \mathcal{O}(\Delta t)^2$$

Since

$$\begin{aligned} u^{k+1}v^k &= \left(u^{k+1/2} + \frac{\Delta t}{2} u_t^{k+1/2} + \mathcal{O}(\Delta t)^2 \right) \left(v^{k+1/2} - \frac{\Delta t}{2} v_t^{k+1/2} + \mathcal{O}(\Delta t)^2 \right) \\ &= u^{k+1/2}v^{k+1/2} + \frac{\Delta t}{2} \left(u_t^{k+1/2} v^{k+1/2} - u^{k+1/2} v_t^{k+1/2} \right) + \mathcal{O}(\Delta t)^2, \end{aligned}$$

we also have

$$\begin{aligned} \mathcal{B}(\boldsymbol{u^{k+1}}, \boldsymbol{u^k}) &= \sum_{i=1}^{n} \left(\boldsymbol{u^{k+1}} \cdot B^i \boldsymbol{u^k} \right) \boldsymbol{e_i} \\ &= \sum_{i=1}^{n} \sum_{p,q=1}^{n} B^i_{pq} u_p^{k+1} u_q^k \boldsymbol{e_i} \\ &= \sum_{i=1}^{n} \sum_{p,q=1}^{n} \left[B^i_{pq} u_p^{k+1/2} u_q^{k+1/2} \boldsymbol{e_i} + \frac{\Delta t}{2} \left(u_{pt}^{k+1/2} u_q^{k+1/2} - u_p^{k+1/2} u_{qt}^{k+1/2} \right) \right] \end{aligned}$$

$$
\begin{aligned}
&+ \mathcal{O}(\Delta t)^2 \\
&= \sum_{i=1}^{n} \sum_{p,q=1}^{n} B_{pq}^{i} u_p^{k+1/2} u_q^{k+1/2} \boldsymbol{e_i} + \mathcal{O}(\Delta t)^2 \\
&= \mathcal{B}(\boldsymbol{u^{k+1/2}}, \boldsymbol{u^{k+1/2}}) + \mathcal{O}(\Delta t)^2
\end{aligned}
$$

Combining the approximations, we get an error of $\mathcal{O}(\Delta t)^2$.

3.1.2 Detailed adaptation model with diffusion

To explore the effect of diffusion on the adaptation property and responses to spatial gradients of the SES system, we perform numerical simulations where only the activated inhibitor (RasGAP) is diffusible and lives in cytosol Ω. The other molecular species live on the membrane $\partial\Omega$. We use the generic notations for the adaptation module. The corresponding signaling species for Ras activation can be found in Table 2.2. The resulting differential equations for Ras activation are

$$\frac{\partial E_2^*}{\partial t} = D_{E_2^*} \nabla^2 E_2^*$$

in Ω and

$$
\begin{aligned}
D_{E_2^*} \frac{\partial E_2^*}{\partial n} &= -\delta k_{E_2}^2 E_2^* - k_{W^*}^f W^* \cdot E_2^* + k_{E_2}^c [SE_2] + (k_{W^*}^c + k_{W^*}^r)[W^* E_2^*] \\
\frac{\partial E_1^*}{\partial t} &= -k_{E_1}^2 E_1^* - \frac{1}{\delta} k_W^f W \cdot E_1^* + k_{E_1}^c [SE_1] + (k_W^c + k_W^r)[W E_1^*] \\
\frac{\partial [SE_i]}{\partial t} &= -(k_{E_i}^r + k_{E_i}^c)[SE_i] + k_{E_i}^f S \cdot E_i \\
\frac{\partial E_1}{\partial t} &= -k_{E_1}^f S \cdot E_1 + k_{E_1}^r [SE_1] + k_{E_1}^2 E_1^* \\
\frac{\partial E_2}{\partial t} &= -k_{E_2}^f S \cdot E_2 + k_{E_2}^r [SE_2] + \delta k_{E_2}^2 E_2^*
\end{aligned}
$$

$$\frac{\partial W}{\partial t} = -\frac{1}{\delta}k_W^f W \cdot E_1^* + k_W^r[WE_1^*] + k_{W^*}^c[W^*E_2^*]$$
$$\frac{\partial W^*}{\partial t} = -k_{W^*}^f W^* \cdot E_2^* + k_{W^*}^r[W^*E_2^*] + k_W^c[WE_1^*]$$
$$\frac{\partial [WE_1^*]}{\partial t} = -(k_W^r + k_W^c)[WE_1^*] + \frac{1}{\delta}k_W^f W \cdot E_1^*$$
$$\frac{\partial [W^*E_2^*]}{\partial t} = -(k_{W^*}^r + k_{W^*}^c)[W^*E_2^*] + k_{W^*}^f W^* \cdot E_2^*$$

on $\partial\Omega$ where δ is the effective length of membrane reactions. Initial conditions are set at steady state under the basal stimulation level S_0.

The finite element method described in section 3.1.1 is implemented with second-order Lagrange elements in MATLAB to numerically solve the problem on a disk. The parameters with arbitrary units from Table 2.3 are used for the simulation. A slight modification is made to compensate for slower dynamics caused by the spatial effect, namely $k_{E_2}^2$ is increased by 10 folds to 0.5. In addition, we use $R = 5$, $D_{E_2^*} = 10$, and $\delta = 1$. Figure 3.2 depicts system responses subjected to successive steps of uniform stimulation. The cell exhibits adaptation responses similarly to the well-mixed system

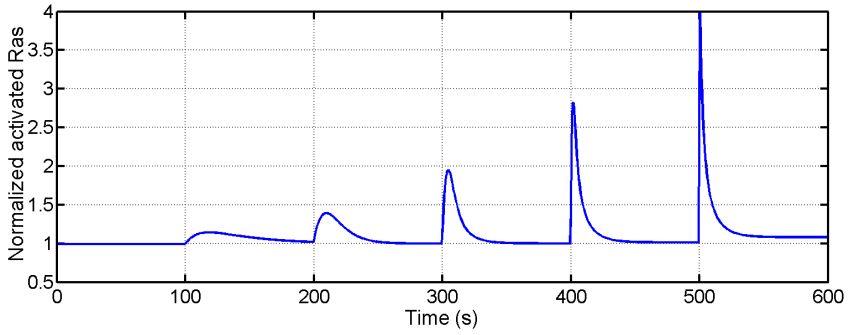

Figure 3.2: Normalized Ras^* concentration at the membrane under successive steps of five-fold increases in uniform cAMP stimulation. The final stimulus level is 3125x the original level, which is comparable to an increase from 0.32 nM to 1 μM. Each stimulation step lasts for 100 seconds.

in Figure 2.3. The smaller peaks of the Ras activity are due to faster activation of RasGEF. At the last activation step, the RasGAP activity starts becoming saturated and causes the response to remain elevated above the basal level.

We then study the response when a linear cAMP gradient with 2:1 front-to-back ratio is applied to the system. Figure 3.3 shows the concentration of activated Ras at different points along the membrane, normalized by the prestimulation level. The

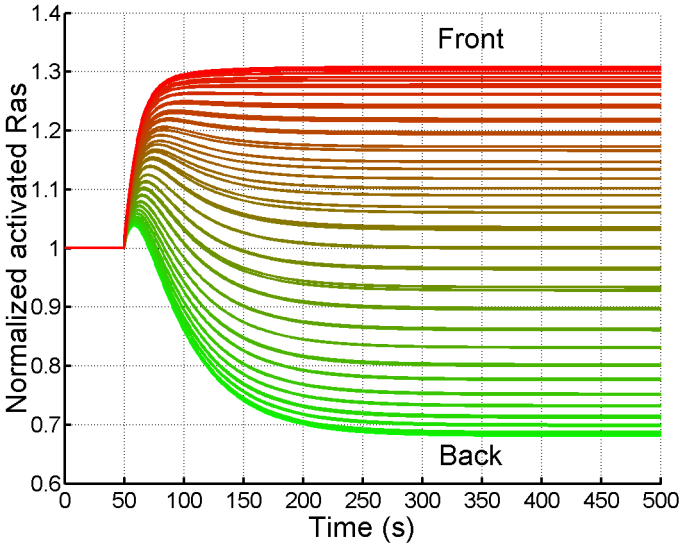

Figure 3.3: Normalized Ras activity at points along the membrane of a 2-dimensional cell subjected to a linear cAMP gradient. The 2-to-1 static gradient with the mean level at the basal level is applied at 50 s. Each line represents the response at a point, ordered by x-coordinate values.

Ras activity along the membrane displays a transient peak while the polarity is being established. At steady state, the cell is able to maintain polarized Ras activity which closely reflects the stimulus gradient. In this case, we see that the spatial gradient is slightly attenuated as the gradient ratio is 96 %. Note that the transient peak of Ras activity at points with high stimulus level is not noticeable because it is dominated by the polarization. Further simulations show that a system which possesses strong

transient activity displays the peak at all points on along the membrane.

The Ras activity in the 2-dimensional cell displays desirable adaptation properties and is capable of maintaining spatial gradients which closely follow the stimuli. To achieve substantial amplification of the spatial gradients as observed in PIP_3 and F-actin, the mean level of Ras activity should robustly coincide with the high-sensitivity region of the gradient-amplification module. We next propose a simple cascade of the adaptation and amplification modules in the context of the PI3K pathway and show that high spatial sensitivity can be achieved using this approach.

3.2 Model for PIP_3 adaptation and gradient amplification

In this section, a cascade of adaptation and gradient amplification modules is used to explain properties of cAMP-induced PIP_3 activities. The model combines adaptation in the Ras-activation step and gradient amplification achieved by positive feedback and implicit cooperativity in the PIP_3 activation step. Reactions are simplified to capture essential mechanisms. They are biologically-faithful and account for established steps in the PI3K pathway. We simulates the system on two-dimensional domains such as a circular disk and more realistic cell shapes to study the chemotactic responses.

3.2.1 Signaling model

The model for PIP_3 activity follows the PI3K-pathway description discussed in section 1.4. Because the heterotrimeric G-protein activity closely reflects extracellular cAMP concentration at the membrane, we consider free $G\beta\gamma$ around the membrane as the input. A wiring diagram which illustrates interactions between model components is shown in Figure 3.4.

The adaptation module accounts for regulation of Ras, a membrane-bound protein. The activity of Ras is positively and negatively controlled by RasGEF and RasGAP

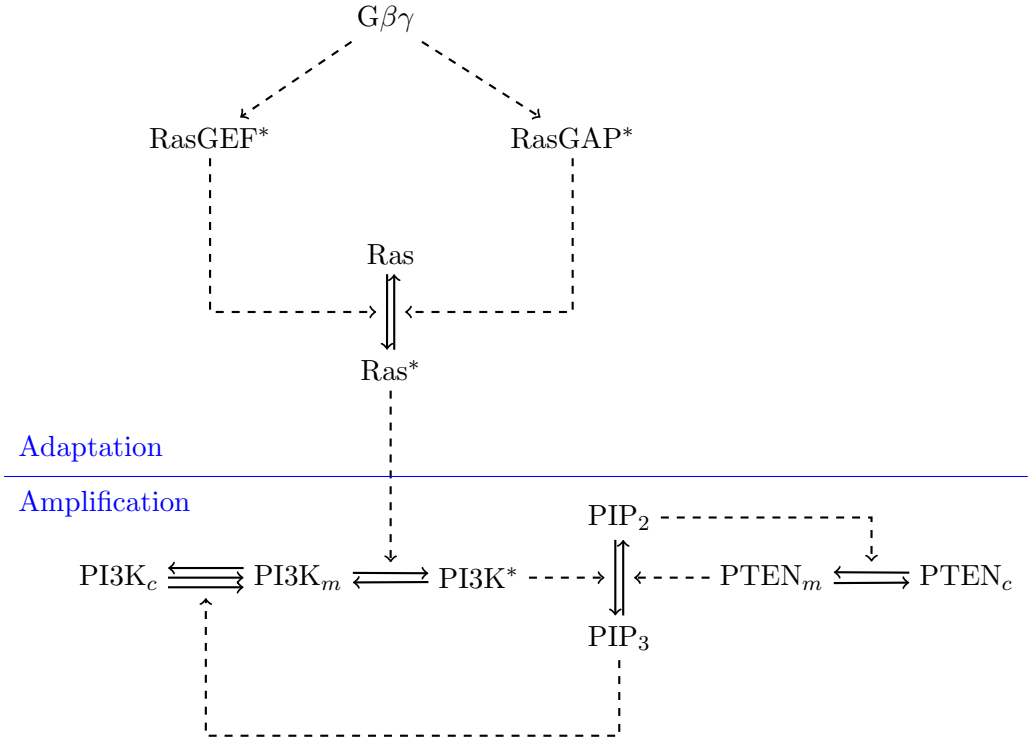

Figure 3.4: A simple model of the PI3K-signaling pathway.

respectively. Both RasGEF and RasGAP are cytosolic proteins which are activated by $G\beta\gamma$ at the membrane. The activation of RasGEF is faster to allow transiently-elevated Ras activity before it adapts.

The activity of Ras is the input for the gradient-amplifying module which has PIP_3 as its response. The module PIP_3 is regulated by PI3K and PTEN. Membrane-bound PI3K is activated by Ras. Activated PI3K then converts membrane lipid PIP_2 into PIP_3. Conversely, membrane-bound PTEN turns PIP_3 into PIP_2. High sensitivity of this module is due to membrane localization of PI3K, which is related to F-actin and is partly downstream of the PIP_3 activity. This mechanism provides both cooperativity and positive feedback which form a basis of this module. We also incorporate PTEN localization, which is known to depend on PIP_2, into our model. This extra step is also

cooperative and should not negatively affect sensitivity of the system.

The full set of reactions which describe our model for PIP_3 activity consists of

$$
\begin{aligned}
G\beta\gamma + RasGEF &\xrightarrow{k_{RasGEF^*}} G\beta\gamma + RasGEF^* && \text{on } \partial\Omega \\
RasGEF^* &\xrightarrow{k_{RasGEF}} RasGEF && \text{in } \Omega \\
G\beta\gamma + RasGAP &\xrightarrow{k_{RasGAP^*}} G\beta\gamma + RasGAP^* && \text{on } \partial\Omega \\
RasGAP^* &\xrightarrow{k_{RasGAP}} RasGAP && \text{in } \Omega \\
RasGEF^* + Ras &\xrightarrow{k_{Ras^*}} RasGEF^* + Ras^* && \text{on } \partial\Omega \\
RasGAP^* + Ras^* &\xrightarrow{k_{Ras}} RasGAP^* + Ras && \text{on } \partial\Omega \\
PIP_3 + PI3K_c &\xrightarrow{k_{PI3K_m}} PIP_3 + PI3K_m && \text{on } \partial\Omega \\
PI3K_c &\underset{k_{PI3K_c}}{\overset{k_{b,PI3K_m}}{\rightleftharpoons}} PI3K_m && \text{on } \partial\Omega \\
Ras^* + PI3K_m &\xrightarrow{k_{PI3K_m^*}} Ras^* + PI3K_m^* && \text{on } \partial\Omega \\
PI3K_m^* &\xrightarrow{k_{d,PI3K_m}} PI3K_m && \text{on } \partial\Omega \\
PI3K_m^* + PIP_2 &\xrightarrow{k_{PIP_3}} PI3K_m^* + PIP_3 && \text{on } \partial\Omega \\
PTEN_m + PIP_3 &\xrightarrow{k_{PIP_2}} PTEN_m + PIP_2 && \text{on } \partial\Omega \\
PIP_2 + PTEN_c &\xrightarrow{k_{PTEN_m}} PIP_2 + PTEN_m && \text{on } \partial\Omega \\
PTEN_m &\xrightarrow{k_{PTEN_c}} PTEN_c && \text{on } \partial\Omega
\end{aligned}
$$

whose evolution can be described by

$$
\begin{aligned}
\frac{\partial RasGEF^*}{\partial t} &= D_{RasGEF}\nabla^2 RasGEF^* - k_{RasGEF} RasGEF^* && \text{in } \Omega \\
\frac{\partial RasGAP^*}{\partial t} &= D_{RasGAP}\nabla^2 RasGAP^* - k_{RasGAP} RasGAP^* && \text{in } \Omega \\
\frac{\partial PI3K_c}{\partial t} &= D_{PI3K}\nabla^2 PI3K_c && \text{in } \Omega \\
\frac{\partial PTEN_c}{\partial t} &= D_{PTEN}\nabla^2 PTEN_c && \text{in } \Omega
\end{aligned}
$$

$$
\begin{aligned}
\frac{\partial Ras^*}{\partial t} &= k_{Ras^*} RasGEF^* \cdot Ras - k_{Ras} RasGAP^* \cdot Ras^* && \text{on } \partial\Omega \\
\frac{\partial PI3K_m}{\partial t} &= \delta k_{b,PI3K_m} PI3K_c + k_{PI3K_m} PIP_3 \cdot PI3K_c + k_{d,PI3K_m} PI3K_m^* \\
&\quad - k_{PI3K_m^*} Ras^* \cdot PI3K_m - k_{PI3K_c} PI3K_m && \text{on } \partial\Omega \\
\frac{\partial PI3K_m^*}{\partial t} &= k_{PI3K_m^*} Ras^* \cdot PI3K_m - k_{d,PI3K_m} PI3K_m^* && \text{on } \partial\Omega \\
\frac{\partial PTEN_m}{\partial t} &= k_{PTEN_m} PIP_2 \cdot PTEN_c - k_{PTEN_c} PTEN_m && \text{on } \partial\Omega \\
\frac{\partial PIP_3}{\partial t} &= k_{PIP_3} PI3K_m^* \cdot PIP_2 - k_{PIP_2} PTEN_m \cdot PIP_3 && \text{on } \partial\Omega
\end{aligned}
$$

with the following boundary conditions for the cytosolic species

$$
\begin{aligned}
D_{RasGEF} \frac{\partial RasGEF^*}{\partial n} &= k_{RasGEF^*} G\beta\gamma \cdot RasGEF \\
D_{RasGAP} \frac{\partial RasGAP^*}{\partial n} &= k_{RasGAP^*} G\beta\gamma \cdot RasGAP \\
D_{PI3K} \frac{\partial PI3K_c}{\partial n} &= k_{PI3K_c} PI3K_m - k_{PI3K_m} PIP_3 \cdot PI3K_c - \delta k_{b,PI3K_m} PI3K_c \\
D_{PTEN} \frac{\partial PTEN_c}{\partial n} &= k_{PTEN_c} PTEN_m - k_{PTEN_m} PIP_2 \cdot PTEN_c
\end{aligned}
$$

on $\partial\Omega$ and conservation laws

$$
\begin{aligned}
RasGEF + RasGEF^* &= RasGEF_0 && \text{in } \Omega \\
RasGAP + RasGAP^* &= RasGAP_0 && \text{in } \Omega \\
Ras + Ras^* &= Ras_0 && \text{on } \partial\Omega \\
PIP_2 + PIP_3 &= P_0 && \text{on } \partial\Omega
\end{aligned}
$$

assuming same diffusion coefficients for active and inactive forms of signaling molecules.

The surface densities of the membrane species in the model are taken from the literature. Typical values of concentration and diffusion constant, which are 0.1 μM and 10 $\mu m^2/s$ respectively, are used for the cytosolic species. The reaction-rate constants are

choosen to match experimentally-observed dynamics. In particular, the dynamics of the cytosolic Ras-binding domain (RBD) reported in [176] is used to match the responses at different levels of uniform stimulation while the responses to static cAMP gradients are matched with the dynamics of PH_{Crac}-GFP, a PIP_3 reporter, at the front and the back of a live cell [196]. Table 3.1 shows the parameters used in our simulations.

Parameter	Value	Description	Source
R	8 μm	Cell radius	
δ	10 nm	Effective length for membrane reactions	
$RasGEF_0$	0.1 μM	Average RasGEF cytosolic concentration	[130]
$RasGAP_0$	0.1 μM	Average RasGAP cytosolic concentration	[130]
Ras_0	2000 $\#/\mu m^2$	Membrane density of Ras	[134]
$PI3K_0$	0.1 μM	Average PI3K cytosolic concentration	[130]
$PTEN_0$	0.1 μM	Average PTEN cytosolic concentration	[130]
PIP_0	1000 $\#/\mu m^2$	Membrane density of PIP_2 and PIP_3	[130, 62]
D_{RasGEF}	10 $\mu m^2/s$	Diffusion constant for RasGEF	[154]
D_{RasGAP}	10 $\mu m^2/s$	Diffusion constant for RasGAP	[154]
D_{PI3K}	10 $\mu m^2/s$	Diffusion constant for PI3K	[154]
D_{PTEN}	10 $\mu m^2/s$	Diffusion constant for PTEN	[154]
k_{RasGEF^*}	93.75 $(\#/\mu m^2)^{-1}\mu m/s$	RasGEF activation by G$\beta\gamma$	
k_{RasGEF}	0.25 s^{-1}	Spontaneous RasGEF* deactivation	
k_{RasGAP^*}	1.5 $(\#/\mu m^2)^{-1}\mu m/s$	RasGAP activation by G$\beta\gamma$	
k_{RasGAP}	0.12 s^{-1}	Spontaneous RasGAP* deactivation	
k_{Ras^*}	800 $\mu M^{-1}s^{-1}$	Ras activation by RasGEF*	
k_{Ras}	2.5×10^6 $\mu M^{-1}s^{-1}$	Ras* deactivation by RasGAP*	
$k_{PI3k^*_m}$	18.75 $(\#/\mu m^2)^{-1}s^{-1}$	PI3K activation by Ras*	
$k_{d,PI3k_m}$	0.844 s^{-1}	Spontaneous PI3K* deactivation	
k_{PI3k_c}	3×10^5 s^{-1}	Spontaneous PI3K membrane dissociation	
k_{PI3k_m}	1500 $\mu M^{-1}s^{-1}$	PI3K membrane binding induced by PIP_3	
k_{PIP_3}	720 $(\#/\mu m^2)^{-1}s^{-1}$	PIP_3 production by PI3K	

Parameter	Value	Description	Source
k_{PIP_2}	1050 $(\#/\mu m^2)^{-1}s^{-1}$	PIP_3 dephosphorylation by PTEN	
$k_{b,PI3k_m}$	1500 s^{-1}	Spontaneous PI3K membrane binding	
k_{PTEN_m}	0.75 $\mu M^{-1}s^{-1}$	PI3K membrane binding induced by PIP_2	
k_{PTEN_c}	0.375 s^{-1}	Spontaneous PTEN membrane dissociation	

Table 3.1: Parameter values used in the model of the PI3K-signaling pathway.

The system is numerically solved on two-dimensional domains by a finite element method with backward differentiation formula (BDF) for time stepping which is implemented by COMSOL Multiphysics package. For each simulation, the system is first simulated with uniform basal cAMP concentration until it reaches a steady state. Then a stimulation is introduced by changing the external cAMP profile. The cAMP level is represented by the surface density of free G$\beta\gamma$, which is the forcing function of the system. We assume that the free G$\beta\gamma$ density is proportional to the cAMP level and that half of the heterotrimetic G protein on the membrane (with the total density of 2000 $\#/\mu m^2$ [134]) is activated at 1 μM cAMP.

3.2.2 Responses to external stimuli

Responses on a circular disk

The system is first simulated on a 2D disk which represents a *Dictyostelium* cell treated with LatA, in which case its shape is round. The inner domain corresponds to cytosol while the boundary corresponds to the cellular membrane. Uniform stimulation leads to transient localization of PIP_3 uniformly throughout the membrane, followed by adaptation. A recent work by Takeda et al. [176] reported quantitative measurements of Ras activation dynamics to uniform stimulations over the physiological range of cAMP

concentration. The Ras activity is represented by depletion of cytosolic RBD, which localizes to the membrane by binding to activated Ras. We model this measurement by solving the equations

$$\begin{aligned} \frac{\partial RBD_c}{\partial t} &= D_{RBD}\nabla^2 RBD_c && \text{in } \Omega \\ D_{RBD}\frac{\partial RBD_c}{\partial n} &= k_{RBD_c}RBD_m - k_{RBD_m}Ras^* \cdot RBD_c && \text{on } \partial\Omega \\ \frac{\partial RBD_m}{\partial t} &= k_{RBD_m}Ras^* \cdot RBD_c - k_{RBD_c}RBD_m && \text{on } \partial\Omega \end{aligned}$$

with the following parameters: $D_{RBD} = 10\ \mu m^2/s$, $RBD_0 = 0.1\ \mu M$, $k_{RBD_c} = 7.5\ s^{-1}$, and $k_{RBD_m} = 1200\ \mu M^{-1}s^{-1}$. Figure 3.5 compares the average cytosolic density of RBD obtained from simulation to the experimental measurements. The Ras activity displays

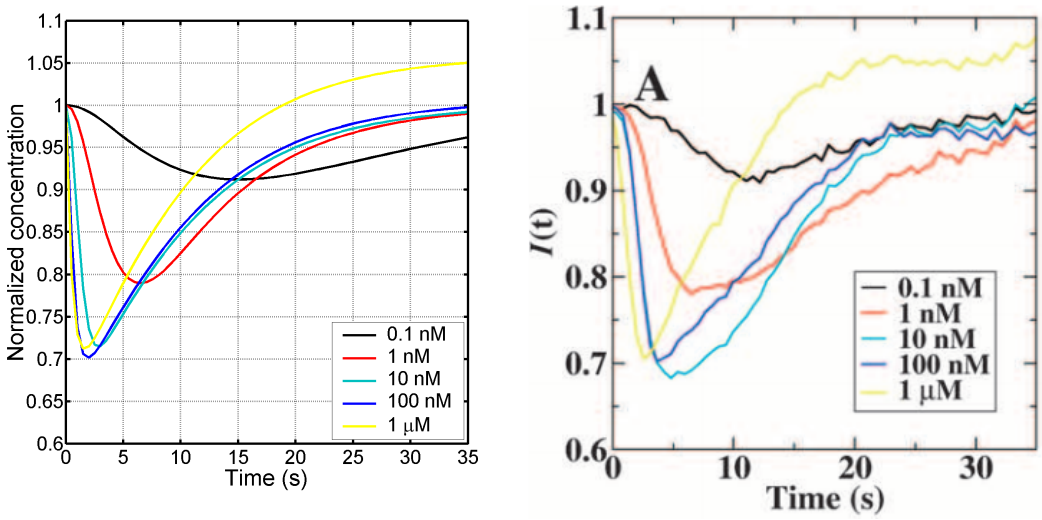

Figure 3.5: Ras-activation dynamics. Uniform stimulation causes a transient decrease in the average cytosolic concentration of RBD. The stimulus is applied at $t = 0$ and response is measured over the physiological range of cAMP concentration. Simulation results *(left)* is compared to experimental measurements *(right)* from [176].

good adaptation over the physiological stimulation range. The dynamics at higher

cAMP concentration is faster as predicted by the analysis in Section 2.2.4. Similarity of the responses between 10 nM and 1 μM cAMP suggests that *Dictyostelium* is capable of exhibiting consistent behaviors under the stimulus range. We found that this robustness is a result of fast Ras activation dynamics, compared to the dynamics of RasGEF and RasGAP. Moreover, the Ras activation dynamics shows that the system is near saturation at 1 μM cAMP. In contrast to the adaptation dynamics in Figure 3.2 and in the work by Takeda et al. [176], the Ras activity has decreased peak and steady-state level in saturation compared to the responses at lower stimulation levels, as depicted by the cytosolic RBD dynamics. The decrease in the peak and the steady-state activity occurs when the RasGEF activity is saturated before the RasGAP activity. When the RasGAP activity is closer to saturation, increasing peak and steady-state level are observed as in Figure 3.2.

The adaptation property of Ras activation is inherited by its down stream effectors. Figure 3.6 displays PIP_3 responses subjected to successive steps of uniform stimulation at two representative points on the membrane which are directly opposite. The concentration level of G$\beta\gamma$ spans over 3 orders of magnitude in this simulation. This result

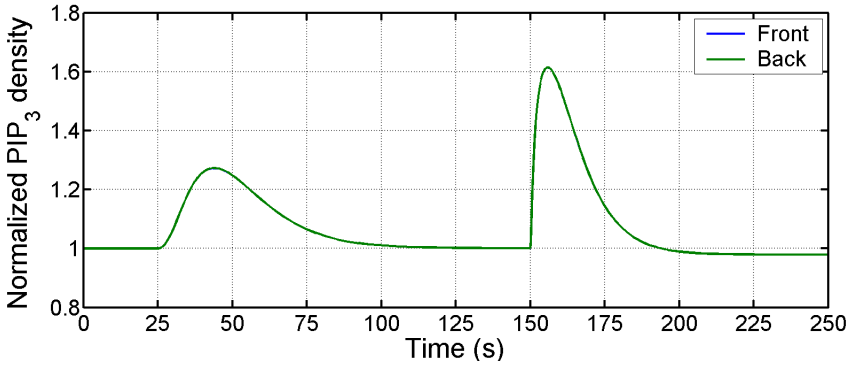

Figure 3.6: PIP_3 localization at two opposite points on the membrane of a circular cell subjected to successive steps of spatially uniform stimulation. The stimulation is represented by the local level of free $G\beta\gamma$ which reflects 0.1 nM and 100 nM cAMP at 25 s and 150 s respectively. The responses at two sites are nearly identical.

of the adaptation-amplification cascade agrees well with the simulation result for the adaptation module in Section 3.1.2.

We next study the responses under a static cAMP gradient. Dallon and Othmer [46] showed that the spatial profile of the stimulus is perturbed by the presence and the shape of the cell. However, we assume here that the cell is superimposed on a predefined cAMP-concentration field. We replicate an experiment by Xu et al. [196] for PIP_3 response under a static cAMP gradient. Dynamics of PIP_3 localization at the anterior and the posterior of the cell under an unknown cAMP gradient from Xu et al. [196] is matched by a model response under a 50 % cAMP gradient in Figure 3.7. The

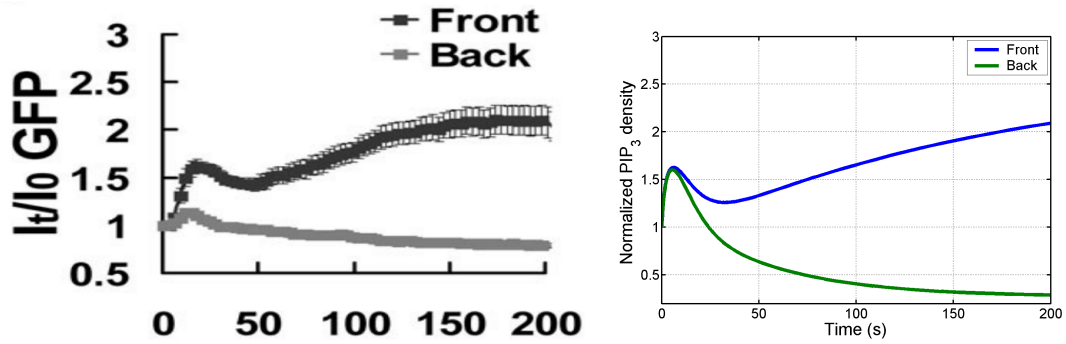

Figure 3.7: PIP_3 responses to a static cAMP gradient. *(Left)* The response at the front and the back of a cell to a cAMP gradient created by a micropipette. The cell is treated by LatA and assumes a circular shape while the responses are measured by local PH_{Crac}-GFP concentration [196]. *(Right)* A simulated PIP_3 response on a circular domain subject to a cAMP gradient with 50 % front-to-back difference.

PIP_3 response is biphasic as the localization level undergoes a transient peak before the cell orientation is established. The dynamics of the simulated response at the front agrees well with the observation. However, the response at the back undergoes a sharp transient peak, as high as the response at the front, before decreasing rapidly to a very low level. Numerical experiments reveal that the separation of the peaks at the front and the back of the cell occurs at a low mean stimulus level. On the other hand, the

relatively steady response at the back may be explained by spontaneous activation of PI3K on the membrane, which is not present in our simplified model. Figure 3.8 shows the evolution of the PIP_3 activity in Figure 3.7 along the membrane. The PIP_3 activity

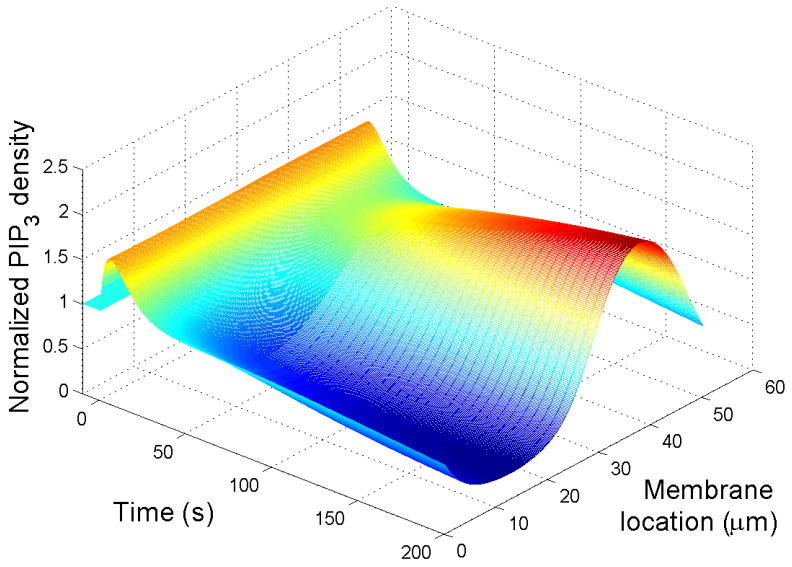

Figure 3.8: Dynamics of the PIP_3 response in Figure 3.7 along the cell membrane. The static gradient is applied to a resting cell at 0 s.

displays the distinctive biphasic reponse with a transient rapid increase in the activity uniformly on the membrane, followed by highly-amplified stimulus-induced polarization. The system is then tested with another experimental measurement where quantitative data at steady state of both stimulus and response is available. In Figure 3.9, the simulated PIP_3 response under a 20 % cAMP gradient is compared to the quantitative data. The front-to-back ratio of the steady-state PIP_3 activity is 280 % which agrees well with the observed value.

It is known that suspended *Dictyostelium* cells are able to reorient themselves when the cAMP gradient is reversed. Meier et al. [133] observed that this ability to reverse

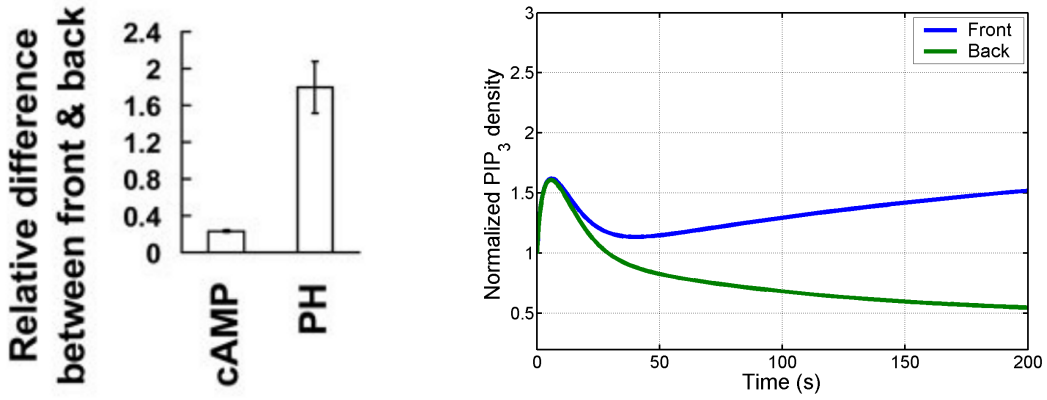

Figure 3.9: Comparison of gradient amplification. *(Left)* A steady-state measurement of cAMP and PIP_3 gradients suggests that a 120 % front-to-back ratio in cAMP induces a 280 % front-to-back PIP_3 ratio [196]. *(Right)* A simulated PIP_3 response under a cAMP gradient with the same strength.

direction is limited by polarization dynamics. Chemotaxing cells move upwards the cAMP gradient with reduced speed when subjected to alternating cAMP gradient with period of 120 seconds compared to 600 seconds. They are completely stalled and trapped within the alternating gradient at period of 20 seconds. We apply alternating gradients at 20 % difference with periods 20, 120, and 300 seconds and observe PIP_3 localization as shown in Figure 3.10. The response develops a very small front-to-back gradient at the high frequency which explains its inability to polarize under the fast-alternating gradient. As the frequency decreases, stronger PIP_3 localization gradients are allowed, leading to the experimentally-observed increase in the chemotaxis speed.

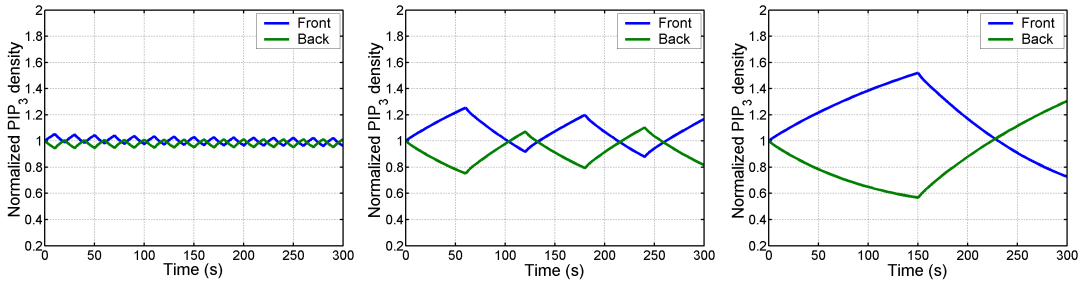

Figure 3.10: PIP_3 responses to alternating gradients at different frequencies. *(Left)* 1/20 Hz, *(middle)* 1/120 Hz, and *(right)* 1/300 Hz.

Responses in nonsymmetric cells

To study the PIP_3 responses in normal cells, we perform simulations on a domain which represents a motile cell. As the domain is fixed, we aim to understand how cAMP stimulation affects polarity and how polarized cells change their direction towards a cAMP source.

Figure 3.11 depicts the steady-state PIP_3 localization subjected to uniform stimulation in domains which resemble normal cells. The steady-state PIP_3 activity is polarized

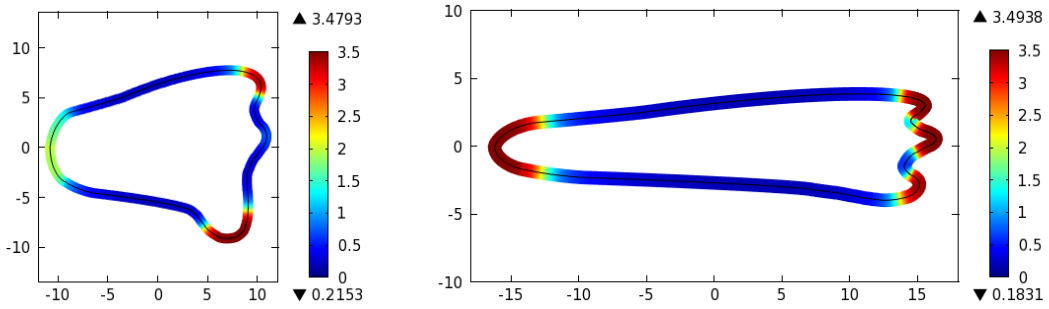

Figure 3.11: Steady-state PIP_3 localization in 2-dimensional cells under uniform stimulation. *(Left)* A moderately polarized cell. *(Right)* A highly polarized cell.

under uniform stimulation with strong localization in regions with high boundary length per domain area. In the moderately polarized cell, these regions include protrusions at the anterior, and the back of the cell. The activity is the highest at the leading edge

corners–cell protrusions connecting to the sides of the cell–and lowest along the lateral of the cell. There is also moderate PIP_3 activity at the back. In the highly-polarized and elongated cell, the PIP_3, and hence F-actin, activity is high at most regions of the anterior and also at the posterior. The high activity at the corners is consistent with the observed angled protrusions and zig-zag motions of unstimulated cells or cells under shallow cAMP gradients [5, 127, 17]. Unlike the activity at the cell anterior, the PIP_3 and associated F-actin activities at the back of the cell have frequently been neglected although they have been reported in many experiments [150, 80, 85, 22, 203, 195]. Figure 3.12 compares the localized activities under cAMP gradients from some of the experiments with simulated PIP_3 activity in an elongated cell.

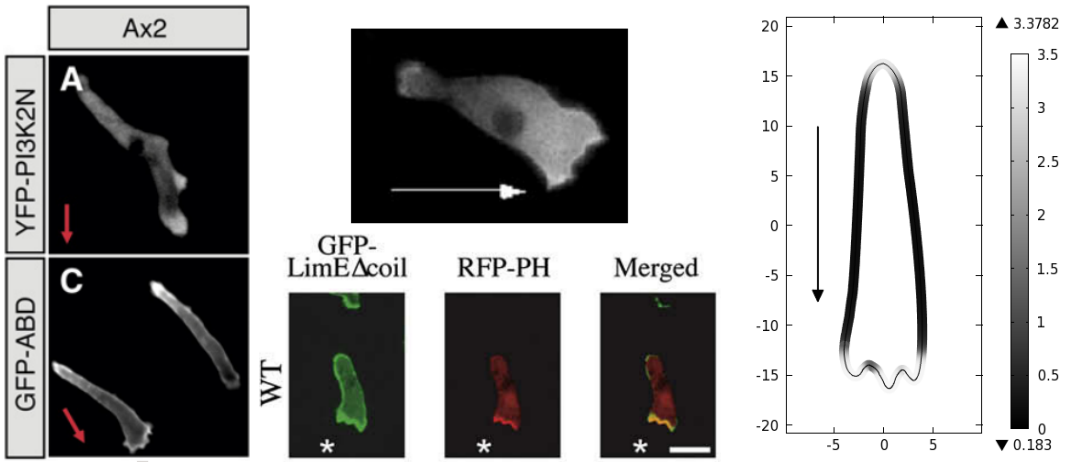

Figure 3.12: Localization of PIP_3 and F-actin activities in highly polarized cells migrating towards cAMP gradients. The directions of the cAMP gradients are indicated by arrows. Stars represent tips of micropipettes. *(Left panel)* F-actin activity *(bottom)* and PI3K localization *(top)* are the highest at the posterior and at protrusions and membrane ruffles near the anterior [85]. *(Middle panel, top)* RacB activity, which is downstream of PIP_3, is high at the front and noticeable at the back of the cell [150]. *(Middle panel, bottom)* F-actin *(green)* and PIP_3 *(red)* activities are the highest near the micropipette. The activity at the back of the cell is also above the normal level [203]. *(Right panel)* The simulated PIP_3 activity under a 50 % front-to-back gradient is the highest at the anterior. There is also significant PIP_3 activity at the posterior.

Experimental observations suggest that *Dictyostelium* cells become more polarized at higher levels of persistent uniform stimulation. Our model, however, fails to capture this behavior. The simulated polarization is insensitive to the stimulus level. This is due to the oversimplified description of the model. To rectify this shortcoming, we apply a simple modification to our model by adding spontaneous activation and inactivation of Ras, which are independent of RasGEF and RasGAP. In addition to providing the stimulus-dependent polarization, this modification sets a lower bound of recovery time after removal of the stimulus. We use rate constants for the spontaneous Ras processes which make the cell recover ~3 minutes after cAMP is completely removed. Figure 3.13 displays the steady-state PIP_3 activity of the modified model at different levels of spatially-uniform stimulation. We can see that the degree of polarization is an increasing

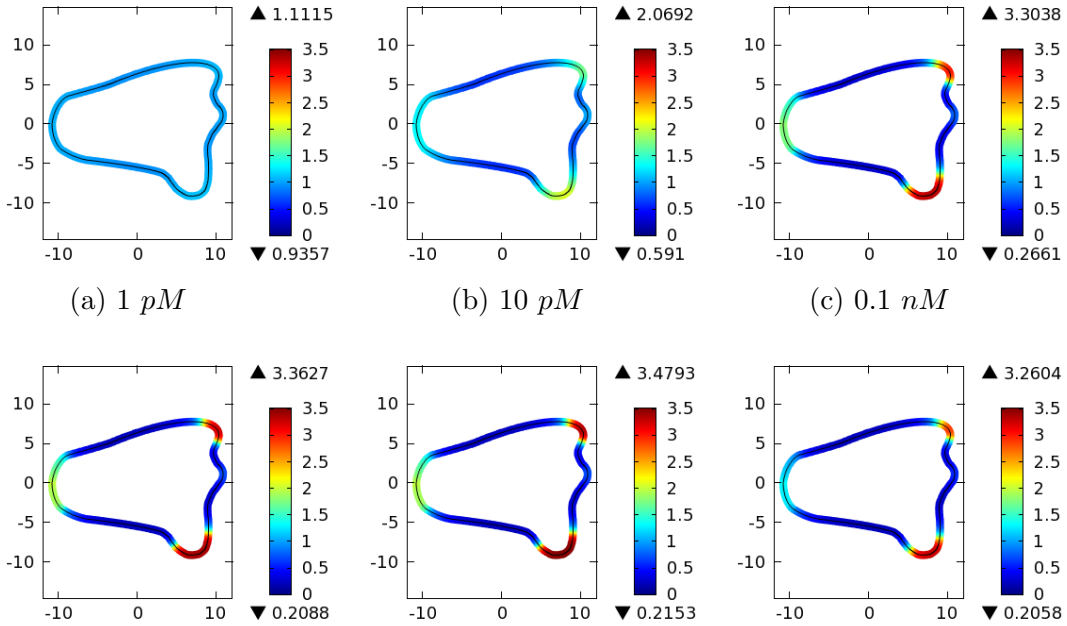

(a) 1 pM (b) 10 pM (c) 0.1 nM

(d) 10 nM (e) 100 nM (f) 1 μM

Figure 3.13: Steady-state PIP_3 localization of a moderately polarized cell at different levels of uniform stimulation.

function of the stimulus level, except at 1 μM cAMP where the saturation occurs.

Figure 3.14 compares the dynamics of the overall PIP_3 response from the simulation to the PIP_3 activity in wild-type cells under uniform stimulation. The overall PIP_3

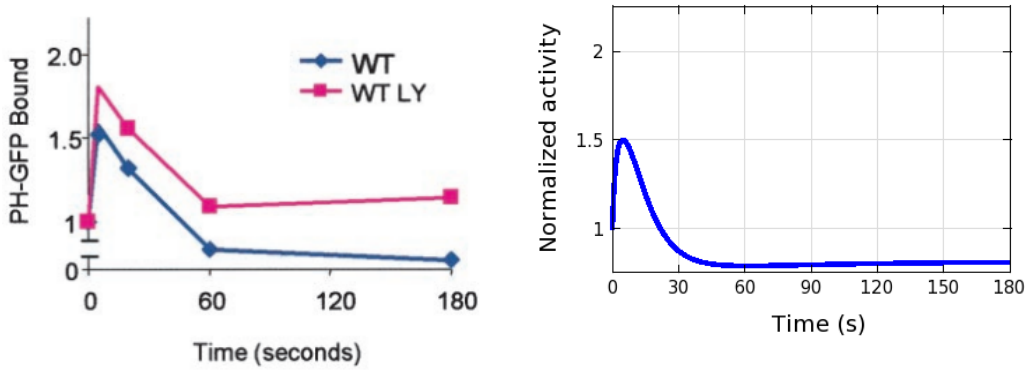

Figure 3.14: Dynamics of overall PIP_3 responses in wild-type cells. Uniform stimulation with 1 μM cAMP is applied at 0 s. *(Left)* Experimental measurement [39]. *(Right)* Simulation of the moderately polarized cell.

dynamics is biphasic and displays saturation with a decreased steady-state level. It is important to note that, however, this modification requires a strict agreement between the levels of Ras activity due to the spontaneous processes and the cAMP-induced processes. Structural-driven mechanisms such as stimulus-dependent deactivation of RasGEF and RasGAP or a feedback control may serve as more realistic alternatives, although we have not investigated these options.

We next study the response under a static cAMP gradient. Before the gradient stimulation, the cell has developed polarization under a small cAMP level. The cell is then subjected to a static cAMP gradient with 50 % front-to-back difference and oriented downwards, at 90 degrees to the current cell polarization axis. At the onset of the stimulation, PIP_3 localization transiently increases around the cell boundary. Then new orientation develops with the peak activity near the previous front, biased towards the cAMP gradient. Figure 3.15 shows the time course of the PIP_3 activity.

Typically, polarized *Dictyostelium* cells gradually turn back while maintaining their

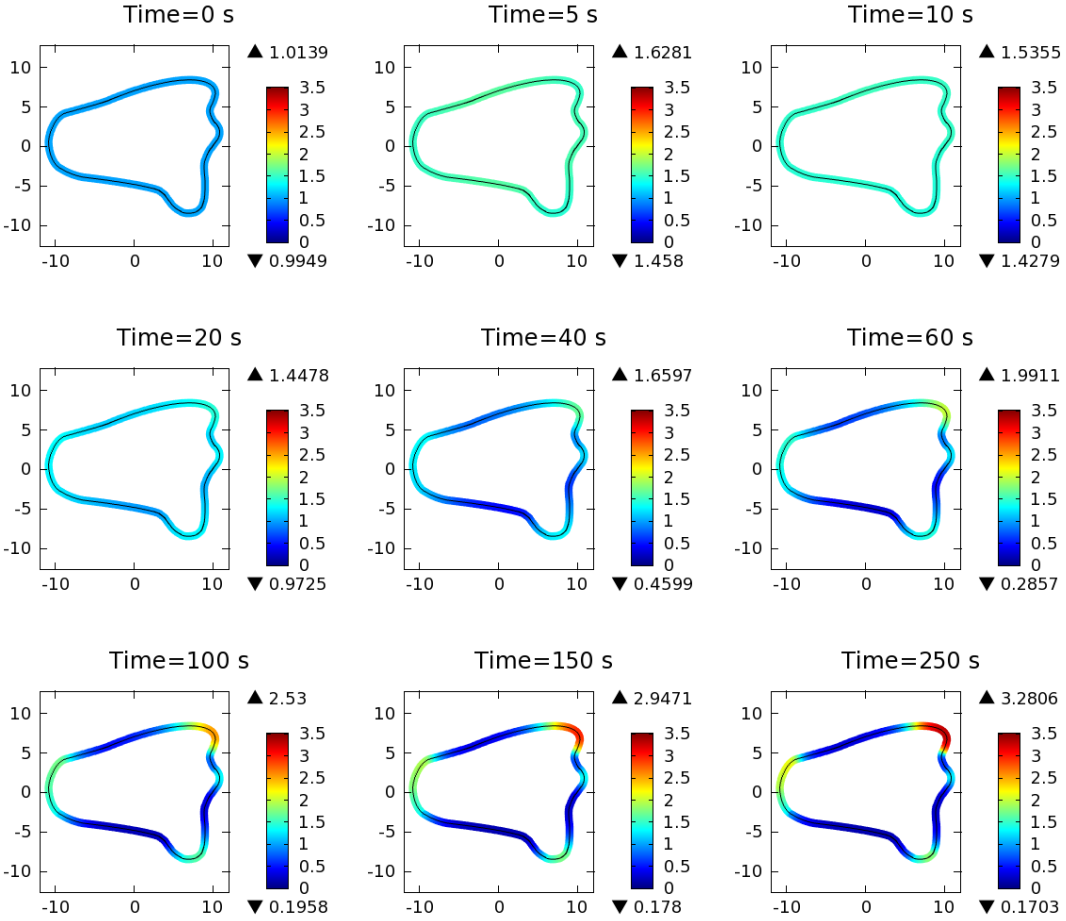

Figure 3.15: PIP_3 localization dynamics subjected to a cAMP gradient aligned normally to the original polarization axis. The downwards cAMP gradient with 100 nM mean concentration and 50 % difference across the cell is applied at 0 s.

polarity when they are subjected to a cAMP gradient in an opposite direction. However, strong gradients may cause them to directly reorient themselves and develop new fronts at the current posterior. We study this behavior by applying cAMP gradients with different strength at 180 degrees to the current front. The resulting steady-state PIP_3 localization displayed in Figure 3.16 suggests that under a low cAMP gradient, the cell is able to maintain its orientation because of the high F-actin activity at a protrusion in the anterior caused by the cell shape. If movement is incorporated, the cell should

gradually turns itself by first extending a pseudopod from the lower protrusion within the old front while maintaining its polarity throughout the process. In contrast, when the gradient is large enough to overcome the intrinsic polarity, the cell may switch its front directly towards the gradient.

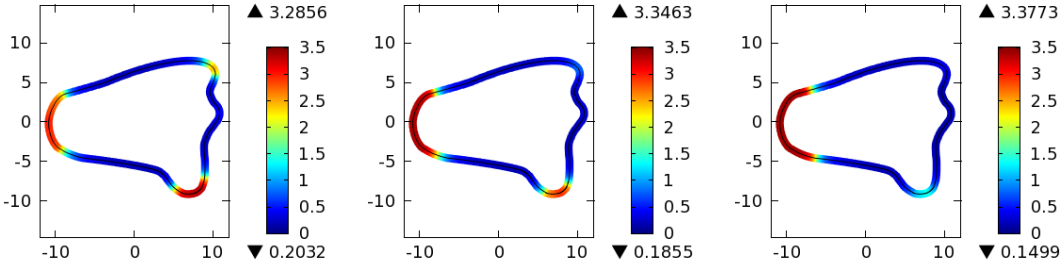

(a) 20 % difference (b) 50 % difference (c) 100 % difference

Figure 3.16: Steady-state PIP_3 activity at different levels of cAMP gradient suggests modes of reorientation. A polarized cell is subjected to static gradients in the opposite direction to the cell polarity. The PIP_3 activity is the highest at the lower protrusion at 20 % back-to-front difference. At 50 % and 100 % difference, the peak PIP_3 activity is at the posterior of the cell.

Finally, Postma et al. [156] observed localization of PIP_3 when a LatA-treated cell is subjected to uniform stimulation. This contrasts with other experimental observation where LatA-treated cells only develop transient responses. We hypothesize that this polarization may be caused by asymmetry of the cell shape as the drug concentration used in Postma et al. [156] is lower than the level used in other experiments (1 μM versus 5 μM or more). A low level of F-actin structure within the cell cortex may remain at this drug concentration, making the cell not perfectly round. A simulation on an elipse suggests that the loss of symmetry may lead to the observed localization of PIP_3 as shown in Figure 3.17.

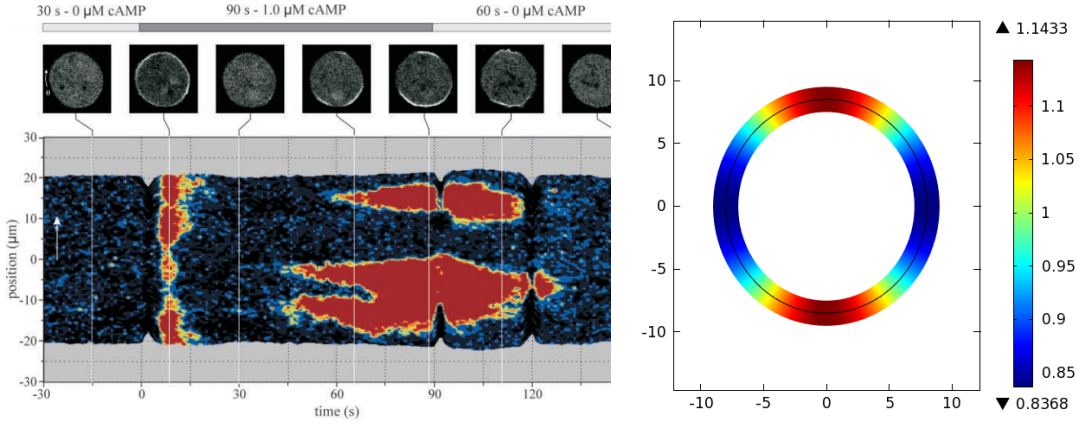

Figure 3.17: Development of PIP_3 localization in cells suspended at low LatA concentration. *(Left)* PIP_3 localization dynamics in a cell treated with 1 μM LatA. The cell develops localized PIP_3 activity under uniform cAMP stimulation Postma et al. [156]. *(Right)* Simulated steady-state PIP_3 localization on a ellipse-shaped cell at a non-saturated cAMP level. The ellipse has 0.94 roundness, which is defined as the ratio between length of the minor axis and the major axis.

3.3 Discussion

The models discussed in Chapter 2 do not account for spatial variations of their components. When they are used in a spatially-distributed system, diffusion of signaling molecules affects behaviors of the systems. For example, dynamics of membrane-activated molecules which are spontaneously deactivated in the domain are altered by diffusion. Characteristic degradation length describes a relationship between the decay rate, the diffusion constant, and the spatial variation of the activated molecules at steady state. For a symmetric domain such as a 1D interval or a 2D disk, the steady-state adaptation property is not altered, although the level of the adapted response may be affected by diffusion. In more general domains, imbalance in distribution of the activated form of the enzymes causes high activity in regions which are not exposed to large domain areas. The effect is prominent if the characteristic length of the

domain is smaller than the characteristic degradation length. A lucid example of this phenomenon is the PKA activity in neuronal dendrites [142]. However, as demonstrated by our model of the PI3K pathway, small domain asymmetry may also lead to large difference in downstream activity when the signal is highly amplified.

The proposed model of the PI3K pathway is a signaling cascade which combines an adaptation module responsible for adapted Ras activity with a highly-sensitive PI3K-PTEN-PIP_3 circuit. This simplified description accurately accounts for many features of the pathway and elucidates connections between seemingly fragmented experimental observations. The model produces biphasic responses which agree well with PIP_3 localization in LatA-treated cells under cAMP gradients [196]. Because the adapted Ras activity is in the sensitive region of the PI3K-PTEN-PIP_3 circuit, the system operates robustly over a wide range of the stimulation level.

The model produces Ras activity which closely matches experimental measurements over the entire range of stimulation levels [176]. Adaptation to successive uniform stimulation occurs at the Ras activation step, where the adaptation capacity is determined by saturation of RasGEF and RasGAP. In *Dictyostelium* cells, the saturation starts at around 1 μM cAMP, at which point the steady-state response drops from the basal level. This strongly suggests a feedforward adaptation model where the drop in the response is caused by saturation of RasGEF. In addition, rapid Ras activation dynamics allows the response with consistent peaks over several orders of magnitude in cAMP concentration.

The biphasic F-actin activity incorporates fast adaptation dictated by the Ras activity and slower polarization developed within the downstream circuit. The slow polarization process prevents *Dictyostelium* cells from reacting to rapidly-alternating cAMP gradients, as observed in [133]. A static cAMP gradient induces rapid uniform PIP_3 localization along the membrane which drops as polarization develops and becomes close

to the steady state level at ~300 s.

Spatially-uniform stimulus induces random patches of F-actin in wild-type *Dictyostelium* cells [156, 22], as depicted in Figure 3.18. This is a result of irregular distribution

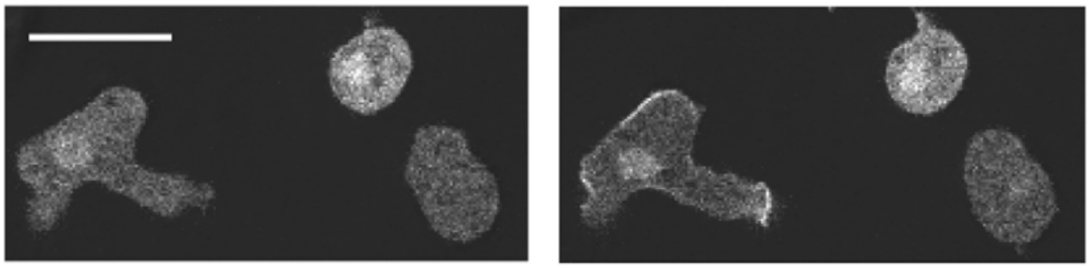

(a) Before stimulation (b) 0.3 nM cAMP

Figure 3.18: F-actin patches caused by uniform cAMP stimulation. The F-actin patches are localized near tips of cell protrusions [22].

of RasGEF and RasGAP activities driven by the cell shape. Because RasGAP has larger characteristic degradation length than RasGEF, high Ras activity is developed in regions which are not well-exposed to large cytosolic areas such as pseudopods, uropods, membrane protrusions, and membrane ruffles. The local activity is then amplified to give the pronounced localization response. It is known that uniformly stimulated cells also display enhanced polarity and increased random-migration speed although the effect is more evident in neutrophils [78]. The dose dependency in the shape-induced polarization may be caused by spontaneous activation and inactivation of Ras although a different, yet unknown, mechanism is more likely. Nevertheless, these spontaneous activities also give a characteristic recevery period after stimulus removal which is otherwise missing from the simple feedforward adaptation model. Because F-actin is enriched at the anterior of polarized cells, it is believed that membrane protrusions, and hence polarization, is driven by the locally-enriched F-actin activity. Our result on the shape-induced PIP_3 activity opens a possibility that there is a positive feedback loop between local F-actin activity and cell morphology. This positive feedback between the local F-actin activity

and the cell shape suggests a scheme for polarization where local irregularity in cell shape induces an F-actin protrusion which, in turn, leads to a stronger localization signal. This mechanism could explain increased polarity and speed of random migration after uniform chemoattractant stimulation, as well as enhanced polarization during prolonged chemotaxis. In fact, *Dictyostelium* mutants which lose the ability to secrete cAMP fail to develop polarity and become immobile. Just as neutrophils, they develop polarity and become motile after uniform stimulation with cAMP [113, 43]. Moreover, it has been observed that filopodia generated by mDia2 formin promote lamellipodia protrusions [201].

Several important features of *Dictyostelium* chemotaxis can be explained by the morphology-induced polarization. First, pseudopods at the anterior of highly-polarized cells induce strong localized PIP_3 activity in this region, which gives rise to directional persistence. New pseudopods are usually extended at the front of the cells, even in absence of chemoattractant. When a polarized cell is subjected to a cAMP gradient, the orientation of the cell is developed as a combination of the intrinsic polarity and the external gradient. Unless the cAMP gradient is strong enough to overcome the shape-induced polarity, the cell gradually turns its front towards the cAMP source. This is usually the case when *Dictyostelium* cells migrate under a shallow cAMP gradient [5]. However, when the gradient overcomes the intrinsic polarity, the cell directly develops new pseudopods upwards the cAMP gradient and switches its front. Next, because pseudopods which are adjacent to the cell sides are less exposed to large cytosolic areas in polarized cells, new pseudopods tend to be extended at an angle from the axis of polarity. This is consistent with studies by Li et al. [127] and Bosgraaf and Haastert [17], although the observed zig-zag motion requires an additional mechanism which favors new protrusions over existing ones. Finally, our model predicts PIP_3 activity at the cell posterior. The F-actin activity at the back may then serve as an ingredient for

formation of the actomyosin network which generates the contractile force and drives motility.

Because of its simplicity, our model cannot account for a few aspects of the chemotactic responses. First, the circular cells are suspended by LatA treatment and should have minimal F-actin activity. When we substantially reduce the positive feedback from PIP_3 to PI3K localization, the spatial sensitivity is deminished. The sensitivity is recovered when we adjust system parameters so that the system relies on cooperativity of PTEN and PIP_2. It may be possible to obtain a parameter set which fully utilizes both kinds of cooperativity so that the system remains highly sensitive to spatial gradients even when the F-actin activity is severely reduced. Furthermore, the F-actin branching process possesses intrinsic cooperativity and positive feedback which can provide additional amplification to the PI3K-PIP_3 feedback loop. An addtional positive feedback from F-actin activity to Ras activation has been observed and can contribute to the sensitivity of the PI3K pathway. Next, after cAMP removal, *Dictyostelium* cells become insensitive to stimulation up to the previous level for several minutes. This is likely due to a negative feedback from the downstream circuit to the adaptation module. This negative feedback could also explain the transient polarity reversal observed when uniform stimulation is applied shortly after removal of a static cAMP gradient Xu et al. [197]. However, currently there is no plausible candidate which negatively links the downstream activities to Ras activation.

In summary, many aspects of the chemotaxis pathway can be explained by a simple model which encompasses known interactions between components of the pathway. The model also illuminates an important role of the cell morphology which controls how *Dictyostelium* cells react to external stimulation. It also suggests a possible function of membrane ruffles and filopodia at the leading front of *Dictyostelium* cells. Recent studies have linked PLA2 and sGC to directional persistence [17, 18]. It is possible

that they are involved in formation of these irregular membrane structures. The dose-dependent polarity indicated by the model also suggests a new role of *Dictyostelium* cAMP secretion in self polarity enhancement. However, future studies are needed to understand more subtle behaviors such as the transient inverse polarization and how intracellular signaling interacts with cell movement. After all, the PI3K pathway is only one of the parallel pathways that contribute to the overall chemotactic responses. It remains elusive how concerted activities of these pathways lead to chemotactic behaviors of *Dictyostelium* cells.

Chapter 4

Models of branched actin network as observed in actin waves

To study the underlying mechanisms of the actin waves discussed in Chapter 1.1, we construct models for the F-actin network and then couple these models with an intracellular signaling pathway for F-actin polymerization. Because the F-actin structures associated with the actin waves are restricted to cell regions close to the cell membrane, especially at the cell-substrate interface, we assume that actin filaments only grow from the bottom of a cell placed on a flat surface. To simplify the analysis, we omit diffusion of actin filaments, which are mostly tethered to the actin network, and filament severing by cofilin and coronin. We also make a simplifying assumption that the actin filaments within the structure are oriented vertically. In the case without barbed-end capping, they are tethered to the cell-substrate interface. If barbed-end capping is considered, it is assumed that all filamenets are par of the actin network. A 2-dimentional model with a rectangular geometry is used to represent a vertical cross section of the cell. As it shall be evident, an extension of the models to a 3-dimensional cube is straightforward.

4.1 Modeling and analysis of filamentous actin network

The actin network is modeled as a collection of actin filaments, or polymers, which polymerize at a rate proportional to local G-actin density and depolymerize at a fixed rate. For simplicity, we assume that polymerization only occurs at filament barbed ends and depolymerization only occurs at filament pointed ends. The actin filaments are created by nucleation, or G-actin dimerization, and branching facilitated by a branching complex of WASP, Arp2/3, and G-actin. Both processes are assumed to take place only at the membrane-substrate interface. Branches are filaments with protected pointed ends and cannot depolymerize. Their pointed ends can be exposed by debranching which is facilitated by coronin. Coronin first binds to the pointed ends and replaces Arp2/3. Bound coronin destabilizes and eventually breaks branches. The broken branches become free filaments with exposed pointed ends and can depolymerize. Because we cannot track individual-filament connections, the possibility that branches are broken by depolymerization of mother filaments is omitted. There are two mechanisms for filament disassembly: by depolymerization of dimers, and by debranching of branches with only one G-actin subunit.

Because filaments align vertically, we further assume that filaments are connected, either directly or indirectly, if and only if they project to the same point on the membrane. We consider models in which barbed ends are always free and polymerize and where barbed ends can be capped and protected. In the first case, filament barbed ends always rest on the substrate-attached membrane. In the case with barbed-end capping, free barbed ends can be bound by capping protein. Because uncapping of barbed ends is very slow we assume that the capping process is irreversible [188]. The capping protein is only free when the capped filaments are disassembled. The capped filaments cannot polymerize and are pushed up by filaments with free barbed ends.

As there is no lateral interaction besides diffusion, discrete models are first developed in one spatial dimension along the filament length, assuming that the horizontal composition of chemical species is uniform. Then appoximations are made to obtain continuous models. Finally, diffusion of free molecules is introduced in 2-dimensional continuous models. Since all variables are functions of time, omission of t from the variables, except when it is explicitly specified, is assumed to simplify the notations throughout the analysis.

4.1.1 Discrete models

In the discrete models, state variables represent average densities of filaments and individual molecules within segments of length δ, the length of an F-actin subunit. For example, $G(1)$ is the average density of G-actin between 0 and δ, i.e.

$$G(1) = \frac{1}{\delta}\int_0^\delta g(z)\ dz$$

where g is the continuous density of G-actin and $z = 0$ represents the membrane hypersurface. Hence, the unit of G is $\#/length$. For simplicity, we first consider an infinite line $z \in [0, \infty)$ with segmentations at $k\delta, k \in \mathrm{N}$.

Discrete model without capping

Without capping, the actin network consists of filaments of different types, distinguished by the state of their pointed ends: free (P), Arp2/3-bound (R), and coronin-bound (C). In this case, barbed ends are always at the interface $z \in [0, \delta)$ and the filaments can be defined by their length l, here taken at discrete locations $n\delta,\ n \in \mathrm{N}$ so that

$$P(n) = \frac{1}{\delta}\int_{(n-1)\delta}^{n\delta} p(l)\ dl$$

where p is the continous density of free filaments. This relation provides a connection between the discrete and continuous densities. Note that the filament length coincides with distance of the filament pointed ends from the interface. In addition, we define

$$B = \sum_{n=1}^{\infty} [P(n) + R(n) + C(n)]$$

as the total amount of barbed ends per segment length. The dynamics of the filament state variables is governed by

$$\begin{aligned}
\frac{\partial B}{\partial t} &= k_B \mathcal{BC} \cdot B + k_N G(1)^2 - k_V P(2) - k_D C(1) \\
\frac{\partial P}{\partial t}(n) &= k_V \Delta_n^f P(n) - k_U G(1) \cdot \Delta_n^b P(n) + k_D C(n) && n > 2 \\
\frac{\partial P}{\partial t}(2) &= k_V \Delta_n^f P(2) - k_U G(1) \cdot P(2) + k_N G(1)^2 + k_D C(2) \\
\frac{\partial R}{\partial t}(n) &= -k_U G(1) \cdot \Delta_n^b R(n) - k_C Cor(n) \cdot R(n) && n > 1 \\
\frac{\partial R}{\partial t}(1) &= -k_U G(1) \cdot R(1) - k_C Cor(1) \cdot R(1) + k_B \mathcal{BC} \cdot B \\
\frac{\partial C}{\partial t}(n) &= -k_U G(1) \cdot \Delta_n^b C(n) + k_C Cor(n) \cdot R(n) - k_D C(n) && n > 1 \\
\frac{\partial C}{\partial t}(1) &= -k_U G(1) \cdot C(1) + k_C Cor(1) \cdot R(1) - k_D C(1)
\end{aligned}$$

where $\Delta_n^f F(n) = F(n+1) - F(n)$, $\Delta_n^b F(n) = F(n) - F(n-1)$ are forward and backward differences in n. $\mathcal{BC}$ is the density of the membrane-bound branching complex, whose evolution is partly determined by intracellular signaling and will be later specified in the full model. Note that, unlike the dynamics for actin filaments *in vitro* [86], here we do not require *de novo* actin filaments to form a trimer before becoming stabilized. This is reasonable for the actin activity *in vivo*, especially in nucleation of membrane-anchored filaments which is assisted by membrane-bound proteins. The dynamics of state variables for Arp2/3, coronin, and G-actin are described by

$$\begin{aligned}
\frac{\partial G}{\partial t}(k) &= \frac{D_g}{\delta^2} \Delta_k^2 G(k) + k_V P(k) && k \geq 2 \\
\frac{\partial G}{\partial t}(1) &= \frac{D_g}{\delta^2} \Delta_k^f G(1) + k_V P(2) + k_D C(1) - \Phi(G(1))
\end{aligned}$$

$$
\begin{aligned}
&\quad - 2k_N G(1)^2 - k_U G(1)\cdot B \\
\frac{\partial Arp}{\partial t}(k) &= \frac{D_{arp}}{\delta^2}\Delta_k^2 Arp(k) + k_C Cor(k)\cdot R(k) && k>1 \\
\frac{\partial Arp}{\partial t}(1) &= \frac{D_{arp}}{\delta^2}\Delta_k^f Arp(1) - \Psi(Arp(1)) + k_C Cor(1)\cdot R(1) \\
\frac{\partial Cor}{\partial t}(k) &= \frac{D_{cor}}{\delta^2}\Delta_k^2 Cor(k) + k_D C(k) - k_C Cor(k)\cdot R(k) && k>1 \\
\frac{\partial Cor}{\partial t}(1) &= \frac{D_{cor}}{\delta^2}\Delta_k^f Cor(1) + k_D C(1) - k_C Cor(1)\cdot R(1)
\end{aligned}
$$

where $\Delta_k^2 F(k) = F(k+1) - 2F(k) + F(k-1)$ is a $2nd$-order diffrernce in k. Φ and Ψ are consumption of G-actin and Arp2/3 for formation of the branching complex respectively. The description of the branching complex depends on signaling and will be defined later.

It is straightforward to check consistency of the free barbed ends

$$\frac{\partial B}{\partial t} = \sum_{n=1}^{\infty}\left[\frac{\partial P}{\partial t}(n) + \frac{\partial R}{\partial t}(n) + \frac{\partial C}{\partial t}(n)\right]$$

and that the total amount of actin subunits is conserved, i.e.

$$\frac{\partial}{\partial t}\sum_{n=1}^{\infty}[n(P(n)+R(n)+C(n)) + G(n)] = k_B\mathcal{BC}\cdot B - \Phi(G(1))$$

Similarly, Arp2/3 and coronin are conserved

$$
\begin{aligned}
\frac{\partial}{\partial t}\sum_{n=1}^{\infty}[R(n) + Arp(n)] &= k_B\mathcal{BC}\cdot B - \Psi(Arp(1)) \\
\frac{\partial}{\partial t}\sum_{n=1}^{\infty}[C(n) + Cor(n)] &= 0
\end{aligned}
$$

The conservation of molecules ensures consistency of the model and is essential for long-time simulations.

Discrete model with capping

In this model, irreversible capping of barbed ends at the interface is introduced. Capped filaments are lifted at the polymerization rate by uncapped filaments whose connection is assumed. We also assume that the complex between G-actin and capping protein dissolves instantenously. Because of lifting, both location of barbed ends and filament length are needed to describe states for capped filaments. They are denoted by $\hat{P}(n,k), \hat{R}(n,k)$, and $\hat{C}(n,k)$ where $n\delta$ is the filament length and $k\delta$ is the barbed-end vertical position. For example,

$$\hat{P}(n,k) = \frac{1}{\delta^2}\int_{(n-1)\delta}^{n\delta}\int_{(k-1)\delta}^{k\delta} \hat{p}(l,z)\ dzdl.$$

The dynamics of the filament state variables is governed by

Uncapped filaments

$$\begin{aligned}
\frac{\partial B}{\partial t} &= k_B\mathcal{BC}\cdot B + k_N G(1)^2 - k_V P(2) - k_D C(1) - k_{CP}Cap(1)\cdot B \\
\frac{\partial P}{\partial t}(n) &= k_V\Delta_n^f P(n) - k_U G(1)\cdot\Delta^b P(n) + k_D C(n) - k_{CP}Cap(1)\cdot P(n) && n>2 \\
\frac{\partial P}{\partial t}(2) &= k_V\Delta_n^f P(2) - k_U G(1)\cdot P(2) + k_N G(1)^2 + k_D C(2) - k_{CP}Cap(1)\cdot P(2) \\
\frac{\partial R}{\partial t}(n) &= -k_U G(1)\cdot\Delta_n^b R(n) - k_C Cor(n)\cdot R(n) - k_{CP}Cap(1)\cdot R(n) && n>1 \\
\frac{\partial R}{\partial t}(1) &= -k_U G(1)\cdot R(1) - k_C Cor(1)\cdot R(1) + k_B\mathcal{BC}\cdot B - k_{CP}Cap(1)\cdot R(1) \\
\frac{\partial C}{\partial t}(n) &= -k_U G(1)\cdot\Delta_n^b C(n) + k_C Cor(n)\cdot R(n) - k_D C(n) - k_{CP}Cap(1)\cdot C(n) && n>1 \\
\frac{\partial C}{\partial t}(1) &= -k_U G(1)\cdot C(1) + k_C Cor(1)\cdot R(1) - k_D C(1) - k_{CP}Cap(1)\cdot C(1)
\end{aligned}$$

Capped filaments

$$\frac{\partial \hat{B}}{\partial t}(k) = -k_U G(1)\cdot\Delta_k^b\hat{B}(k) - k_V\hat{P}(2,k) - k_D\hat{C}(k,1) \qquad k>1$$

$$\frac{\partial \hat{B}}{\partial t}(1) = -k_U G(1) \cdot \hat{B}(1) - k_V \hat{P}(2,1) - k_D \hat{C}(1,1) + k_{CP} Cap(1) \cdot B$$

$$\frac{\partial \hat{P}}{\partial t}(n,k) = k_V \Delta_n^f \hat{P}(n,k) - k_U G(1) \cdot \Delta_k^b \hat{P}(n,k) + k_D \hat{C}(n,k) \qquad n \geq 2, k > 1$$

$$\frac{\partial \hat{P}}{\partial t}(n,1) = k_V \Delta_n^f \hat{P}(n,1) - k_U G(1) \cdot \hat{P}(n,1) + k_D \hat{C}(n,1) + k_{CP} Cap(1) \cdot P(n) \qquad n \geq 2$$

$$\frac{\partial \hat{R}}{\partial t}(n,k) = -k_U G(1) \cdot \Delta_k^b \hat{R}(n,k) - k_C Cor(n+k-1) \cdot \hat{R}(n,k) \qquad n \geq 1, k > 1$$

$$\frac{\partial \hat{R}}{\partial t}(n,1) = -k_U G(1) \cdot \hat{R}(n,1) - k_C Cor(n) \cdot \hat{R}(n,1) + k_{CP} Cap(1) \cdot R(n) \qquad n \geq 1$$

$$\frac{\partial \hat{C}}{\partial t}(n,k) = -k_U G(1) \cdot \Delta_k^b \hat{C}(n,k) + k_C Cor(n+k-1) \cdot \hat{R}(n,k) - k_D \hat{C}(n,k) \qquad n \geq 1, k > 1$$

$$\frac{\partial \hat{C}}{\partial t}(n,1) = -k_U G(1) \cdot \hat{C}(n,1) + k_C Cor(n) \cdot \hat{R}(n,1) - k_D \hat{C}(n,1) + k_{CP} Cap(1) \cdot C(n) \qquad n \geq 1$$

while state variables for G-actin, Arp2/3, coronin, and capping protein are described by

$$\frac{\partial G}{\partial t}(k) = \frac{D_g}{\delta^2} \Delta_k^2 G(k) + k_V \left(\hat{P}(2,k) + \hat{P}(2,k-1) + P(k) \right) + k_D \hat{C}(1,k) + k_V \sum_{n=3}^{k} \hat{P}(n, k-n+1) \qquad k \geq 2$$

$$\frac{\partial G}{\partial t}(1) = \frac{D_g}{\delta^2} \Delta_k^f G(1) + k_V \left(\hat{P}(2,1) + P(2) \right) + k_D \left(\hat{C}(1,1) + C(1) \right) - \Phi\left(G(1)\right) - 2k_N G(1)^2 - k_U G(1) \cdot B$$

$$\frac{\partial Cap}{\partial t}(k) = \frac{D_{cap}}{\delta^2} \Delta_k^2 Cap(k) + k_V \hat{P}(2,k) + k_D \hat{C}(1,k) \qquad k > 1$$

$$\frac{\partial Cap}{\partial t}(1) = \frac{D_{cap}}{\delta^2} \Delta_k^f Cap(1) - k_{CP} Cap(1) \cdot B + k_V \hat{P}(2,1) + k_D \hat{C}(1,1)$$

$$\frac{\partial Arp}{\partial t}(k) = \frac{D_{arp}}{\delta^2} \Delta_k^2 Arp(k) + k_C Cor(k) \cdot \left(R(k) + \sum_{n=1}^{k} \hat{R}(n, k-n+1) \right) \qquad k > 1$$

$$\frac{\partial Arp}{\partial t}(1) = \frac{D_{arp}}{\delta^2} \Delta_k^f Arp(1) - \Psi(Arp(1)) + k_C Cor(1) \cdot \left(R(1) + \hat{R}(1,1) \right)$$

$$\frac{\partial Cor}{\partial t}(k) = \frac{D_{cor}}{\delta^2} \Delta_k^2 Cor(k) + k_D \left(C(k) + \sum_{n=1}^{k} \hat{C}(n, k-n+1) \right)$$

$$- k_C Cor(k) \cdot \left(R(k) + \sum_{n=1}^{k} \hat{R}(n, k-n+1) \right) \qquad k > 1$$

$$\frac{\partial Cor}{\partial t}(1) = \frac{D_{cor}}{\delta^2} \Delta_k^f Cor(1) + k_D \left(C(1) + \hat{C}(1,1) \right) - k_C Cor(1) \cdot \left(R(1) + \hat{R}(1,1) \right)$$

Note that the equation for $\hat{B}$ is redundant and can be omitted.

Similar to the case without capping, it is straightforward to check that

$$\frac{\partial \hat{B}}{\partial t}(k) = \sum_{n=1}^{\infty} \left[\frac{\partial \hat{P}}{\partial t}(n,k) + \frac{\partial \hat{R}}{\partial t}(n,k) + \frac{\partial \hat{C}}{\partial t}(n,k) \right]$$

and that total actin subunits, Arp2/3, coronin, and capping protein are conserved.

$$\frac{\partial}{\partial t} \left[\sum_{n=1}^{\infty} n(P(n) + R(n) + C(n)) + \sum_{k=1}^{\infty} \left(G(k) + \sum_{n=1}^{\infty} n \left(\hat{P}(n,k) + \hat{R}(n,k) + \hat{C}(n,k) \right) \right) \right] = k_B \mathcal{BC} \cdot B - \Phi(G(1))$$

$$\frac{\partial}{\partial t} \left[\sum_{n=1}^{\infty} R(n) + \sum_{k=1}^{\infty} \left(Arp(k) + \sum_{n=1}^{\infty} \hat{R}(n,k) \right) \right] = k_B \mathcal{BC} \cdot B - \Psi(Arp(1))$$

$$\frac{\partial}{\partial t} \left[\sum_{n=1}^{\infty} C(n) + \sum_{k=1}^{\infty} \left(Cor(k) + \sum_{n=1}^{\infty} \hat{C}(n,k) \right) \right] = 0$$

$$\frac{\partial}{\partial t} \left[\sum_{k=1}^{\infty} \left(Cap(k) + \sum_{n=1}^{\infty} \left(\hat{P}(n,k) + \hat{R}(n,k) + \hat{C}(n,k) \right) \right) \right] = 0$$

4.1.2 Continuous models

Continuous model without capping

We first obtain a continuous model without capping. In the discrete description, $F(n)$ stands for an average concentration in the interval $l \in [(n-1)\delta, n\delta)$. So continuous

concentration f satisfies

$$F(n) = \frac{1}{\delta}\int_{(n-1)\delta}^{n\delta} f(l)\ dl.$$

We make an additional assumption that concentrations in the continuous models are smooth so that we can use Taylor expansions. Now

$$\begin{aligned}
F(n) &= f(s) + \mathcal{O}(\delta)\\
\Delta_n^f F(n) &= \frac{1}{\delta}\int_{(n-1)\delta}^{n\delta}\left(\delta\frac{\partial f}{\partial l}(s) + \frac{\delta^2}{2}\frac{\partial^2 f}{\partial l^2}(s) + \mathcal{O}(\delta^3)\right) dl = \delta\frac{\partial f}{\partial l}(s) + \frac{\delta^2}{2}\frac{\partial^2 f}{\partial l^2}(s) + \mathcal{O}(\delta^2)\\
\Delta_n^b F(n) &= \frac{1}{\delta}\int_{(n-1)\delta}^{n\delta}\left(\delta\frac{\partial f}{\partial l}(s) - \frac{\delta^2}{2}\frac{\partial^2 f}{\partial l^2}(s) + \mathcal{O}(\delta^3)\right) dl = \delta\frac{\partial f}{\partial l}(s) - \frac{\delta^2}{2}\frac{\partial^2 f}{\partial l^2}(s) + \mathcal{O}(\delta^2)\\
\Delta_n^2 F(n) &= \frac{1}{\delta}\int_{(n-1)\delta}^{n\delta}\left(\delta^2\frac{\partial^2 f}{\partial l^2}(s) + \mathcal{O}(\delta^3)\right) dl = \delta^2\frac{\partial^2 f}{\partial l^2}(s) + \mathcal{O}(\delta^3)
\end{aligned}$$

for each $s \in [(n-1)\delta, n\delta)$ where δ is assumed to be small compared to the characteristic length of actin wave structures. The discrete equations for filaments become

$$\begin{aligned}
\frac{\partial p}{\partial t}(s) &= (\delta k_V)\left(\frac{\partial p}{\partial l}(s) + \frac{\delta}{2}\frac{\partial^2 p}{\partial l^2}(s)\right) - (\delta k_U)g(0)\cdot\left(\frac{\partial p}{\partial l}(s) - \frac{\delta}{2}\frac{\partial^2 p}{\partial l^2}(s)\right) + k_D c(s) + \mathcal{O}(\delta)\\
\frac{\partial r}{\partial t}(s) &= -(\delta k_U)g(0)\cdot\left(\frac{\partial r}{\partial l}(s) - \frac{\delta}{2}\frac{\partial^2 r}{\partial l^2}(s)\right) - k_C cor(s)\cdot r(s) + \mathcal{O}(\delta)\\
\frac{\partial c}{\partial t}(s) &= -(\delta k_U)g(0)\cdot\left(\frac{\partial c}{\partial l}(s) - \frac{\delta}{2}\frac{\partial^2 c}{\partial l^2}(s)\right) + k_C cor(s)\cdot r(s) - k_D c(s) + \mathcal{O}(\delta)
\end{aligned}$$

for $s \in [(n-1)\delta, n\delta)\,,\ n > 2$. Recognizing $k_v = \delta k_V$ and $k_u = \delta k_U$ as shrinking and elongation (per subunit density) rates of actin filaments, we take the zero-order approximation of the above equations to obtain evolution equations for the actin filaments. To obtain boundary conditions for the filament densities, we model the evolution of the short filaments with length 2 or less, which have different dynamics, seperately with discrete densities and use their polymerization fluxes as the boundary conditions. In particular, by taking $l' = l - 3\delta$, we have the following equations, for $l' \geq 0$,

$$\frac{\partial p}{\partial t}(l') = k_v\left(\frac{\partial p}{\partial l'}(l') + \frac{\delta}{2}\frac{\partial^2 p}{\partial l'^2}(l')\right) - k_u g(0)\cdot\left(\frac{\partial p}{\partial l'}(l') - \frac{\delta}{2}\frac{\partial^2 p}{\partial l'^2}(l')\right) + k_D c(l')$$

$$\frac{\partial r}{\partial t}(l') = -k_u g(0) \cdot \left(\frac{\partial r}{\partial l'}(l') - \frac{\delta}{2} \frac{\partial^2 r}{\partial l'^2}(l') \right) - k_C cor(l') \cdot r(l')$$
$$\frac{\partial c}{\partial t}(l') = -k_u g(0) \cdot \left(\frac{\partial c}{\partial l'}(l') - \frac{\delta}{2} \frac{\partial^2 c}{\partial l'^2}(l') \right) + k_C cor(l') \cdot r(l') - k_D c(l')$$

Filaments of length 3 are assumed to equilibrate quickly to their pseudo steady states

$$p_3 = \delta p(0), \qquad r_3 = \delta r(0), \qquad c_3 = \delta c(0)$$

while coronin binding of r_3 and debranching of c_3 are neglected. The short filaments are defined as

$$p_2 = \delta P(2), \qquad r_1 = \delta R(1), \qquad r_2 = \delta R(2), \qquad c_1 = \delta C(1), \qquad c_2 = \delta C(2)$$

and the boundary conditions are obtained from the fluxes between filaments of length 3 and dimers. From this point, we use l for l' unless it is explicitly noted. Within this setting, the continuous density of uncapped filaments and the amount of short uncapped filaments are given by

$$\mathcal{L}(l) = p(l) + r(l) + c(l)$$
$$\mathcal{S} = \mathcal{S}_1 + \mathcal{S}_2 + \mathcal{S}_3$$

where

$$\mathcal{S}_1 = r_1 + c_1$$
$$\mathcal{S}_2 = p_2 + r_2 + c_2$$
$$\mathcal{S}_3 = p_3 + r_3 + c_3$$

are the total amount of filaments of length 1, length 2, and length 3 respectively. Note that our pseudo steady-state assumption leads to $\dot{\mathcal{S}}_3 = 0$ in the time scale of interest. The total amount of barbed ends is

$$b = \delta B = \mathcal{S} + \int_0^\infty \mathcal{L}(l)\ dl.$$

Using the zero-order approximation, we have ordinary differential equations for the short filaments

$$\begin{aligned}
\frac{\partial p_2}{\partial t} &= k_v p(0) - k_V p_2 - k_U g(0) \cdot p_2 + k_n g(0)^2 + k_D c_2 \\
\frac{\partial r_1}{\partial t} &= -k_U g(0) \cdot r_1 - k_C cor(0) \cdot r_1 + \frac{1}{\delta} k_B \boldsymbol{bc} \cdot b \\
\frac{\partial r_2}{\partial t} &= -k_U g(0) \cdot (r_2 - r_1) - k_C cor(0) \cdot r_2 \\
\frac{\partial c_1}{\partial t} &= -k_U g(0) \cdot c_1 + k_C cor(0) \cdot r_1 - k_D c_1 \\
\frac{\partial c_2}{\partial t} &= -k_U g(0) \cdot (c_2 - c_1) + k_C cor(0) \cdot r_2 - k_D c_2
\end{aligned}$$

while the boundary conditions for the long filaments are

$$\begin{aligned}
(k_u g(0) - k_v) p(0) - \frac{\delta}{2}(k_u g(0) + k_v) \frac{\partial p}{\partial l}(0) &= k_U g(0) \cdot p_2 - k_v p(0) \\
k_u g(0) \cdot r(0) - \frac{\delta}{2} k_u g(0) \cdot \frac{\partial r}{\partial l}(0) &= k_U g(0) \cdot r_2 \\
k_u g(0) \cdot c(0) - \frac{\delta}{2} k_u g(0) \cdot \frac{\partial c}{\partial l}(0) &= k_U g(0) \cdot c_2
\end{aligned}$$

where $\boldsymbol{bc} = \delta \mathcal{BC}$ is the amount of the branching complex at the membrane and $k_n = \delta k_N$.

Similarly, the zero-order approximation to the discrete equations of free molecules yields

$$\begin{aligned}
\frac{\partial g}{\partial t}(z') &= D_g \frac{\partial^2 g}{\partial z'^2}(z') + k_V p(z') \\
\frac{\partial arp}{\partial t}(z') &= D_{arp} \frac{\partial^2 arp}{\partial z'^2}(z') + k_C cor(z') \cdot r(z')
\end{aligned}$$

$$\frac{\partial cor}{\partial t}(z') = D_{cor}\frac{\partial^2 cor}{\partial z'^2}(z') + k_D c(z') - k_C cor(z') \cdot r(z')$$

for $z' > 0$, where $z' = z - 3\delta$. We now replace z' by z unless otherwise noted. To simplify the system, the amount of these molecules in the region $k \leq 3$ is assumed to be in the steady state and their consumption and production fluxes are used for boundary conditions

$$\begin{aligned}
-D_g\frac{\partial g}{\partial z}(0) &= 2k_V p_2 + k_v p(0) + k_D c_1 - \phi(g(0)) - 2k_n g(0)^2 - k_U g(0) \cdot b \\
-D_{arp}\frac{\partial arp}{\partial z}(0) &= -\psi(arp(0)) + k_C cor(0) \cdot (r_1 + r_2) \\
-D_{cor}\frac{\partial cor}{\partial z}(0) &= k_D\,(c_1 + c_2) - k_C cor(0) \cdot (r_1 + r_2)
\end{aligned}$$

where $\phi(g(0)) = \delta\Phi(G(1)) + o(\delta)$ and $\psi(arp(0)) = \delta\Psi(Arp(1)) + o(\delta)$. However, the total amount of actin is not preserved in this system because contributions from the second-order derivative terms (which are first-order terms in δ) in filament equations are not accounted for in the equations for G-actin. In addition, the consumption of G-actin by polymerization of $\mathcal{S}_3$ is already incorporated into the fluxes because of the pseudo steady-state assumption. To balance these contributions, correction terms for consumption and production by the second-order terms at barbed-end and pointed-end locations are introduced while the consumption by $\mathcal{S}_3$ polymerization is removed to avoid double counting.

$$\begin{aligned}
\frac{\partial g}{\partial t}(z) &= D_g\frac{\partial^2 g}{\partial z^2}(z) + k_V p(z) + \frac{k_v}{2}\frac{\partial p}{\partial l}(z) \\
-D_g\frac{\partial g}{\partial z}(0) &= 2k_V p_2 + k_v p(0) + k_D c_1 - \phi(g(0)) - 2k_n g(0)^2 - k_U g(0) \cdot (b - \mathcal{S}_3) \\
&\quad + \frac{k_u}{2} g(0) \cdot (\mathcal{L}(\infty) - \mathcal{L}(0))
\end{aligned}$$

with $\mathcal{L}(\infty) = p(\infty) + r(\infty) + c(\infty) = 0$. A thorough analysis for these correction terms will be given later in this section.

In summary, we have obtained a set of partial differential equations for the actin

structure and directly related molecules in the case without capping as an approximation of the discrete equations. The model is one-dimensional and assumes an infinite spatial domain. It can be shown that this model also conserves the total amount of actin, Arp2/3, and coronin. Proposition 2 establishes conservation of actin in a finite domain.

Restriction of the spatial domain to an interval is done by imposing no-flux boundary conditions in both filaments and diffusing molecules at the maximum length. Moreover, the model can be easily extended to two- and three-asdimensional spatial domains by allowing lateral diffusion of free molecules with no flux at the boundary.

A rectangular spatial domain $\Omega^{x,z} = \{(x,z) : 0 \le x \le L_x, 0 \le z \le L_z\}$ leads to a filament domain $\Omega^{x,l} = \{(x,l) : 0 \le x \le L_x, 0 \le l \le L_z\}$ where pointed ends of filaments are located at $(x,z) = (x,l)$. Taking $\Omega = \Omega^{x,z} = \Omega^{x,l}$, we have

$$\begin{aligned}
\frac{\partial p}{\partial t}(x,l) + \frac{\partial}{\partial l}\Bigg[& \left(k_u g(x,0) - k_v\right) p(x,l) \\
& - \frac{\delta}{2}\left(k_u g(x,0) + k_v\right) \frac{\partial p}{\partial l}(x,l)\Bigg] = k_D c(x,l) \\
\frac{\partial r}{\partial t}(x,l) + \frac{\partial}{\partial l}\left[k_u g(x,0)\cdot r(x,l) - \frac{\delta}{2} k_u g(x,0)\cdot \frac{\partial r}{\partial l}(x,l)\right] &= -k_C cor(x,l)\cdot r(x,l) \\
\frac{\partial c}{\partial t}(x,l) + \frac{\partial}{\partial l}\left[k_u g(x,0)\cdot c(x,l) - \frac{\delta}{2} k_u g(x,0)\cdot \frac{\partial c}{\partial l}(x,l)\right] &= k_C cor(x,l)\cdot r(x,l) - k_D c(x,l) \\
\frac{\partial g}{\partial t}(x,z) - D_g\left(\frac{\partial^2}{\partial x^2} + \frac{\partial^2}{\partial z^2}\right) g(x,z) &= k_V p(x,z) + \frac{k_v}{2}\frac{\partial p}{\partial l}(x,z) \\
\frac{\partial arp}{\partial t}(x,z) - D_{arp}\left(\frac{\partial^2}{\partial x^2} + \frac{\partial^2}{\partial z^2}\right) arp(x,z) &= k_C cor(x,z)\cdot r(x,z) \\
\frac{\partial cor}{\partial t}(x,z) - D_{cor}\left(\frac{\partial^2}{\partial x^2} + \frac{\partial^2}{\partial z^2}\right) cor(x,z) &= k_D c(x,z) - k_C cor(x,z)\cdot r(x,z)
\end{aligned}$$

in Ω with boundary fluxes

$$\begin{aligned}
& \left(k_u g(x,0) - k_v\right) p(x,0) \\
& \quad - \frac{\delta}{2}\left(k_u g(x,0) + k_v\right)\frac{\partial p}{\partial l}(x,0) = k_U g(x,0)\cdot p_2(x) - k_v p(x,0) \\
& k_u g(x,0)\cdot r(x,0) - \frac{\delta}{2} k_u g(x,0)\cdot \frac{\partial r}{\partial l}(x,0) = k_U g(x,0)\cdot r_2(x) \\
& k_u g(x,0)\cdot c(x,0) - \frac{\delta}{2} k_u g(x,0)\cdot \frac{\partial c}{\partial l}(x,0) = k_U g(x,0)\cdot c_2(x)
\end{aligned}$$

$$
\begin{aligned}
-D_g \frac{\partial g}{\partial z}(x,0) &= 2k_V p_2(x) + k_v p(x,0) + k_D c_1(x) - \phi(x, g(x,0)) \\
&\quad - 2k_n g(x,0)^2 - k_U g(x,0) \cdot (b(x) - \mathcal{S}_3(x)) \\
&\quad + \frac{k_u}{2} g(x,0) \cdot (\mathcal{L}(x, L_z) - \mathcal{L}(x,0)) \\
-D_{arp} \frac{\partial arp}{\partial z}(x,0) &= -\psi(x, arp(x,0)) + k_C cor(x,0) \cdot (r_1(x) + r_2(x)) \\
-D_{cor} \frac{\partial cor}{\partial z}(x,0) &= k_D \left(c_1(x) + c_2(x)\right) - k_C cor(x,0) \cdot (r_1(x) + r_2(x))
\end{aligned}
$$

on $\partial\Omega|_{z=0}$ and no-flux conditions

$$
\begin{aligned}
(k_u g(x,0) - k_v) p(x,z) - \frac{\delta}{2}(k_u g(x,0) + k_v) \frac{\partial p}{\partial l}(x,z) &= 0 \\
k_u g(x,0) \cdot r(x,z) - \frac{\delta}{2} k_u g(x,0) \cdot \frac{\partial r}{\partial l}(x,z) &= 0 \\
k_u g(x,0) \cdot c(x,z) - \frac{\delta}{2} k_u g(x,0) \cdot \frac{\partial c}{\partial l}(x,z) &= 0 \\
-D_g \frac{\partial g}{\partial z}(x,z) &= 0 \\
-D_{arp} \frac{\partial arp}{\partial z}(x,z) &= 0 \\
-D_{cor} \frac{\partial cor}{\partial z}(x,z) &= 0
\end{aligned}
$$

on $\partial\Omega|_{z=L_z} \bigcup \partial\Omega|_{x=0} \bigcup \partial\Omega|_{x=L_x}$. Complementary equations for short filaments are

$$
\begin{aligned}
\frac{\partial p_2}{\partial t}(x) &= k_v p(x,0) - k_V p_2(x) - k_U g(x,0) \cdot p_2(x) + k_n g(x,0)^2 + k_D c_2(x) \\
\frac{\partial r_1}{\partial t}(x) &= -k_U g(x,0) \cdot r_1(x) - k_C cor(x,0) \cdot r_1(x) + \frac{1}{\delta} k_B \mathbf{bc}(x) \cdot b(x) \\
\frac{\partial r_2}{\partial t}(x) &= -k_U g(x,0) \cdot (r_2(x) - r_1(x)) - k_C cor(x,0) \cdot r_2(x) \\
\frac{\partial c_1}{\partial t}(x) &= -k_U g(x,0) \cdot c_1(x) + k_C cor(x,0) \cdot r_1(x) - k_D c_1(x) \\
\frac{\partial c_2}{\partial t}(x) &= -k_U g(x,0) \cdot (c_2(x) - c_1(x)) + k_C cor(x,0) \cdot r_2(x) - k_D c_2(x)
\end{aligned}
$$

in $\Omega^x = \partial\Omega|_{z=0}$ with no diffusion in x and no-flux conditions at the boundaries.

Continuous model with capping

In addition to the species found in the model with no capping, there are capped filaments $\hat{p}, \hat{r}$, and $\hat{c}$ which are two-dimensional filament densities. Under similar assumptions, the continuous model for filament length is obtained by a zero-order approximation of the discrete model. In particular, we have

$$\hat{\mathcal{L}}(l,z) = \hat{p}(l,z) + \hat{r}(l,z) + \hat{c}(l,z)$$
$$\hat{\mathcal{S}}(z) = \hat{r}_1(z) + \hat{c}_1(z) + \hat{p}_2(z) + \hat{r}_2(z) + \hat{c}_2(z) + \hat{p}_3(z) + \hat{r}_3(z) + \hat{c}_3(z)$$

for the density of long capped filaments and the density of short capped filaments. Because $\hat{p}, \hat{r}$, and $\hat{c}$ are two-dimensional densities, the 3δ offset is applied only to the filament length l and not to the barbed-end location z.Analogously,

$$\hat{\mathcal{S}}_1(z) = \hat{r}_1(z) + \hat{c}_1(z)$$
$$\hat{\mathcal{S}}_2(z) = \hat{p}_2(z) + \hat{r}_2(z) + \hat{c}_2(z)$$
$$\hat{\mathcal{S}}_3(z) = \hat{p}_3(z) + \hat{r}_3(z) + \hat{c}_3(z)$$

denote the density of the short filaments of various length. As for uncapped filaments, we assume that $\hat{p}_3, \hat{r}_3$, and $\hat{c}_3$ are in the pseudo steady state. Furthermore, the capping of p_3, r_3, c_3 and the vertical fluxes of $\hat{p}_3, \hat{r}_3$, $\hat{c}_3$ are neglected so that

$$\hat{p}_3(z) = \delta\hat{p}(0,z), \qquad \hat{r}_3(z) = 0, \qquad \hat{c}_3(z) = 0$$

and $\hat{\mathcal{S}}_3(z) = \delta\hat{p}(0,z)$ with

$$-k_u g(0)\frac{\partial\hat{\mathcal{S}}_3}{\partial z}(z) + \frac{\delta}{2}k_u g(0)\frac{\partial^2\hat{\mathcal{S}}_3}{\partial z^2}(z) = 0$$

for all $z \in [0, L_z]$. The density of barbed ends at each z is

$$\hat{b}(z) = \hat{\mathcal{S}}(z) + \int_0^\infty \hat{\mathcal{L}}(l, z)\ dl$$

where

$$\hat{B}(k) = \frac{1}{\delta} \int_{(k-1)\delta}^{k\delta} b(z)\ dz.$$

The system is then restricted to a finite domain and lateral diffusion is incorporated. The model includes equations for capped filaments, uncapped filaments, and diffusable molecules.

In two spatial dimensions, a rectangular cell of width L_x and height L_z leads to a spatial domain $\Omega^{x,z} = \{(x, z) : 0 \le x \le L_x, 0 \le z \le L_z\}$ for diffusable molecules and short capped filaments. Uncapped filaments are defined in $\Omega^{x,l} = \{(x, l) : 0 \le x \le L_x, 0 \le l \le L_z\}$ and capped filaments are defined in $\Omega = \left\{(x, l, z) \in \mathbb{R}^3_+ : 0 \le x \le L_x, 0 \le l + z \le L_z\right\}$. Finally, fixed molecules on membrane and short uncapped filaments are defined in $\Omega^x = \{x : 0 \le x \le L_x\}$. To simplify notations, x and t are omitted. In addition, no-flux boundary condition is applied to all equations unless otherwise stated. The equations for the capped filaments are

$$\begin{aligned}
&\frac{\partial \hat{p}}{\partial t}(l, z) + \frac{\partial}{\partial l}\left(-k_v \hat{p}(l, z) - \frac{\delta}{2} k_v \frac{\partial \hat{p}}{\partial l}(l, z)\right) \\
&\qquad + \frac{\partial}{\partial z}\left(k_u g(0) \hat{p}(l, z) - \frac{\delta}{2} k_u g(0) \frac{\partial \hat{p}}{\partial z}(l, z)\right) = k_D \hat{c}(l, z) \\
&\frac{\partial \hat{r}}{\partial t}(l, z) + \frac{\partial}{\partial z}\left(k_u g(0) \cdot \hat{r}(l, z) - \frac{\delta}{2} k_u g(0) \cdot \frac{\partial \hat{r}}{\partial z}(l, z)\right) = -k_C cor(z + l) \cdot \hat{r}(l, z) \\
&\frac{\partial \hat{c}}{\partial t}(l, z) + \frac{\partial}{\partial z}\left(k_u g(0) \cdot \hat{c}(l, z) - \frac{\delta}{2} k_u g(0) \cdot \frac{\partial \hat{c}}{\partial z}(l, z)\right) = k_C cor(z + l) \cdot \hat{r}(l, z) - k_D \hat{c}(l, z)
\end{aligned}$$

in Ω with boundary conditions

$$\begin{aligned}
k_u g(0) \hat{p}(l, 0) - \frac{\delta}{2} k_u g(0) \frac{\partial \hat{p}}{\partial z}(l, 0) &= k_{CP} cap(0) \cdot p(l) \\
k_u g(0) \hat{r}(l, 0) - \frac{\delta}{2} k_u g(0) \frac{\partial \hat{r}}{\partial z}(l, 0) &= k_{CP} cap(0) \cdot r(l)
\end{aligned}$$

$$k_u g(0)\hat{c}(l,0) - \frac{\delta}{2} k_u g(0) \frac{\partial \hat{c}}{\partial z}(l,0) = k_{CP} cap(0) \cdot c(l)$$

on $\partial\Omega|_{z=0}$ and

$$-k_v \hat{p}(0,z) - \frac{\delta}{2} k_v \frac{\partial \hat{p}}{\partial l}(0,z) = -k_v \hat{p}(0,z)$$

on $\partial\Omega|_{l=0}$. Uncapped filaments follow

$$\begin{aligned}
\frac{\partial p}{\partial t}(l) + \frac{\partial}{\partial l}\left((k_u g(0) - k_v)p(l) - \frac{\delta}{2}(k_u g(0) + k_v)\frac{\partial p}{\partial l}(l)\right) &= k_D c(l) - k_{CP} cap(0) \cdot p(l) \\
\frac{\partial r}{\partial t}(l) + \frac{\partial}{\partial l}\left(k_u g(0) \cdot r(l) - \frac{\delta}{2} k_u g(0) \cdot \frac{\partial r}{\partial l}(l)\right) &= -k_C cor(l) \cdot r(l) - k_{CP} cap(0) \cdot r(l) \\
\frac{\partial c}{\partial t}(l) + \frac{\partial}{\partial l}\left(k_u g(0) \cdot c(l) - \frac{\delta}{2} k_u g(0) \cdot \frac{\partial c}{\partial l}(l)\right) &= k_C cor(l) \cdot r(l) - k_D c(l) \\
&\quad - k_{CP} cap(0) \cdot c(l)
\end{aligned}$$

in $\Omega^{x,l} = \partial\Omega|_{z=0}$ with the following influxes on $\partial\Omega^{x,l}|_{l=0}$

$$\begin{aligned}
(k_u g(0) - k_v)p(0) - \frac{\delta}{2}(k_u g(0) + k_v)\frac{\partial p}{\partial l}(0) &= k_U g(0) \cdot p_2 - k_v p(0) \\
k_u g(0) \cdot r(0) - \frac{\delta}{2} k_u g(0) \cdot \frac{\partial r}{\partial l}(0) &= k_U g(0) \cdot r_2 \\
k_u g(0) \cdot c(0) - \frac{\delta}{2} k_u g(0) \cdot \frac{\partial c}{\partial l}(0) &= k_U g(0) \cdot c_2
\end{aligned}$$

Dynamics of short capped filaments and diffusable molecules is described by

$$\begin{aligned}
\frac{\partial \hat{p}_2}{\partial t}(z) + \frac{\partial}{\partial z}\left(k_u g(0) \cdot \hat{p}_2(z) - \frac{\delta}{2} k_u g(0) \cdot \frac{\partial \hat{p}_2}{\partial z}(z)\right) &= -k_V \hat{p}_2(z) + k_v \hat{p}(0,z) + k_D \hat{c}_2(z) \\
\frac{\partial \hat{r}_2}{\partial t}(z) + \frac{\partial}{\partial z}\left(k_u g(0) \cdot \hat{r}_2(z) - \frac{\delta}{2} k_u g(0) \cdot \frac{\partial \hat{r}_2}{\partial z}(z)\right) &= -k_C cor(z) \hat{r}_2(z) \\
\frac{\partial \hat{r}_1}{\partial t}(z) + \frac{\partial}{\partial z}\left(k_u g(0) \cdot \hat{r}_1(z) - \frac{\delta}{2} k_u g(0) \cdot \frac{\partial \hat{r}_1}{\partial z}(z)\right) &= -k_C cor(z) \hat{r}_1(z) \\
\frac{\partial \hat{c}_2}{\partial t}(z) + \frac{\partial}{\partial z}\left(k_u g(0) \cdot \hat{c}_2(z) - \frac{\delta}{2} k_u g(0) \cdot \frac{\partial \hat{c}_2}{\partial z}(z)\right) &= k_C cor(z) \hat{r}_2(z) - k_D \hat{c}_2(z) \\
\frac{\partial \hat{c}_1}{\partial t}(z) + \frac{\partial}{\partial z}\left(k_u g(0) \cdot \hat{c}_1(z) - \frac{\delta}{2} k_u g(0) \cdot \frac{\partial \hat{c}_1}{\partial z}(z)\right) &= k_C cor(z) \hat{r}_1(z) - k_D \hat{c}_1(z)
\end{aligned}$$

$$\begin{aligned}
\frac{\partial g}{\partial t}(z) - D_g \nabla^2 g(z) &= k_V p(z) + \frac{k_v}{2}\frac{\partial p}{\partial l}(z) + \int_0^z k_V \hat{p}(h, z-h)dh \\
&\quad + \int_0^z \frac{k_v}{2}\frac{\partial \hat{p}}{\partial l}(h, z-h)dh + 2k_V \hat{p}_2(z) \\
&\quad + k_v \hat{p}(0,z) + k_D \hat{c}_1(z) \\
\frac{\partial arp}{\partial t}(z) - D_{arp}\nabla^2 arp(z) &= k_C cor(z)\cdot r(z) + k_C cor(z)\cdot(\hat{r}_2(z) + \hat{r}_1(z)) \\
&\quad + \int_0^z k_C cor(z)\hat{r}(h, z-h)dh \\
\frac{\partial cor}{\partial t}(z) - D_{cor}\nabla^2 cor(z) &= k_D\left(c(z) + \int_0^z \hat{c}(h, z-h)dh\right) \\
&\quad - k_C cor(z)\cdot\left(r(z) + \int_0^z \hat{r}(h, z-h)dh\right) \\
&\quad + k_D\left(\hat{c}_2(z) + \hat{c}_1(z)\right) \\
&\quad - k_C cor(z)\cdot(\hat{r}_2(z) + \hat{r}_1(z)) \\
\frac{\partial cap}{\partial t}(z) - D_{cap}\nabla^2 cap(z) &= k_V \hat{p}_2(z) + k_D \hat{c}_1(z)
\end{aligned}$$

in $\Omega^{x,z} = \partial\Omega|_{l=0}$ with boundary conditions

$$\begin{aligned}
k_u g(0)\cdot\hat{p}_2(0) - \frac{\delta}{2}k_u g(0)\cdot\frac{\partial \hat{p}_2}{\partial z}(0) &= k_{CP} cap(0)\cdot p_2 \\
k_u g(0)\cdot\hat{r}_2(0) - \frac{\delta}{2}k_u g(0)\cdot\frac{\partial \hat{r}_2}{\partial z}(0) &= k_{CP} cap(0)\cdot r_2 \\
k_u g(0)\cdot\hat{r}_1(0) - \frac{\delta}{2}k_u g(0)\cdot\frac{\partial \hat{r}_1}{\partial z}(0) &= k_{CP} cap(0)\cdot r_1 \\
k_u g(0)\cdot\hat{c}_2(0) - \frac{\delta}{2}k_u g(0)\cdot\frac{\partial \hat{c}_2}{\partial z}(0) &= k_{CP} cap(0)\cdot c_2 \\
k_u g(0)\cdot\hat{c}_1(0) - \frac{\delta}{2}k_u g(0)\cdot\frac{\partial \hat{c}_1}{\partial z}(0) &= k_{CP} cap(0)\cdot c_1 \\
-D_g\frac{\partial g}{\partial z}(0) &= -k_U g(0)\cdot(b - \mathcal{S}_3) - 2k_n g(0)^2 + 2k_V p_2 + k_v p(0) + k_D c_1 \\
&\quad - \phi(g(0)) + \frac{k_u}{2}g(0)\left(\mathcal{L}(L_z) - \mathcal{L}(0)\right) \\
-D_{arp}\frac{\partial arp}{\partial z}(0) &= k_C cor(0)\cdot r_1 + k_C cor(0)\cdot r_2 - \psi(arp(0)) \\
-D_{cor}\frac{\partial cor}{\partial z}(0) &= k_D c_1 + k_D c_2 - k_C cor(0)\cdot r_1 - k_C cor(0)\cdot r_2 \\
-D_{cap}\frac{\partial cap}{\partial z}(0) &= -k_{CP} cap(0)\cdot b
\end{aligned}$$

on $\partial\Omega^{x,z}|_{z=0}$. Finally, short uncapped filaments and total uncapped filaments are described by

$$\begin{aligned}
\frac{\partial p_2}{\partial t} &= k_n g(0)^2 - k_V p_2 + k_v p(0) - k_U g(0) \cdot p_2 + k_D c_2 - k_{CP} cap(0) \cdot p_2 \\
\frac{\partial r_1}{\partial t} &= \frac{1}{\delta} k_B \boldsymbol{bc} \cdot b - k_C cor(0) \cdot r_1 - k_U g(0) \cdot r_1 - k_{CP} cap(0) \cdot r_1 \\
\frac{\partial r_2}{\partial t} &= k_U g(0) \cdot r_1 - k_U g(0) \cdot r_2 - k_C cor(0) \cdot r_2 - k_{CP} cap(0) \cdot r_2 \\
\frac{\partial c_1}{\partial t} &= k_C cor(0) \cdot r_1 - k_D c_1 - k_U g(0) \cdot c_1 - k_{CP} cap(0) \cdot c_1 \\
\frac{\partial c_2}{\partial t} &= k_C cor(0) \cdot r_2 - k_D c_2 + k_U g(0) \cdot c_1 - k_U g(0) \cdot c_2 - k_{CP} cap(0) \cdot c_2
\end{aligned}$$

in $\Omega^x = \partial\Omega^{x,l}|_{l=0} = \partial\Omega^{x,z}|_{z=0}$ where there is no diffusion in x.

Evolution of integrals and conservation of molecular constituents

This section contains some analytical results on our continuous models of actin waves. The analysis is performed for the case with barbed-end capping, and the results for the case without barbed-end capping is obtained as a special case when $k_{CP} = 0$ and the initial conditions for capped filaments are zero.

The amount of uncapped barbed ends b and the density of capped barbed ends $\hat{b}(z)$ were given as integrals in the continuous model. On a 2D rectangle $\Omega^{x,z} = [0, L_x] \times [0, L_z]$, they are

$$\begin{aligned}
b(x) &= \mathcal{S}(x) + \int_0^{L_z} \mathcal{L}(x, l)\ dl \\
\hat{b}(x, z) &= \hat{\mathcal{S}}(x, z) + \int_0^{L_z - z} \hat{\mathcal{L}}(x, l, z)\ dl
\end{aligned}$$

It is beneficial to obtain equations which describe their evolution, especially since b is used to describe the system dynamics. Solving an equation for b simultaneously

eliminates the need to perform the integration at each time step of the numerical solver. The following result describes how b and $\hat{b}(z)$ evolve in the model with capping on the rectangular domain $\Omega^{x,z}$.

Proposition 3. *Let $\mathbb{b}$ and $\hat{\mathbb{b}}$ be described by*

$$\frac{\partial \mathbb{b}}{\partial t} = \frac{1}{\delta} k_B \mathbb{bc} \cdot \mathbb{b} + k_n g(0)^2 - k_V p_2 - k_D c_1 - k_{CP} cap(0) \cdot (\mathbb{b} - \mathcal{S}_3)$$

and

$$\begin{aligned}\frac{\partial \hat{\mathbb{b}}}{\partial t}(z) + \frac{\partial}{\partial z}\left(k_u g(0) \cdot \hat{\mathbb{b}}(z) - \frac{\delta}{2} k_u g(0) \cdot \frac{\partial \hat{\mathbb{b}}}{\partial z}(z) \right) &= -k_V \hat{p}_2(z) - k_D \hat{c}_1(z) - k_u g(0) \cdot \hat{\mathcal{L}}(L_z - z, z) \\ &\quad + \delta k_u g(0) \frac{\partial \hat{\mathcal{L}}}{\partial z}(L_z - z_1, z_1) \\ &\quad - \frac{\delta}{2} k_u g(0) \frac{\partial \hat{\mathcal{L}}}{\partial l}(L_z - z_1, z_1)\end{aligned}$$

with boundary conditions

$$\begin{aligned} k_u g(0) \cdot \hat{\mathbb{b}}(0) - \frac{\delta}{2} k_u g(0) \cdot \frac{\partial \hat{\mathbb{b}}}{\partial z}(0) &= k_{CP} cap(0) \cdot \mathbb{b} + \frac{\delta}{2} k_u g(0) \cdot \hat{\mathcal{L}}(L_z, 0) && \text{at } z = 0 \\ k_u g(0) \cdot \hat{\mathbb{b}}(L_z) - \frac{\delta}{2} k_u g(0) \cdot \frac{\partial \hat{\mathbb{b}}}{\partial z}(L_z) &= \frac{\delta}{2} k_u g(0) \cdot \hat{\mathcal{L}}(0, L_z) && \text{at } z = L_z \end{aligned}$$

and no fluxes at the lateral boundaries $x = 0$, and $x = L_x$. If $b(x) = \mathbb{b}(x)$ for each x and $\hat{b}(x, z) = \hat{\mathbb{b}}(x, z)$ for each (x,z) at $t = 0$, then $\mathbb{b} \equiv b$ and $\hat{\mathbb{b}} \equiv \hat{b}$ for all $t \geq 0$.

Proof. We first show that $\mathbb{b} \equiv b$. Since,

$$\begin{aligned}\frac{\partial \mathcal{S}}{\partial t} &= \frac{\partial \mathcal{S}_1}{\partial t} + \frac{\partial \mathcal{S}_2}{\partial t} + \frac{\partial \mathcal{S}_3}{\partial t} \\ &= \frac{1}{\delta} k_B \mathbb{bc} \cdot b - k_D c_1 + k_v p(0) - k_V p_2 + k_n g(0)^2 - k_U g(0) \cdot \mathcal{S}_2 - k_{CP} cap(0) \cdot (\mathcal{S} - \mathcal{S}_3)\end{aligned}$$

and

$$\frac{\partial}{\partial t} \int_0^{L_z} \mathcal{L}(l)\, dl = -\int_0^{L_z} k_{CP} cap(0) \cdot \mathcal{L}\, dl - k_u g(0) \int_0^{L_z} \frac{\partial}{\partial l}\left(r(l) - \frac{\delta}{2} \frac{\partial r}{\partial l}(l) \right) dl$$

$$
\begin{aligned}
&- \int_0^{L_z} \frac{\partial}{\partial l}\left((k_u g(0) - k_v)p(l) - \frac{\delta}{2}(k_u g(0) + k_v)\frac{\partial p}{\partial l}(l)\right)\, dl \\
&- k_u g(0) \int_0^{L_z} \frac{\partial}{\partial l}\left(c(l) - \frac{\delta}{2}\frac{\partial c}{\partial l}(l)\right)\, dl \\
= &- \int_0^{L_z} k_{CP} cap(0) \cdot \mathcal{L}\, dl + k_U g(0) \cdot \mathcal{S}_2 - k_v p(0)
\end{aligned}
$$

we have

$$
\begin{aligned}
\frac{\partial b}{\partial t} &= \frac{\partial \mathcal{S}}{\partial t} + \frac{\partial}{\partial t}\int_0^{L_z} \mathcal{L}(l)\, dl \\
&= \frac{1}{\delta} k_B \boldsymbol{b}\boldsymbol{c} \cdot b - k_D c_1 - k_V p_2 + k_n g(0)^2 - k_{CP} cap(0) \cdot (b - \mathcal{S}_3)
\end{aligned}
$$

So,

$$
\frac{\partial}{\partial t}\left[b(x,t) - \boldsymbol{b}(x,t)\right] = \left(\frac{1}{\delta} k_B \boldsymbol{b}\boldsymbol{c}(x,t) - k_{CP} cap(x,0,t)\right) \cdot \left[b(x,t) - \boldsymbol{b}(x,t)\right]
$$

for all $t \geq 0$ and all x. Because $b(x,0) - \boldsymbol{b}(x,0) = 0$, we have $b(x,t) = \boldsymbol{b}(x,t)$ for all $t \geq 0$ and all x.

Similarly, we compute, for each $z_1 \in [0, L_z]$,

$$
\begin{aligned}
\frac{\partial \hat{\mathcal{S}}}{\partial t}(z_1) &= \frac{\partial \hat{\mathcal{S}}_1}{\partial t}(z_1) + \frac{\partial \hat{\mathcal{S}}_2}{\partial t}(z_1) + \frac{\partial \hat{\mathcal{S}}_3}{\partial t}(z_1) \\
&= -k_D \hat{c}_1(z_1) - k_V \hat{p}_2(z_1) + k_v \hat{p}(0, z_1) - k_u g(0)\frac{\partial \hat{\mathcal{S}}}{\partial z}(z_1) + \frac{\delta}{2} k_u g(0)\frac{\partial^2 \hat{\mathcal{S}}}{\partial z^2}(z_1)
\end{aligned}
$$

and

$$
\begin{aligned}
\frac{\partial}{\partial t}\int_0^{L_z - z_1} \hat{\mathcal{L}}(l, z_1) dl &= -k_v \int_0^{L_z - z_1} \frac{\partial}{\partial l}\left(-\hat{p}(l, z_1) - \frac{\delta}{2}\frac{\partial \hat{p}}{\partial l}(l, z_1)\right) dl \\
&\quad - k_u g(0) \int_0^{L_z - z_1} \frac{\partial \hat{\mathcal{L}}}{\partial z}(l, z_1) dl + \frac{\delta}{2} k_u g(0) \int_0^{L_z - z_1} \frac{\partial^2 \hat{\mathcal{L}}}{\partial z^2}(l, z_1) dl \\
&= -k_v \hat{p}(0, z_1) - k_u g(0) \int_0^{L_z - z_1} \frac{\partial \hat{\mathcal{L}}}{\partial z}(l, z_1) dl + \frac{\delta}{2} k_u g(0) \int_0^{L_z - z_1} \frac{\partial^2 \hat{\mathcal{L}}}{\partial z^2}(l, z_1) dl
\end{aligned}
$$

to get

$$\begin{aligned}
\frac{\partial \hat{b}}{\partial t}(z_1) &= \frac{\partial \hat{\mathcal{S}}}{\partial t}(z_1) + \frac{\partial}{\partial t}\int_0^{L_z - z_1} \hat{\mathcal{L}}(l, z_1)\, dl \\
&= -k_D \hat{c}_1(z_1) - k_V \hat{p}_2(z_1) - k_u g(0) \cdot \frac{\partial \hat{b}}{\partial z}(z_1) + \frac{\delta}{2} k_u g(0) \cdot \frac{\partial^2 \hat{b}}{\partial z^2}(z_1) \\
&\quad - k_u g(0) \left(\int_0^{L_z - z_1} \frac{\partial \hat{\mathcal{L}}}{\partial z}(l, z_1)\, dl - \frac{\partial}{\partial z}\int_0^{L_z - z_1} \hat{\mathcal{L}}(l, z_1)\, dl \right) \\
&\quad + \frac{\delta}{2} k_u g(0) \left(\int_0^{L_z - z_1} \frac{\partial^2 \hat{\mathcal{L}}}{\partial z^2}(l, z_1)\, dl - \frac{\partial^2}{\partial z^2}\int_0^{L_z - z_1} \hat{\mathcal{L}}(l, z_1)\, dl \right) \\
&= -k_V \hat{p}_2(z_1) - k_D \hat{c}_1(z_1) - k_u g(0) \cdot \frac{\partial \hat{b}}{\partial z}(z_1) + \frac{\delta}{2} k_u g(0) \cdot \frac{\partial^2 \hat{b}}{\partial z^2}(z_1) \\
&\quad - k_u g(0) \cdot \hat{\mathcal{L}}(L_z - z_1, z_1) + \frac{\delta}{2} k_u g(0) \left(2\frac{\partial \hat{\mathcal{L}}}{\partial z}(L_z - z_1, z_1) - \frac{\partial \hat{\mathcal{L}}}{\partial l}(L_z - z_1, z_1) \right)
\end{aligned}$$

So,

$$\frac{\partial}{\partial t}\left[\hat{b} - \hat{\boldsymbol{b}}\right](x, z, t) = -k_u g(0)\frac{\partial}{\partial z}\left[\hat{b} - \hat{\boldsymbol{b}}\right](x, z, t) + \frac{\delta}{2} k_u g(0)\frac{\partial^2}{\partial z^2}\left[\hat{b} - \hat{\boldsymbol{b}}\right](x, z, t)$$

for all $t \geq 0$ and all x, z. Because $\hat{b}(x, z, 0) - \hat{\boldsymbol{b}}(x, z, 0) = 0$ for all x, z and

$$\begin{aligned}
k_u g(0)\left[\hat{b} - \hat{\boldsymbol{b}}\right](x, 0, t) - \frac{\delta}{2} k_u g(0)\frac{\partial}{\partial z}\left[\hat{b} - \hat{\boldsymbol{b}}\right](x, 0, t) = 0 \\
k_u g(0)\left[\hat{b} - \hat{\boldsymbol{b}}\right](x, L_z, t) - \frac{\delta}{2} k_u g(0)\frac{\partial}{\partial z}\left[\hat{b} - \hat{\boldsymbol{b}}\right](x, L_z, t) = 0
\end{aligned}$$

for all $t > 0$ and for all x, which are easily checked, we have $\hat{b}(x, z, t) = \hat{\boldsymbol{b}}(x, z, t)$ for all $t > 0$ and all $(x, z) \in \Omega^{x,z}$. □

Corollary 1. *The total amount of barbed ends follows*

$$\frac{\partial \boldsymbol{b}}{\partial t} = \frac{1}{\delta} k_B \boldsymbol{b}\boldsymbol{c} \cdot \boldsymbol{b} + k_n g(0)^2 - k_V p_2 - k_D c_1$$

in the case without capping.

Note that although the evolution of b obtained from the explicit calculation and

the differential equation are equivalent, a small discrepency in the initial condition may develop into large difference because of the positive feedback of b onto itself. Therefore, the initial conditions for the system must be choosen carefully.

Another important issue that needs to be addressed is the conservation of physical quantities. Although all molecules are conserved in the discrete models, it is not clear that they are also conserved in the approximation, especially for G-actin, which can become a part of actin filaments. The density of F-actin at (x, z) is given by

$$F(x,z,t) = \frac{1}{\delta}\int_z^{L_z} \mathcal{L}(x,l)\ dl + \frac{1}{\delta}\int_0^z \int_{z-\psi}^{L_z-\psi} \hat{\mathcal{L}}(x,l,\psi)\ dl\ d\psi + 3\int_0^{L_z-z} \hat{\mathcal{L}}(x,l,z)\ dl$$
$$+ \hat{\mathcal{S}}_1(x,z) + 2\hat{\mathcal{S}}_2(x,z) + 3\hat{\mathcal{S}}_3(x,z).$$

Similarly, the density of F-actin localized at the interface is

$$F_{mem}(x,t) = 3\int_0^{L_z} \mathcal{L}(x,l)\ dl + \mathcal{S}_1(x) + 2\mathcal{S}_2(x) + 3\mathcal{S}_3(x).$$

Let $G_{bound}(x,t)$ be the lateral density of actin which is either F-actin or bound to the membrane. Then

$$G_{bound}(x,t) = \int_0^{L_z} F(x,z,t)\ dz + F_{mem}(x,t) + \mathcal{bc}(x,t)$$

and the total amount of actin is the sum of the free G-actin and the sequestered actin

$$G_{total}(t) = \int_0^{L_x} G_{bound}(x,t)\ dx + \int_0^{L_x}\int_0^{L_z} g(x,z,t)\ dz\ dx.$$

The amount of G-actin is conserved when the consumption of g is balanced by the production of G_{bound}.

Proposition 4. *Suppose that the continuous model with capping of actin filaments is*

defined on $\Omega^{x,z}$ *and that*

$$\frac{\partial \mathcal{bc}}{\partial t}(x,t) = -\frac{1}{\delta} k_B \mathcal{bc}(x,t) \cdot b(x,t) + \phi(x, g(x,0,t), t).$$

Then

$$\int_0^{L_z} \left(\frac{\partial g}{\partial t}(x,z,t) - D_g \frac{\partial^2 g}{\partial x^2}(x,z,t) \right) \, dz = -\frac{\partial G_{bound}}{\partial t}(x,t)$$

In particular, $G_{total}(t) = G_{total}(0)$ *for all* $t \geq 0$.

Proof. We compute $\dfrac{\partial G_{bound}}{\partial t}$ by individual terms. First,

$$\begin{aligned}
\frac{\partial}{\partial t} \int_0^{L_z} F(z) \, dz = \frac{1}{\delta} \int_0^{L_z} \int_z^{L_z} \frac{\partial \mathcal{L}}{\partial t}(l) \, dl \, dz + \frac{1}{\delta} \int_0^{L_z} \int_0^{z} \int_{z-\psi}^{L_z - \psi} \frac{\partial \hat{\mathcal{L}}}{\partial t}(l, \psi) \, dl \, d\psi \, dz \\
+ 3 \int_0^{L_z} \int_0^{L_z - z} \frac{\partial \hat{\mathcal{L}}}{\partial t}(l, z) \, dl \, dz + \int_0^{L_z} \left(\frac{\partial \hat{\mathcal{S}}_1}{\partial t}(z) + 2 \frac{\partial \hat{\mathcal{S}}_2}{\partial t}(z) + 3 \frac{\partial \hat{\mathcal{S}}_3}{\partial t}(z) \right) dz
\end{aligned}$$

where

$$\begin{aligned}
\int_0^{L_z} \int_z^{L_z} \frac{\partial \mathcal{L}}{\partial t}(l) \, dl \, dz &= -k_{CP} cap(0) \int_0^{L_z} \int_z^{L_z} \mathcal{L}(l) \, dl \, dz \\
&\quad - \int_0^{L_z} \int_z^{L_z} \frac{\partial}{\partial l} \left((k_u g(0) - k_v) p(l) - \frac{\delta}{2} (k_u g(0) + k_v) \frac{\partial p}{\partial l}(l) \right) \, dl \, dz \\
&\quad - k_u g(0) \int_0^{L_z} \int_z^{L_z} \frac{\partial}{\partial l} \left(r(l) - \frac{\delta}{2} \frac{\partial r}{\partial l}(l) \right) \, dl \, dz \\
&\quad - k_u g(0) \int_0^{L_z} \int_z^{L_z} \frac{\partial}{\partial l} \left(c(l) - \frac{\delta}{2} \frac{\partial c}{\partial l}(l) \right) \, dl \, dz \\
&= -k_{CP} cap(0) \int_0^{L_z} \int_0^{l} \mathcal{L}(l) \, dz \, dl - k_v \int_0^{L_z} \left(p(z) + \frac{\delta}{2} \frac{\partial p}{\partial l}(z) \right) \, dz \\
&\quad + k_u g(0) \int_0^{L_z} \left(\mathcal{L}(z) - \frac{\delta}{2} \frac{\partial \mathcal{L}}{\partial l}(z) \right) \, dz \\
&= -k_{CP} cap(0) \int_0^{L_z} l \mathcal{L}(l) \, dl - k_v \int_0^{L_z} \left(p(z) + \frac{\delta}{2} \frac{\partial p}{\partial l}(z) \right) \, dz \\
&\quad + k_u g(0) \left(b - \mathcal{S} - \frac{\delta}{2} \left(\mathcal{L}(L_z) - \mathcal{L}(0) \right) \right)
\end{aligned}$$

$$\begin{aligned}
\int_0^{L_z}\int_0^{z}\int_{z-\psi}^{L_z-\psi}\frac{\partial\hat{\mathcal{L}}}{\partial t}(l,\psi)\ dl\ d\psi\ dz &= \int_0^{L_z}\int_{\psi}^{L_z}\int_{z-\psi}^{L_z-\psi}\frac{\partial\hat{\mathcal{L}}}{\partial t}(l,\psi)\ dl\ dz\ d\psi \\
&= \int_0^{L_z}\int_0^{L_z-\psi}\int_{\psi}^{\psi+l}\frac{\partial\hat{\mathcal{L}}}{\partial t}(l,\psi)\ dz\ dl\ d\psi \\
&= k_v\int_0^{L_z}\int_0^{L_z-\psi} l\left(\frac{\partial\hat{p}}{\partial l}(l,\psi)+\frac{\delta}{2}\frac{\partial^2\hat{p}}{\partial l^2}(l,\psi)\right)\ dl\ d\psi \\
&\quad - k_u g(0)\int_0^{L_z}\int_0^{L_z-\psi} l\left(\frac{\partial\hat{\mathcal{L}}}{\partial z}(l,\psi)-\frac{\delta}{2}\frac{\partial^2\hat{\mathcal{L}}}{\partial z^2}(l,\psi)\right) dl\ d\psi \\
&= -k_v\int_0^{L_z}\int_0^{L_z-\psi}\left(\hat{p}(l,\psi)+\frac{\delta}{2}\frac{\partial\hat{p}}{\partial l}(l,\psi)\right)\ dl\ d\psi \\
&\quad - k_u g(0)\int_0^{L_z}\int_0^{L_z-l} l\left(\frac{\partial\hat{\mathcal{L}}}{\partial z}(l,\psi)-\frac{\delta}{2}\frac{\partial^2\hat{\mathcal{L}}}{\partial z^2}(l,\psi)\right)\ d\psi\ dl \\
&= -k_v\int_0^{L_z}\int_0^{u}\left(\hat{p}(v,u-v)+\frac{\delta}{2}\frac{\partial\hat{p}}{\partial l}(v,u-v)\right)\ dv\ du \\
&\quad + k_{CP}cap(0)\int_0^{L_z} l\mathcal{L}(l)\ dl
\end{aligned}$$

$$\begin{aligned}
\int_0^{L_z}\int_0^{L_z-z}\frac{\partial\hat{\mathcal{L}}}{\partial t}(l,z)\ dl\ dz &= k_v\int_0^{L_z}\int_0^{L_z-z}\frac{\partial}{\partial l}\left(\hat{p}(l,z)+\frac{\delta}{2}\frac{\partial\hat{p}}{\partial l}(l,z)\right)\ dl\ dz \\
&\quad - k_u g(0)\int_0^{L_z}\int_0^{L_z-z}\frac{\partial}{\partial z}\left(\hat{\mathcal{L}}(l,z)-\frac{\delta}{2}\frac{\partial\hat{\mathcal{L}}}{\partial z}(l,z)\right)\ dl\ dz \\
&= -k_v\int_0^{L_z}\hat{p}(0,z)\ dz \\
&\quad - k_u g(0)\int_0^{L_z}\int_0^{L_z-l}\frac{\partial}{\partial z}\left(\hat{\mathcal{L}}(l,z)-\frac{\delta}{2}\frac{\partial\hat{\mathcal{L}}}{\partial z}(l,z)\right)\ dz\ dl \\
&= -k_v\int_0^{L_z}\hat{p}(0,z)\ dz + k_{CP}cap(0)\int_0^{L_z}\mathcal{L}(l)\ dl
\end{aligned}$$

$$\begin{aligned}
\int_0^{L_z}\left(\frac{\partial\hat{\mathcal{S}}_1}{\partial t}(z)+2\frac{\partial\hat{\mathcal{S}}_2}{\partial t}(z)+3\frac{\partial\hat{\mathcal{S}}_3}{\partial t}(z)\right)\ dz &= \int_0^{L_z}\left(-2k_V\hat{p}_2(z)+2k_v\hat{p}(0,z)-k_D\hat{c}_1(z)\right)\ dz \\
&\quad + k_{CP}cap(0)\cdot(\mathcal{S}_1+2\mathcal{S}_2)
\end{aligned}$$

so

$$\int_0^{L_z} \frac{\partial F}{\partial t}(z)\ dz = \int_0^{L_z} \left[-k_V p(z) - \frac{k_v}{2}\frac{\partial p}{\partial l}(z) - \int_0^z \left(k_V \hat{p}(v, z-v) + \frac{k_v}{2}\frac{\partial \hat{p}}{\partial l}(v, z-v) \right)\ dv \right.$$
$$\left. + 3k_{CP} cap(0) \cdot \mathcal{L}(z) - 2k_V \hat{p}_2(z) - k_v \hat{p}(0,z) - k_D \hat{c}_1(z) \right]\ dz$$
$$+ k_U g(0)\,(b - \mathcal{S}) - \frac{k_u}{2} g(0)\,(\mathcal{L}(L_z) - \mathcal{L}(0)) + k_{CP} cap(0) \cdot (\mathcal{S}_1 + 2\mathcal{S}_2)$$

Next,

$$\frac{\partial F_{mem}}{\partial t} = 3\int_0^{L_z} \frac{\partial \mathcal{L}}{\partial t}(l)\ dl + \frac{\partial \mathcal{S}_1}{\partial t} + 2\frac{\partial \mathcal{S}_2}{\partial t} + 3\frac{\partial \mathcal{S}_3}{\partial t}$$
$$= -3k_{CP} cap(0) \int_0^{L_z} \mathcal{L}(l)\ dl - 3\int_0^{L_z} \frac{\partial}{\partial l}\left((k_u g(0) - k_v) p(l) - \frac{\delta}{2}(k_u g(0) + k_v)\frac{\partial p}{\partial l}(l) \right) dl$$
$$- 3k_u g(0) \int_0^{L_z} \frac{\partial}{\partial l}\left(r(l) - \frac{\delta}{2}\frac{\partial r}{\partial l}(l) \right)\ dl - 3k_u g(0) \int_0^{L_z} \frac{\partial}{\partial l}\left(c(l) - \frac{\delta}{2}\frac{\partial c}{\partial l}(l) \right)\ dl$$
$$+ 2k_n g(0)^2 - 2k_V p_2 + 2k_v p(0) + \frac{1}{\delta} k_B \boldsymbol{bc} \cdot b - k_D c_1 + k_u g(0) \cdot \mathcal{S}_1 - 2k_u g(0) \cdot \mathcal{S}_2$$
$$- k_{CP} cap(0) \cdot (\mathcal{S}_1 + 2\mathcal{S}_2)$$
$$= -3k_{CP} cap(0) \int_0^{L_z} \mathcal{L}(l)\ dl + 2k_n g(0)^2 - 2k_V p_2 - k_v p(0) + \frac{1}{\delta} k_B \boldsymbol{bc} \cdot b - k_D c_1$$
$$+ k_u g(0) \cdot (\mathcal{S}_1 + \mathcal{S}_2) - k_{CP} cap(0) \cdot (\mathcal{S}_1 + 2\mathcal{S}_2)$$

Therefore

$$\frac{\partial G_{bound}}{\partial t} = \int_0^{L_z} \frac{\partial F}{\partial t}(z)\ dz + \frac{\partial F_{mem}}{\partial t} + \frac{\partial \boldsymbol{bc}}{\partial t}$$
$$= \int_0^{L_z} \left[-k_V p(z) - \frac{k_v}{2}\frac{\partial p}{\partial l}(z) - \int_0^z \left(k_V \hat{p}(v, z-v) + \frac{k_v}{2}\frac{\partial \hat{p}}{\partial l}(v, z-v) \right) dv - 2k_V \hat{p}_2(z) \right.$$
$$\left. - k_v \hat{p}(0,z) - k_D \hat{c}_1(z) \right] dz + k_U g(0)\,(b - \mathcal{S}_3) - \frac{k_u}{2} g(0)\,(\mathcal{L}(L_z) - \mathcal{L}(0)) + 2k_n g(0)^2$$
$$- 2k_V p_2 - k_v p(0) - k_D c_1 + \phi(g(0))$$

Next, taking an integral of the equation for g in z, we get

$$\int_0^{L_z} \left(\dot{g}(z) - D_g \frac{\partial^2 g}{\partial x^2}(z) \right)\ dz = \int_0^{L_z} \left(\dot{g}(z) - D_g \nabla^2 g(z) \right)\ dz + \int_0^{L_z} D_g \frac{\partial^2 g}{\partial z^2}(z)\ dz$$

$$
\begin{aligned}
&= \int_0^{L_z} \Big(k_V p(z) + \frac{k_v}{2}\frac{\partial p}{\partial l}(z) + \int_0^z k_V \hat{p}(h, z-h)\ dh \\
&\quad + \int_0^z \frac{k_v}{2}\frac{\partial \hat{p}}{\partial l}(h, z-h)\ dh + 2k_V \hat{p}_2(z) + k_v \hat{p}(0,z) \\
&\quad + k_D \hat{c}_1(z) \Big)\, dz - k_U g(0)\cdot(b - \mathcal{S}_3) - 2k_n g(0)^2 + 2k_V p_2 \\
&\quad + k_v p(0) + k_D c_1 - \phi(g(0)) + \frac{k_u}{2} g(0)\cdot(\mathcal{L}(L_z) - \mathcal{L}(0)) \\
&= -\frac{\partial G}{\partial t}_{bound}
\end{aligned}
$$

The second assertion follows automatically since $\dfrac{\partial g}{\partial x}(0,z) = \dfrac{\partial g}{\partial x}(L_x, z) = 0$ for all z and all $t \geq 0$. □

Corollary 2. *The total amount of G-actin is conserved in the model without capping.*

The above result ensures the conservation of actin in our models. Using the same approach, the conservation of the other molecules can be shown as well.

4.2 Signaling pathway

The activity of PIP_3 is indispensable for formation of actin waves and random protrusions of pseudopods [162, 65]. It is known that Rac, a downstream effector of PIP_3 via its activator RacGEF, activates WASP in *Dictyostelium*. The activated WASP then presumably binds to Arp2/3 and G-actin, leading to nucleation of new branches on the side of existing filaments. The F-actin-dependent spontaneous activity of Ras and PIP_3 was also observed in wild-type cells [162]. These observations suggest that the spontaneous activity of F-actin is a result of the positive feedback between F-actin and PIP_3. A qualitative schematic showing the positive feedback is depicted in Figure 4.1. We hypothesize that this positive feedback is fundamental to the actin waves and will integrate a simplified signaling network into our model.

The signaling network is simplified so that a minimal number of the intermediate

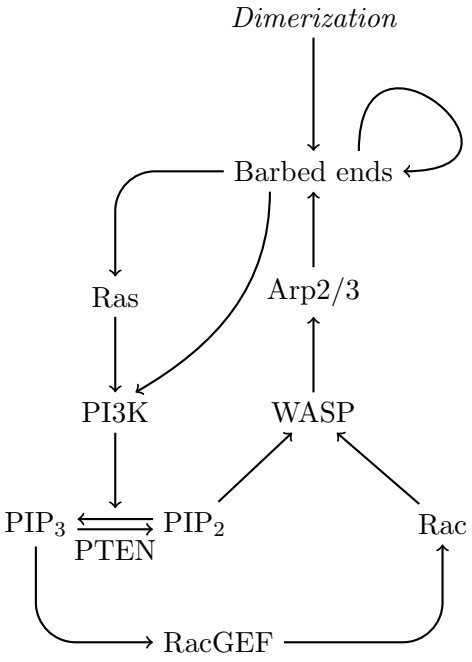

Figure 4.1: A simplified diagram for the feedback between F-actin and PI3K. This diagram shows qualitative relationships between molecular components related to branching of actin filaments.

effectors are included. These molecules are RacGEF, WASP, and Arp2/3. Although WASP is found to localize at the leading edge, it preferentially binds to both PIP_2 and PIP_3 [139]. We make a simplifying assumption that it is uniformly localized on the membrane and its activity solely depends on its activation via RacGEF. Using f^* and $(f * g)$ to denote the activated form of f and a complex between f and g respectively, the simplified signaling network involved in the positive feedback is described by

$$b + racgef \xrightarrow{k_{1f}} b + racgef^* \qquad \text{membrane}$$

$$racgef^* \underset{k_{2r}}{\overset{k_{2f}}{\rightleftharpoons}} racgef \qquad \text{cytosol}$$

$$racgef^* + wasp \xrightarrow{k_{3f}} racgef^* + wasp^* \qquad \text{membrane}$$

$$wasp^* \xrightarrow{k_{4f}} wasp \qquad \text{membrane}$$

$$wasp^* + arp \underset{k_{5r}}{\overset{k_{5f}}{\rightleftharpoons}} (wasp^* * arp) \qquad \text{membrane}$$

$$wasp^* * arp + g \underset{k_{6r}}{\overset{k_{6f}}{\rightleftharpoons}} (wasp^* * arp * g) \qquad \text{membrane}$$

$$(wasp^* * arp * g) + b \xrightarrow{k_{7f}} 2b + wasp^* \qquad \text{membrane}$$

where b denotes membrane-attached barbed ends and g denotes G-actin. The reactions can be described in the context of cell signaling as followed. Free barbed ends serve as scaffolds for membrane activation of RacGEF via Ras and PI3K. The activated RacGEF stimulates releasing of GDP from Rac, allowing its binding of GTP, which leads to WASP activation. Finally, the activated WASP binds to Arp2/3 and G-actin allowing their incorporation to an existing filament, generating a branch whch is a new barbed end.

In the rectangular domain $\Omega^{x,z}$, the activity of effectors in the simplified PI3K feedback loop are described by

$$\frac{\partial racgef}{\partial t}(z) - D_{racgef} \nabla^2 racgef(z) = k_{2f} racgef^*(z) - k_{2r} racgef(z)$$
$$\frac{\partial racgef^*}{\partial t}(z) - D_{racgef^*} \nabla^2 racgef^*(z) = -k_{2f} racgef^*(z) + k_{2r} racgef(z)$$

with boundary conditions

$$-D_{racgef} \frac{\partial racgef}{\partial z}(0) = -k_{1f} racgef(0) \cdot b$$
$$-D_{racgef^*} \frac{\partial racgef^*}{\partial z}(0) = k_{1f} racgef(0) \cdot b$$

on $\partial\Omega^{x,z}|_{z=0}$ and no-flux conditions on the other boundaries. The membrane-bound molecules follows

$$\frac{\partial wasp}{\partial t} = -k_{3f} wasp \cdot racgef^*(0) + k_{4f} wasp^*$$

$$\begin{aligned}
\frac{\partial wasp^*}{\partial t} &= k_{7f}(wasp^* * arp * g) \cdot b + k_{3f} wasp \cdot racgef^*(0) - k_{5f} arp(0) \cdot wasp^* \\
&\quad + k_{5r}(wasp^* * arp) - k_{4f} wasp^* \\
\frac{\partial (wasp^* * arp)}{\partial t} &= -k_{6f} g(0) \cdot (wasp^* * arp) + k_{6r}(wasp^* * arp * g) + k_{5f} arp(0) \cdot wasp^* \\
&\quad - k_{5r}(wasp^* * arp) \\
\frac{\partial (wasp^* * arp * g)}{\partial t} &= -k_{7f}(wasp^* * arp * g) \cdot b + k_{6f} g(0) \cdot (wasp^* * arp) - k_{6r}(wasp^* * arp * g)
\end{aligned}$$

in Ω^x without diffusion in x.

The connection between the signaling pathway and the actin network is via branching by the branching complex $\mathcal{bc} = (wasp^* * arp * g)$, with $k_{7f} = k_B/\delta$, and the activation of $racgef$ by b. In addition, the recruitment fluxes, for formation of the branching complex, of G-actin and Arp2/3 at the membrane are given by

$$\begin{aligned}
\phi(g(0)) &= k_{6f} g(0) \cdot (wasp^* * arp) - k_{6r}(wasp^* * arp * g) \\
\psi(arp(0)) &= k_{5f} arp(0) \cdot wasp^* - k_{5r}(wasp^* * arp)
\end{aligned}$$

4.3 Continuous model for actin waves

In this section, we numerically study activities of the actin waves using a model which combines a continuous model for the actin structure and PIP_3 signaling. The integrated model is then used to study properties of the actin waves and their underlying dynamics.

We assume local transient bursts of F-actin activity as seeds for actin waves. The source of the local F-actin activity could be either connected to cell-substrate adhesion, endocytosis, or merely a stochastic F-actin activity on the membrane. Nevertheless, identification of this origin is beyond the scope of the current work. For practical purposes, we replicate this activity by imposing a local and transient increase in the dimerization rate constant k_N.

4.3.1 Actin-wave model

The model used for simulation is obtained by combining the continuous model for the actin structure without capping activity and the PIP_3 signaling dynamics. The evolution of the total barb-end density at the membrane is incorporated into the model so that explicit integration of filament densities is avoided. The model is also slightly modified by adding an extra G-actin binding step to the membrane before polymerization, nucleation, and branching of actin filaments. This step is intended to capture the effect membrane-bound proteins such as formin and ponticulin, which facilitate polymerization and branching of actin filaments [41, 74], and make the model more realistic. There is no significant difference in the simulation results when compared to the original model with explicit integration for the barb-end density.

Equations

The resulting equations which fully describe the system consist of cytosolic variables described on the entire spatial domain Ω, which may be either two-dimensional (rectangular $[0, L_x]\times[0, L_z]$) or three-dimensional (cube $[0, L_x]\times[0, L_y]\times[0, L_z]$), and membrane variables defined on the bottom boundary $\Omega^0 = \partial\Omega|_{z=0}$. The evolution of the cytosolic variables are described by

$$
\begin{aligned}
\frac{\partial p}{\partial t} + \frac{\partial}{\partial z}\left(\left(k_u g_m - k_v\right) p - \frac{\delta}{2}\left(k_u g_m + k_v\right)\frac{\partial p}{\partial z}\right) &= k_D c \\
\frac{\partial r}{\partial t} + \frac{\partial}{\partial z}\left(k_u g_m \cdot r - \frac{\delta}{2} k_u g_m \cdot \frac{\partial r}{\partial z}\right) &= -k_C cor \cdot r \\
\frac{\partial c}{\partial t} + \frac{\partial}{\partial z}\left(k_u g_m \cdot c - \frac{\delta}{2} k_u g_m \cdot \frac{\partial c}{\partial z}\right) &= k_C cor \cdot r - k_D c \\
\frac{\partial g}{\partial t} - D_g \nabla^2 g &= k_V p + \frac{k_v}{2}\frac{\partial p}{\partial z} \\
\frac{\partial arp}{\partial t} - D_{arp} \nabla^2 arp &= k_C cor \cdot r \\
\frac{\partial cor}{\partial t} - D_{cor} \nabla^2 cor &= k_D c - k_C cor \cdot r
\end{aligned}
$$

$$\frac{\partial racgef}{\partial t} - D_{racgef}\nabla^2 racgef = k_{2f} racgef^* - k_{2r} racgef$$
$$\frac{\partial racgef^*}{\partial t} - D_{racgef^*}\nabla^2 racgef^* = -k_{2f} racgef^* + k_{2r} racgef$$

in Ω. All boundary conditions are specified by fluxes, which are

$$\begin{aligned}
(k_u g_m - k_v)p - \frac{\delta}{2}(k_u g_m + k_v)\frac{\partial p}{\partial z} &= k_U g_m \cdot p_2 - k_v p \\
k_u g_m \cdot r - \frac{\delta}{2} k_u g_m \cdot \frac{\partial r}{\partial z} &= k_U g_m \cdot r_2 \\
k_u g_m \cdot c - \frac{\delta}{2} k_u g_m \cdot \frac{\partial c}{\partial z} &= k_U g_m \cdot c_2 \\
-D_g \frac{\partial g}{\partial z} &= 2k_V p_2 + k_v p + k_D c_1 - k_{8f} g + k_{8r} g_m \\
-D_{arp}\frac{\partial arp}{\partial z} &= -k_{5f} arp \cdot wasp^* + k_{5r}(wasp^* * arp) + k_C cor \cdot (r_1 + r_2) \\
-D_{cor}\frac{\partial cor}{\partial z} &= k_D\,(c_1 + c_2) - k_C cor \cdot (r_1 + r_2) \\
-D_{racgef}\frac{\partial racgef}{\partial z} &= -k_{1f} racgef \cdot \mathcal{b} \\
-D_{racgef^*}\frac{\partial racgef^*}{\partial z} &= k_{1f} racgef \cdot \mathcal{b}
\end{aligned}$$

on $\partial\Omega|_{z=0}$. No-flux conditions are imposed on the other boundaries. The evolution of the one-dimensional variables are described by

$$\begin{aligned}
\frac{\partial \mathcal{b}}{\partial t} &= k_{7f}(wasp^* * arp * g_m) \cdot \mathcal{b} + k_N g_m^2 - k_V p_2 - k_D c_1 \\
\frac{\partial p_2}{\partial t} &= k_v p - k_V p_2 - k_U g_m \cdot p_2 + k_N g_m^2 + k_D c_2 \\
\frac{\partial r_1}{\partial t} &= -k_U g_m \cdot r_1 - k_C cor \cdot r_1 + k_{7f}(wasp^* * arp * g_m) \cdot \mathcal{b} \\
\frac{\partial r_2}{\partial t} &= -k_U g_m \cdot (r_2 - r_1) - k_C cor \cdot r_2 \\
\frac{\partial c_1}{\partial t} &= -k_U g_m \cdot c_1 + k_C cor \cdot r_1 - k_D c_1 \\
\frac{\partial c_2}{\partial t} &= -k_U g_m \cdot (c_2 - c_1) + k_C cor \cdot r_2 - k_D c_2 \\
\frac{\partial wasp}{\partial t} &= -k_{3f} wasp \cdot racgef^* + k_{4f} wasp^* \\
\frac{\partial wasp^*}{\partial t} &= k_{7f}(wasp^* * arp * g_m) \cdot \mathcal{b} + k_{3f} wasp \cdot racgef^* - k_{5f} arp \cdot wasp^* \\
&\quad + k_{5r}(wasp^* * arp) - k_{4f} wasp^*
\end{aligned}$$

$$\begin{aligned}
\frac{\partial(wasp^* * arp)}{\partial t} &= -k_{6f} g_m \cdot (wasp^* * arp) + k_{6r}(wasp^* * arp * g_m) + k_{5f} arp \cdot wasp^* \\
&\quad - k_{5r}(wasp^* * arp) \\
\frac{\partial(wasp^* * arp * g_m)}{\partial t} &= -k_{7f}(wasp^* * arp * g_m) \cdot \mathfrak{b} + k_{6f} g_m \cdot (wasp^* * arp) \\
&\quad - k_{6r}(wasp^* * arp * g_m) \\
\frac{\partial g_m}{\partial t} &= k_{8f} g - k_{8r} g_m - k_{6f} g_m \cdot (wasp^* * arp) + k_{6r}(wasp^* * arp * g_m) - 2k_N g^2 \\
&\quad - k_U g_m \cdot (\mathfrak{b} - \mathcal{S}_3) + \frac{k_u}{2} g_m \cdot (\mathcal{T}(\mathcal{L}) - \mathcal{F}(\mathcal{L}))
\end{aligned}$$

in Ω^x where $\mathcal{S}_3 = \delta\mathcal{F}(\mathcal{L})$ and $\mathcal{L} = p + r + c$ while $\mathcal{F}(\mathcal{L}) = \mathcal{L}(\cdot, 0)$ and $\mathcal{T}(\mathcal{L}) = \mathcal{L}(\cdot, L_z)$ are projections to $z = L_z$ and $z = L_z$ respectively. There is no diffusion in x and no-flux conditions at the boundaries. Note that some parameters are scaled by $1/\delta$ because of g_m.

Parameter values

Protein concentrations and diffusion constants used in the simulations are choosen within the physiological ranges. Other parameters are then obtained by matching the simulation results with experimental observations. The parameter set used in the base simulation is presented in Table 4.1.

Parameter	Value	Description	References
δ	2.7 nm	Actin-subunit length in filaments	[1]
$actin_T$	10 μM	Total F-actin concentration	[33]
arp_T	10 nM	Total Arp2/3 concentration	
cor_T	10 nM	Total coronin concentration	
$racgef_T$	0.5 μM	Total RacGEF concentration	
$wasp_T$	2.7×10^4 $\mu M \cdot nm$	Total WASP density on the interface	
D_g	5 $\mu m^2/s$	G-actin diffusion constant	[173]
D_{arp}	3 $\mu m^2/s$	Arp2/3 diffusion constant	[48]
D_{cor}	5 $\mu m^2/s$	Coronin diffusion constant	

Parameter	Value	Description	References
D_{racgef}	3.5 $\mu m^2/s$	RacGEF diffusion constant	
k_N	1.1×10^{-9} $\mu M^{-1} nm^{-1} s^{-1}$	Dimerization rate constant	
k_D	5 s^{-1}	Branch-detachment rate constant	
k_C	66.67 $\mu M^{-1} s^{-1}$	Coronin binding rate constant	
k_U	1.48×10^{-2} $\mu M^{-1} nm^{-1} s^{-1}$	polymerization rate constant	
k_V	400 s^{-1}	depolymerization rate constant	
k_u	δk_U	polymerization speed constant	
k_v	δk_V	depolymerization speed	
k_{1f}	10^4 $\mu M^{-1} s^{-1}$	RacGEF activation by barb ends	
k_{2f}	3.33×10^4 s^{-1}	Spontaneous RacGEF deactivation	
k_{2r}	3.33×10^{-6} s^{-1}	Spontaneous RacGEF activation	
k_{3f}	10^6 $\mu M^{-1} s^{-1}$	WASP activation by RacGEF	
k_{4f}	10 s^{-1}	Spontaneous WASP deactivation	
k_{5f}	100 $\mu M^{-1} s^{-1}$	Arp2/3 binding to activated WASP	
k_{5r}	1 s^{-1}	Spontaneous unbinding of Arp2/3	
k_{6f}	0.37 $\mu M^{-1} nm^{-1} s^{-1}$	G-actin binding to WASP-Arp2/3	
k_{6r}	0.1 s^{-1}	Spontaneous unbinding of G-actin	
k_{7f}	3×10^{-2} $\mu M^{-1} nm^{-1} s^{-1}$	Branching	
k_{8f}	2×10^7 nm/s	Membrane binding of G-actin	
k_{8r}	2×10^4 s^{-1}	Membrane detachment of G-actin	

Table 4.1: Parameter values used in the actin-wave model.

Experimental measurements

In the experiments, two imaging techniques are used to measure the density of molecular constituents within actin waves. First, total internal reflection fluorescence (TIRF) microscopy is used to measure the density near the bottom surface of the cell. TIRF

images are two dimensional and the measured intensity represents the density within $\sim 100nm$ from the bottom surface. In our simulation we replicate this measurement by taking the integral of the concentration within 100 nm from the interface. For the F-actin density, we have

$$F_{TIRF}(\cdot) \approx \int_0^{z_0} (z/\delta)\mathcal{L}(\cdot, z)\ dz + \int_{z_0}^{L_z} (z_0/\delta)\mathcal{L}(\cdot, z)\ dz$$

where $z_0 = 100\ nm$. Note that this expression neglects the first three actin subunits of filaments. We also have

$$arp_{TIRF}(\cdot) \approx \int_0^{z_0} (r(\cdot, z) + arp(\cdot, z))\ dz$$

$$cor_{TIRF}(\cdot) \approx \int_0^{z_0} (c(\cdot, z) + cor(\cdot, z))\ dz$$

Because the PIP_3 activity is integrated into the RacGEF-activation step, TIRF images of PIP_3 cannot be directly obtained. The best indicator for PIP_3 localization in our model is the level of RacGEF activation at the interface, $racgef^*(\cdot, 0)$. The other imaging technique is confocal microscopy. It is mainly used to construct z-scans which reveals three-dimensional structures. Molecular concentrations obtained from simulations are directly used to represent these images. For example, the F-actin concentration at $(\cdot, z)$ is

$$F(\cdot, z) = \frac{1}{\delta} \int_z^{L_z} \mathcal{L}(\cdot, z)\ dl$$

4.3.2 Numerical simulation

We perform simulations of the system on a 5 $\mu m \times 5\ \mu m$ rectangular, which is a cross section of the three-dimensional system. The simulation results which represent z-scans are used to study properties of the actin waves.

The problem is solved in Comsol Multiphysics. In particular, all equations are discretized using second-order Lagrange elements and coupled into a system of ODEs, which are then solved by the backward differentiation formula of order 2 (BDF2). Because the system is described by diffusion-convection-reaction equations which are convection- and reaction-dominated, especially by reactions at the lower boundary $z = 0$, the system has a boundary layer near $z = 0$. Furthermore, because the system is laterally connected only by diffusion of RacGEF, the problem becomes very stiff. The stability of the numerical algorithm is improved by employing consistent streamline-diffusion and crosswind-diffusion stabilization schemes. In Comsol, streamline diffusion is implemented using the Galerkin-least-square (GLS) method (see [58], for example) while consistent crosswind-diffusion term is nonlinear and discussed in [94]. In addition to these stabilization techniques, small laterral diffusion ($D_{lateral} = 10^{-3}\ \mu m^2/s$), which may be regarded as lateral diffusion of membrane bound species, is also added to all species except RacGEF to improve the numerical stability.

The two-dimensional problem on the $5\ \mu m \times 5\ \mu m$ domain is solved using $\sim 200,000$ degrees of freedom (DOF). A simulation of actin waves with 40-second duration takes ~80 minutes to complete on a dedicated server with dual Intel X5355 processors and 16GB memory. Simulations on a larger domain (W 15 μm × H 5 μm) which better represents a typical cell size require $\sim 800,000$ DOF and take ~400 minutes on the same server. Because a three-dimensional simulation on a $5\ \mu m \times 5\ \mu m \times 5\ \mu m$ domain, which requires $> 20,000,000$ DOF at a similar resolution to the two-dimensional problems, cannot be completed in a reasonable amount of time, we are computationally limited to simulations of two-dimensional systems.

The initial condition of the system is set to the completely unpolymerized state caused by LatA. Other species are given spatially-uniform distributions at approximate steady-state concentration, assuming there are no filaments. The origination of the

actin spots is imposed by temporarily increasing the actin dimerization rate constant in a small region. The stimulation is then removed and the actin network is allowed develop autonomously.

4.3.3 Activities of spontaneous actin waves

Initialization and characteristics of the actin waves

The transient elevation of the nucleation activity on a 0.2 μm region induces a burst of an F-actin network in the area. The network primarily extends vertically while the filament density near the membrane increases. The lateral propagation, or expansion, of the network is very slow until the F-actin density reaches its peak. Then the network rapidly extends both horizontally and vertically, becoming a large spot, before the dense area in the middle collapses and the actin network spilts into wave fronts propagating out of the center in the opposite directions. Figure 4.2 depicts early phases of F-actin network accumulation and separation of wave fronts. The shape of the wave fronts is similar to experimental observations. In addition to the high-intensity wave fronts, we observe F-actin network with lower intensity in the area enclosed by the wave fronts. This feature of the actin waves is also present in the experimental setting although its relation to the actin waves has not been identified.

As the wave fronts are propagating out, their shape is retained while their intensity is slowly attenuated, primarily due to limited avalability of Arp2/3 in the small simulation domain and not because the system slowly dissipates the dynamics set out by the initial condition. Simulations on a larger domain (15 $\mu m \times 5$ μm) which more accurately represents the cell size confirm this observation. At half of its peak level, the actin waves in this domain cover most of the cell length, which is three-time further than their coverage on the small domain at the same level of attenuation. Figure 4.3 compares simulated TIRF intensity of F-actin and Arp2/3 on the 15 $\mu m \times 5$ μm domain to a line

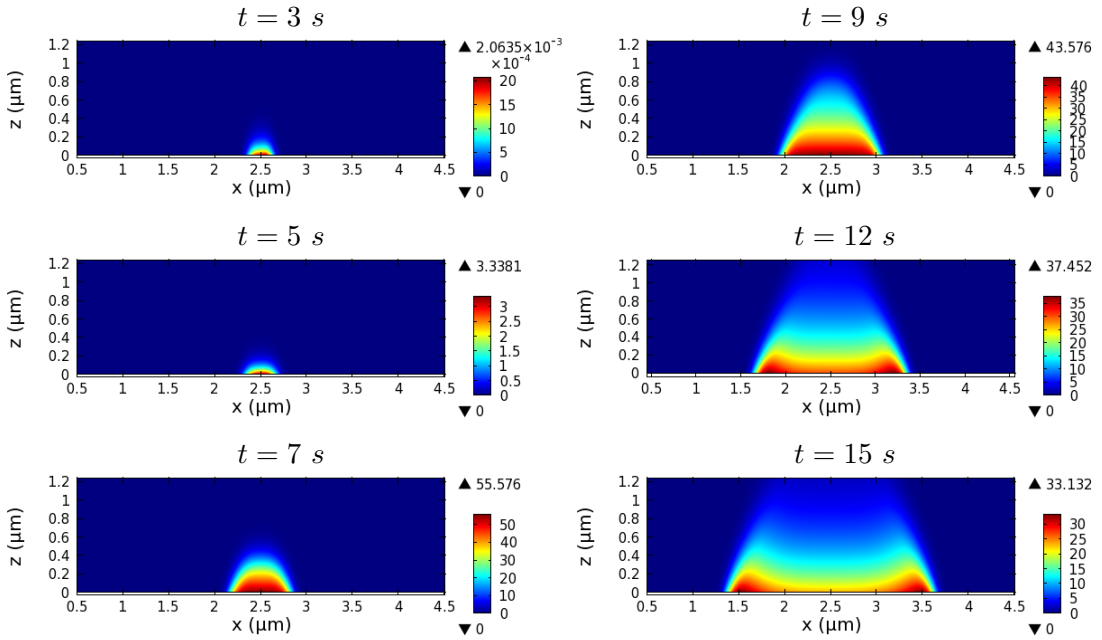

Figure 4.2: Development of actin waves from local F-actin activity. A time course of F-actin concentration (in μM) shows accumulation at a spot, spot expansion, and separation of wave fronts.

scan of a TIRF image of experimentally observed actin waves.

Using fixed protein concentrations and diffusion constants, the reaction-rate constants have been choosen so that the propagation speed, and the shape characteristics of the actin waves quantitatively agree with experimental observations. Figure 4.4 compares an actin wave obtained by simulation to a z-scan from a live cell. When using the signal cutoff at 5 μM, the height of the simulated actin wave is ~0.8 μm while the width of the wave front is ~0.5 μm. The propagation speed of the actin wave is 0.1 $\mu m/s$.

The initial nucleation condition determines the development time of the actin spot and whether the actin waves are subsequently formed. Figure 4.5 depicts parametric dependence of the initialization time on the initial nucleation strength. At the nucleation strength used in simulations and higher nucleation levels, the wave-inititalization

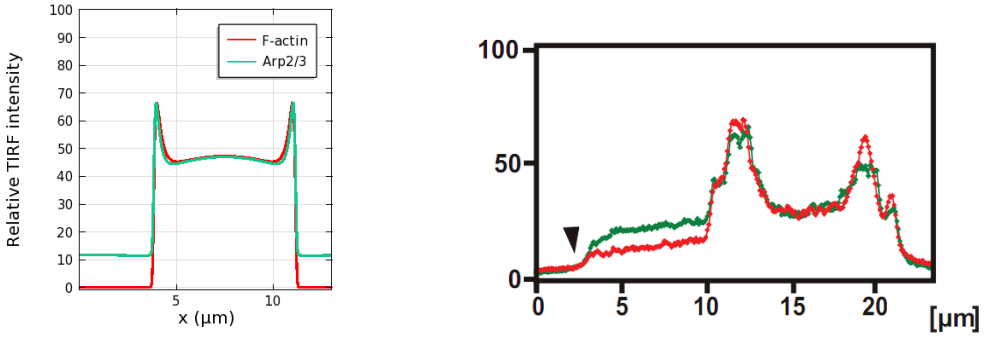

Figure 4.3: Localization of F-actin *(red)* and Arp2/3 *(green)* in actin waves. TIRF intensity along a line scan shows relative localization of F-actin and Arp2/3 near the bottom surface. *(Left)* Simulation on a 15 $\mu m \times 5$ μm domain. *(Right)* Experimental observation from [24].

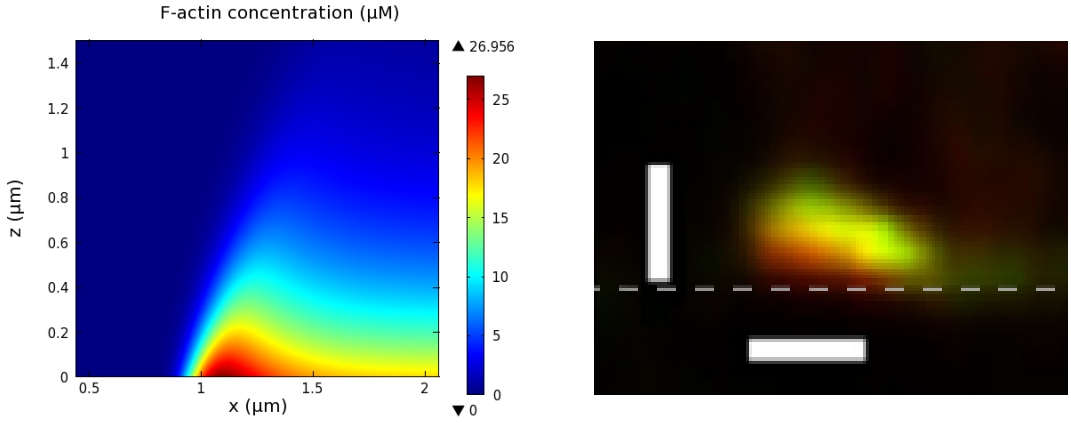

Figure 4.4: Shape of actin waves. *(Left)* F-actin concentration within a simulated actin wave. *(Right)* A z-scan of an actin wave from [24], showing F-actin *(red)* and coronin *(green)*. The dashed grey line approximates the bottom surface. Bars are 1 μm.

stage does not change significantly. The initialization time decreases approximately linearly with the logarithm of the strength. Decreasing the nucleation strength, however, significantly increases the initialization time once it reaches a certain level. At $10^{-3.75}$ folds of the reference k_N level, the actin waves do not reach the propagation stage after

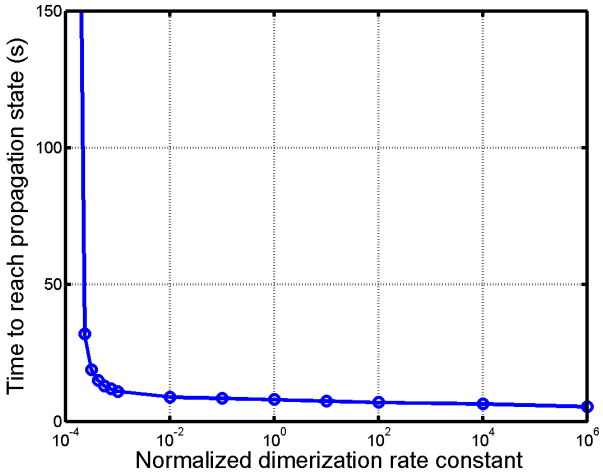

Figure 4.5: Time required for actin waves to develop under a transient increase in the normalized dimerization rate constant (k_N) and propagate 0.5 μm away from the nucleation center as a function of normalized k_N.

$>$ 250 seconds while the propagation occurs within 30 seconds under a 30% increase in the nucleation strength at $10^{-3.625}$ folds. During the prolonged initialization stage, the actin structure is contained within the initialization zone while it may extend vertically. Figure 4.6 displays the actin structure during the initailization stage under a low initial nucleation level.

Interestingly, the characteristics of the actin waves do not depend on the initial wave-formation stage, but are rather internal properties of the underlying system. Ten-fold changes in the initial nucleation strength, its duration, or its coverage affect neither height, speed, nor width of the propagating waves. As the wave characteristics are internal properties, they are dependent on the system parameters. Given that the actin waves assume the experimentally-observed shape, by a mechanism discussed next, the dependence of the wave characteristics on various system processes can be described as follows. First, as the wave propagation depends on a local positive feedback triggered by

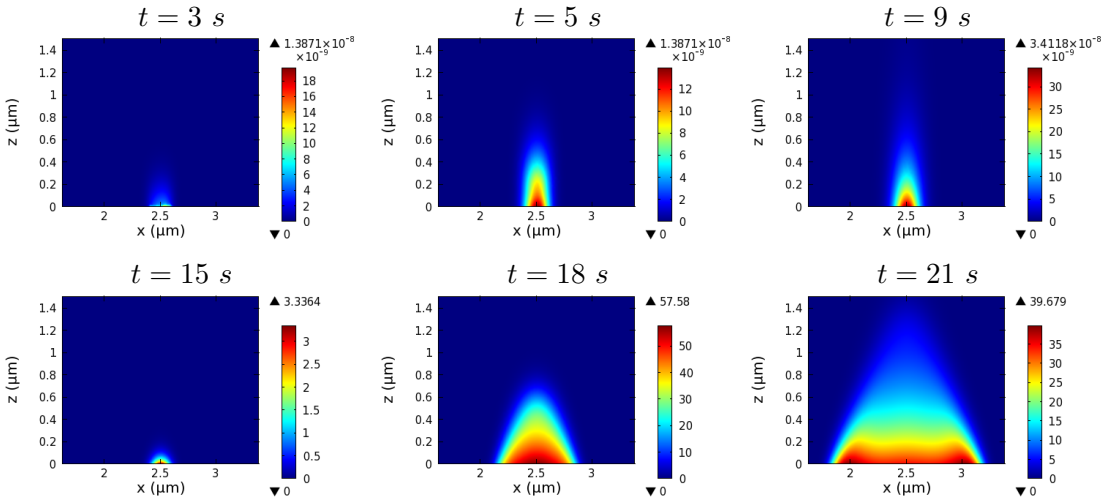

Figure 4.6: Initialization with low F-actin activity. A low level of initial F-actin activity leads to a prolonged initial stage, where the actin network displays vertical extension before reaching its critical density. F-actin concentration (in μM) within the structure is depicted at different times during the initiation phase.

activated RacGEF, the propagation speed is determined by both characteristic degradation length of activated RacGEF and responsiveness of the positive feedback loop that drives branch nucleation. Note that high the branch-necleation rate also leads to actin waves with increased network density and lower height. Then, assuming a fixed propagation speed, the shape of the actin waves depends on relative speed between various processes. In particular, the inclination of the wave front is determined by the ratio between the propagation speed and the barbed-end polymerization rate. The height of the actin waves is determined by the ratio between the polymerization rate and the branch-turnover rate. The width of the wave front, from its boundary to its vertical peak, is determined by the ratio between the propagation speed and the branch-turnover rate. Similarly, inclination and length at the back are controlled by the depolymerization rate.

Mechanism for propagation of separated wave fronts

Unlike existing models which rely either on diffusion of the actin structure or lateral displacement due to polymerization of directionally-oriented filaments, our model for actin waves, because of the simplifying assumption that actin filaments align vertically, strictly utilizes a different mechanism for propagation of the actin structure. Our system is laterally disconnected except for diffusion of signaling molecules within the feedback loop, represented by RacGEF. The signal for local organization of the actin network is propagated by RacGEF diffusion, which activates WASP thus promotes nucleation of new filament branches. This signal is then coupled with basal nucleation, branching, and polymerization activities, which alone are not strong enough to organize the local actin network. The coupling is multiplicative as new branches are nucleated by barbed ends and a complex containing activated WASP. Once the organization of the actin structure is triggered by the propagating signal, the local network is built up quickly due to the superlinear positive feedbacks through barbed ends and locally activated RacGEF due to the barbed ends.

An important feature of the actin waves is that they are characterized by propagating peaks with lower F-actin activity in the back. Existing models describe this system as excitable media produced by bistability. This mechanism is capable of creating propagating fronts while the back is inhibited by a slow inhibitor, leading to a temporarily unresponsive region behind the wave front. However, this mechanism does not allow expanding wave fronts to stop or to reverse into retracting waves, which is another important feature of the actin waves. Our model is based on a different mechanism. We hypothesize that the peaks of the actin waves are created by scarcity of basic constituents of the actin network in the middle region. Under this scheme, the suspension and the retraction of wave fronts are possible and will be shown in numerical experiments with PTEN activity. In addition to the wave fronts, the mechanism based

on scarcity leads to lower, yet active, F-actin activity in the region enclosed by the waves, which is also present in live cells.

Possible exhausted molecules which induce scarcity include G-actin and Arp2/3, both of which are incorporated into the actin network as new filaments are created. Because the actin network is originated from the middle by positive feedbacks both directly through barbed ends and via RacGEF, the scarcity needs to outweight the positive feedbacks. We found that this happens when the activation of an intermediate step in the positive feedback is saturated, *i.e.* the majority of the molecules at this step are activated under intermediate F-actin activity. In addition, sufficiently high turnover of barbed ends, caused by dissociation of actin filaments, is required. Because our regulatory network is simplified, the only step we can apply this condition is the activation of WASP. By our choice of parameters, the spatial difference in availability of Arp2/3 and G-actin dominates the spatial gradient in WASP activity, causing lower Arp2/3 activity in the area where significant branching has occurred. Coupled with adequately fast turnover of barbed ends, peaks of actin waves can be observed. Figure 4.7 shows that there is a large spatial gradient of free Arp2/3 and there is very low availability of free Arp2/3 in the area covered by actin waves, which leads to defined backs of the waves.

The condition for high barbed-end turnover, without barbed-end capping activity, imposes a requirement for a high spontaneous depolymerization and debranching rates. Fast depolymerization does not allow the back of the actin waves to extend as far as observed in experiments while fast debranching limits the height of the waves and reduces the extent that coronin localization lags F-actin. Enhancing scarcity of Arp2/3 by reducing its total concentration allows actin waves with more height and more defined back. However, this comes with an expense of slower propagation. Figure 4.8 displays an actin wave with lower Arp2/3 concentration on the 15 $\mu m \times 5$ μm domain. Although

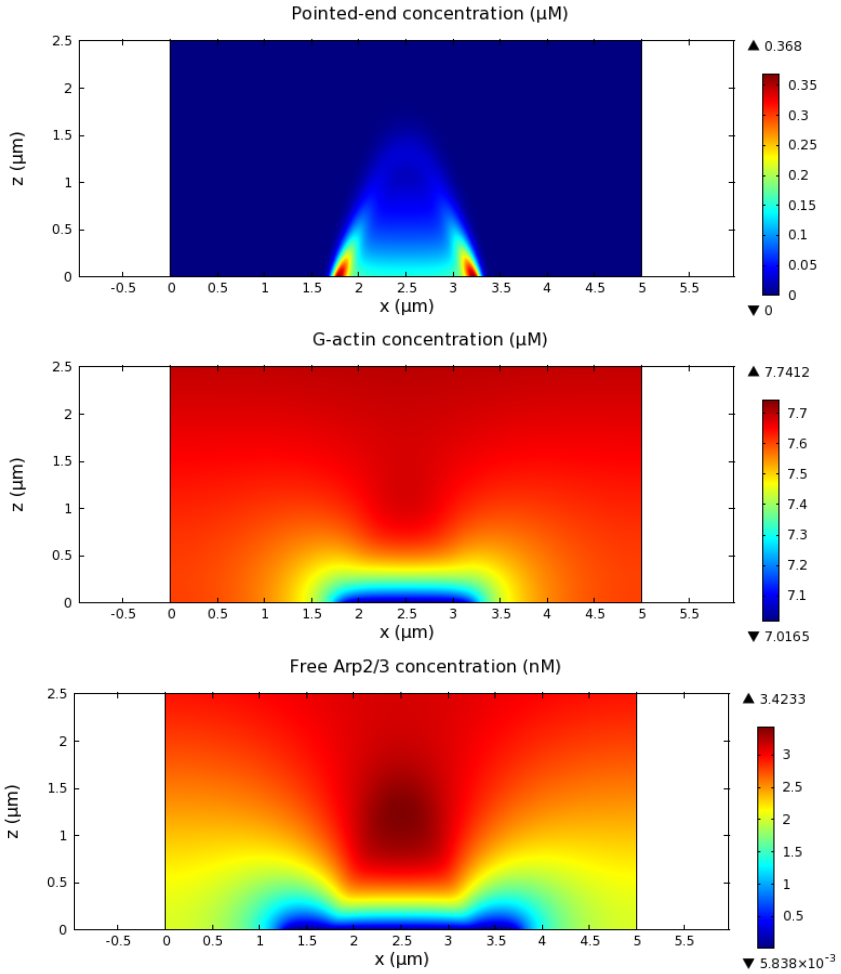

Figure 4.7: Scarcity of free Arp2/3 within actin waves. The distributions of free Arp2/3 *(bottom)* and G-actin *(middle)* are depicted with the corresponding pointed-end density *(top)*. The Arp2/3 profile displays a large gradient with low concentration near the bottom region covered by the actin waves.

the high depolymerization rate may be partially considered as a simplification of accelerated filament disassembly by activities of proteins such as cofilin and coronin [117], it is apparent that the capping activity is required for observed characteristics at the back. Unfortunately, inclusion of the capping activity, which requires three-dimensional simulations, is currently not computationally feasible.

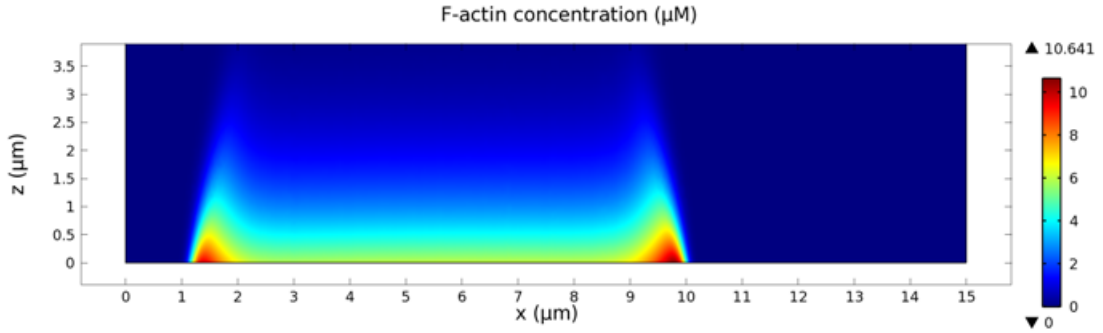

Figure 4.8: Actin waves under low Arp2/3 concentration. Threefold reduction of Arp2/3 concentration leads to the actin waves with a more defined shape. The propagation speed is reduced to 0.06 $\mu m/s$.

Localization and roles of coronin and PIP_3

Debranching of actin filaments is sufficient to allow deconstruction of the actin network in the back. As coronin is experimentally observed at the top of the actin waves, we assume that it is responsible for debranching of the filaments. Inhibition of coronin would slow debranching which leads to actin waves with increased height and possibly alters the entire actin structure, due to imbalanced branching dynamics. Indeed, simulation results without coronin suggests that coronin is not explicitly required in actin-wave formation as long as debranching is equally fast. On the other hand, if the debranching rate is not sufficiently compensated by other mechanisms, other structures such as an expanding dome may be observed instead of the actin waves. Figure 4.9 shows F-actin structures when the effective debranching rate is reduced by inhibition of coronin activity.

When coronin is assumed to be responsible for debranching, it is found at the top of the actin waves, similarly to experimental observations. However, it does not appear that coronin is most concentrated at the roof of the actin network. In fact, the simulated coronin localization lags the F-actin localization and its peak density is relatively close

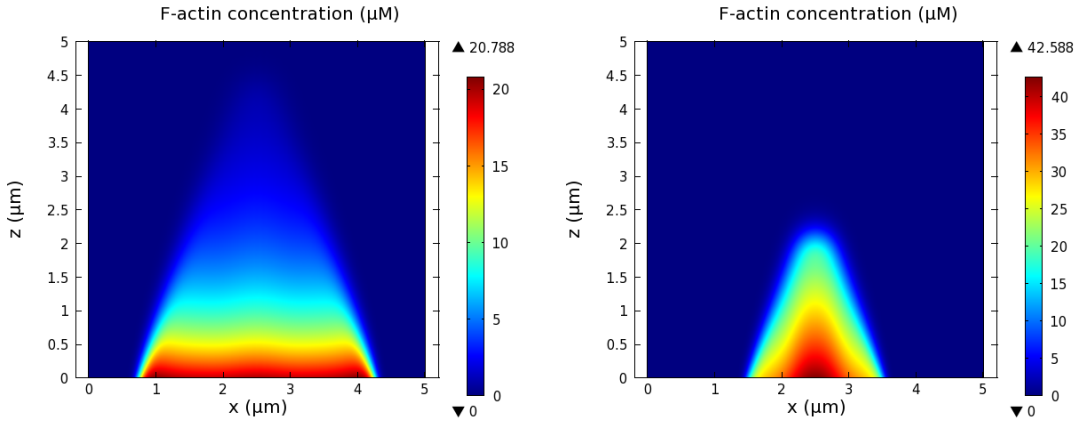

(a) 3-fold reduction (b) 5-fold reduction

Figure 4.9: F-actin structures without coronin activity. Lower effective debranching rates caused by lack of coronin activity lead to altered actin structures.

to the F-actin peak density. Nevertheless, the coronin localization appears to follow the F-actin localization laterally and entirely covers the back of the actin waves as in the experiments. Figure 4.10 depicts relative localization of coronin and F-actin on the network. A similar result is obtained when coronin also accelerates depolymerization at pointed ends.

The localization of PIP_3 and Ras activity, approximated by the concentration of RacGEF near the membrane, is concentrated in the area enclosed by the fronts of the actin waves, as shown in Figure 4.11. Because RacGEF diffuses in the cytosol, the observed region of high intensity slightly extends past the actin-wave fronts. We expect that if PIP_3 and Ras are included explicitly in a more detailed model, as in the model for directional sensing in Chapter 3, their transition zones would coincide with the wave fronts. The experimentally-observed necessity of the PIP_3 activity for the presence of the actin waves is apparent. If the PIP_3 activity is inhibited, i.e. RacGEF cannot be activated, the branching process is inturrupted and the actin waves are not observed.

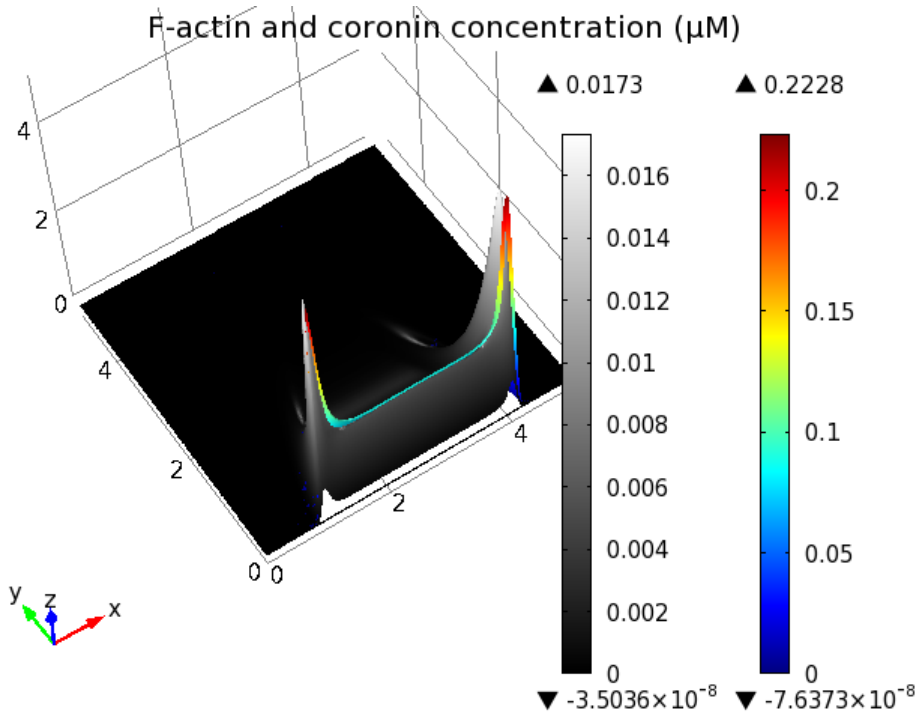

Figure 4.10: Relative coronin localization on the F-actin network in actin waves. Concentration of F-actin *(right bar)* and coronin-bound pointed ends *(left bar)* is plotted together, showing relative localization on the actin waves. The height displays relative concentration levels.

More complicated behaviors of the actin waves

In real cells, when two fronts of actin waves collide, both of them are annihilated. The same is observed in the simulations. The colliding wave fronts annihilate each other even when they are not equally matured. On the other hand, when an actin wave reaches a cell boundary, it causes extension of the boundary as it propagates outward. When the wave separates from the border, the expanded region is paralyzed and eventually retracts. This experimentally-observed behavior of the actin waves cannot be captured by our model where the cell boundary is fixed. Our model also cannot account for the F-actin activity beyond the cell-substrate surface although some actin waves are

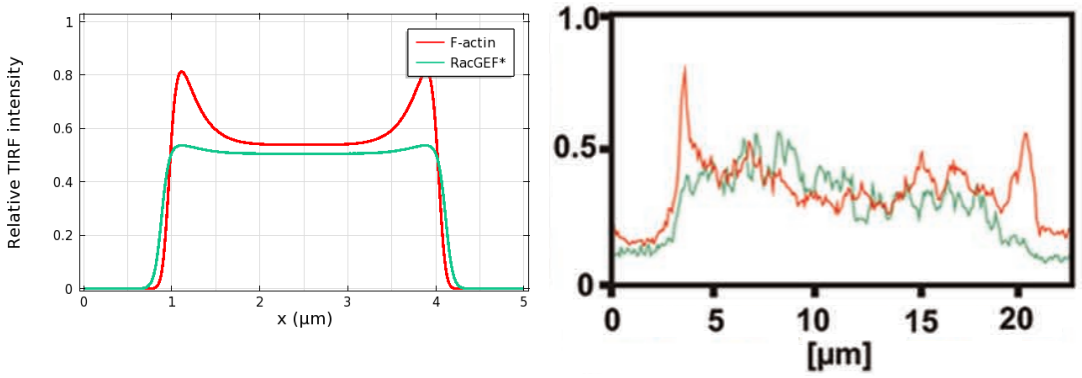

Figure 4.11: Relative localization of PIP_3 activity. TIRF images show localization of PIP_3 activity within the region enclosed by actin waves. *(Left)* Simulated RacGEF concentration is used to represent PIP_3 activity. *(Right)* Experimentally-observed TIRF image from [67].

observed on the unattached boundary adjacent to the attached surface. However, our model captures the increased height when an actin wave is adjacent to a cell boundary, as depicted in Figure 4.12.

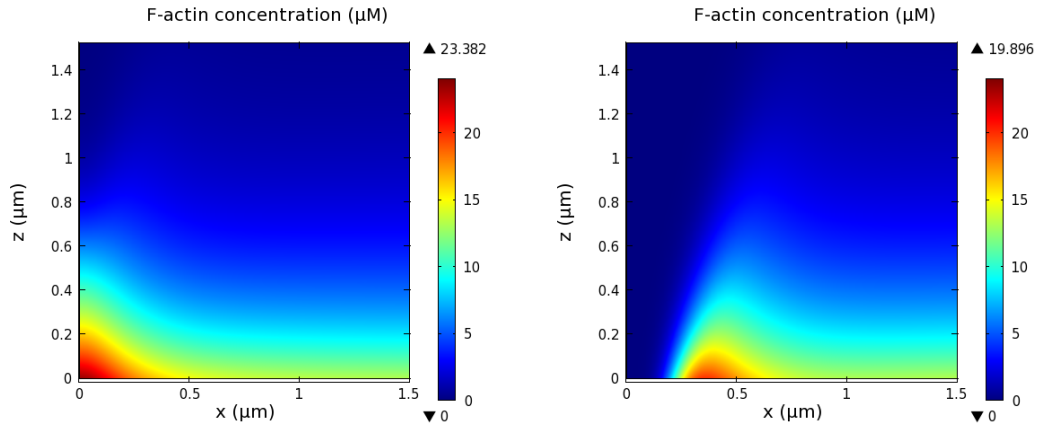

Figure 4.12: Increased height of actin waves at the cell boundary. The structure of an actin wave touching the cell boundary *(left)* is compared to its structure at an earlier time *(right)*.

Areas of the cell membrane not enclosed by the actin waves are decorated with

myosin II, cortexillin I, and PTEN. Experimental results show that exclusion of myosin II does not affect the actin waves. However, cells lacking PTEN creates actin waves which cannot retract. We seek to better understand the role of PTEN on the behaviors of the actin waves and how retraction of the waves occurs. Because experimental observations suggest that PTEN is not only passively regulated by its localization to PIP_2, we study controlled numerical experiments where PTEN activity is explicitly specified. This activity is modeled by local inability of barbed ends to activate RacGEF. When we add the PTEN activity to a fixed region, the actin waves cannot propagate through the region. Instead, it propagation is halted at around the border of the region and the wave front becomes a standing wave. If the PTEN region moves into the area covered by the actin wave, the wave front propagates backward as the wave-covered area retracts. The relative localization of coronin agrees with experimental observations as it follows the wave front, in this case appearing outside the enclosed area. Figure 4.13 displays a retracting wave front.

We next study PTEN ingression into an area enclosed by actin waves and separation of a toroid-like wave into two closed waves. Although they are different behaviors, depending on whether there exists a broken wave front or not, the behavior along a line cut through by PTEN ingression appears to be identical. We model z-scans of this line by introducing PTEN activity in a region enclosed by the waves. Introduction of the PTEN activity inhibits the positive feedback through PIP_3 in this area, leading to eradication of the actin structure. New wave fronts are subsequently formed at the border of the region, separating the former area into two enclosed area. This can either be considered as PTEN ingression or breakage of a toroid-like wave into two separated actin waves, depending on connectivity of the actual area on the cell-substrate surface. Figure 4.14 depicts formation of new wave fronts around the ingressed region.

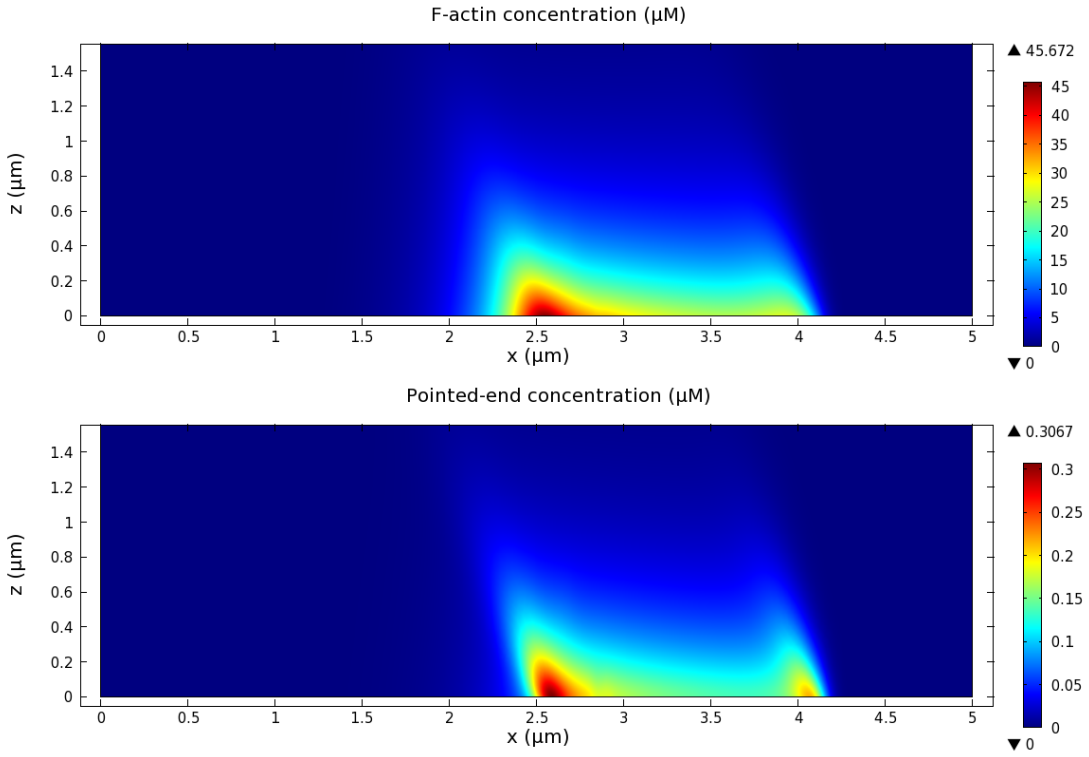

Figure 4.13: Retraction of wave front. Actin waves *(upper)* are restricted by PTEN activity, whose window is moving to the right with speed 0.1 $\mu m/s$. The right front expands while the left front retracts. The retraction is better visualized by the pointed-end concentration *(lower)*, which reflects filament height.

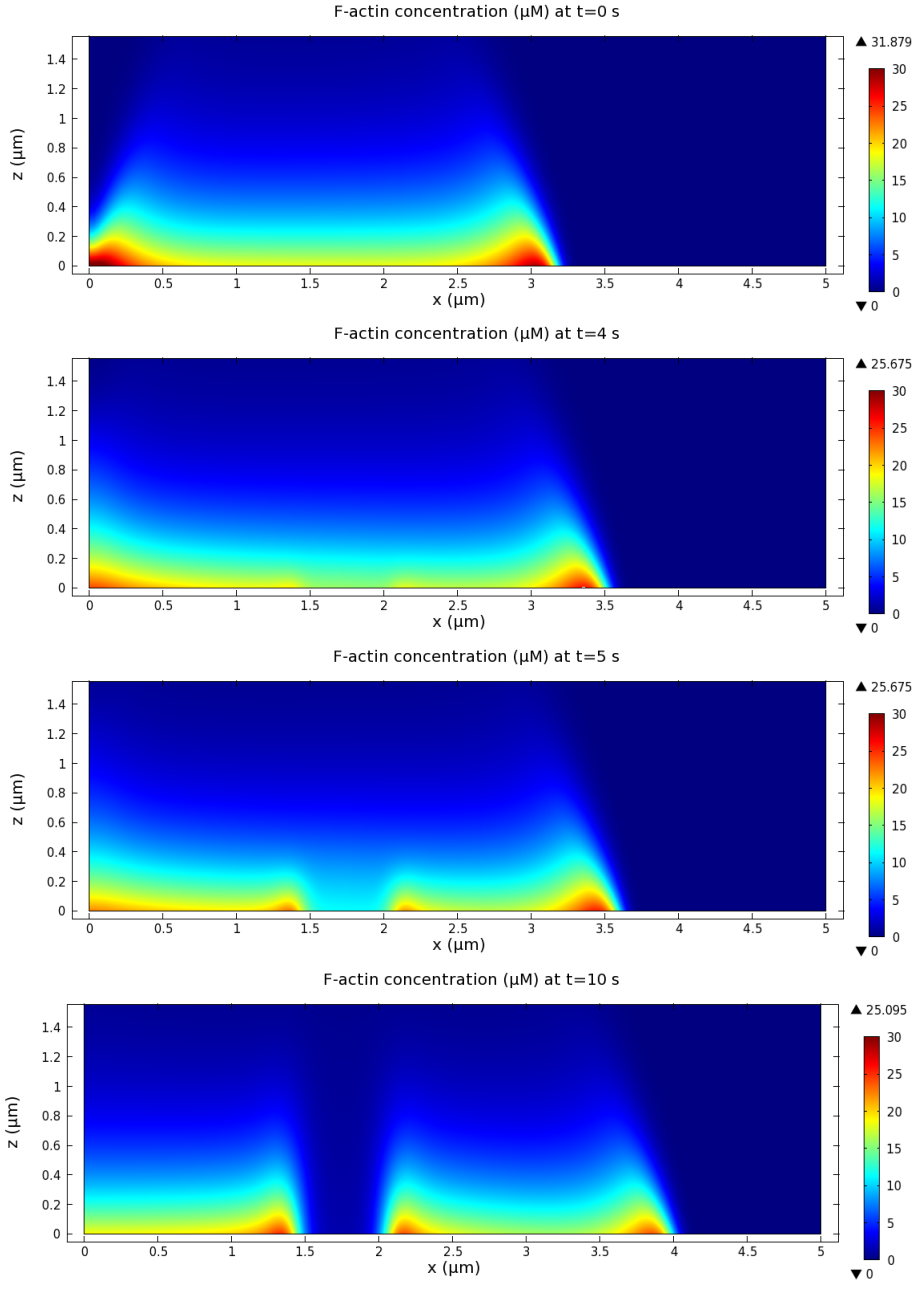

Figure 4.14: Inhibition of PIP_3 by PTEN activity induces formation of new wave fronts. RacGEF activation is inhibited between 1.5 μm and 2 μm at $t = 0$ s. F-actin activity in this area is abolished while new wave fronts are formed within 5 seconds.

4.4 Discussion

A continuous description for actin waves with consistent F-actin dynamics was carefully developed. The model combines the dynamics of the F-actin network with signaling components whose necessity is suggested by experimental observations. The detailed actin dynamics allows modeling and visualization of the actual actin structure. On the other hand, the inclusion of the signaling elements allows numerical studies of their roles and connection with the actin waves. The model is able to explain many important features of the actin waves. It also allows future inclusion of other processes, such as substrate adhesion and bundling of actin filaments, which may interact with the actin waves.

The development of the actin structure from small F-actin activity is achieved by superlinear positive feedbacks which incorporate the autocatalytic nature of filament branching and PIP_3 activity. Consistently with experimental observations, inhibition of PIP_3 disrupts the cooperativity and results in rapid dissociation of the actin structure. Furthermore, locally-targeted inhibition of PIP_3 by PTEN causes disruption of the F-actin network within the region, which explains complementary localization of PTEN relative to the actin waves.

Although the model was not developed to explain the initialization process of the actin waves and the behavior of motile actin spots, it captures the transition from the actin spots into the actin waves. The development of individual actin spots depends on the initialization and there is a threshold for network density within the spots which dictates whether they eventually develops into actin waves. The development time of the actin spots also depends on their initialization, especially near the threshold. Despite the influence of the initialization process on their development, actin-wave characteristics is universally determined by system properties such as rate constants and availability of actin-network constituents. The shape of the actin waves is consistent while the

propagation speed may be limited by availability of free Arp2/3 and G-actin.

By restricting filament orientation to be normal to the bottom surface, we demonstrated an alternative mechanism for wave propagation based on local organization of the actin structure induced by diffusion of signaling molecules. Although the propagation of the actin waves may be caused by a combination of polarized filament orientation and this mechanism, the dependence on the PIP_3 activity suggests that this mechanism is a main driver for the actin-wave propagation.

The collapsing back of actin waves has been previously modeled by bistability of excitable media, which is the fundamental process of all existing actin-wave models. This scheme does not allow presence of standing waves and retracting waves as there is a long recovery period after activation where the inhibitor dominates. We propose a new mechanism based on local scarcity of actin-network constituents such as Arp2/3 and free G-actin. While this mechanism requires rapid dissociation of the actin network in absence of barbed-end capping, it does not prohibit retraction and suspension of the actin waves. Similarly to the waves in live cells, this mechanism creates a region with moderate F-actin activity behind the propagating wave fronts. Therefore, local disruption of the positive feedback by PIP_3 inhibition via PTEN causes an inactive region where actin waves cannot propagate into. Because of availability of the constituents within the inactive region, wave fronts are formed at the transition even if a wave front has previously propagated over the region. Therefore, standing waves, retracting waves, and formation of new wave fronts, as in breakage of a toroid-like structure, may be controlled by this inactive zone. Similarly to the excitable-media scheme, colliding wave fronts are annihilated in this case as both wave fronts induce scarcity in the region.

Localization and roles of actin-wave associated proteins have been highlighted by experimental observations. Our model suggests that the localization of coronin is caused

by its debranching activity. Binding and replacing Arp2/3 at branch points make coronin appear to decorate at the top of the actin waves. Slow debranching caused by inhibition of coronin activity may lead to altered actin structures which lack pronounced wave fronts. The localization of PIP_3 and Ras activity behind the actin waves is a direct consequence of the activity within the region enclosed by wave fronts. Because expansion and retraction of this region is led by the actin waves, their locations coincide with the transition zone of the PIP_3 activity.

Unfortunately, full behaviors of PTEN ingression and separation of a toroid-like wave cannot be studied on a two-dimensional domain. However, we believe that they are results of a competition between dynamics of the area enclosed by the actin waves and dynamics within the external area. The dynamics at the fronts of the actin waves are likely stronger, as the enclosed area generally expands. The expansion may stop after the active area reaches a critical size and the availability of Arp2/3 or G-actin become limited. This is when retraction and PTEN ingression occur. An oscillation around this equilibrium can cause observed behaviors such as the alternate PTEN ingression and the periodic expansion and retraction of the active area [68]. If there is a point along the wave front with unusually weak F-actin dynamics, the external-area dynamics, reflected by PTEN activity may break through, causing separation of a toroid-like wave into two disconnected waves. If a new wave front is not formed and become mature before an area is totally consumed, that part of the actin waves may collapse.

Although PTEN activity may not be necessary for the external-area dynamics as the inner area can collapse after reaching a critical size without its presence, it undoubtedly plays a role in balancing the internal and external dynamics because actin waves do not retract when the PTEN activity is inhibited. To fully understand the dynamics of the actin waves, a model which captures the underlying dynamics within the external area is needed, along with a capability to perform three-dimensional simulations. Most

likely, this dynamics is tightly related to the activities of PTEN and bundling proteins such as cortexillin which are integral to the external dynamics. New experiments will be needed to elucidate their connected roles and their regulation before the competing dynamics between the actin waves and the external area can be understood.

Chapter 5

Conclusions and future work

Cell motility is a complex process which depends on detection of extracellular signals, transduction and integration of intracellular signals, remodeling of the cytoskeleton and other subcellular structures, and controlled deformation of cell shape and cell-substrate interaction. A thorough understanding of each subprocess and their interactions is required to deduce the cell-level behavior. Experimental studies have identified many essential components of these processes including molecular players, their interactions, and their physical properties, and have provided us with macroscopic measurements, both biochemically and physically, of the system. However, current understanding of the subprocesses is fragmented.

Our work attempts to integrate essential molecular components of the signal transduction network and the actin cytoskeleton and understand how they could give rise to observed cellular behaviors. The theoretical study has elucidated not only the mechanisms which structurally lead to the prominent properties of the PI3K signaling pathway and the actin waves, but also the roles of mean stimulus level and cell shape in the overall response of the cells. Moreover, the derived models produce responses which closely

match experimental measurements under tightly-controlled environments in both stimulated and resting *Dictyostelium* cells. Numerical experiments of the models also suggest physiological conditions which are difficult to observe experimentally – but are crucial for observed cellular behaviors – such as saturation of RasGEF activity at high cAMP level and local exhaustion of free Arp2/3 in actin waves.

In Chapter 2, a modular framework for analysis of protein regulatory network was developed. This framework allows separation of both steady-state and dynamic behaviors between subsystems. Under a hypothesis that adaptation and gradient-amplification properties of the chemotactic pathway belonged to different subsystems, they were analyzed independently. Quantitative measures for adaptation and gradient amplification were rigorously defined and a collection of modules which exhibit these properties was proposed and analyzed.

Among adaptation modules, feedforward adaptation fitted best with the chemotactic pathway, and its local dynamics was analyzed in great details in the context of mass action kinetics. As it turned out, adaptation is achieved when intermediate complexes are negligible and activity of both activating and inhibiting enzymes are non-saturated. Under these conditions, the feedforward adaptation system can be approximated by the LEGI model, whose steady state had been previously analyzed by Levchenko and Iglesias [125]. In fact, the system can be further simplified into a two-state model which qualitatively preserves the dynamics of the full model. Linearization of this two-state model gives us the cartoon adaptation model proposed by Othmer and Schaap [146].

When diffusion of activating and inhibiting enzymes is considered, the adaptation property is preserved in radially-symmetric geometry. Localization of the response induced by a non-uniform stimulus depends on characteristic degradation length of the enzymes, which is a function of their diffusion and degradation constants. In non-symmetric domains, the adaptation property remains preserved although the system

response becomes localized, even under uniform stimulation. The localization may become dose-dependent when spontaneous activation and inactivation are incorporated. This shape-induced polarity provides a plausible mechanism for directional persistence in polarized *Dictyostelium* cells and partially explains why a polarized cell gradually turns towards a cAMP source instead of directly reestablishing its polarity.

The gradient-amplification module was placed downstream of the adaptation module so that small local differences in Ras activity, which are diluted by diffusion of its activator and inhibitor, can result in strong PIP_3 polarity. The gradient-amplification property is intimately connected to sensitivity of the local dynamics. We showed that local dynamics can become highly sensitive, comparable to a Hill constant larger than 10, when the pathway is structurally cooperative and a positive feedback is present. This cooperativity may arise simply from membrane recruitment and subsequent activation of a cytosolic protein. This realistic scheme allows us to construct a highly sensitive subsystem which agrees well with experimentally-suggested regulation steps in this pathway.

Responses of the composite system after introduction of cAMP exhibit two distinct phases. The first phase is characterized by adaptive activity in response to a step change in the mean stimulus level. Within 30-50 s after the stimulation, the second phase, where strong localization of response activity develops, is driven by the positive feedback and cooperativity within the downstream subsystem. The polarization rate is limited by diffusion constant of cytosolic molecules such as PI3K. Because of this limitation, *Dictyostelium* cells are not able to effectively reorient their polarity and appear to be trapped when they are subjected to rapidly switching cAMP gradients [133].

In Chapter 4, a continuous description of actin networks was developed and used to create a model for actin waves. We used normally aligned F-actin, which approximately

represents mean orientation of uniformly-oriented actin filaments that are derived from membrane-attached filaments. The network dynamics captures many fundamental processes exhibited by F-actin including polymerization, depolymerization, *de novo* filament nucleation, branching from mother filaments, detachment of branches, and dissociation of filaments due to depolymerization. The actin network was then coupled with a simplified model for PI3K activity, which is required for existence of the actin waves in experiments.

The model was employed to reveal possible mechanisms which underline the dynamics of actin waves. We showed that spontaneous generation of actin waves can be caused by cooperativity and positive feedback within the system. In contrast to earlier models whose wave propagation relies on threadmilling or diffusion of actin filaments, our model suggests that diffusion of a cytosolic molecule, which regulates branching of F-actin, can lead to wave propagation as well. Furthermore, the model suggests that decay of F-actin intensity at the back of actin waves may be caused by local scarcity of free cytosolic molecules such as Arp2/3 and G-actin, which are fundamental components of the actin network. The gradual decay of wave backs leads to the observed three-dimensional structure of actin waves.

Experimental measurements suggested that peak intensity of actin waves occurs where the PIP_3 gradient is the highest. This observation is consistent with a situation where the PIP_3 activity is saturated at low F-actin density within the wave back. In fact, experimental data showed that there is nontrivial F-actin intensity behind actin waves although this was not depicted in fluorescence images. When actin waves collide, they annihilate and subregions enclosed by individual actin waves combine. This occurs in our simulation because continuous supplies of Arp2/3 and G-actin are required to maintain wave fronts. When inner regions combine, limited availability of either Arp2/3 or G-actin in the vicinity causes both wave fronts to collapse.

The role of PTEN in actin waves is unclear. However, it was observed experimentally that disruption of PTEN affects actin wave dynamics. Without PTEN activity, actin waves are unable to retract. Because our model employed a simplified description of PI3K signaling, PTEN activity could not be captured in the simulation. In this respect, our model is more suitable for actin waves in PTEN-disrupted cells. Actin waves generated by our model continuously propagate away from the center and cannot retract. However, when we artificially imposed PTEN-dominated regions by locally disrupting PIP_3 activity, we were able to simulate both standing and retracting actin waves. Moreover, when PTEN was imposed within a region enclosed by actin waves, new wave fronts were formed near the boundary of the PTEN-dominated region. This result resembles a cross section of an actin wave ingressed by PTEN.

Because our models provide a simple description of the signaling pathway and a modularized continuous dynamics for actin dynamics, the current work lays a solid foundation for future development of integrative models in which many facets of cell motility can be dealt with simultaneously. For example, a model which combines the stimulus-level and cell-shape dependent polarization of PIP_3 and F-actin with cell deformation could provide interesting insights into the characteristics of *Dictyostelium* migration. Integration of the PI3K pathway with F-actin dynamics would also allow us to understand the biased random F-actin activity. The model for F-actin dynamics may also be applied to the study of actin cortex structure and its reconstruction in contractile cell blebs while the resulting cell shape and contractile dynamics can be studied when a description of various forces is incorporated. On the other hand, molecular dynamics within the external area of actin waves which involves PTEN, cortexillin, and myosin II, still remains unknown. A careful study of this dynamics could yield better understanding of the loose and contractile network of bundled actin filaments.

Bibliography

[1] V. C. Abraham, V. Krishnamurthi, D. L. Taylor, and F. Lanni. The actin-based nanomachine at the leading edge of migrating cells. *Biophys J*, 77(3):1721–1732, Sep 1999.

[2] Aiman Alam-Nazki and J. Krishnan. A mathematical modelling framework for understanding chemorepulsive signal transduction in Dictyostelium. *J Theor Biol*, 266(1):140–153, Sep 2010.

[3] Uri Alon. Network motifs: theory and experimental approaches. *Nat Rev Genet*, 8(6):450–461, Jun 2007.

[4] J. Christopher Anderson, Christopher A Voigt, and Adam P Arkin. Environmental signal integration by a modular AND gate. *Mol Syst Biol*, 3:133, 2007.

[5] Natalie Andrew and Robert H Insall. Chemotaxis in shallow gradients is mediated independently of PtdIns 3-kinase by biased choices between random protrusions. *Nat Cell Biol*, 9(2):193–200, Feb 2007.

[6] B. Andrews, E.D. Sontag, and P. Iglesias. An approximate internal model principle: Applications to nonlinear models of biological systems. In *Proc. 17th IFAC World Congress, Seoul*, pages Paper FrB25.3, 6 pages, 2008.

[7] David Angeli, James E Ferrell, and Eduardo D Sontag. Detection of multistability, bifurcations, and hysteresis in a large class of biological positive-feedback systems. *Proc Natl Acad Sci U S A*, 101(7):1822–1827, Feb 2004.

[8] Yoshiyuki Arai, Tatsuo Shibata, Satomi Matsuoka, Masayuki J Sato, Toshio Yanagida, and Masahiro Ueda. Self-organization of the phosphatidylinositol lipids signaling system for random cell migration. *Proc Natl Acad Sci U S A*, 107(27): 12399–12404, Jul 2010.

[9] A. Arkin, J. Ross, and H. H. McAdams. Stochastic kinetic analysis of developmental pathway bifurcation in phage lambda-infected Escherichia coli cells. *Genetics*, 149(4):1633–1648, Aug 1998.

[10] Cécile Arrieumerlou and Tobias Meyer. A local coupling model and compass parameter for eukaryotic chemotaxis. *Dev Cell*, 8(2):215–227, Feb 2005.

[11] N. Barkai and S. Leibler. Robustness in simple biochemical networks. *Nature*, 387 (6636):913–917, Jun 1997.

[12] Nicholas P Barry and Mark S Bretscher. Dictyostelium amoebae and neutrophils can swim. *Proc Natl Acad Sci U S A*, 107(25):11376–11380, Jun 2010.

[13] Carsten Beta. Bistability in the actin cortex. *PMC Biophys*, 3(1):12, 2010.

[14] Parvin Bolourani, George B Spiegelman, and Gerald Weeks. Rap1 activation in response to cAMP occurs downstream of ras activation during Dictyostelium aggregation. *J Biol Chem*, 283(16):10232–10240, Apr 2008.

[15] A. A. Bominaar and P. J. Van Haastert. Chemotactic antagonists of cAMP inhibit Dictyostelium phospholipase C. *J Cell Sci*, 104 (Pt 1):181–185, Jan 1993.

[16] A. A. Bominaar and P. J. Van Haastert. Phospholipase C in Dictyostelium discoideum. Identification of stimulatory and inhibitory surface receptors and G-proteins. *Biochem J*, 297 (Pt 1):189–193, Jan 1994.

[17] Leonard Bosgraaf and Peter J M Van Haastert. The ordered extension of pseudopodia by amoeboid cells in the absence of external cues. *PLoS One*, 4(4):e5253, 2009.

[18] Leonard Bosgraaf and Peter J M Van Haastert. Navigation of chemotactic cells by parallel signaling to pseudopod persistence and orientation. *PLoS One*, 4(8): e6842, 2009.

[19] Leonard Bosgraaf and Peter J M van Haastert. The regulation of myosin II in Dictyostelium. *Eur J Cell Biol*, 85(9-10):969–979, Sep 2006.

[20] Leonard Bosgraaf, Henk Russcher, Janet L Smith, Deborah Wessels, David R Soll, and Peter J M Van Haastert. A novel cGMP signalling pathway mediating myosin phosphorylation and chemotaxis in Dictyostelium. *EMBO J*, 21(17):4560–4570, Sep 2002.

[21] Leonard Bosgraaf, Arjen Waijer, Ruchira Engel, Antonie J W G Visser, Deborah Wessels, David Soll, and Peter J M van Haastert. RasGEF-containing proteins GbpC and GbpD have differential effects on cell polarity and chemotaxis in Dictyostelium. *J Cell Sci*, 118(Pt 9):1899–1910, May 2005.

[22] Leonard Bosgraaf, Ineke Keizer-Gunnink, and Peter J M Van Haastert. PI3-kinase signaling contributes to orientation in shallow gradients and enhances speed in steep chemoattractant gradients. *J Cell Sci*, 121(Pt 21):3589–3597, Nov 2008.

[23] Till Bretschneider, Stefan Diez, Kurt Anderson, John Heuser, Margaret Clarke, Annette Mller-Taubenberger, Jana Khler, and Gnther Gerisch. Dynamic actin

patterns and Arp2/3 assembly at the substrate-attached surface of motile cells. *Curr Biol*, 14(1):1–10, Jan 2004.

[24] Till Bretschneider, Kurt Anderson, Mary Ecke, Annette Mller-Taubenberger, Britta Schroth-Diez, Hellen C Ishikawa-Ankerhold, and Gnther Gerisch. The three-dimensional dynamics of actin waves, a model of cytoskeletal self-organization. *Biophys J*, 96(7):2888–2900, Apr 2009.

[25] William M Brieher, Hao Yuan Kueh, Bryan A Ballif, and Timothy J Mitchison. Rapid actin monomer-insensitive depolymerization of Listeria actin comet tails by cofilin, coronin, and Aip1. *J Cell Biol*, 175(2):315–324, Oct 2006.

[26] G. C. Brown and B. N. Kholodenko. Spatial gradients of cellular phospho-proteins. *FEBS Lett*, 457(3):452–454, Sep 1999.

[27] Frank J Bruggeman, Hans V Westerhoff, Jan B Hoek, and Boris N Kholodenko. Modular response analysis of cellular regulatory networks. *J Theor Biol*, 218(4): 507–520, Oct 2002.

[28] Hanna Brzeska, Jake Guag, G. Michael Preston, Margaret A Titus, and Edward D Korn. The molecular basis of the dynamic relocalization of dictyostelium Myosin IB. *J Biol Chem*, Feb 2012.

[29] Joseph A Brzostowski, Carole A Parent, and Alan R Kimmel. A G alpha-dependent pathway that antagonizes multiple chemoattractant responses that regulate directional cell movement. *Genes Dev*, 18(7):805–815, Apr 2004.

[30] Huaqing Cai, Satarupa Das, Yoichiro Kamimura, Yu Long, Carole A Parent, and Peter N Devreotes. Ras-mediated activation of the TORC2-PKB pathway is critical for chemotaxis. *J Cell Biol*, 190(2):233–245, Jul 2010.

[31] Liang Cai, Alexander M Makhov, Dorothy A Schafer, and James E Bear. Coronin 1B antagonizes cortactin and remodels Arp2/3-containing actin branches in lamellipodia. *Cell*, 134(5):828–842, Sep 2008.

[32] Kenneth G Campellone and Matthew D Welch. A nucleator arms race: cellular control of actin assembly. *Nat Rev Mol Cell Biol*, 11(4):237–251, Apr 2010.

[33] Anders E Carlsson. Dendritic actin filament nucleation causes traveling waves and patches. *Phys Rev Lett*, 104(22):228102, Jun 2010.

[34] Lindsay B Case and Clare M Waterman. Adhesive F-actin waves: a novel integrin-mediated adhesion complex coupled to ventral actin polymerization. *PLoS One*, 6(11):e26631, 2011.

[35] Pascale G Charest and Richard A Firtel. Feedback signaling controls leading-edge formation during chemotaxis. *Curr Opin Genet Dev*, 16(4):339–347, Aug 2006.

[36] Pascale G Charest, Zhouxin Shen, Ashley Lakoduk, Atsuo T Sasaki, Steven P Briggs, and Richard A Firtel. A Ras signaling complex controls the RasC-TORC2 pathway and directed cell migration. *Dev Cell*, 18(5):737–749, May 2010.

[37] Chun-Lin Chen, Yu Wang, Hiromi Sesaki, and Miho Iijima. Myosin I links PIP3 signaling to remodeling of the actin cytoskeleton in chemotaxis. *Sci Signal*, 5 (209):ra10, 2012.

[38] K. C. Chen, A. Csikasz-Nagy, B. Gyorffy, J. Val, B. Novak, and J. J. Tyson. Kinetic analysis of a molecular model of the budding yeast cell cycle. *Mol Biol Cell*, 11(1):369–391, Jan 2000.

[39] Lingfeng Chen, Chris Janetopoulos, Yi Elaine Huang, Miho Iijima, Jane Borleis,

and Peter N Devreotes. Two phases of actin polymerization display different dependencies on PI(3,4,5)P3 accumulation and have unique roles during chemotaxis. *Mol Biol Cell*, 14(12):5028–5037, Dec 2003.

[40] Lingfeng Chen, Miho Iijima, Ming Tang, Mark A Landree, Yi Elaine Huang, Yuan Xiong, Pablo A Iglesias, and Peter N Devreotes. PLA2 and PI3K/PTEN pathways act in parallel to mediate chemotaxis. *Dev Cell*, 12(4):603–614, Apr 2007.

[41] C. P. Chia, A. Shariff, S. A. Savage, and E. J. Luna. The integral membrane protein, ponticulin, acts as a monomer in nucleating actin assembly. *J Cell Biol*, 120(4):909–922, Feb 1993.

[42] C. Y. Chung, G. Potikyan, and R. A. Firtel. Control of cell polarity and chemotaxis by Akt/PKB and PI3 kinase through the regulation of PAKa. *Mol Cell*, 7 (5):937–947, May 2001.

[43] Frank I Comer, Christopher K Lippincott, Joseph J Masbad, and Carole A Parent. The PI3K-mediated activation of CRAC independently regulates adenylyl cyclase activation and chemotaxis. *Curr Biol*, 15(2):134–139, Jan 2005.

[44] J. Condeelis, A. Bresnick, M. Demma, S. Dharmawardhane, R. Eddy, A. L. Hall, R. Sauterer, and V. Warren. Mechanisms of amoeboid chemotaxis: an evaluation of the cortical expansion model. *Dev Genet*, 11(5-6):333–340, 1990.

[45] Attila Csiksz-Nagy and Orkun S Soyer. Adaptive dynamics with a single two-state protein. *J R Soc Interface*, 5 Suppl 1:S41–S47, Aug 2008.

[46] J. C. Dallon and H. G. Othmer. A continuum analysis of the chemotactic signal seen by Dictyostelium discoideum. *J Theor Biol*, 194(4):461–483, Oct 1998.

[47] Adriana T Dawes and Leah Edelstein-Keshet. Phosphoinositides and Rho proteins

spatially regulate actin polymerization to initiate and maintain directed movement in a one-dimensional model of a motile cell. *Biophys J*, 92(3):744–768, Feb 2007.

[48] Adriana T Dawes, G. Bard Ermentrout, Eric N Cytrynbaum, and Leah Edelstein-Keshet. Actin filament branching and protrusion velocity in a simple 1D model of a motile cell. *J Theor Biol*, 242(2):265–279, Sep 2006.

[49] P. N. Devreotes and T. L. Steck. Cyclic 3',5' AMP relay in Dictyostelium discoideum. II. Requirements for the initiation and termination of the response. *J Cell Biol*, 80(2):300–309, Feb 1979.

[50] P. N. Devreotes and S. H. Zigmond. Chemotaxis in eukaryotic cells: a focus on leukocytes and Dictyostelium. *Annu Rev Cell Biol*, 4:649–686, 1988.

[51] Stefan Diez, Gnther Gerisch, Kurt Anderson, Annette Mller-Taubenberger, and Till Bretschneider. Subsecond reorganization of the actin network in cell motility and chemotaxis. *Proc Natl Acad Sci U S A*, 102(21):7601–7606, May 2005.

[52] M. C. Dinauer, T. L. Steck, and P. N. Devreotes. Cyclic 3',5'-AMP relay in Dictyostelium discoideum IV. Recovery of the cAMP signaling response after adaptation to cAMP. *J Cell Biol*, 86(2):545–553, Aug 1980.

[53] K. Doubrovinski and K. Kruse. Self-organization of treadmilling filaments. *Phys Rev Lett*, 99(22):228104, Nov 2007.

[54] K. Doubrovinski and K. Kruse. Cytoskeletal waves in the absence of molecular motors. *EPL (Europhysics Letters)*, 83(1):18003, 2008.

[55] K. Doubrovinski and K. Kruse. Self-organization in systems of treadmilling filaments. *Eur Phys J E Soft Matter*, 31(1):95–104, Jan 2010.

[56] James E. Ferrell and Wen Xiong. Bistability in cell signaling: How to make continuous processes discontinuous, and reversible processes irreversible. *Chaos*, 11(1):227–236, Mar 2001.

[57] P. R. Fisher, R. Merkl, and G. Gerisch. Quantitative analysis of cell motility and chemotaxis in Dictyostelium discoideum by using an image processing system and a novel chemotaxis chamber providing stationary chemical gradients. *J Cell Biol*, 108(3):973–984, Mar 1989.

[58] Leopoldo P. Franca, Guillermo Hauke, and Arif Masud. Revisiting stabilized finite element methods for the advective-diffusive equation. *Computer Methods in Applied Mechanics and Engineering*, 195(1316):1560 – 1572, 2006. ISSN 0045-7825. ¡ce:title¿A Tribute to Thomas J.R. Hughes on the Occasion of his 60th Birthday¡/ce:title¿.

[59] B. A. Francis and W. M. Wonham. The internal model principle for linear multivariable regulators. *Applied Mathematics & Optimization*, 2:170–194, 1975. ISSN 0095-4616. 10.1007/BF01447855.

[60] S. Funamoto, K. Milan, R. Meili, and R. A. Firtel. Role of phosphatidylinositol 3' kinase and a downstream pleckstrin homology domain-containing protein in controlling chemotaxis in dictyostelium. *J Cell Biol*, 153(4):795–810, May 2001.

[61] Satoru Funamoto, Ruedi Meili, Susan Lee, Lisa Parry, and Richard A Firtel. Spatial and temporal regulation of 3-phosphoinositides by PI 3-kinase and PTEN mediates chemotaxis. *Cell*, 109(5):611–623, May 2002.

[62] Andrea Gamba, Antonio de Candia, Stefano Di Talia, Antonio Coniglio, Federico Bussolino, and Guido Serini. Diffusion-limited phase separation in eukaryotic chemotaxis. *Proc Natl Acad Sci U S A*, 102(47):16927–16932, Nov 2005.

[63] Meghal Gandhi and Bruce L Goode. Coronin: the double-edged sword of actin dynamics. *Subcell Biochem*, 48:72–87, 2008.

[64] G. L. Garcia and C. A. Parent. Signal relay during chemotaxis. *J Microsc*, 231 (3):529–534, Sep 2008.

[65] Gnther Gerisch. Self-organizing actin waves that simulate phagocytic cup structures. *PMC Biophys*, 3(1):7, 2010.

[66] Gnther Gerisch, Till Bretschneider, Annette Mller-Taubenberger, Evelyn Simmeth, Mary Ecke, Stefan Diez, and Kurt Anderson. Mobile actin clusters and traveling waves in cells recovering from actin depolymerization. *Biophys J*, 87(5): 3493–3503, Nov 2004.

[67] Gnther Gerisch, Mary Ecke, Britta Schroth-Diez, Silke Gerwig, Ulrike Engel, Lucinda Maddera, and Margaret Clarke. Self-organizing actin waves as planar phagocytic cup structures. *Cell Adh Migr*, 3(4):373–382, 2009.

[68] Gnther Gerisch, Mary Ecke, Dirk Wischnewski, and Britta Schroth-Diez. Different modes of state transitions determine pattern in the Phosphatidylinositide-Actin system. *BMC Cell Biol*, 12:42, 2011.

[69] L. Giot, J. S. Bader, C. Brouwer, A. Chaudhuri, B. Kuang, Y. Li, Y. L. Hao, C. E. Ooi, B. Godwin, E. Vitols, G. Vijayadamodar, P. Pochart, H. Machineni, M. Welsh, Y. Kong, B. Zerhusen, R. Malcolm, Z. Varrone, A. Collis, M. Minto, S. Burgess, L. McDaniel, E. Stimpson, F. Spriggs, J. Williams, K. Neurath, N. Ioime, M. Agee, E. Voss, K. Furtak, R. Renzulli, N. Aanensen, S. Carrolla, E. Bickelhaupt, Y. Lazovatsky, A. DaSilva, J. Zhong, C. A. Stanyon, R. L. Finley, K. P. White, M. Braverman, T. Jarvie, S. Gold, M. Leach, J. Knight, R. A.

Shimkets, M. P. McKenna, J. Chant, and J. M. Rothberg. A protein interaction map of Drosophila melanogaster. *Science*, 302(5651):1727–1736, Dec 2003.

[70] Jonathan M Goldberg, Eric S Wolpin, Leonard Bosgraaf, Bryan K Clarkson, Peter J M Van Haastert, and Janet L Smith. Myosin light chain kinase A is activated by cGMP-dependent and cGMP-independent pathways. *FEBS Lett*, 580(8):2059–2064, Apr 2006.

[71] A. Goldbeter and D. E. Koshland. An amplified sensitivity arising from covalent modification in biological systems. *Proc Natl Acad Sci U S A*, 78(11):6840–6844, Nov 1981.

[72] A. Goldbeter and D. E. Koshland. Sensitivity amplification in biochemical systems. *Q Rev Biophys*, 15(3):555–591, Aug 1982.

[73] B.D. Gomperts, I.M. Kramer, and P.E.R. Tatham. *Signal transduction*. Elsevier Academic Press, 2002.

[74] Bruce L Goode and Michael J Eck. Mechanism and function of formins in the control of actin assembly. *Annu Rev Biochem*, 76:593–627, 2007.

[75] Roger Guimer and Lus A Nunes Amaral. Functional cartography of complex metabolic networks. *Nature*, 433(7028):895–900, Feb 2005.

[76] P. J. Van Haastert and P. R. Van der Heijden. Excitation, adaptation, and deadaptation of the cAMP-mediated cGMP response in Dictyostelium discoideum. *J Cell Biol*, 96(2):347–353, Feb 1983.

[77] Peter J M Van Haastert. A stochastic model for chemotaxis based on the ordered extension of pseudopods. *Biophys J*, 99(10):3345–3354, Nov 2010.

[78] Peter J M Van Haastert and Peter N Devreotes. Chemotaxis: signalling the way forward. *Nat Rev Mol Cell Biol*, 5(8):626–634, Aug 2004.

[79] A. L. Hall, A. Schlein, and J. Condeelis. Relationship of pseudopod extension to chemotactic hormone-induced actin polymerization in amoeboid cells. *J Cell Biochem*, 37(3):285–299, Jul 1988.

[80] Ji W Han, Laura Leeper, Francisco Rivero, and Chang Y Chung. Role of RacC for the regulation of WASP and phosphatidylinositol 3-kinase during chemotaxis of Dictyostelium. *J Biol Chem*, 281(46):35224–35234, Nov 2006.

[81] L. H. Hartwell, J. J. Hopfield, S. Leibler, and A. W. Murray. From molecular to modular cell biology. *Nature*, 402(6761 Suppl):C47–C52, Dec 1999.

[82] Inbal Hecht, David A Kessler, and Herbert Levine. Transient localized patterns in noise-driven reaction-diffusion systems. *Phys Rev Lett*, 104(15):158301, Apr 2010.

[83] Inbal Hecht, Monica L Skoge, Pascale G Charest, Eshel Ben-Jacob, Richard A Firtel, William F Loomis, Herbert Levine, and Wouter-Jan Rappel. Activated membrane patches guide chemotactic cell motility. *PLoS Comput Biol*, 7(6):e1002044, Jun 2011.

[84] Doris Heinrich, Simon Youssef, Britta Schroth-Diez, Ulrike Engel, Daniel Aydin, Jacques Blmmel, Joachim P Spatz, and Gnther Gerisch. Actin-cytoskeleton dynamics in non-monotonic cell spreading. *Cell Adh Migr*, 2(2):58–68, 2008.

[85] Oliver Hoeller and Robert R Kay. Chemotaxis in the absence of PIP3 gradients. *Curr Biol*, 17(9):813–817, May 2007.

[86] Jifeng Hu, Anastasios Matzavinos, and Hans Othmer. A theoretical approach to

actin filament dynamics. *Journal of Statistical Physics*, 128:111–138, 2007. ISSN 0022-4715. 10.1007/s10955-006-9204-x.

[87] C. Y. Huang and J. E. Ferrell. Ultrasensitivity in the mitogen-activated protein kinase cascade. *Proc Natl Acad Sci U S A*, 93(19):10078–10083, Sep 1996.

[88] R. Insall, A. Kuspa, P. J. Lilly, G. Shaulsky, L. R. Levin, W. F. Loomis, and P. Devreotes. CRAC, a cytosolic protein containing a pleckstrin homology domain, is required for receptor and G protein-mediated activation of adenylyl cyclase in Dictyostelium. *J Cell Biol*, 126(6):1537–1545, Sep 1994.

[89] C. Janetopoulos, T. Jin, and P. Devreotes. Receptor-mediated activation of heterotrimeric G-proteins in living cells. *Science*, 291(5512):2408–2411, Mar 2001.

[90] Chris Janetopoulos, Lan Ma, Peter N Devreotes, and Pablo A Iglesias. Chemoattractant-induced phosphatidylinositol 3,4,5-trisphosphate accumulation is spatially amplified and adapts, independent of the actin cytoskeleton. *Proc Natl Acad Sci U S A*, 101(24):8951–8956, Jun 2004.

[91] Taeck J Jeon, Dai-Jen Lee, Susan Lee, Gerald Weeks, and Richard A Firtel. Regulation of Rap1 activity by RapGAP1 controls cell adhesion at the front of chemotaxing cells. *J Cell Biol*, 179(5):833–843, Dec 2007.

[92] Alexandra Jilkine, Athanasius F M Mare, and Leah Edelstein-Keshet. Mathematical model for spatial segregation of the Rho-family GTPases based on inhibitory crosstalk. *Bull Math Biol*, 69(6):1943–1978, Aug 2007.

[93] T. Jin, N. Zhang, Y. Long, C. A. Parent, and P. N. Devreotes. Localization of the G protein betagamma complex in living cells during chemotaxis. *Science*, 287 (5455):1034–1036, Feb 2000.

[94] Volker John and Petr Knobloch. On spurious oscillations at layers diminishing (SOLD) methods for convectiondiffusion equations: Part I A review. *Computer Methods in Applied Mechanics and Engineering*, 196(1720):2197 – 2215, 2007. ISSN 0045-7825.

[95] G. Jung, K. Remmert, X. Wu, J. M. Volosky, and J. A. Hammer. The Dictyostelium CARMIL protein links capping protein and the Arp2/3 complex to type I myosins through their SH3 domains. *J Cell Biol*, 153(7):1479–1497, Jun 2001.

[96] Helmut Kae, Chinten James Lim, George B Spiegelman, and Gerald Weeks. Chemoattractant-induced Ras activation during Dictyostelium aggregation. *EMBO Rep*, 5(6):602–606, Jun 2004.

[97] Helmut Kae, Arjan Kortholt, Holger Rehmann, Robert H Insall, Peter J M Van Haastert, George B Spiegelman, and Gerald Weeks. Cyclic AMP signalling in Dictyostelium: G-proteins activate separate Ras pathways using specific RasGEFs. *EMBO Rep*, 8(5):477–482, May 2007.

[98] D. Kahn and H. V. Westerhoff. Control theory of regulatory cascades. *J Theor Biol*, 153(2):255–285, Nov 1991.

[99] Yoichiro Kamimura and Peter N Devreotes. Phosphoinositide-dependent protein kinase (PDK) activity regulates phosphatidylinositol 3,4,5-trisphosphate-dependent and -independent protein kinase B activation and chemotaxis. *J Biol Chem*, 285(11):7938–7946, Mar 2010.

[100] Yoichiro Kamimura, Yuan Xiong, Pablo A Iglesias, Oliver Hoeller, Parvin Bolourani, and Peter N Devreotes. PIP3-independent activation of TorC2 and PKB at the cell's leading edge mediates chemotaxis. *Curr Biol*, 18(14):1034–1043, Jul 2008.

[101] Minchul Kang and Hans G Othmer. The variety of cytosolic calcium responses and possible roles of PLC and PKC. *Phys Biol*, 4(4):325–343, Dec 2007.

[102] Ineke Keizer-Gunnink, Arjan Kortholt, and Peter J M Van Haastert. Chemoattractants and chemorepellents act by inducing opposite polarity in phospholipase C and PI3-kinase signaling. *J Cell Biol*, 177(4):579–585, May 2007.

[103] B. N. Kholodenko, J. B. Hoek, H. V. Westerhoff, and G. C. Brown. Quantification of information transfer via cellular signal transduction pathways. *FEBS Lett*, 414 (2):430–434, Sep 1997.

[104] Dongsan Kim, Yung-Keun Kwon, and Kwang-Hyun Cho. The biphasic behavior of incoherent feed-forward loops in biomolecular regulatory networks. *Bioessays*, 30(11-12):1204–1211, Nov 2008.

[105] K. W. Kohn. Molecular interaction map of the mammalian cell cycle control and DNA repair systems. *Mol Biol Cell*, 10(8):2703–2734, Aug 1999.

[106] Arjan Kortholt and Peter J M van Haastert. Highlighting the role of Ras and Rap during Dictyostelium chemotaxis. *Cell Signal*, 20(8):1415–1422, Aug 2008.

[107] Arjan Kortholt, Holger Rehmann, Helmut Kae, Leonard Bosgraaf, Ineke Keizer-Gunnink, Gerald Weeks, Alfred Wittinghofer, and Peter J M Van Haastert. Characterization of the GbpD-activated Rap1 pathway regulating adhesion and cell polarity in Dictyostelium discoideum. *J Biol Chem*, 281(33):23367–23376, Aug 2006.

[108] Arjan Kortholt, Jason S King, Ineke Keizer-Gunnink, Adrian J Harwood, and Peter J M Van Haastert. Phospholipase C regulation of phosphatidylinositol 3,4,5-trisphosphate-mediated chemotaxis. *Mol Biol Cell*, 18(12):4772–4779, Dec 2007.

[109] Arjan Kortholt, Parvin Bolourani, Holger Rehmann, Ineke Keizer-Gunnink, Gerald Weeks, Alfred Wittinghofer, and Peter J M Van Haastert. A Rap/phosphatidylinositol 3-kinase pathway controls pseudopod formation. *Mol Biol Cell*, 21(6):936–945, Mar 2010.

[110] Arjan Kortholt, Rama Kataria, Ineke Keizer-Gunnink, Wouter N Van Egmond, Ankita Khanna, and Peter J M Van Haastert. Dictyostelium chemotaxis: essential Ras activation and accessory signalling pathways for amplification. *EMBO Rep*, 12(12):1273–1279, Dec 2011.

[111] D. E. Koshland, A. Goldbeter, and J. B. Stock. Amplification and adaptation in regulatory and sensory systems. *Science*, 217(4556):220–225, Jul 1982.

[112] A. Kremling, K. Bettenbrock, and E. D. Gilles. A feed-forward loop guarantees robust behavior in Escherichia coli carbohydrate uptake. *Bioinformatics*, 24(5): 704–710, Mar 2008.

[113] Paul W Kriebel, Valarie A Barr, and Carole A Parent. Adenylyl cyclase localization regulates streaming during chemotaxis. *Cell*, 112(4):549–560, Feb 2003.

[114] J. Krishnan and P. A. Iglesias. Analysis of the signal transduction properties of a module of spatial sensing in eukaryotic chemotaxis. *Bull Math Biol*, 65(1):95–128, Jan 2003.

[115] J. Krishnan and P. A. Iglesias. A modeling framework describing the enzyme regulation of membrane lipids underlying gradient perception in Dictyostelium cells. *J Theor Biol*, 229(1):85–99, Jul 2004.

[116] J. Krishnan and P. A. Iglesias. Receptor-mediated and intrinsic polarization and their interaction in chemotaxing cells. *Biophys J*, 92(3):816–830, Feb 2007.

[117] Hao Yuan Kueh, Guillaume T Charras, Timothy J Mitchison, and William M Brieher. Actin disassembly by cofilin, coronin, and Aip1 occurs in bursts and is inhibited by barbed-end cappers. *J Cell Biol*, 182(2):341–353, Jul 2008.

[118] Frank P L Lai, Malgorzata Szczodrak, Jennifer Block, Jan Faix, Dennis Breitsprecher, Hans G Mannherz, Theresia E B Stradal, Graham A Dunn, J. Victor Small, and Klemens Rottner. Arp2/3 complex interactions and actin network turnover in lamellipodia. *EMBO J*, 27(7):982–992, Apr 2008.

[119] Paul D Langridge and Robert R Kay. Mutants in the Dictyostelium Arp2/3 complex and chemoattractant-induced actin polymerization. *Exp Cell Res*, 313 (12):2563–2574, Jul 2007.

[120] Susan Lee, Francisco Rivero, Kyung Chan Park, Emerald Huang, Satoru Funamoto, and Richard A Firtel. Dictyostelium PAKc is required for proper chemotaxis. *Mol Biol Cell*, 15(12):5456–5469, Dec 2004.

[121] Susan Lee, Frank I Comer, Atsuo Sasaki, Ian X McLeod, Yung Duong, Koichi Okumura, John R Yates, Carole A Parent, and Richard A Firtel. TOR complex 2 integrates cell movement during chemotaxis and signal relay in Dictyostelium. *Mol Biol Cell*, 16(10):4572–4583, Oct 2005.

[122] Susan Lee, Zhouxin Shen, Douglas N Robinson, Steven Briggs, and Richard A Firtel. Involvement of the cytoskeleton in controlling leading-edge function during chemotaxis. *Mol Biol Cell*, 21(11):1810–1824, Jun 2010.

[123] Stefan Legewie, Nils Blthgen, and Hanspeter Herzel. Quantitative analysis of ultrasensitive responses. *FEBS J*, 272(16):4071–4079, Aug 2005.

[124] Stefan Legewie, Nils Blthgen, Reinhold Schfer, and Hanspeter Herzel. Ultrasensitization: switch-like regulation of cellular signaling by transcriptional induction. *PLoS Comput Biol*, 1(5):e54, Oct 2005.

[125] Andre Levchenko and Pablo A Iglesias. Models of eukaryotic gradient sensing: application to chemotaxis of amoebae and neutrophils. *Biophys J*, 82(1 Pt 1): 50–63, Jan 2002.

[126] Herbert Levine, David A Kessler, and Wouter-Jan Rappel. Directional sensing in eukaryotic chemotaxis: a balanced inactivation model. *Proc Natl Acad Sci U S A*, 103(26):9761–9766, Jun 2006.

[127] Liang Li, Simon F Nrrelykke, and Edward C Cox. Persistent cell motion in the absence of external signals: a search strategy for eukaryotic cells. *PLoS One*, 3 (5):e2093, 2008.

[128] Xin-Hua Liao, Jonathan Buggey, and Alan R Kimmel. Chemotactic activation of Dictyostelium AGC-family kinases AKT and PKBR1 requires separate but coordinated functions of PDK1 and TORC2. *J Cell Sci*, 123(Pt 6):983–992, Mar 2010.

[129] Harrit M Loovers, Marten Postma, Ineke Keizer-Gunnink, Yi Elaine Huang, Peter N Devreotes, and Peter J M van Haastert. Distinct roles of PI(3,4,5)P3 during chemoattractant signaling in Dictyostelium: a quantitative in vivo analysis by inhibition of PI3-kinase. *Mol Biol Cell*, 17(4):1503–1513, Apr 2006.

[130] Lan Ma, Chris Janetopoulos, Liu Yang, Peter N Devreotes, and Pablo A Iglesias. Two complementary, local excitation, global inhibition mechanisms acting in parallel can explain the chemoattractant-induced regulation of PI(3,4,5)P3 response in dictyostelium cells. *Biophys J*, 87(6):3764–3774, Dec 2004.

[131] Athanasius F M Mare, Alexandra Jilkine, Adriana Dawes, Vernica A Grieneisen, and Leah Edelstein-Keshet. Polarization and movement of keratocytes: a multi-scale modelling approach. *Bull Math Biol*, 68(5):1169–1211, Jul 2006.

[132] J. M. Mato, A. Losada, V. Nanjundiah, and T. M. Konijn. Signal input for a chemotactic response in the cellular slime mold Dictyostelium discoideum. *Proc Natl Acad Sci U S A*, 72(12):4991–4993, Dec 1975.

[133] Brn Meier, Alejandro Zielinski, Christoph Weber, Delphine Arcizet, Simon Youssef, Thomas Franosch, Joachim O Rdler, and Doris Heinrich. Chemotactic cell trapping in controlled alternating gradient fields. *Proc Natl Acad Sci U S A*, 108(28):11417–11422, Jul 2011.

[134] Martin Meier-Schellersheim, Xuehua Xu, Bastian Angermann, Eric J Kunkel, Tian Jin, and Ronald N Germain. Key role of local regulation in chemosensing revealed by a new molecular interaction-based modeling method. *PLoS Comput Biol*, 2(7):e82, Jul 2006.

[135] H. Meinhardt. Orientation of chemotactic cells and growth cones: models and mechanisms. *J Cell Sci*, 112 (Pt 17):2867–2874, Sep 1999.

[136] Subhanjan Mondal, Deenadayalan Bakthavatsalam, Paul Steimle, Berthold Gassen, Francisco Rivero, and Angelika A Noegel. Linking Ras to myosin function: RasGEF Q, a Dictyostelium exchange factor for RasB, affects myosin II functions. *J Cell Biol*, 181(5):747–760, Jun 2008.

[137] Travis I Moore, Ching-Shan Chou, Qing Nie, Noo Li Jeon, and Tau-Mu Yi. Robust spatial sensing of mating pheromone gradients by yeast cells. *PLoS One*, 3(12): e3865, 2008.

[138] Yoichiro Mori, Alexandra Jilkine, and Leah Edelstein-Keshet. Wave-pinning and cell polarity from a bistable reaction-diffusion system. *Biophys J*, 94(9):3684–3697, May 2008.

[139] Scott A Myers, Ji W Han, Yoonsung Lee, Richard A Firtel, and Chang Y Chung. A Dictyostelium homologue of WASP is required for polarized F-actin assembly during chemotaxis. *Mol Biol Cell*, 16(5):2191–2206, May 2005.

[140] Atul Narang. Spontaneous polarization in eukaryotic gradient sensing: a mathematical model based on mutual inhibition of frontness and backness pathways. *J Theor Biol*, 240(4):538–553, Jun 2006.

[141] Matthew P Neilson, Douwe M Veltman, Peter J M van Haastert, Steven D Webb, John A Mackenzie, and Robert H Insall. Chemotaxis: a feedback-based computational model robustly predicts multiple aspects of real cell behaviour. *PLoS Biol*, 9(5):e1000618, May 2011.

[142] Susana R Neves, Panayiotis Tsokas, Anamika Sarkar, Elizabeth A Grace, Padmini Rangamani, Stephen M Taubenfeld, Cristina M Alberini, James C Schaff, Robert D Blitzer, Ion I Moraru, and Ravi Iyengar. Cell shape and negative links in regulatory motifs together control spatial information flow in signaling networks. *Cell*, 133(4):666–680, May 2008.

[143] P. C. Newell. Signal transduction and motility of Dictyostelium. *Biosci Rep*, 15 (6):445–462, Dec 1995.

[144] Xiao Yu Ni, Tormod Drengstig, and Peter Ruoff. The control of the controller: molecular mechanisms for robust perfect adaptation and temperature compensation. *Biophys J*, 97(5):1244–1253, Sep 2009.

[145] Matthew Onsum and Christopher V Rao. A mathematical model for neutrophil gradient sensing and polarization. *PLoS Comput Biol*, 3(3):e36, Mar 2007.

[146] Hans G. Othmer and Pauline Schaap. Oscillatory cAMP Signaling in the Development of Dictyostelium discoideum. *Comments on Theor Biol*, 5:175–282, 1998.

[147] Mikiya Otsuji, Shuji Ishihara, Carl Co, Kozo Kaibuchi, Atsushi Mochizuki, and Shinya Kuroda. A mass conserved reaction-diffusion system captures properties of cell polarity. *PLoS Comput Biol*, 3(6):e108, Jun 2007.

[148] Alessia Para, Miriam Krischke, Sylvain Merlot, Zhouxin Shen, Michael Oberholzer, Susan Lee, Steven Briggs, and Richard A Firtel. Dictyostelium Dock180-related RacGEFs regulate the actin cytoskeleton during cell motility. *Mol Biol Cell*, 20(2):699–707, Jan 2009.

[149] C. A. Parent and P. N. Devreotes. A cell's sense of direction. *Science*, 284(5415): 765–770, Apr 1999.

[150] Kyung Chan Park, Francisco Rivero, Ruedi Meili, Susan Lee, Fabio Apone, and Richard A Firtel. Rac regulation of chemotaxis and morphogenesis in Dictyostelium. *EMBO J*, 23(21):4177–4189, Oct 2004.

[151] T. D. Pollard, L. Blanchoin, and R. D. Mullins. Molecular mechanisms controlling actin filament dynamics in nonmuscle cells. *Annu Rev Biophys Biomol Struct*, 29: 545–576, 2000.

[152] Thomas D Pollard and Gary G Borisy. Cellular motility driven by assembly and disassembly of actin filaments. *Cell*, 112(4):453–465, Feb 2003.

[153] Alice Y Pollitt and Robert H Insall. WASP and SCAR/WAVE proteins: the drivers of actin assembly. *J Cell Sci*, 122(Pt 15):2575–2578, Aug 2009.

[154] M. Postma and P. J. Van Haastert. A diffusion-translocation model for gradient sensing by chemotactic cells. *Biophys J*, 81(3):1314–1323, Sep 2001.

[155] Marten Postma, Jeroen Roelofs, Joachim Goedhart, Theodorus W J Gadella, Antonie J W G Visser, and Peter J M Van Haastert. Uniform cAMP stimulation of Dictyostelium cells induces localized patches of signal transduction and pseudopodia. *Mol Biol Cell*, 14(12):5019–5027, Dec 2003.

[156] Marten Postma, Jeroen Roelofs, Joachim Goedhart, Harrit M Loovers, Antonie J W G Visser, and Peter J M Van Haastert. Sensitization of Dictyostelium chemotaxis by phosphoinositide-3-kinase-mediated self-organizing signalling patches. *J Cell Sci*, 117(Pt 14):2925–2935, Jun 2004.

[157] E. Ravasz, A. L. Somera, D. A. Mongru, Z. N. Oltvai, and A. L. Barabsi. Hierarchical organization of modularity in metabolic networks. *Science*, 297(5586): 1551–1555, Aug 2002.

[158] Alexander W Rives and Timothy Galitski. Modular organization of cellular networks. *Proc Natl Acad Sci U S A*, 100(3):1128–1133, Feb 2003.

[159] Jeroen Roelofs and Peter J M Van Haastert. Characterization of two unusual guanylyl cyclases from dictyostelium. *J Biol Chem*, 277(11):9167–9174, Mar 2002.

[160] Erich Sackmann, Felix Keber, and Doris Heinrich. Physics of cellular movements. *Annual Review of Condensed Matter Physics*, 1(1):257–276, 2010.

[161] Atsuo T Sasaki, Cheryl Chun, Kosuke Takeda, and Richard A Firtel. Localized

Ras signaling at the leading edge regulates PI3K, cell polarity, and directional cell movement. *J Cell Biol*, 167(3):505–518, Nov 2004.

[162] Atsuo T Sasaki, Chris Janetopoulos, Susan Lee, Pascale G Charest, Kosuke Takeda, Lauren W Sundheimer, Ruedi Meili, Peter N Devreotes, and Richard A Firtel. G protein-independent Ras/PI3K/F-actin circuit regulates basic cell motility. *J Cell Biol*, 178(2):185–191, Jul 2007.

[163] P. Schaap and H.G. Othmer. Oscillatory cAMP signaling in the development of Dictyostelium discoideum. *Comments on Theoretical Biology*, 1998.

[164] R. Schaloske, J. Sonnemann, D. Malchow, and C. Schlatterer. Fatty acids induce release of Ca2+ from acidosomal stores and activate capacitative Ca2+ entry in Dictyostelium discoideum. *Biochem J*, 332 (Pt 2):541–548, Jun 1998.

[165] Britta Schroth-Diez, Silke Gerwig, Mary Ecke, Reiner Hegerl, Stefan Diez, and Gnther Gerisch. Propagating waves separate two states of actin organization in living cells. *HFSP J*, 3(6):412–427, Dec 2009.

[166] S. Y. Shvartsman, H. S. Wiley, W. M. Deen, and D. A. Lauffenburger. Spatial range of autocrine signaling: modeling and computational analysis. *Biophys J*, 81 (4):1854–1867, Oct 2001.

[167] Monica Skoge, Micha Adler, Alex Groisman, Herbert Levine, William F Loomis, and Wouter-Jan Rappel. Gradient sensing in defined chemotactic fields. *Integr Biol (Camb)*, 2(11-12):659–668, Nov 2010.

[168] R. Skupsky, W. Losert, and R. J. Nossal. Distinguishing modes of eukaryotic gradient sensing. *Biophys J*, 89(4):2806–2823, Oct 2005.

[169] E.D. Sontag. Adaptation and regulation with signal detection implies internal model. *Systems Control Lett.*, 50(2):119–126, 2003.

[170] C. Sordano, E. Cristino, F. Bussolino, B. Wurster, and S. Bozzaro. Platelet activating factor modulates signal transduction in Dictyostelium. *J Cell Sci*, 104 (Pt 1):197–202, Jan 1993.

[171] Victor Spirin and Leonid A Mirny. Protein complexes and functional modules in molecular networks. *Proc Natl Acad Sci U S A*, 100(21):12123–12128, Oct 2003.

[172] P. A. Spiro, J. S. Parkinson, and H. G. Othmer. A model of excitation and adaptation in bacterial chemotaxis. *Proc Natl Acad Sci U S A*, 94(14):7263–7268, Jul 1997.

[173] Bjrn Stuhrmann, Florian Huber, and Josef Ks. Robust organizational principles of protrusive biopolymer networks in migrating living cells. *PLoS One*, 6(1):e14471, 2011.

[174] K. K. Subramanian and Atul Narang. A mechanistic model for eukaryotic gradient sensing: spontaneous and induced phosphoinositide polarization. *J Theor Biol*, 231(1):49–67, Nov 2004.

[175] Kristen F Swaney, Chuan-Hsiang Huang, and Peter N Devreotes. Eukaryotic chemotaxis: a network of signaling pathways controls motility, directional sensing, and polarity. *Annu Rev Biophys*, 39:265–289, Jun 2010.

[176] Kosuke Takeda, Danying Shao, Micha Adler, Pascale G Charest, William F Loomis, Herbert Levine, Alex Groisman, Wouter-Jan Rappel, and Richard A Firtel. Incoherent feedforward control governs adaptation of activated Ras in a eukaryotic chemotaxis pathway. *Sci Signal*, 5(205):ra2, Jan 2012.

[177] Y. Tang and H. G. Othmer. A G protein-based model of adaptation in Dictyostelium discoideum. *Math Biosci*, 120(1):25–76, Mar 1994.

[178] Y. Tang and H. G. Othmer. Excitation, oscillations and wave propagation in a G-protein-based model of signal transduction in Dictyostelium discoideum. *Philos Trans R Soc Lond B Biol Sci*, 349(1328):179–195, Aug 1995.

[179] Georgios Tsiavaliaris, Setsuko Fujita-Becker, Ulrike Drrwang, Ralph P Diensthuber, Michael A Geeves, and Dietmar J Manstein. Mechanism, regulation, and functional properties of Dictyostelium myosin-1B. *J Biol Chem*, 283(8):4520–4527, Feb 2008.

[180] John J. Tyson and Hans G. Othmer. The dynamics of feedback control circuits in biochemical pathways. *Prog Theor Biol*, 5:1–60, 1978.

[181] John J Tyson, Katherine C Chen, and Bela Novak. Sniffers, buzzers, toggles and blinkers: dynamics of regulatory and signaling pathways in the cell. *Curr Opin Cell Biol*, 15(2):221–231, Apr 2003.

[182] Peter J M van Haastert and Marten Postma. Biased random walk by stochastic fluctuations of chemoattractant-receptor interactions at the lower limit of detection. *Biophys J*, 93(5):1787–1796, Sep 2007.

[183] Peter J M van Haastert, Ineke Keizer-Gunnink, and Arjan Kortholt. Essential role of PI3-kinase and phospholipase A2 in Dictyostelium discoideum chemotaxis. *J Cell Biol*, 177(5):809–816, Jun 2007.

[184] Domitilla Del Vecchio, Alexander J Ninfa, and Eduardo D Sontag. Modular cell biology: retroactivity and insulation. *Mol Syst Biol*, 4:161, 2008.

[185] Douwe M Veltman and Peter J M Van Haastert. Guanylyl cyclase protein and

cGMP product independently control front and back of chemotaxing Dictyostelium cells. *Mol Biol Cell*, 17(9):3921–3929, Sep 2006.

[186] Douwe M Veltman, Ineke Keizer-Gunnik, and Peter J M Van Haastert. Four key signaling pathways mediating chemotaxis in Dictyostelium discoideum. *J Cell Biol*, 180(4):747–753, Feb 2008.

[187] Michael G Vicker. Eukaryotic cell locomotion depends on the propagation of self-organized reaction-diffusion waves and oscillations of actin filament assembly. *Exp Cell Res*, 275(1):54–66, Apr 2002.

[188] Martin A Wear, Atsuko Yamashita, Kyoungtae Kim, Yuichiro Mada, and John A Cooper. How capping protein binds the barbed end of the actin filament. *Curr Biol*, 13(17):1531–1537, Sep 2003.

[189] Orion D Weiner, William A Marganski, Lani F Wu, Steven J Altschuler, and Marc W Kirschner. An actin-based wave generator organizes cell motility. *PLoS Biol*, 5(9):e221, Sep 2007.

[190] Matthew D Welch and R. Dyche Mullins. Cellular control of actin nucleation. *Annu Rev Cell Dev Biol*, 18:247–288, 2002.

[191] D. Wessels, H. Vawter-Hugart, J. Murray, and D. R. Soll. Three-dimensional dynamics of pseudopod formation and the regulation of turning during the motility cycle of Dictyostelium. *Cell Motil Cytoskeleton*, 27(1):1–12, 1994.

[192] Stephen Whitelam, Till Bretschneider, and Nigel J Burroughs. Transformation from spots to waves in a model of actin pattern formation. *Phys Rev Lett*, 102 (19):198103, May 2009.

[193] L. Wu, R. Valkema, P. J. Van Haastert, and P. N. Devreotes. The G protein beta

subunit is essential for multiple responses to chemoattractants in Dictyostelium. *J Cell Biol*, 129(6):1667–1675, Jun 1995.

[194] Jianhua Xing and Jing Chen. The Goldbeter-Koshland switch in the first-order region and its response to dynamic disorder. *PLoS One*, 3(5):e2140, 2008.

[195] Yuan Xiong, Chuan-Hsiang Huang, Pablo A Iglesias, and Peter N Devreotes. Cells navigate with a local-excitation, global-inhibition-biased excitable network. *Proc Natl Acad Sci U S A*, 107(40):17079–17086, Oct 2010.

[196] Xuehua Xu, Martin Meier-Schellersheim, Xuanmao Jiao, Lauren E Nelson, and Tian Jin. Quantitative imaging of single live cells reveals spatiotemporal dynamics of multistep signaling events of chemoattractant gradient sensing in Dictyostelium. *Mol Biol Cell*, 16(2):676–688, Feb 2005.

[197] Xuehua Xu, Martin Meier-Schellersheim, Jianshe Yan, and Tian Jin. Locally controlled inhibitory mechanisms are involved in eukaryotic GPCR-mediated chemosensing. *J Cell Biol*, 178(1):141–153, Jul 2007.

[198] Xuehua Xu, Tobias Meckel, Joseph A Brzostowski, Jianshe Yan, Martin Meier-Schellersheim, and Tian Jin. Coupling mechanism of a GPCR and a heterotrimeric G protein during chemoattractant gradient sensing in Dictyostelium. *Sci Signal*, 3(141):ra71, 2010.

[199] Jianshe Yan, Vassil Mihaylov, Xuehua Xu, Joseph A Brzostowski, Hongyan Li, Lunhua Liu, Timothy D Veenstra, Carole A Parent, and Tian Jin. A G$\beta\gamma$ Effector, ElmoE, Transduces GPCR Signaling to the Actin Network during Chemotaxis. *Dev Cell*, 22(1):92–103, Jan 2012.

[200] Changsong Yang, Martin Pring, Martin A Wear, Minzhou Huang, John A Cooper,

Tatyana M Svitkina, and Sally H Zigmond. Mammalian CARMIL inhibits actin filament capping by capping protein. *Dev Cell*, 9(2):209–221, Aug 2005.

[201] Changsong Yang, Lubov Czech, Silke Gerboth, Shin ichiro Kojima, Giorgio Scita, and Tatyana Svitkina. Novel roles of formin mDia2 in lamellipodia and filopodia formation in motile cells. *PLoS Biol*, 5(11):e317, Nov 2007.

[202] T. M. Yi, Y. Huang, M. I. Simon, and J. Doyle. Robust perfect adaptation in bacterial chemotaxis through integral feedback control. *Proc Natl Acad Sci U S A*, 97(9):4649–4653, Apr 2000.

[203] Sheng Zhang, Pascale G Charest, and Richard A Firtel. Spatiotemporal regulation of Ras activity provides directional sensing. *Curr Biol*, 18(20):1587–1593, Oct 2008.

[204] Tongli Zhang, Paul Brazhnik, and John J Tyson. Computational analysis of dynamical responses to the intrinsic pathway of programmed cell death. *Biophys J*, 97(2):415–434, Jul 2009.